UNIVERSITY OF LIEGE
Faculty of Sciences
Department of Chemistry

Center for Education and Research on Macromolecules (CERM)
Professor C. JEROME

Design of a dynamic covalent composite network for smart reprocessable shape memory systems

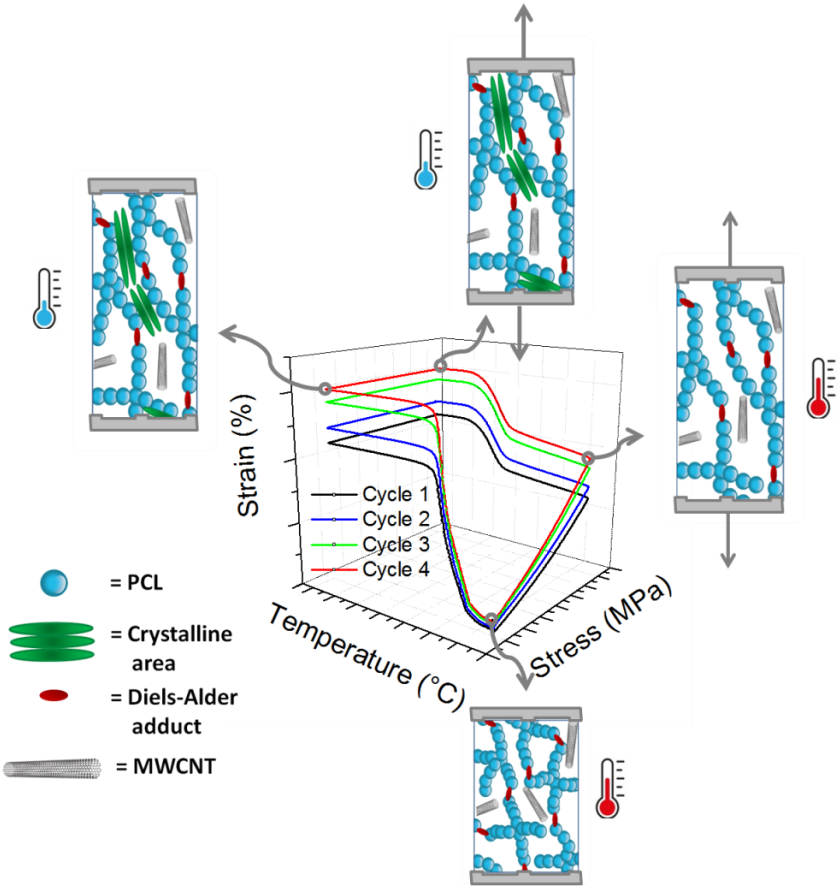

Dissertation presented by
Maxime HOUBBEN
To obtain the grade of
Doctor in Sciences
Academic Year 2022-2023

This research was funded by the '***Actions de recherche concertées 2017 – Synthesis, Characterization, and MultiScale Model of Smart Composite Materials (S3CM3) 17/21-07***', financed by the Directorate General for Non-Compulsory Education and Scientific Research (DGESVR), Direction of Scientific Research, Fédération Wallonie-Bruxelles and granted by the Académie Universitaire Wallonie Europe.

Evaluation committee:

Dr. Christophe DETREMBLEUR, University of Liège (President)
Prof. Philippe POULIN, University of Bordeaux
Prof. Jean-Marie RAQUEZ, University of Mons
Prof. Ludovic NOELS, University of Liège
Prof. Philippe VANDERBEMDEN, University of Liège (Secretary)
Prof. Christine JÉRÔME, University of Liège (Promoter)

Acknowledgements

A doctoral thesis results from a long and rigorous teamwork, so I would first like to thank everyone who took part in it, directly or indirectly. I could not have done it without your work, your support and encouragement.

First, I would like to thank Professor Christine Jérôme for allowing me to carry out this doctoral thesis in her laboratory. Christine, thank you for all your efforts to bring this project to life. I was lucky to benefit not only from your expertise and your foresight all these years, but also from the wonderful person that you are. Thank you for all the hours spent together, for your support, your constructive comments and encouragements. It has been a real pleasure to work with you, and as proof, almost all our meetings ended in sincere laughter. Thank you also for the many hours spent reviewing my work, especially this manuscript.

I would like to thank all the members of the S3CM3 project. Many thanks especially to Professor Ludovic Noels and Professor Philippe Vanderbemden for monitoring the project and bringing your expertise together. Your excellent suggestions and advices taught me many things and you were without a doubt an invaluable help during this research. You brought me a different vision to my usual chemist approach, taught me (a little bit) to think as an engineer, I learned a lot and continue to learn from you.

Thank you to you, now newly and freshly diplomed, Dr. Clara Andrea Pereira Sánchez, my closest partner in this adventure. I could not express how lucky and happy I am to have you by my side during these years. Thank you for your availability and the precious help you gave me from the beginning of this thesis until the very end. You have been an exceptional work partner, an attentive and kind friend. Thank you also to Vinayak Gopal, Hasan Gülaşik, Miguel Pareja Muñoz and Calleja Juan Manuel, the other PhD students and researchers involved in the S3CM3 project. It has been a pleasure to work with you. I would also like to

thank Doctor Jean-Michel Thomassin for his help and his expertise at the beginning of the project. You guided me during the first steps of this work and it was greatly appreciated.

I would also like to thank Doctor Detrembleur Christophe for agreeing to chair my thesis jury and to Professor Jean-Marie Raquez and Professor Philippe Poulin for paying attention to my work by accepting to be part of my thesis jury.

Thank you also to all the members of CERM who make this laboratory a pleasant workspace. Thank you to you all for the past years, it has been my privilege to be part of this CERM family. Thank you especially to the laboratory technicians: Valérie, Charlotte, Martine and Greg, who are essential to the proper functioning of the laboratory.

In a broader way, thank you to the Chemistry department and the University of Liège for the funding which gave me the opportunity to carry out this doctoral thesis.

Finally, my thanks go to my family and friends. Thank you to my parents for giving me the opportunity to do the studies I wanted, for following me and supporting me all these years. Thank you to all of you my friends, I would not dare to cite names, I would hate to forget a single one. Thank you for supporting me, helping me, pushing me forward and simply for your presence next to me. I would have never been able to do it without you all !

Abstract

Temperature-responsive shape memory polymers (SMPs) have gained significant attention for their use in various fields, including biomedical, aerospace, textiles, sensors, and actuators due to their low cost, easy processing, low density and large recoverable strains. In addition, improvement of their stiffness can be achieved by combining a shape memory polymer with various fillers leading to shape memory composites. Advantageously, the judicious selection of conductive or magnetic fillers also allows triggering the shape memory effect by internal resistive Joule heating or by the application of a magnetic field. Such remotely actuated SMPs are especially of interest for applications where the actuation by heating via increasing the temperature of the surrounding environment is not feasible, e.g., in implanted biomedical devices, or self-deployable aerospace structures. However, challenges remain, such as controlling fillers dispersion and interfacial strength, so as developing recyclable polymer materials and reprocessable networks in order to be part of an ecoresponsible and sustainable development fitting applications relevant for the future generation.

The objective of this thesis is to design high-performance shape-memory composites that can be reprocessed and/or recycled and internally actuated by Joule or magnetothermal effects. The strategy involves functionalizing the chain-ends of star-shaped poly-(ε-caprolactone) (PCL) by furan and maleimide moieties in order to reach a covalent adaptable network by the thermoreversible Diels-Alder addition. By adding fillers, i.e., multi-walled carbon nanotubes (MWCNTs) or Fe_3O_4 nanoparticles (NP) during blending, conductive or magnetic composite networks are obtained exhibiting a shape recovery actuated by Joule effect or magnetothermal effect. Semi-crystalline PCL was selected for its biocompatibility and remarkable mechanical and shape-memory properties. The impact of the diene nature (furan

or anthracene) and of the type of filler on the shape memory performances of composite stripes has been deeply investigated.

In addition, a solvent-free batch foaming process utilizing supercritical carbon dioxide ($scCO_2$) has been developed to produce recyclable shape-memory foams starting from the furan/maleimide PCL stars. Thanks to the thermal control of the PCL network density throughout the foaming process, foams with an unprecedented low density and exhibiting shape memory properties with high fixity and recovery ratios have been achieved. Additionally, these PCL shape memory foams are fully reprocessable. Application of these foams as self-deploying implant for vessel occlusion has been demonstrated in this work.

Résumé

Les polymères à mémoire de forme sensibles à la température ont fait l'objet d'une attention particulière pour leur utilisation dans divers domaines, notamment le biomédical, l'aérospatial, les textiles et les capteurs en raison de leur faible coût, de leur facilité de mise en œuvre, de leur faible densité et de leurs grandes déformations réversibles. En outre, il est possible d'améliorer leur rigidité en combinant un polymère à mémoire de forme avec diverses charges, ce qui permet d'obtenir des composites à mémoire de forme. De plus, la sélection judicieuse de charges conductrices ou magnétiques permet avantageusement de déclencher l'effet de mémoire de forme par chauffage interne par effet Joule ou par l'application d'un champ magnétique. De tels composites à mémoire de forme actionnée à distance sont particulièrement intéressants pour les applications où l'actionnement par chauffage via l'augmentation de la température du milieu environnant n'est pas réalisable, par exemple dans les dispositifs biomédicaux implantés ou les structures aérospatiales auto-déployables. Toutefois, il reste des défis à relever, tels que le contrôle de la dispersion des charges et de la résistance interfaciale, ainsi que le développement de matériaux recyclables et de réseaux remodelables pour s'inscrire dans un développement écoresponsable et durable et ainsi s'adapter à des applications pertinentes pour la génération future.

L'objectif de cette thèse est de concevoir des composites à mémoire de forme de haute performance qui peuvent être retraités et/ou recyclés et actionnés en interne par des effets Joule ou magnétothermiques. La stratégie consiste à fonctionnaliser les extrémités des chaînes de poly-(ε-caprolactone) (PCL) en forme d'étoile par des groupements furanes et maléimides afin d'obtenir un réseau covalent adaptable par addition de Diels-Alder thermoréversible. En ajoutant des charges, à savoir des nanotubes de carbone ou des

nanoparticules de Fe_3O_4 pendant le mélange, on obtient des réseaux composites conducteurs ou magnétiques capable de retrouver leur forme via un effet Joule ou un effet magnétothermique. La PCL semi-cristalline a été choisie pour sa biocompatibilité et ses remarquables propriétés mécaniques et de mémoire de forme. L'impact de la nature du diène (furane ou anthracène) et du type de charge sur les performances de mémoire de forme de rubans de ces composites a été étudié en profondeur.

De plus, un processus de moussage sans solvant utilisant du dioxyde de carbone supercritique ($scCO_2$) a été mis au point pour produire des mousses à mémoire de forme recyclables à partir des étoiles de PCL fonctionnalisées par les furane/maléimide. Grâce au contrôle thermique de la densité du réseau PCL tout au long du processus de moussage, des mousses inédites d'une faible densité et présentant des propriétés de mémoire de forme avec des taux de fixité et de récouvrance élevés ont été obtenues. En outre, ces mousses à mémoire de forme PCL sont entièrement recyclables. L'application de ces mousses en tant qu'implant auto-déployable pour l'occlusion de vaisseaux sanguins a été démontrée dans ce travail.

Table of contents

Chapter I

Introduction

Covalent Adaptable Networks: bringing a new dimension to shape memory polymers and composites

Chapter I

- List of abbreviations -

SM	Shape memory
SMP	Shape memory polymer
SMPC	Shape memory polymer composite
SMC	Shape memory composites
m-SMPs	Multiple shape memory polymers
SME	Shape memory effect
SCP	Shape changing polymer
CC-SMP	Chemical crosslinked SMP
PC-SMP	Physically crosslinked SMP
T	Temperature
T_m	Melting transition temperature
T_g	Glass transition temperature
R_f	Shape fixity ration
R_c	Shape recovery ratio
1W-SMPs	One-way shape memory polymers
2W-SMPs	Two-way shape memory polymers
2W-SMLs	Two-way shape memory laminates
SCN	Semi-crystalline networks
LC	Liquid crystalline
LCE	Liquid crystalline elastomers
IPNs	Interpenetrating polymer networks
CIE	Crystallization-induced elongation
MIC	Melt-induced contraction
UV	Ultraviolet
λ	Wavelength
PCL	Poly(ε-caprolactone)
PU	Polyurethane
PCO	Poly(cyclooctene)
PPD	Poly(pentadecalactone)
PEG	Poly(ethylene glycol)
PTMEG	Poly(tetramethylene ether) glycol

TEMPO	Tetramethylpiperidinyl-1-oxyl
TBD	1,5,7-triazabicyclo[4.4.0]dec-5-ene
CAN	Covalent adaptable network
DCB	Dynamic covalent bond
DA	Diels-Alder
R.T.	Room temperature
SMASH	Shape memory assisted self-healing
NMP	Nitroxide mediated polymerization
CRP	Controlled radical polymerization
NIR	Near infrared light
TE	Transesterification
TTE	Transthioesterification
PHU	Polyhydroxyurethanes
TCM	Transcarbamoylation
CB	Carbon black
GO	Graphene oxide
CNT	Carbon nanotube
SWCNT	Single-walled carbon nanotube
MWCNT	Multi-walled carbon nanotube
ETA	Electrothermal actuators

Chapter I: Introduction

Covalent Adaptable Networks: bringing a new dimension to shape memory polymers and composites

I.1 Basics on shape memory effect in polymers

Stimuli-responsive materials are considered as smart because they can sense their surroundings and produce direct and straightforward responses[1]. Shape memory materials were discovered in 1932 by Olander Sweden who observed a gold-cadmium with shape memory properties. Once deformed, the alloy was capable of automatic recovery of its original shape when heated above a critical temperature. Shape memory polymers (SMPs) on the other hand were first mentioned by Vernon et al. in a dental patent in 1941[2] and mostly provoked interest since the 1960s. The first commercial product of SMPs, thermal-shrinkable polyethylene pipe, came out at that time. A decade later, the National Aeronautics and Space Administration launched the application of SMPs in aerospace industry, and started a research program for it. SMPs are part of this unique class of active smart materials capable of a controlled and reversible shape-change by the exposure to a specific external stimulus[3]. SMPs can "memorize" a manufactured permanent shape then be deformed in a macroscopic temporary shape, which can be freely designed, and come back to the initial permanent shape by the application of an appropriate trigger. The shape memory effect has been found in a variety of polymers including amorphous polymers[4,5], semi-crystalline polymers[6,7] and liquid crystalline elastomers (LCE)[8] and has been a growing interest for the past couple of decades as demonstrated on figure I.1. They are used in a broad range of applications such as smart textiles[9,10], smart medical devices[11,12], thermal sensors and actuators[13,14], aerospace applications[15,16], soft robotics[17,18] or 4D printing[19,20].

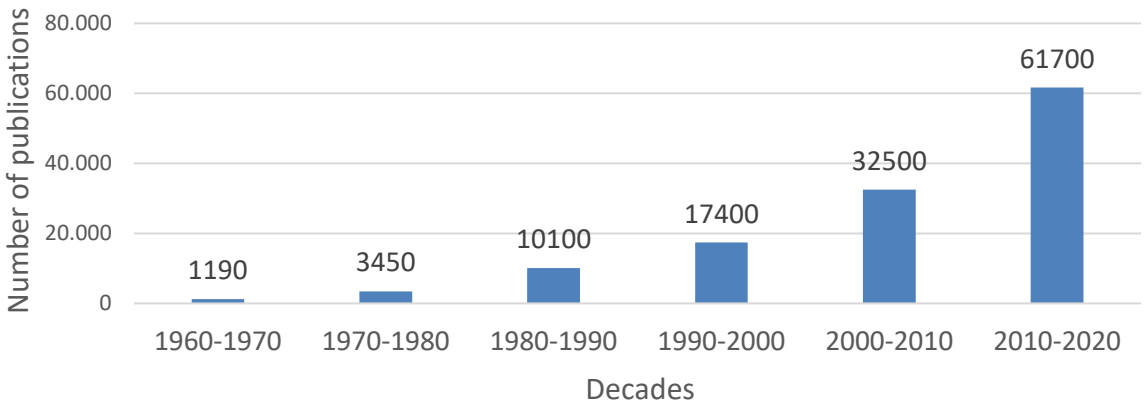

Figure I.1 – Publication trends of research on SMPs sorted by past decades. The data were obtained from Google Scholar on May 23rd 2022 by researching publications and patents with the term "Shape memory polymer".

Herein, we will introduce the basics on shape memory polymers. The concepts required to understand the shape memory effect in polymers will first be summarized, followed by the description of one-way, two-way, and multiple ways SMPs. Focus will then be made on reversibly crosslinked shape memory polymers in section I.2 and their advantages. Insights into the design of shape-memory polymer composites (SMPCs) with improved performances and controllable activation will then be given evidencing the main parameters influencing the shape memory behavior. Shape memory actuation methods as electrical current, magnetic field, light, and water will be illustrated so as recent progresses in shape memory applications.

I.1.1. Mechanism of the shape memory effect in polymers

The shape memory effect observed in polymers able to switch upon an external trigger from a programmed shape back to the original memorized shape, as represented in figure I.2, is a specific mechanical phenomenon finding its essence in the combination of two interacting domains[21]; one is elastic while the other is reversibly switchable from hard to soft[22]. A network either covalently (covalent bonds) or physically (intermolecular secondary interactions) crosslinked is required to observe the shape memory process. This network insures the memorization of the original shape. This first macroscopic original shape (figure I.2) is the starting point of this process. This shape can be deformed and fixed in a deformed state called

"programmed shape" (figure I.2). Under the right external stimulus, the material recovers the original shape ending the shape-memory cycle. Polymer networks exhibiting this shape memory cycling are called shape memory polymers (SMPs).

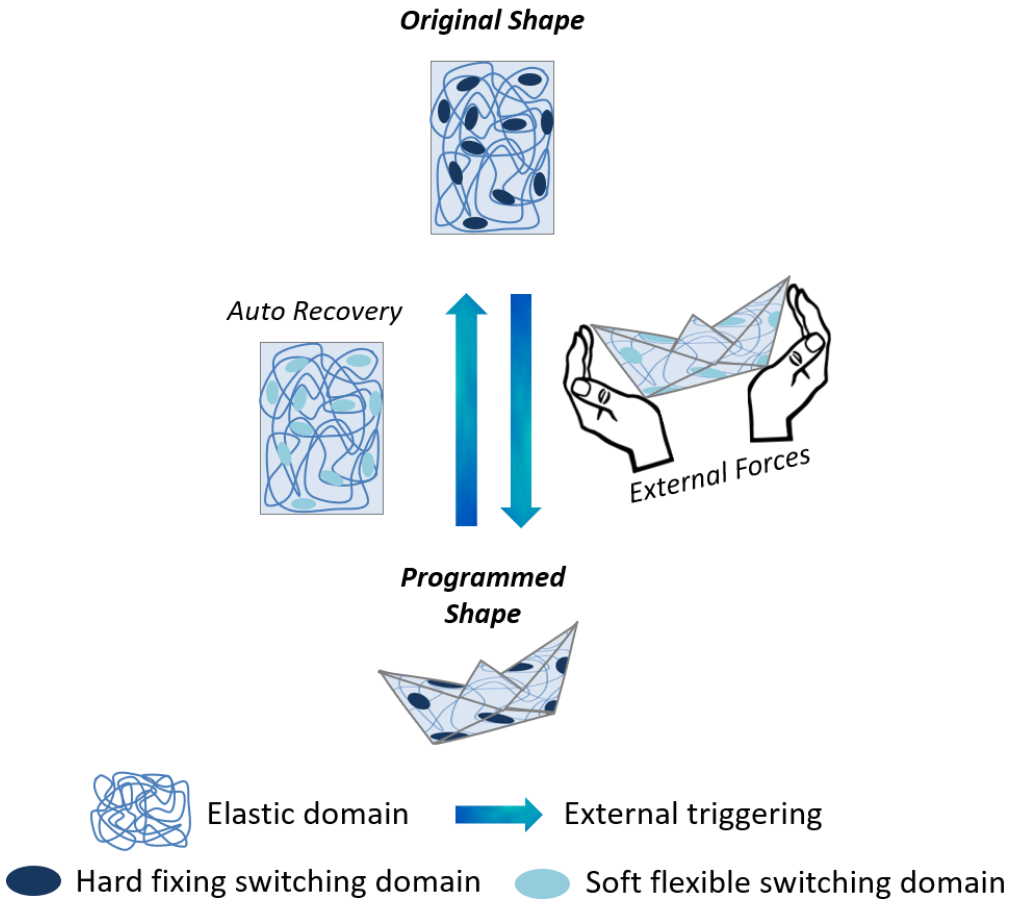

Figure I.2 – Description of a shape memory cycle.

The first step of the shape memory cycle consists in programming mechanically another shape. It requires first to switch the switching domain from hard to soft under the appropriate stimulus, most of the time by increasing the temperature[23]. Other stimuli such as light[24] or microwave[25], solvent vapors exposure[26], pH[27] or pressure variations[28] are also reported to trigger switching domains of different natures. The switching domain controls the morphing ability of the SMP. Under the right stimulus, this domain switches from a hard to its soft flexible state allowing macroscopic elastic deformation of the SMP. Increasing the temperature above glass transition temperature (T_g) for amorphous polymers or melting

transition temperature (T_m) for semi-crystalline ones switches the material to a rubbery state, which makes the crosslinked rubber easy to deform in a desired programmed shape also called temporary shape by application of the required stress (external forces). This shape is fixed by decreasing the temperature which reversibly hardens the switchable domain that prevent macroscopic elastic relaxation of the SMP upon stress release. This phenomenon stores the mechanical stress applied to previously deform the elastic material up to its programmed shape. Thanks to the crosslinking, irreversible deformation of the material is prevented during this programming step. Therefore, application of the physical or chemical trigger that softens again the switching domain allows the SMP to come back to the original shape by spontaneous stress release of the stored entropic energy in the deformed elastomer. Besides crystallization/melting transition[23] and rubber/glass state transition[29], liquid crystal anisotropic/isotropic transition[30] or supramolecular association/disassociation[31] can be found to actuate the shape memory process. In some cases, a shape alteration during shape programming is observed, for example, when a polymer is swelling in a good solvent. In this case, the polymer will be referred as a shape changing polymer (SCP) rather than an SMP[32]. For SMP, the procedure of programming/relaxation is qualified as an 'induced shape-memory effect' or 'shape-memory cycle'[33]. A combination of a well-defined molecular polymer network (elastic domain) and a reversible switching transition sensitive to external stimulus (transition domain)[3] allows this unique behavior as depicted in figure I.2. The programming process can be repeated multiple times; therefore, SMPs can be programmed in many different temporary shapes while returning always to a unique permanent shape.

The shape memory cycle can be used to evaluate the quality of a shape memory effect generally by describing some representative parameters of the cycle, namely the fixity and recovery ratios. The elasticity of the polymer network is responsible for the recovery of the original shape by recoiling of the polymer chains. Recovery properties of SMPs are thus dependent on the network properties such as crosslinking density and strength, length or entanglement of the chains. On the other hand, the transition domain is responsible for the fixity of the temporary shape. By switching from a soft to hard stiffness, it allows to store entropic energy in the programmed shape of the material. Shape fixity is defined as the ability

of the SMP material to keep the programmed shape when the programming load is released, i.e., the ability to sustain and store the entropic energy while the recovery ratio is the ability of the material to recover its permanent shape after the SMP cycle. Considering a one-dimensional case, the fixity (R_f) and recovery (R_c) ratios are expressed according to equation I.1 and equation I.2.

$$R_f = \frac{\text{strain after hardening of the transition domain and stress release}}{\text{strain after hardening of the transition domain without stress release}} * 100 \quad \text{(I.1)}$$

$$R_c = \frac{\text{strain after softening of the transition domain at the end of the SM cycle}}{\text{strain after softening of the transition domain at the end of the previous SM cycle}} * 100 \quad \text{(I.2)}$$

It should be noted that the decrease of the fixity ratio is induced by two factors; the restoring force of the stretched elastomer which tends to recover the original shape when the load is removed at the end of the programming step of the SMP cycle and a so-called cold recovery observed after long-term storage. Cold recovery is related to the material relaxation upon storage conditions. This relaxation process depends on temperature, internal forces stored in the material, external force that could be applied to the material during storage, time and chemical environment[3]. The higher the temperature and the greater the stored energy, the more rapidly cold recovery can occur.

Multiple programming processes can be applied to the SMP material if multiple hard domains are present, allowing multiple programming of the material in different temporary shapes and their stepwise recovery during the shape-memory cycles. Most of the SMPs are dual-shape materials, also called one-way SMP, which means that two different shapes are involved during the thermo-mechanical process. Recently, multi-shape polymers capable of fixing two or more tunable temporary shapes have been introduced[34].

Considering the nature of the switchable segments, the netpoints and the different triggers involved in the shape memory process, SMP can be classified as follows:

- One way shape memory polymers

  One-Way SMPs based on thermal state transitions
  One-Way SMPs based on reversible bonds

- Two-way shape memory polymers

  Two-way SMPs based on semicrystalline polymers
  Two-Way SMPs based on liquid crystal elastomers
  Two-Way SMPs based on interpenetrating networks
  Two-Way shape memory laminates

- Multiple way SMPs

I.1.2. One way shape memory polymers

One-Way SMPs triggered by the temperature

One-way SMPs (1W-SMPs) based on thermal transition (melting or glass transitions) as switching domain are the most commonly found thanks to their ease of production[35]. They consist of polymer chains with varying motion states across temperature as switchable segment[22]. Conventional thermoplastics; such as polyethylene (T_m ~ 160 °C), poly-ε-caprolactone (T_m ~ 60 °C), polypropylene (T_m ~ 160 °C) or polyvinyl chloride (T_m ~ 180 °C); covalently crosslinked or not have been developed for numerous commercial applications, thanks to their easily achieved switching temperature that is close to the body temperature for some of them. These SMP materials are characterized by the high deformation that can be achieved for the temporary shape. Therefore, these SMPs find applications as heat-shrinkable tubes[36], self-deployable stents[37] or self-tightening sutures[38]. Addition of different reinforcement fillers allows the production of shape memory composites with high mechanical performances and remote shape memory actuation capability (see section I.3).

One-Way SMPs triggered by UV light

Common methods to actuate SMPs with light while keeping constant the temperature are based on the use of reversibly photocleavable covalent bonds as additional crosslinks of elastomers. In 2005, Lendlein et al.[21] demonstrated that elastomers containing cinnamic groups can be deformed in a temporary shape and fixed by ultraviolet (UV) light irradiation. Indeed, the photoresponsive cinnamic groups dimerize when irradiated under UV light that is above a wavelength (λ) of 260 nm, forming additional crosslinks to fix the temporary shape. These dimers being thermally stable, the temporary shape is stable at temperature reaching 50 °C. Recovery is insured at room temperature when exposed to ultraviolet light of a wavelength below 260nm that reversibly cleaves the dimers and restores the initial elastomer network (figure I.3). As compared to thermal triggered SMPs, these systems exhibit lower fixity ratios due to the limited efficiency of the UV light induced dimerization. As elastomers, they are also characterized by lower stiffness as compared to thermoplastics.

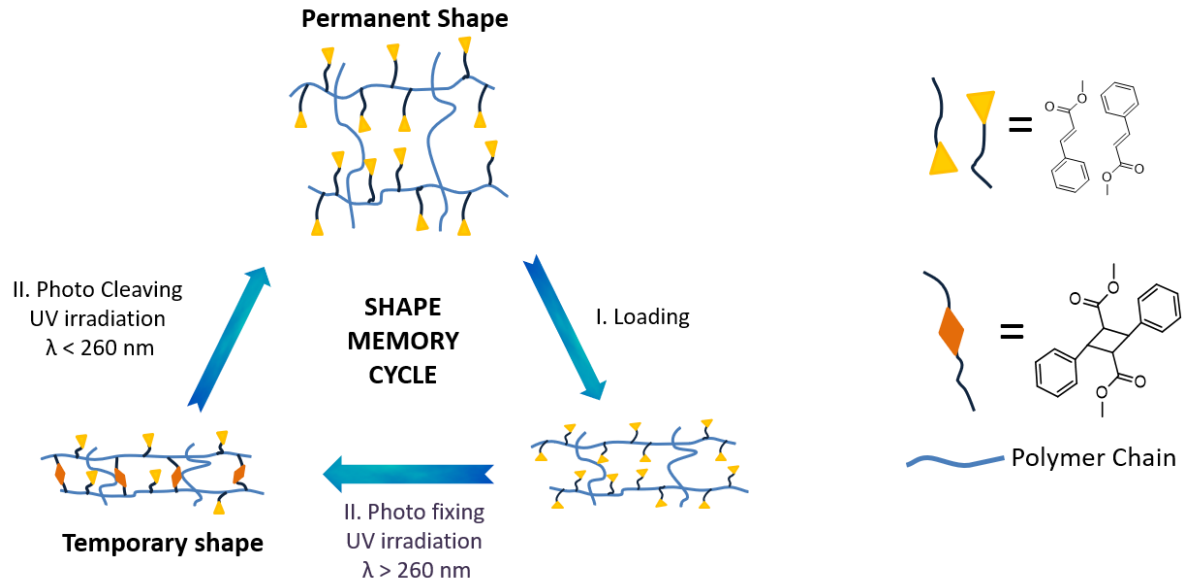

Figure I.3 - Photoresponsive cinnamic acid and cinnamylidene acetic acid grafted on a permanent network as switchable segments for UV light shape memory actuation (Adapted from Lendlein et al. 2005[21]).

Besides, another athermal light-triggered SMPs was developed by Yanlei Yu et al.[39] by inserting azobenzene moieties in a polymer network. The photoreversible cis-trans isomerization of these moieties allows the glass transition temperature of the material to be shifted above and below the room temperature as illustrated in figure I.4.

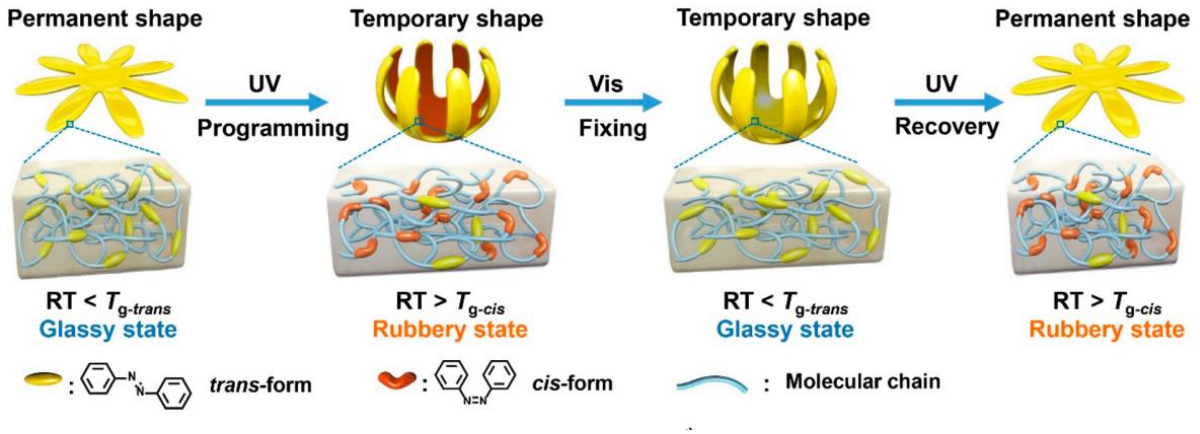

Figure I.4 – UV light actuated SMP shape memory cycle based on the shift of the Tg associated to the cis or trans isomers (Reproduced from ref[42]).

Other related light-triggered processes based on such light-induced isomerization were developed by Bowman[40,41], and Lendlein[42], where the trans-cis-trans rapid (< 5 min) reorientation of azobenzene chromophores induces twisting or uniaxial contraction and expansion of the macromolecular system leading to decrease of the T_g. These systems combine advantageously the high fixity and recovery insured by crossing the glass transition at constant the temperature using light as a trigger.

I.1.3. Two-way shape memory polymers

Reversibility of shape shifting can be a necessary requirement for some applications[43]. While 1W-SMPs consist of one-shot irreversible shape recovery and require subsequent reprogramming[38], two-way SMPs (2W-SMPs) exhibit self-contained and reversible shape change between the temporary and permanent shape simultaneously with temperature cycling. The term 2W-SMPs refers thus to smart materials capable of remembering two different shapes, each stable at different temperature allowing reversible switching by simple control of the temperature. Different strategies allow getting this interesting behavior as described below.

Two-way SMPs based on semi-crystalline networks

Semi-crystalline networks (SCN) conventionally used for 1W-SMP applications also exhibit 2W-SM properties. As firstly reported by Mather et al. in 2008[44], this property relies on the application of an external stress along one axis that induces an anisotropic arrangement of the chains under stress which modifies the crystallization process upon cooling. Under constant stress, the chain alignment of a crosslinked poly(cyclooctene) (PCO) network leads to an anisotropic crystallization upon cooling responsible for an increased elongation in the stress direction[45]. The resulting elongated material defines the new temporary shape. Elongations up to 20 % are generally achieved for such materials. Subsequently, a melt-induced contraction (MIC) is observed upon heating whereas the tensile stress remains

constant, leading to reversible shape switch. Under constant stress, crystallization induces a strain increment while melting induces a contraction, hence the 2W-SMP. Remarkably, this PCO based SMP exhibits both the 2W-SM and the 1W-SM behavior, as schematically presented in figure I.5. In stress-free recovery condition, the PCO behavior can be referred as a 1W-SME. Removing the external loading after programming allows full recovery and return to the original shape. The two-way actuation relies on crystallization induced elongation (CIE) and MIC under constant stress conditions allowing repeated shape memory behavior. Nevertheless, this 2W-SM strategy requires the constant application of an externally applied stress to be observed.

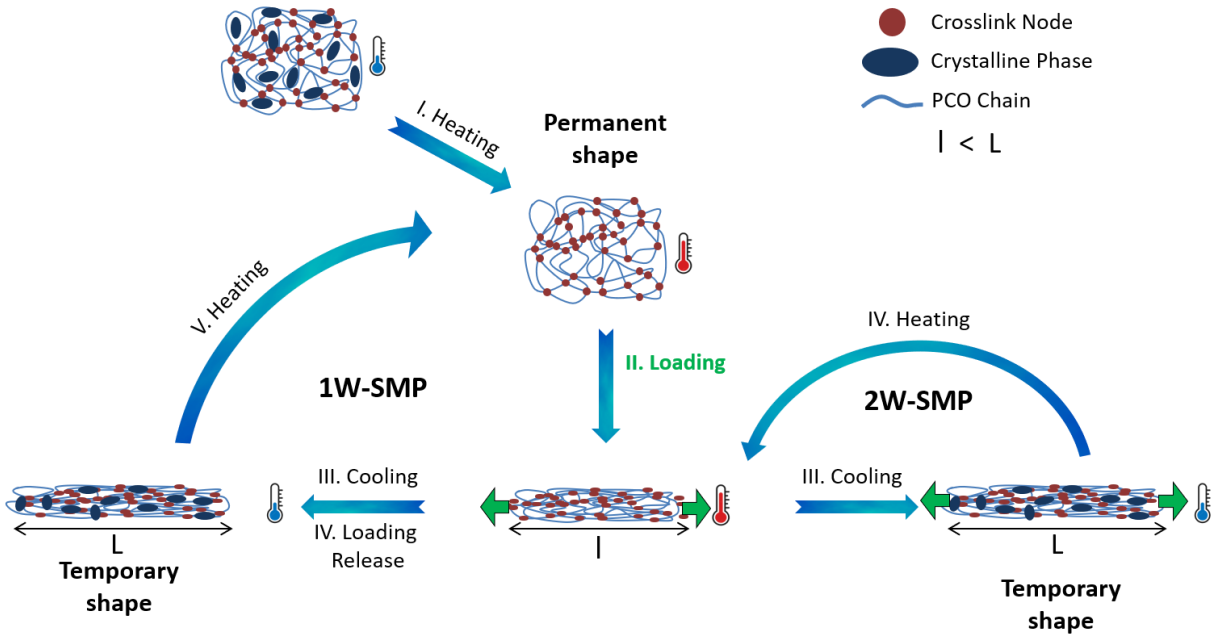

Figure I.5 – *Comparison between 1W-SMP and 2W-SMP.*

Later, 2W SMPs operating in stress-free conditions were developed notably by Leindlein et al.[46]. Multiphase copolyester-urethane networks containing two different types of crystallizable chain segments, namely poly(pentadecalactone) (PPD) ($T_{m\text{-}PPD}$ ~ 64 °C) and poly(ε-caprolactone) (PCL) ($T_{m\text{-}PCL}$ ~ 34°C) were designed with purposely two separated domains: the geometry-determining domain and the actuator domain. Crystallization of PPD segments acts as an internal stress application function and determines the geometry of the sample, while the PCL crystallization (actuator domain), acts as a trigger of the shape memory

effect. This 2Wmulti-phase SMP requires firstly programming above T_m of PPD to implement the shape shifting geometry (figure I.6 – a). The determining domains formed by crystallized PPD segments (figure I.6 – a, red) after cooling will ensure the internal stress during shape memory (SM) cycling. From that point, the multi-phase polyester acts as the previously described 2W-SMP. PCL segments will expand during cooling through CIE and collapse during heating through MIC (figure I.6 - a, green) in the direction influenced by the geometry-determining domain of PPD. Two different programmed shapes are thus obtained. Remarkably, Lendlein's work has overcome the external stress application concern while also allowing re-shaping of the temporary shape through heating above the melting temperature of the geometry-determining domain (T reset, figure I.6). Sample pictures showing the reversible SM effect is depicted in figure I.6 – b.

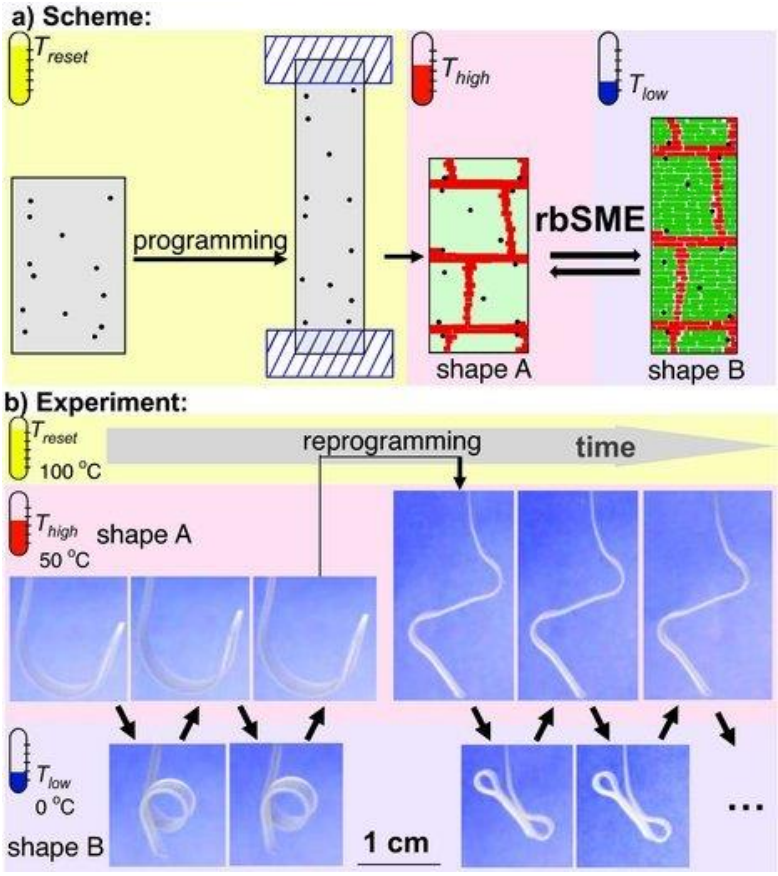

Figure I.6 – (a) Illustration of repeatedly reversible shape memory effect between shape A and B of PPD-PCL copolymer: the PPD crystalline domains (red) fix the shape A, and the reversible crystallization (dark green) and melting (light green) of PCL allows the back-and-forth switch to shape B. The black dots are crosslinks nodes; (b) Sample pictures showing the reversible SM effect (Reproduced from ref [46]).

Two-Way SMPs based on liquid crystal elastomers

Liquid crystalline elastomers (LCE) were synthesized for the first time by Finkelmann group in 1981[47] and the first reports of their shape memory abilities appeared in the 1990s[48,49]. LCEs exhibits remarkable thermo-mechanical behaviors thanks to the combination of the entropic elasticity of a crosslinked polymer network and the liquid crystalline (LC) anisotropy properties brought by their main-chain or side-chain groups, called mesogens. The principle behind the shape change relies on alignment directions during anisotropic phase transitions[50]. The mesogens can experience reversible mesomorphic to anisotropic phase transitions[43,51]. This thermally induced order–disorder of the mesogens is responsible for the thermal actuation of LCE based 2W-SMPs[52].

In stress free condition, those mesogens are disorderly oriented with respect to each other. This configuration is called LC poly-domain state (figure I.7, A) and represents the permanent shape of the SMP. Any external factor changing the underlying order parameter induces a transition from poly-domain to mono-domain LC phase (P-M transition), in which the LC domains align along the stress axis[43]. This anisotropic alignment leads to a crystallization-induced elongation upon cooling[53] (figure I.7 – B). As for 2W-SMPs based on SCN, the temporary shape is defined by the resulting macroscopic elongation. The reverse transition from mono-domain to poly-domain (M-P transition) induces a melt-induced contraction upon heating over the isotropization temperature. Impressive elongations are reached thanks to the LC network soft elastic property[54], exceeding 200 to 300 %, which can be actuated not only by temperature but also by light irradiation and solvents exposure[55].

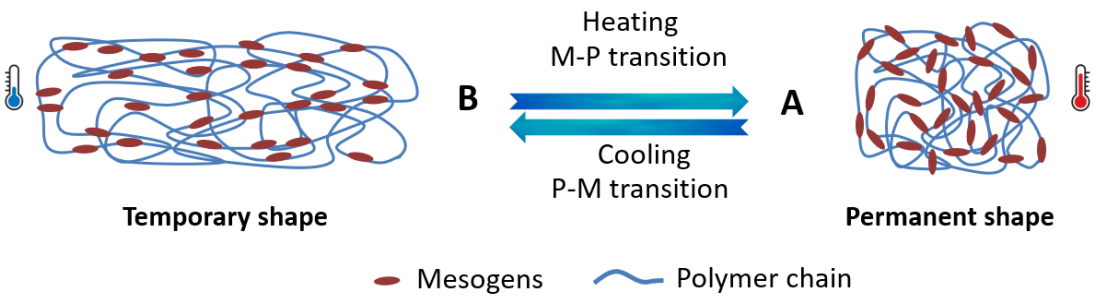

Figure I.7 - Mechanism of liquid crystal elastomer shape change of the polymer chains influenced by the anisotropic/isotropic deformation to its retracted configuration during M-P / P-M transition.

Two-Way SMPs based on interpenetrating networks

While 2W-SMPs based on SCN and LCE rely on single covalent networks, 2W-SMPs based on interpenetrated networks (IPNs) is based on physical embracing of two different networks and were introduced by Wu et al. in 2014[53]. The principle of these SM materials relies on a "switch-spring" composition. Classically, they are composed of one crystalline network (switch) and one elastomeric one (spring), which are respectively the geometry-determining and actuator domains. Phase separation can be observed between the two networks as they present physical entanglement but no chemical crosslinks between them[56]. The complex IPNs macromolecular architecture results from this kinetically entrapped mixing and thermodynamically driven phase separation[57].

In Wu et al. work, switch domains are ensured by a PCL crystalline network while a poly(tetramethylene ether) glycol (PTMEG) elastomeric network acts as the spring, bypassing the need for traditional external load application in 2W-SMPs cycling. Pre-programming is however also compulsory during the IPNs preparations. Figure I.8 schematically describes the sequential synthesis process used for the creation of a built-in force during preparation. Firstly, the PCL network is created and external load is applied. The elastomeric inter-penetrating PTMEG network is then synthesized in this elongated shape. By heating the system above the PCL transition temperature, compression is induced by the PCL shrinkage in the PTMEG network which compresses it as a spring. During cooling, the crystal-induced elongation of the PCL is driven in the spring direction by the elastic recovery of the PTMEG resulting in a permanent 2W-SMP without any need of external load or additional programming.

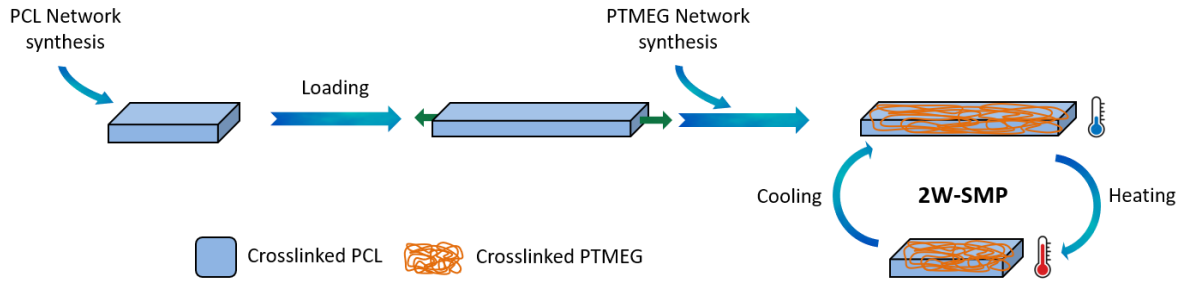

***Figure* I.*8 - Sketch of 2W-SMP based on interpenetrating network preparation and shape memory cycling* (Reproduced from ref[53]).**

Easy and inexpensive to synthesize, sequential synthesis can be used to prepare IPNs through different methods. While the majority of IPNs consist in covalently crosslinked interpenetrated networks, other works report on the preparation of "semi-IPN", consisting in a linear physically entangled polymer network in a second chemically crosslinked network[58]. Double crystalline networks presenting sufficiently different crystallization temperature can also be used for IPNs preparation. IPNs presenting low transition temperature, do not lose their 2W-SME at high temperature (as compared to LCEs) and have no need for an external force application for SM programming.

Two-Way shape memory laminates

2W-SM effect can also result from the macroscopic association of two different materials. This is the case of shape memory laminates (2W-SMLs) composed of a bilayer of two polymer networks, generally held together with the help of adhesives. In 2008, Chen et al reported on a method of lamination for an elastomeric film on an SM polyurethane film[59]. Classically, those composites are composed of one 1W-SMP layer combined to an elastomer layer. As for 2W-SMPs based on IPNs, a pre-programming step is required during the laminate preparation (figure I.9). The 1W-SMP layer is shaped over its transition temperature and cooled down through a classical shape memory programming. The elastomer layer is then laminated on top of the first layer using adhesive. Upon heating, the first SMP layer tends to recover its initial shape, supplying a compressive force to the top elastomeric layer, resulting in the overall bending of the laminate[60]. A similar "switch-spring" phenomenon is ensured as for IPNs-SMPs. Under cooling, the elastomeric top layer expands due to crystallization and acts as a tensile force orienting the crystallization of the first layer, resulting in a reversible bending[61].

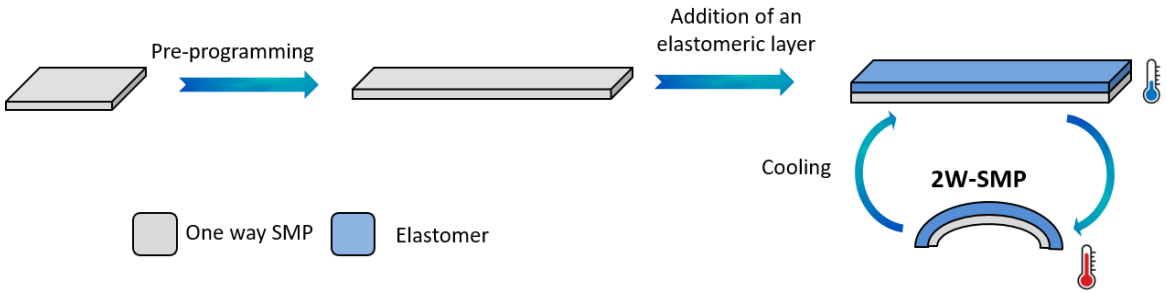

Figure I.9 - Sketch of two-way shape memory laminate preparation and shape memory cycling.

2W-SMLs are the easy and cheap ways to produce 2W-SME since the synthesis of each layer is straightforward and applies to many materials. Control over the processing parameters as layer thickness or initial 1W-SMP deformation allows the modulation of their physical properties and shape memory effect. The limitation results from the layer morphology that requires strong interfacial bonding to avoid alteration of the shape memory performances.

I.1.4. Multiple SMPs

Most SMPs are dual SMPs, switching from their temporary to permanent shape. However, some polymers are capable of memorizing more than one temporary shape in each shape memory cycle, they are called multiple SMPs (m-SMPs). They rely on polymers with multiple different segregated switching segments. The fixation of different temporary shapes is referred as multi-step programming and traditionally is based on separated phase transitions, broad phase transition and molecular switches domains.

Separated transition temperatures in a polymer blend or copolymers is the easiest way to prepare m-SMPs[62,63]. As previously described, multiple temporary shapes can be fixed through thermo-mechanical programming at different temperatures. Different temperature triggering over the involved temperature range will result in a triple, quadruple or other multiple-shape memory effect from the polymer.

In a similar way, a polymer presenting a broad T_m region can also exhibit some multiple-shape memory effects[64,65]. A broad thermal transition occurring on a large range of temperatures can be divided in several transitions in narrow temperature windows. As long as partial molecular mobility is activated in each temperature window, the m-SMP is able to exhibit some shape memory effect so that a different shape can be programmed for each window of temperature.

Finally, the use of several molecular switches in a same SMP or in combination with other 1W-SMPs also leads to m-SMPs[66]. The synergic combination of multiple photo-sensitive

units (sensitive at different wavelength), thermo-sensitive units (sensitive at different temperature) or the combination of one of them with a different photo-, water-, thermo-sensitive units all lead to the formation of m-SMPs. The use of polymer laminates with layers of different transition temperature[67] can also provide m-SMPs.

As illustrated on figure I.10, a trilayer laminate with layers exhibiting different T_g and thickness can store three temporal shapes and progressively recover the permanent shape by controlling the temperature. At a temperature of -25 °C, the thickest 250 µm middle layer holds the compressed spring shape – i.e., temporal shape III. Then, the spring unfolds into temporal shape II at 0 °C, i.e., the shape maintained by the 100 µm thick layer. At 45 °C temporal shape I (a reversed spring) is recovered as programmed within the last, thinnest layer. At 75 °C the recovery track is completed when the permanent shape is recovered.

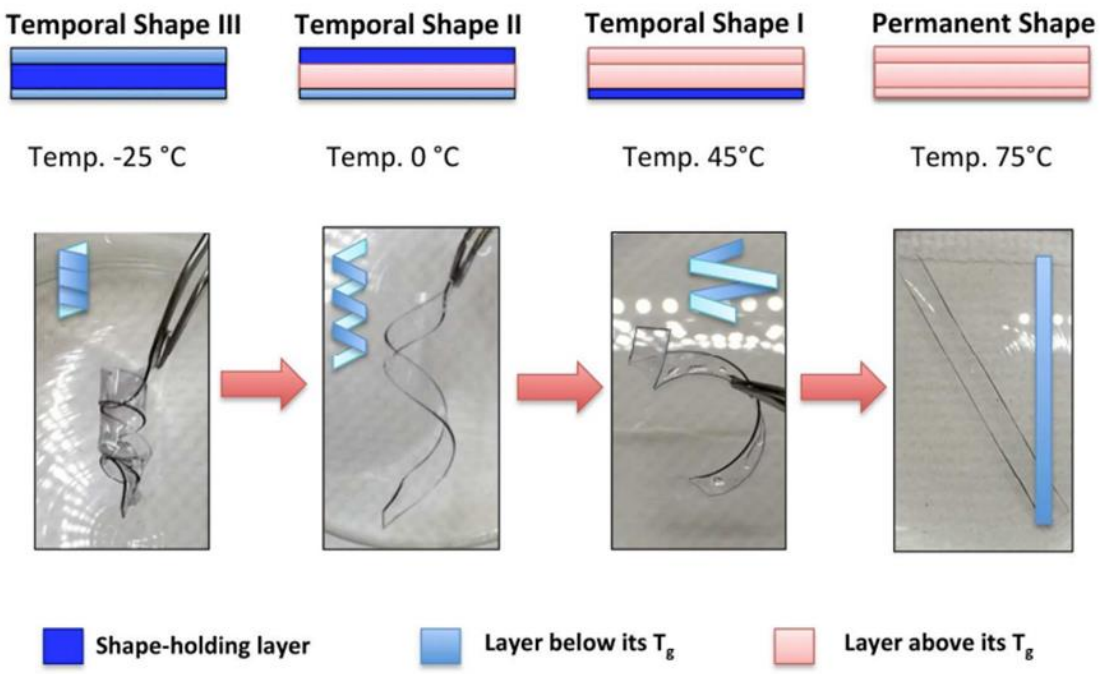

***Figure* I.10 – *Scheme of quadruple shape recovery cycle in a trilayer laminate* (Reproduced from ref [46]).**

I.2 SMPs based on dynamic covalent interactions

Covalent networks SMPs materials are improved by the resulting three-dimensional network formed. This results in an increased glass temperature and prevents the material from flowing at any temperature, thus enhancing the mechanical properties, particularly the elastic behavior when subjected to strain deformations. However, although this property is highly desirable for some applications, it also limits their processing and completely prevents recycling, since crosslinked polymers become insoluble and infusible. To address these processing limitations of polymer networks while preserving their remarkable properties, polymer chemists have developed several strategies. One of these involves creating covalent networks that include stimuli-reversible bonds. In 2010, C. Kloxin and C. Bowman[68] introduced the concept of covalent adaptable networks (CANs) as a family of materials that possess reversible covalent bonds in their structure. These bonds can repeatedly form and break via a reversible rearrangement reaction triggered by an external stimulus, such as changes in temperature or light irradiation. The stimulus-triggered rupture of these dynamic covalent bonds (DCBs) provides powerful properties brought by the possible topological network rearrangements, i.e., reshuffling of the network joints. Beside possible reprocessing, self-healing, welding and permanent shape reconfiguration can be considered while still promoting high fixity, high controllability by external stimuli and ease of programming[69]. The design of various original shapes and subsequently complex shape recovery pathways are also two of the main leading interests that triggered the development of this SMP class. With such reconfigurable networks, the design of permanent shapes with complex 3D geometries is easily achieved without the need to design complex molds. Furthermore, beside rigids DCB-SMPs, DCB-SM hygrogels have also drawn lots of attention recently thanks to their unique biocompatibility and structure with a wide variety of applications in medicine as biosensors and biomimetic systems[70]. Finally, novel 3D printing techniques are emerging nowadays with convenient and programmable design for which DCB-SMPs are perfectly suited.

Naturally, the inherent counterpart of those dynamic covalent bonding would be supramolecular bonding. Interactions of non-covalent bonds are generally much faster and

require less intensive stimuli (ex. lower temperature) to be triggered. But the slow kinetics of DCB allows for a much more stable thermodynamic equilibrium, in comparison to the relatively fragile assembly provided by non-covalent interactions[71]. Not surprisingly, higher performances can be expected by dynamically covalently bonded systems over supramolecular bonded systems which are commonly less stable leading to creep[72]. Supramolecular interactions being deeply described in other works[73,74], we will here discuss which and how dynamic bonds and dynamic exchange can be used for the design of shape memory materials.

DCBs-SMPs are stable in ambient conditions but have a dynamic behavior under stimuli resulting in bond exchanges either by associative or dissociative pathways (figure I.11). An associative substitution mechanism is a type of organic chemical reaction in which a new bond is formed before the rupture of the initial one. On the other hand, a dissociative substitution first requires the rupture of a bond before creating the new one.

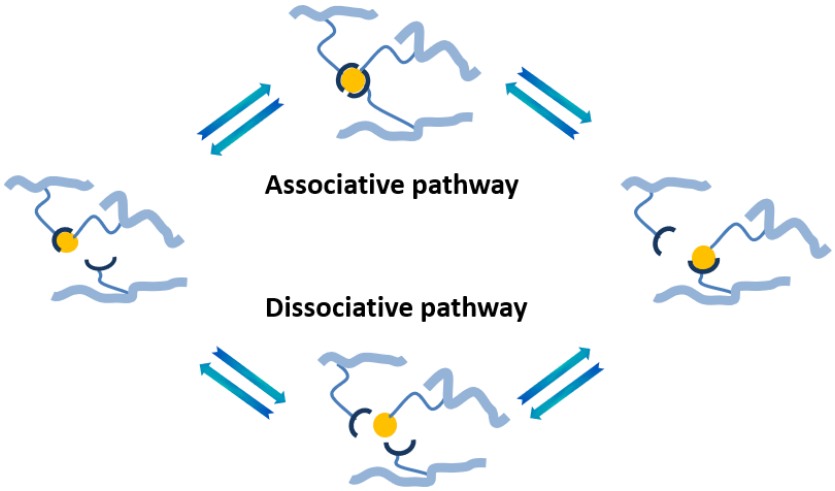

Figure I.11 - Associative and dissociative exchange pathways.

Crosslinked SMPs based on dissociative mechanism can be returned either to a thermoplastic-like behavior or back to the original monomer/oligomer thanks to the linkage dissociation in separated units. They present a sudden change from solid (amorphous I) to liquid (amorphous II) when T>Tg (figure I.12 - A). Those based on associative mechanisms exhibit constant crosslink density leading to a glass-forming behavior at the processing condition[75,76]. The latter are designed as vitrimers because of the resemblance of their thermal

properties to that of vitreous silica. Vitrimers design principle is based on the concept of reversible network topology freezing[77]. Through bond exchange reactions, the network can change its topology, which enables the material to relax stresses and flow, while maintaining a constant number of bonds that does not fluctuate over time. As a result, the material exhibits properties similar to those of a viscoelastic melt (similar to a glass-forming behavior). In vitrimers, exchange reactions are thermally activated, and upon cooling, the relaxation time and viscosity controlled by exchange reaction rates increase slowly and follow an Arrhenius law (figure I.12 - B). At a temperature Tv, the mechanical relaxation time controlled by the exchange reaction rate becomes much longer than the experimental time scale, and the network topology is frozen on this time scale. Consequently, the material appears as an elastic solid with an elastic modulus depending on the cross-link density. This gradual change of volume and thus viscosity (figure I.12 - B) differs from traditional thermosets in that they demonstrate a certain type of malleability[75]. This unique feature of the vitrimers allows reprocessing by stress relaxation. Moreover, it has been demonstrated that mechanical activation can also induce stress relaxation by the same pathway[78]. The incorporation of both thermal and mechanical activation in vitrimers provides a novel and advantageous reprocessing mechanism that enhances the usability of repairable polymer networks and broadens the range of chemical transformations possible with these materials.

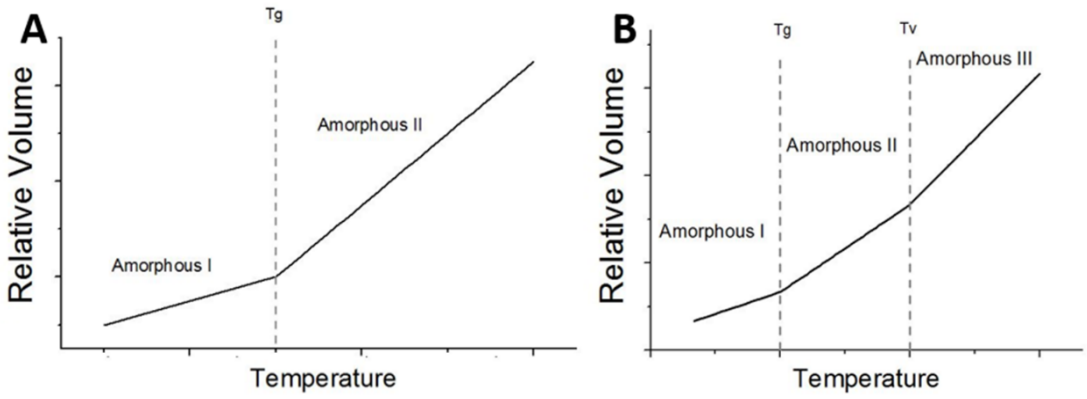

Figure I.12 - (A) Volume vs. temperature characteristics of a thermoplastic with a sudden change from solid (amorphous I) to liquid (amorphous II) when $T>T_g$; (B) Volume vs temperature characteristics of a vitrimer with gradual change in viscosity when T crosses T_g then T_v; at T_v the viscoelastic solid becomes a viscoelastic liquid.

The various reversible covalent bonds used in DCBs-SMPs based on both dissociative and associative pathways are summarized in figure I.13. The following will illustrate and discuss them when applied to SMPs.

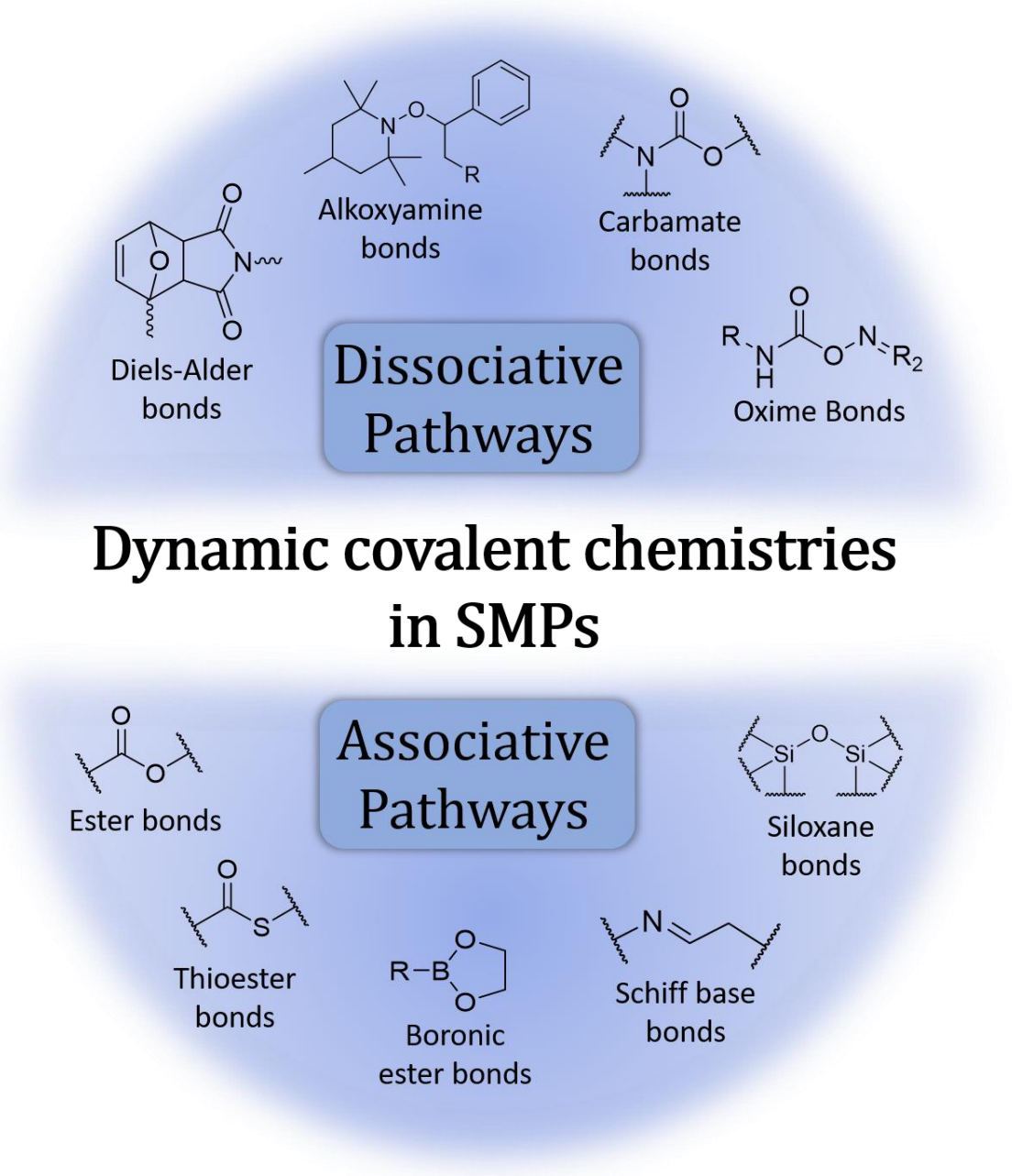

Figure I.13 - Reversible covalent bonds used for the preparation of DCB-SMPs.

I.2.1 SMPs including dissociative dynamic covalent bonds

The formation of Diels-Alder (DA) adducts is a representative example of a reaction allowing the introduction of dissociative dynamic bonds. First reported by Otto Diels and Kurt Alder in 1928 for which they were awarded in 1950 the Nobel Prize in Chemistry, this cycloaddition between furan and maleic anhydride is suitable for the formation of carbon-carbon bonds in a six membered ring with high stereochemical control (figure I.14). This DA cycloaddition thus proceed between a conjugated diene and an electro-deficient dienophile, leading to the formation of a six-membered ring via [4+2] cycloaddition. Characterized by an equilibrium, the forward reaction for the furane maleimide couple already occurs at room temperature (R.T.) and is dominant below 100°C while the retro-reaction occurs above 100 °C[79]. This DA adduct formation and cycloreversion (retro-DA) proceed thus in a convenient accessible temperature range to allow easy reprocessing of polymer network by increasing the temperature, while keeping a stable network in the conventional temperature range observed for shape memory thermoplastics. Additionally, the DA reaction is classified as a "click" reaction due to its excellent selectivity and efficiency[80]. Therefore, furan diene and maleimide dienophile were widely used to reversibly crosslink thermoplastic SMPs[81–91].

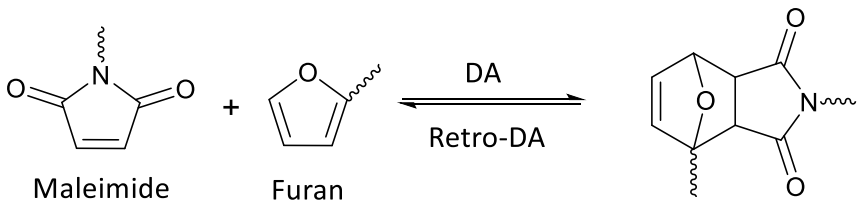

Figure I.14 – Thermoreversible DA reaction between furan and maleimide via concerted mechanism.

Stevens and Jenkins were the first to use the furan/maleimide addition to cross-link a polymer matrix in 1979[92]. Polystyrene with pending maleimide groups was used to react with a low molar mass bis-furan. Nowadays, the furan/maleimide DA reaction has been introduced in a wide variety of matrices such as poly(ε-caprolactone)[88]., poly(lactic-acid[93]), polyurethane[94], polyamides[95], polyketones[96], ethylene/propylene/diene rubbers[97] and epoxy resins[98]. It is worth also noticing that furan and furan derivatives can be produced from renewable resources which is particularly appealing in developing sustainable approaches.

Lately, our group participated in the preparation of star-shaped poly(ε-caprolactone) networks, already known to exhibit shape-memory properties when chemically or physically crosslinked, to create a new class of shape-memory polymers[88,89]. Using the thermoreversible Diels-Alder cycloaddition, this new DCB-SMP combines the advantages of both chemical crosslinked SMPs (CC-SMPs), such as excellent fixity and recovery ratios with minimal training cycles, and physically crosslinked SMPs (PC-SMPs), such as reprocessing and recyclability. The two functional polymers, respectively 4-arm star-shaped PCL end-capped by either maleimide or furan moieties (figure I.15), can be melt-blended together without significant torque increase when processed at a temperature favoring retro Diels-Alder reactions (125 °C). Curing the resulting blend at a lower temperature (65 °C) promotes Diels-Alder cycloaddition between furan and maleimide end groups, resulting in the formation of a PCL-based polymer network (figure I.15).

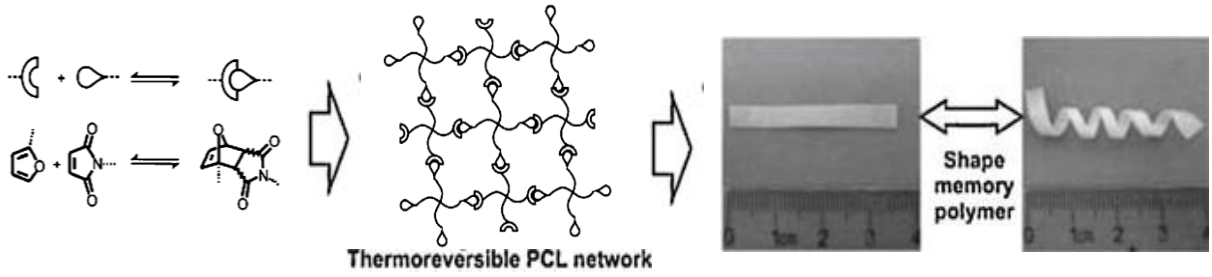

Figure I.15 – DA reaction between furan and maleimide chain-end of PCL-4MAL and PCL-4FUR forming a thermoreversible PCL network showing shape memory properties (Reproduced from ref[89]).

The resulting semi-crystalline crosslinked material exhibits excellent shape memory properties, with very high fixity ratios (above 99%) and excellent recovery ratios (88% for the first cycle and around 99% for subsequent cycles), both recorded by cyclic thermomechanical analysis (figure 15 - a). Unfortunately, the intrinsic dynamic behavior of the Diels-Alder bond leads to drawbacks in terms of mechanical properties. Indeed, just as previously described for vitrimers, induce stress relaxation by bond breaking through mechanical activation can occur causing a stress relaxation behavior during mechanical cycling. This behavior can be observed on the cyclic thermomechanical analysis where the mechanical properties of DCB-SMPs gradually decrease through cycling, resulting in a more ductile material after each cycle. A

consistent and significant rise in maximal strain for the same stress applied throughout the multiple cycling is observed and can be attributed to this presence of retro Diels-Alder reactions during testing (figure I.16 - a). This behavior, which is not present with a not dynamically crosslinked sample, may be presented as a disadvantage but represents a small price to pay to impart the sample with recyclability.

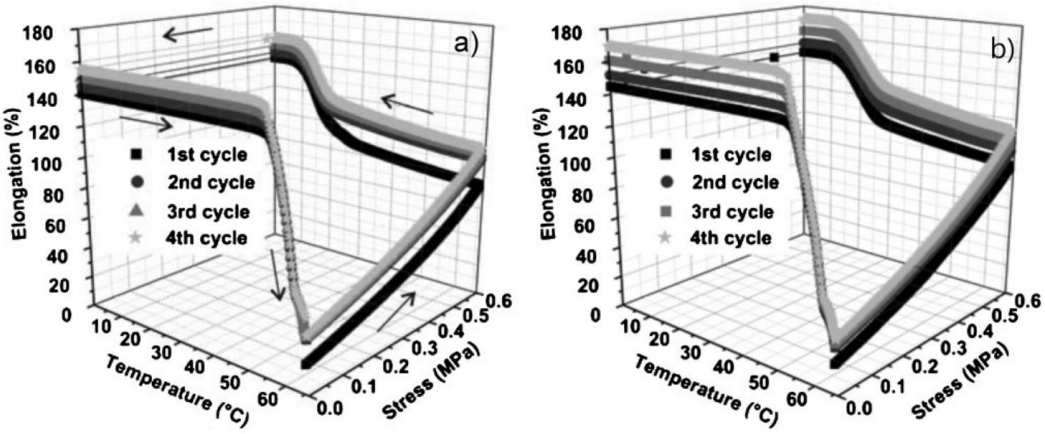

Figure I.16 – Shape-memory properties evaluated by thermomechanical cycling of (a) the initial PCL-4FUR/PCL-4MAL network; (b) the recycled PCL-4FUR/PCL-4MAL network (stress ramp: 0.06 MPa.min^{-1} ; temperature ramp: 3 °C .min^{-1} on heating and cooling (Reproduced from ref[89]).

Speaking of recyclability, the thermoreversible nature of the Diels-Alder adducts linking the star-shaped PCLs allows for easy disruption of the formed network by thermal treatment at 130 °C, enabling reprocessing of the SMP. Since the Diels-Alder chemistry follows a dissociative exchange pathway, the network can be reverted to the original monomers. Once returned to its low viscosity melt, the material can be reprocessed over and over again by the same initial method which is a huge benefit from the DCB chemistry. Upon curing the recycled material at 65 °C, the resulting recycled-SMP still exhibits excellent fixity and recovery ratios (figure I.16 – b) despite the same rise in maximal strain attributed to the presence of retro Diels-Alder reactions during testing. Using thermoreversible reactions to crosslink semi-crystalline polymers, such as PCL, has proven to be a highly effective technique for creating recyclable SMPs. This approach produces a material similar to CC-SMPs, but with the added benefit of recycling that is typical of PC-SMPs. The availability of various diene and dienophile pairs, which possess a broad range of Diels-Alder and retro Diels-Alder temperatures, enables

tuning of the thermoreversible bond equilibrium temperature. Coupled with a wide range of polymers that exhibit shape memory properties, this expands the potential applications of this innovative class of SMPs.

Another benefit of this SMP class was demonstrated by Du Prez's group who evidenced that the DA reaction reversibility allows shape memory assisted self-healing (SMASH)[94,99–101] of such damaged material. Indeed, they observed that when a crack occurs in a polyurethane network based on PCL and furan-maleimide DA linkages (figure I.17)[94], the heating of the material induces a shape memory response leading to a shrinking of the wounded area promoting contact between the damaged surfaces. Consequently, both reactive furan and maleimide moieties are brought in close contact so that the formation of the DA adduct is facilitated, hence the consequent healing of the material. The crack closure resulting on the account of shape memory function and the dynamic reaction resulting in healing is a common property observed for DCB-SMPs and is thus reported for a broad range of systems besides DA adducts chemistry. Other DCB-SMPs including a dissociative dynamic system exist relying on different chemistries such as alkoxyamine exchange or oxime bonds

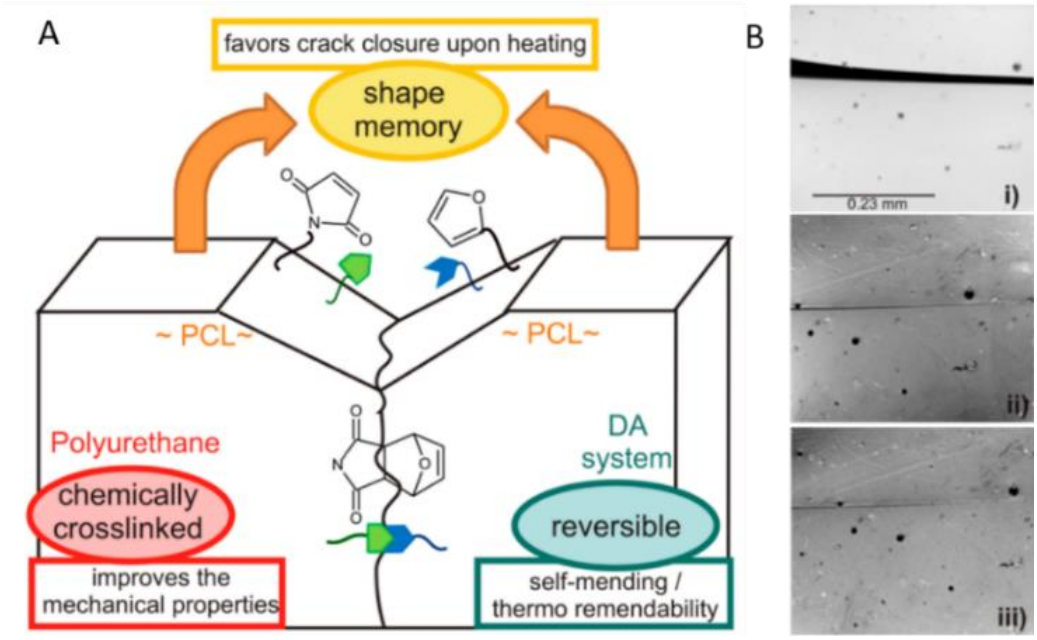

Figure I.17 – Shape memory assisted healing of damaged material based on PCL and furan-maleimide based DA linkages; (B) SEM images of (i) the original scratch, (ii) scratch after healing at 50 °C for 24 h, and (iii) scratch after heating at 100 °C for 1 h and healing for 24 h at 50°C (Reproduced from ref[94]).

Alkoxyamine exchange is a thermoreversible formation and dissociation proceeding via free radicals widely used in dynamic polymers synthesis. Crossover recombination of alkoxyamine (C-ON) bonds can occur by dissociation into nitroxide and carbon-centered radicals (figure I.18 – A). These inspired the controlled radical polymerization (CRP) and were extensively used in nitroxide mediated polymerization (NMP)[102]. Otsuka and Zang's groups were the first to report alkoxyamines as exchangeable sites for the preparation of self-healing polyurethane[103,104]. They discovered that this reversible reaction is sensitive to oxygen which requires the use of an inert gas such as argon to achieve high self-healing efficiency and thus limits possible applications of this chemistry as part of SMPs systems. Later, Zhang et al. proposed a new alkoxyamine based on 5-hydroxy-2-(4-hydroxy-2,2,6,6-tetramethylpiperidin-1-yloxy)-2- methyl pentanenitrile (CTPO) which contains a nitrile group attached to the carbon atom of the C−ON alkoxyamine bond (figure I.18 – B) allowing air insensitivity due to electron withdrawing ability of the nitrile that keeps the carbon radicals stable [105]. Just as CRP, these networks are living networks in the sense that monomers can be further incorporated through TEMPO mediated CRP allowing a modulation of the network mesh size and crosslinking density[106] . The use of this alkoxyamine exchange reaction can thus be particularly appealing for specific systems requiring this modulation.

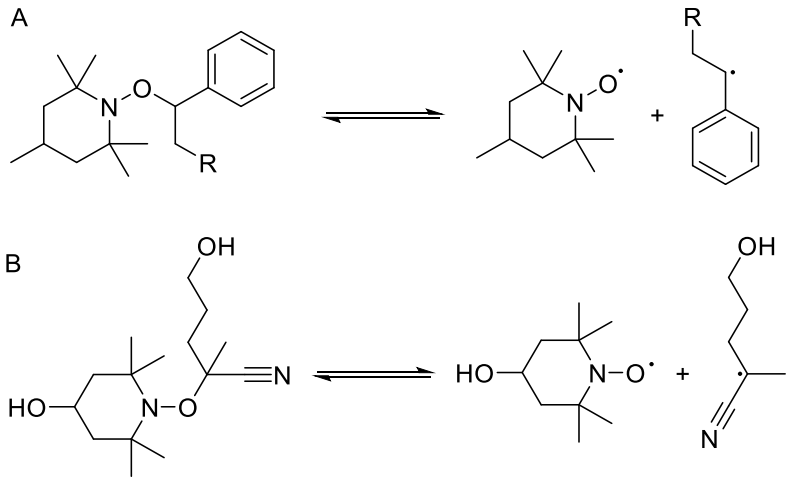

Figure I.18 – Thermoreversible homolytic rupture of an alkoxyamine bond: (A) classical air sensitive alkoxyamine (B) Oxygen stable CTPO.

Recently, by making use of this C-ON dynamic equilibrium, a 2W-SM behavior has been developed in a polyurethane (PU) network by Fan et al. [107]. The bond rupture / radical

recombination of a C-ON based PU leads to uneven stress relaxation through a whole SMP sample (figure I.19 - A & B). This heterogeneity induces a different relaxing behavior during the more classical 1W-SM cycling of the PU through induced melting/recrystallization. Nearly unrelaxed portions tend to recover their original shape in opposition to relaxed portions that maintain the extended status. In stress-free conditions, this internal stress ensures the 2W-SM behavior just as previously described in Leindlein et al. work[46] (section I.1.3). Moreover, reversibility of the C–ON bonds can be used for self-healing after crack through SM retractation[108] and endow recyclability to the material.

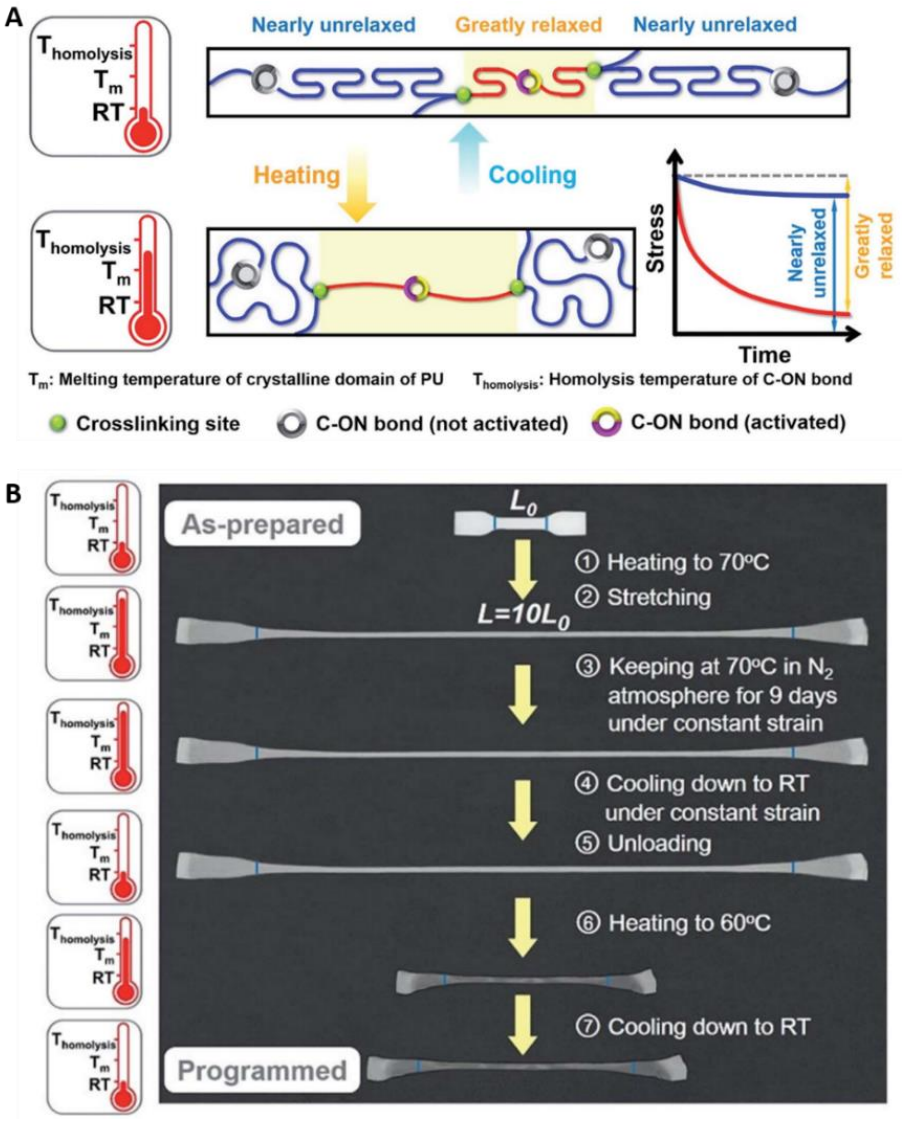

Figure I.19 – (A) Operation principle of the two-way shape memory effect of the programmed crosslinked PU; (B) Programming of the crosslinked PU towards the two-way shape-memory effect (Reproduced from ref [107]).

More recently, oxime-carbamate bonds have drawn lots of attention as a new kind of DCBs[109,110]. The fast reversibility of heat activated oxime-carbamate bond rupture (figure I.20) is particularly appealing to construct thermoreversible networks[111]. This reaction was thus successfully applied to develop reusable adhesives[112] or recyclable elastomers[113].

Figure I.20 – Thermoreversible formation of an oxime-carbamate bond (Reproduced from ref[111]).

Wang et al. recently developed a novel thermoplastic polyurethane by introducing dynamic oxime–carbamate bonds into PCL chains with the goal of enhancing mechanical properties of 3D/4D printed objects[110] (figure I.21 - A). Thanks to the rapid photothermal activation of the dissociation of these bonds, they achieved support-free printing of the material that exhibits excellent mechanical properties and possible healing of damaged printed products thanks to self-healing (figure I.21 – B). Moreover, as the printed products exhibit shape-memory properties by NIR irradiation or direct heating, potential in 4D applications were considered by the authors.

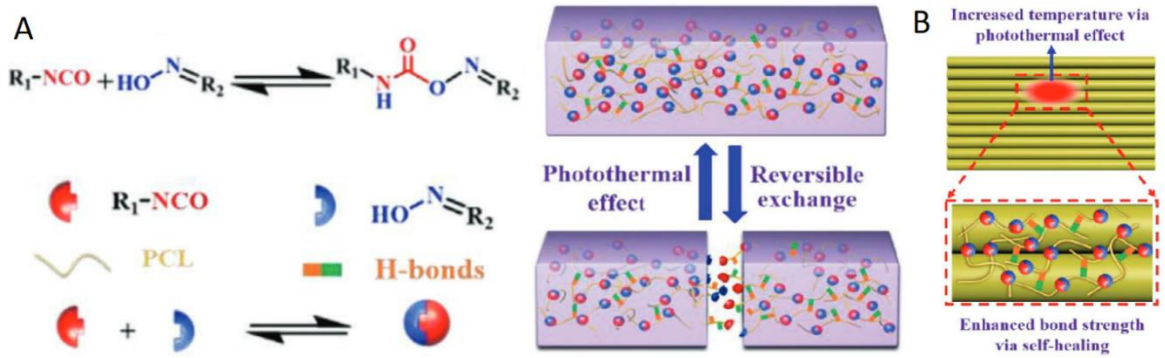

Figure I.21 – (A) Schematic of the self-healing process; (B) Schematic of the enhancement of the bond strength between the deposited layers of the 3D printed products (Adapted from ref[110]).

I.2.2 Shape memory vitrimers

Transesterification (TE) is one of the most representative reactions used in vitrimers[114]. This dynamic exchange-reaction consists in a substitution between an ester and an alcohol via an addition-elimination mechanism, i.e. an associative mechanism (figure I.22). The rate of this dynamic equilibrium is increased by rising the temperature and in most cases, it is activated by an acid or a base catalyst [115]. Transesterification as tool for producing DCBs-SMPs was firstly reported by Leibler et al. in 2011 who implemented TE in polyester materials crosslinked with epoxy acid or epoxy anhydride units by means of zinc acetate catalysis[116]. TE being an associative-based reaction, materials where these reactions are occurring, combine the mechanical advantages of thermosets with the reprocessing/recyclability of thermoplastics. TE vitrimers thus draw lots of attention in the recent years [117–122].

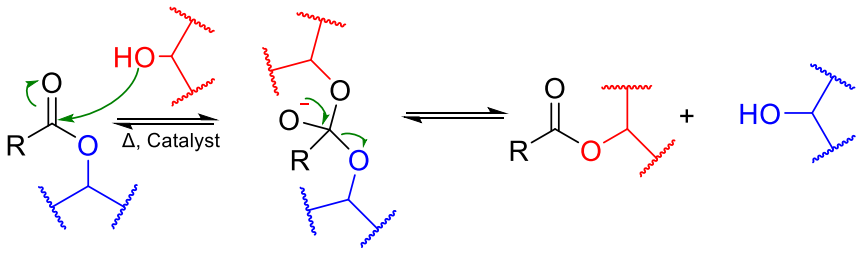

Figure I.22 – Mechanism of the thermo-activated equilibrium of associative bond exchange between ester and hydroxyl moieties through transesterification.

The main obstacles to the use of TE for SMPs are the potential hydrolysis of the esters, their degradation due to the high temperature required for the relaxation or the leaching of the catalyst. Interestingly, these are not always considered as drawbacks, temperature is no longer an issue with thermally stable materials, such as polycondensates, or the hydrolysis can be used for self-degrading implants. Interestingly, An-Chang Shi et al. recently took advantage of the needed Zn^{2+} catalyst to impart additional crosslinking to TE vitrimer network[123]. Copolymers obtained by radical polymerization of a vinylic monomers mixture containing carboxylic acid and zinc carboxylate groups, are converted into vitrimers in a single step by curing with diglycidylether of bisphenol A (figure I.23 – A). The added Zn^{2+} ions act not only as TE catalyst but also as crosslinking agents through ionic coordination with carboxylate groups, so that two different temporary shape can be programmed in the material (figure I.23 - B) [123]. Other multiple shapes TE-based SMPs materials have been developed on the same concept

from epoxy resins to bio-based elastomers targeting applications in various fields[124–128]. Similar materials have been obtained by urethane and urea-based vitrimers undergoing analogous exchange mechanism[129,130].

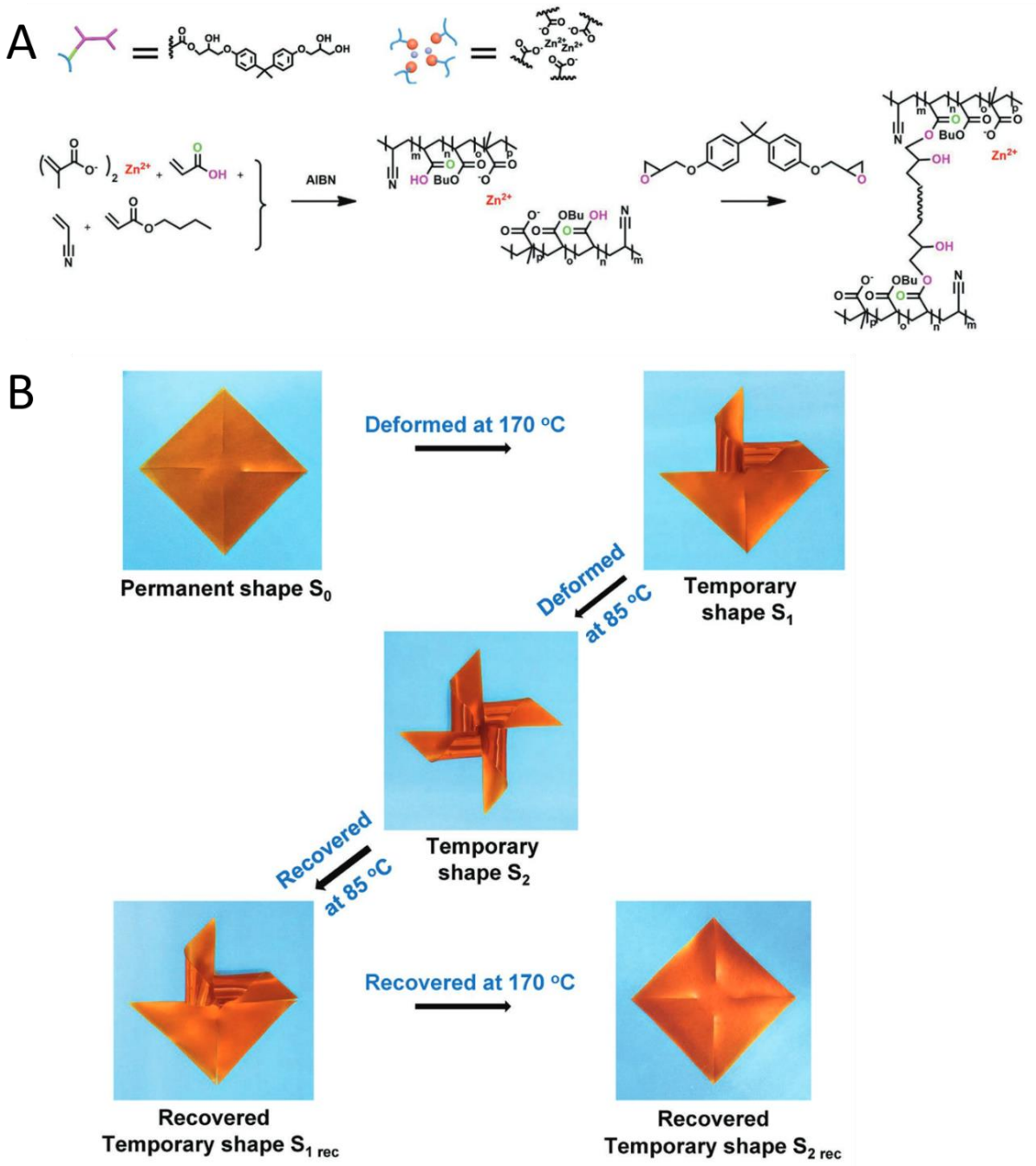

Figure I.23 – (A) Synthesis pathway of ionic cross-linked vitrimer Zn-PABAM; (B) Illustration of the triple shape memory effect of 7.5% Zn-PABAM vitrimers (Reproduced from ref [123]).

In terms of shape memory performances, considering similar matrices, SM vitrimers offer similar shape reconfiguration and recycling abilities as DCBs-SMPs based on a dissociative mechanism at the only condition that the temporary shape storage time scale is set much shorter than the mechanical relaxation time controlled by the exchange reaction rate. Indeed, the latent plasticity of vitrimers might affect the temporary shape fixity and thus shape recovery process. Another main difference between those two systems can rise from the exogenous catalysts typically needed to catalyze the curing reaction and activate the bond exchange process in vitrimers. As example, Zinc (II) salts are frequently used as a catalyst for transesterification reactions in epoxy vitrimers. According to Leibler et al., adjusting the amount of zinc acetate can significantly modulate the transesterification reaction rate in soft epoxy resin networks[77]. Nevertheless, adding a catalyst may cause adverse effects, such as bringing some toxicity, altering the mechanical properties at high catalyst loading levels, as well as decreasing the thermostability. Consequently, significant efforts have been directed towards the development of catalyst-free vitrimers.

Initially viewed as substitutes for transesterification, transamidation (figure I.24 - A) and transamination (figure I.24 - B) have gained significant interest after Du Prez's team investigated the catalyst-free transamination of vinylogous urethanes as a vitrimer exchange reaction[131]. Bulk polymerization of cyclohexane dimethanol bis-acetoacetate with excess of m-xylylene diamine and tris(2-aminoethyl)amine gave the concerned vinylogous urethane (figure I.24 – B). Vinylogous urethane are more thermodynamically favored and less sensitive to hydrolysis as compared to esters and can still undergo bond exchanges through an intermediate nucleophilic addition of an amine groups at elevated temperatures without any catalyst (>120 °C). Short relaxation times are observed and reprocessing at 150°C for 30 minutes gave recycled material without any degradation of the mechanical or chemical properties. Furthermore, poly(vinylogous urethane) networks are made from easily accessible chemicals. Since its introduction, academic interest in vinylogous urethane chemistry has rapidly increased with exploration of numerous applications from simple vitrimers preparation[132–137] to SM vitrimers[138–141].

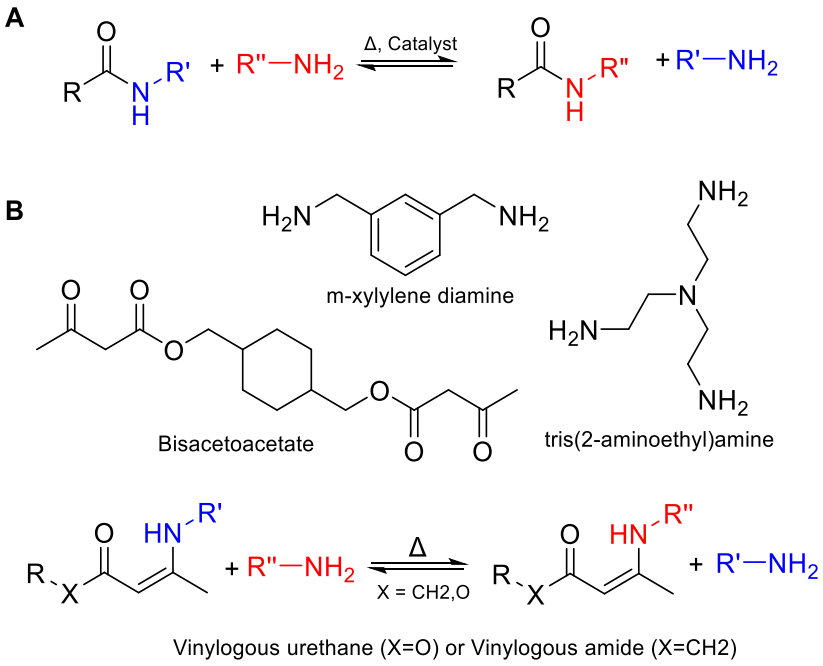

Figure I.24 – (A) Thermoreversible transamidation; (B) Thermoreversible transamination of vinylogous amides (X=CH_2) or urethanes (X=O) (Reproduced from ref[131]).

Since then, other examples of catalyst-free vitrimers based on fast exchange reactions were proposed such as hydroxy-urethane[78], hemiacetal esters[142], trialkylsulfonium salts[143] and imines[144]. Moreover, instead of relying on a specific fast exchange reaction, some vitrimers were also synthesized with a catalyst site embedded in the network. Ladmiral et al.[123] recently described the use of α-difluoromethylene as activating group positioned close to the ester bonds. The strong electronegativity of CF_2 groups activates the TE on adjacent esters and avoid thus the use of metallic or organic exogenous catalyst. Highly recyclable materials with lower additive or contaminant content is surely an upcoming goal and very promising property for new emerging materials, even if it appears that the bond exchange reaction in vitrimers is tolerant to a few unknown additives or contaminants[145].

Analogous to the TE reaction, transthioesterification (TTE) involving an exchange between a free thiol and a thioester (figure 24 – A) or hydroxyl-thioester exchange (figure I.25 – B) is vastly used to endow epoxy or hydrogel materials with reprocessability[146]. Recently, the Bowman group deeply studied TTE in organic media and reported that an easy integration into dynamic polymer networks such as vitrimers was possible[147]. They used TTE for the

preparation of dynamic hydrogels, which can exhibit modulated dynamic behavior through the introduction of acid or base[148]. Vitrimers derivated from this chemistry can be easily develop considering the mild conditions for the exchange.

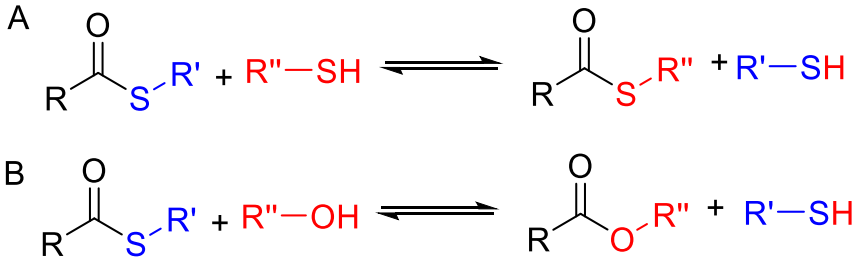

Figure I.25 – (A) Thiol-thioester exchange; (B) Hydroxyl-thioester exchange.

Zhang's team lately introduced thioester groups into epoxy resins which can under appropriate conditions, exchange with the hydroxyl groups present in the epoxy and produce thiol and ester groups. The thiol-thioester exchange can later be triggered subsequently (figure I.26 - A)[146]. This epoxy resin has excellent mechanical properties and in contrast to transesterification generally needing a strong base such as TBD or zinc acetate as a catalyst, catalyst free reprocessing of these thioester-containing epoxy resins was achieved by hot-pressing epoxy granules at 120 °C for 5 h under 5 MPa. These reprocessable materials having a T_g at 100°C demonstrate shape-memory abilities. As shown in figure I.26 - B, various temporary shapes can be programmed by simply shaping at 100°C and fixing at ambient temperature for 5 min. These shapes are stable without thermal stimulation and return to the original shape within 20s when the temperature reaches 100°C. Moreover, the initial shape can be curved as an arc (figure I.26 – B, E) and when the temporary shape is reshaped into a reverse arc, it can be restored to the original arc shape after thermal stimulation. In addition, due to the excellent mechanical properties of the epoxy resin, it can withstand 2400 times its own weight even after 10 times of reshaping. This demonstrates the excellent shape memory properties of the material expected to be used in aerospace and other fields.

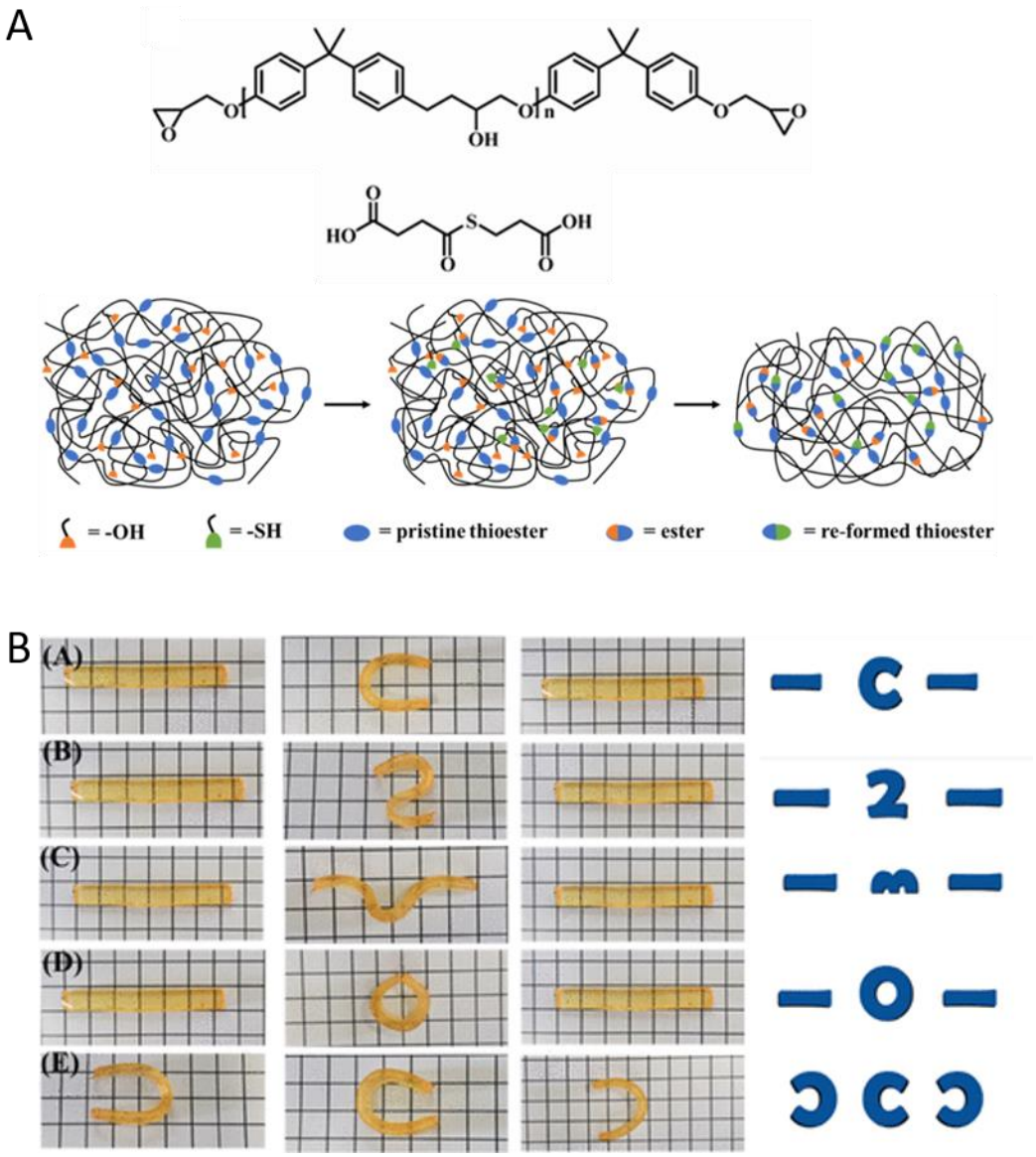

Figure I.26 – (A) Starting compounds and schematic diagram of the reprocessing of thioester-containing epoxy resin (B) Shape memory properties of the epoxy material. (A–E) The epoxy resin material was folded into different shapes and then heated at 100°C to recover the original shape (Reproduced from ref[149]).

Polyurethanes are one of the most commonly used polymers for shape memory materials. Recent researches to produce them in a greener and safer way led to innovative polyhydroxyurethanes (PHU)[150]. Interestingly, in 2015, Hillmyer et al. investigated the reprocessability of PHU networks and concluded that the presence of hydroxyl groups allows transcarbamoylation (TCM) which imparts PHU networks with dynamic behavior[151.] They

reacted a bis-(six-membered cyclic carbonate) compound with a polyfunctional amine to prepare a PHU vitrimer without the use of catalyst (figure I.27 – A). This isocyanate-free reaction generates a carbamate linkage and a hydroxyl group similar to hydroxyl esters in epoxy vitrimers. In this material, stress relaxation was observed and attributed to an associative transcarbamoylation process (figure I.27 – B). Associative TCM of carbamates or dissociative reversion to isocyanates and alcohols typically occurs at high temperature (> 200 °C) and produces unwanted side reactions. The activation energy measured in the present polymer being lower than expected from molecular modeling and density functional theory calculations, the developed PHU network was able to undergo stress relaxation and reprocessing at a temperature of 160 °C and a pressure of 4 MPa in the absence of an external catalyst. This behavior was attributed to mechanical activation of the transcarbamoylation by high pressure.

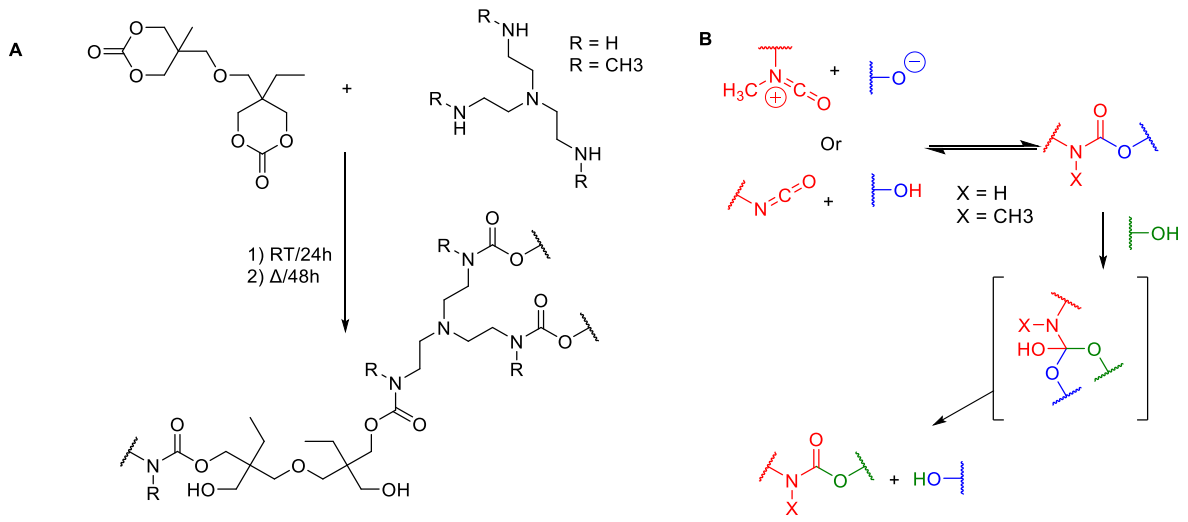

Figure I.27 – (A) Polyhydroxyurethane network formation from cyclic carbonate and polyamine compounds; (B) Mechanism of hydroxyl mediated transcarbamoylation (Reproduced from ref[151]).

Later, Tao Xie and coworkers pioneered investigations of the carbamate bond reversibility for the preparation of PU vitrimers with the help of catalysts[152]. They synthetized a PU thermoset from polyethylene glycol cured with hexamethylene diisocyanate and glycerol in the presence of 1 % dibutyltin dilaurate catalyst. The resulting network could fully relax at 130 °C. Due to the “sluggish” behavior of this reaction, vitrimers prepared via the isocyanate-alcohol route has only lately been described[153,154]. In this recent context, Jingxin Lei et al.

developed a multifunctional SMP polyurethane-vitrimer based on renewable castor oil[155]. A classical shape memory effect was obtained by transitioning over the melting temperature of the material (> 40 °C) while shape reconfiguration was obtained at 140 °C where transcarbamoylation of the carbamate bonds allows a topological network reconfiguration (figure I.28).

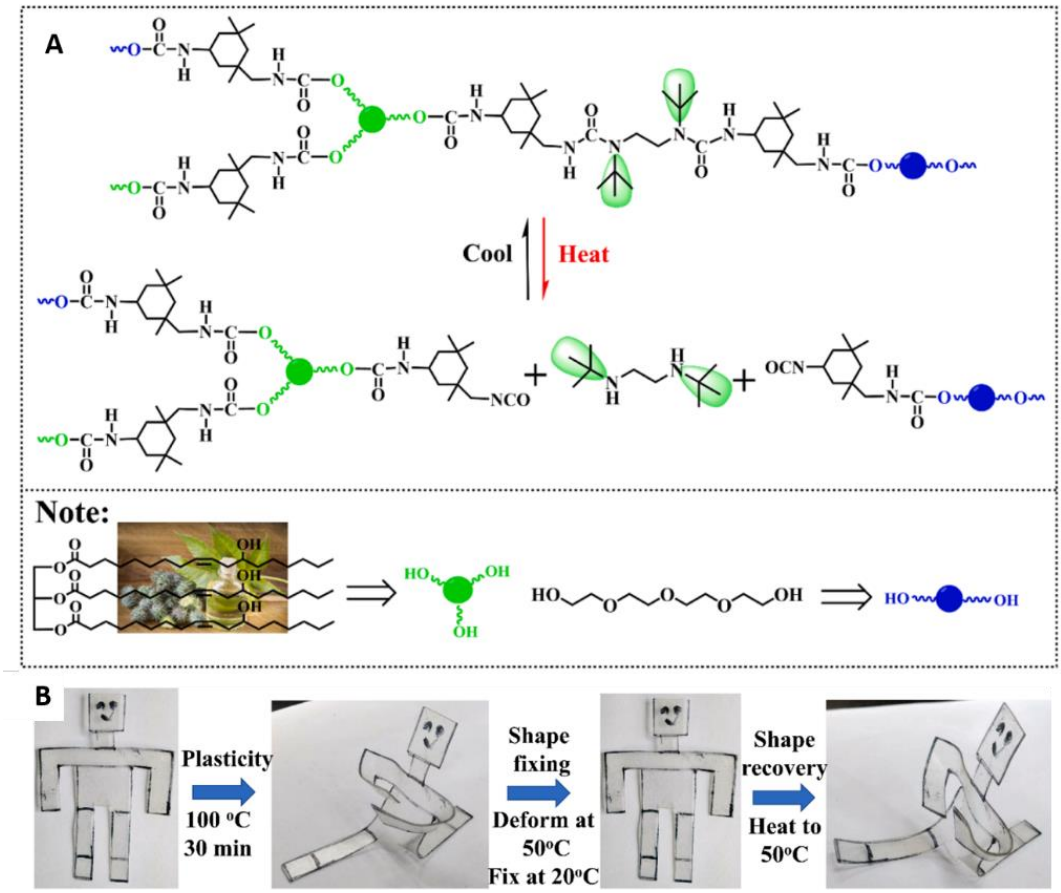

Figure I.28 – (A) Scheme of dynamic exchange in castor oil PU thermoset; (B) Illustration of the reconfiguration by plasticity and shape memory behavior of this material (Reproduced from ref[155]).

Another interesting chemistry for the preparation of shape memory vitrimers is the imine chemistry. Also known as Schiff base chemistry, this is one of the most often employed reversible covalent reaction involving carbonyls and amines those could proceed to yield imine type compounds (imines, hydrazones, oxime, etc.) by distinct processes[156–158]. Imines results from the condensation between an aldehyde or ketone with a primary amine or ammonia and can be reverted to their original monomers (figure I.29 – A). In the absence of water and upon introduction of another amine, imines undergo transimination (monomer

exchange) with or without addition of catalysts (figure I.29 – B)[157]. Additionally, imine metathesis can occur between two imines by exchange of amines to form new imines in the presence of catalysts (figure I.29 - C)[157]. One of the first reports of polyimine materials was by Wei et al. for the preparation of multi stimuli-responsive dynamic and self-healing hydrogels[159]. Due to the efficient reversible formation and rupture of imine bonds, imine chemistry has been widely adopted in dynamic polymers especially in vitrimers[160–163].

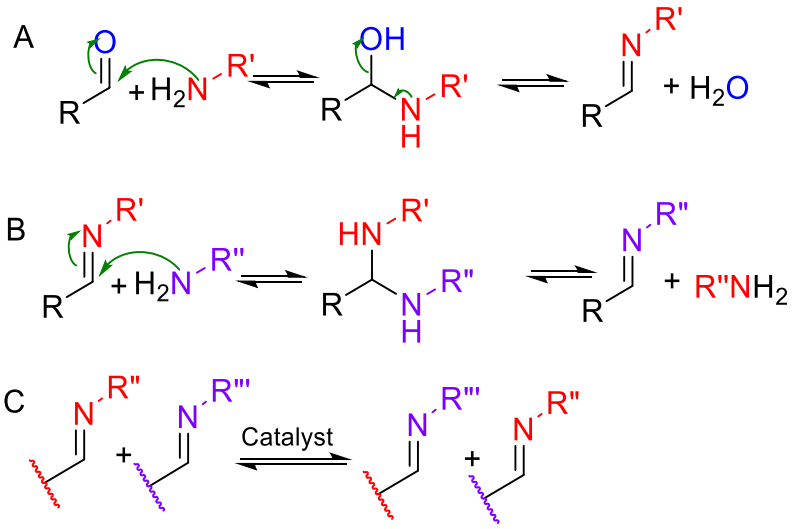

Figure I.29 – Reversible (A) imine condensation; (B) Transimination and (C) imine metathesis.

Interestingly, Zeng et al. reported the first example of polyimine vitrimer exhibiting NIR-light induced shape memory effect at room temperature[164]. Incorporating aniline trimer (ACAT), into the traditional imine-type vitrimers (figure I.30 - A) endowed the vitrimer with an excellent photothermal property. With 10 mol % ACAT, the vitrimer demonstrates a Tg of 107 °C. A temporary shape can thus be programmed by heating at 110 °C and fixed at room temperature (spiral shape, figure I.30 - B). When the sample is heated to 110 °C again, it recovers its original strip shape within about 80s. The shape recovery rate (Rr) was calculated to be 87.89 % from DMA analysis. Figure I.30 - C shows a similar shape recovery when the sample is exposed to NIR (808 nm, 1.5 W/cm2) laser, the original shape being recovered within 30 s. Under the irradiation with NIR light, the ACAT-vitrimer converted the light energy into heat and so exhibited a distinct photoinduced shape memory property. In addition, thanks to imine exchange allowing to release the stress, the permanent shape of this vitrimer can be reconfigured (reshaping). In this material with 10% ACAT, the network relaxation time was

measured to range from 249 s at 100 °C to 65 s at 160 °C. This allowed to reshape the strip to a spiral shape at 110 °C for 24 h (figure I.30 - B).

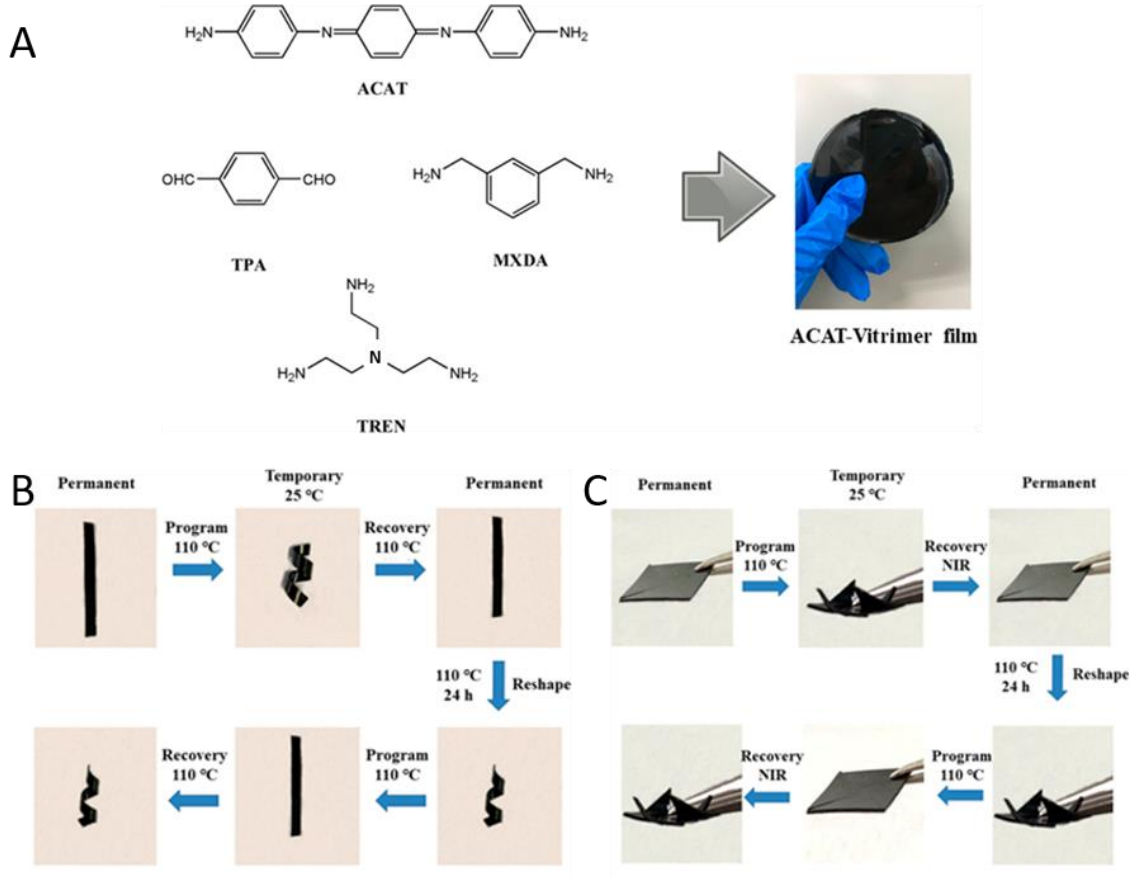

Figure I.30 - (A) Monomers used in ACAT-vitrimer films. The right picture shows the ACAT-vitrimer containing 10 mol % ACAT; Photos illustrating the permanent shape reconfiguration (reshape) and the shape recovery performance for ACAT-vitrimer by heat (B) and by NIR irradiation (C) (Reproduced from reference[164]).

While first mentioned by Grubb and coworkers in 1954[165] and implemented in self-healing materials by McCarthy's group in 2012[166], the Si-O-Si ionic exchange with a silanolate, a second order nucleophilic substitution occurring at high temperature in presence of a catalyst, remains weakly applied in DCB materials because of the moderate equilibrium rate ($\tau^* > 250$ s at 180 °C). By optimizing the reaction conditions, notably using an alcohol in presence of 1,5,7-triazabicyclo[4.4.0]dec-5-ene (TBD) as catalyst, Du Prez's group recently boosted this exchange reaction allowing a fast dynamic siloxane exchange mechanism ($\tau^* < 30$ s at 180 °C) triggering interest for the use of this reaction in vitrimers (figure I.31)[167]. For that purpose, they crosslinked a readily available epoxy resin with a siloxane-amine hardener. The resulting

vitrimer exhibits remarkable stress-relaxation characteristics (relaxation times less than 10 s), The low viscosity siloxane-containing vitrimer resin has made it possible to produce glass fiber-reinforced vitrimer composites using an industrially relevant vacuum-assisted resin infusion technique. They also demonstrated that these composites can be thermoformed into new shapes[167]. The recently highlighted performances of this reaction to crosslink materials with DCB open thus promise for further developments in shape memory materials and composites.

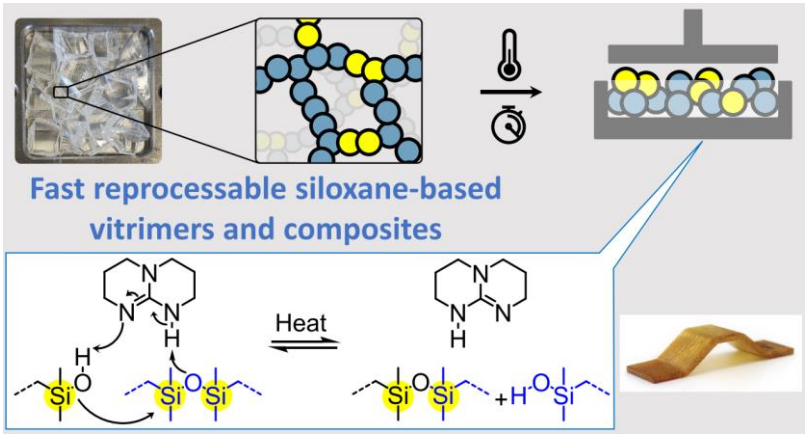

Figure I.31 – Schematic reprocessing of siloxane-based epoxy-resin thanks to TBD catalyzed Si-O bond exchange present in the crosslinker (Reproduced from ref[167]).

The last chemistry we will discuss here relates to the sulfur chemistry. Historically, sulfur chemistry has already drastically impacted rubber science by the invention of rubber vulcanization by Charles Goodyear in 1833. Long ago, Tobolsky et al. attributed the observed stress relaxation in polysulfide rubber to rapid disulfide interchange in presence of catalyst[168]. The complex mechanisms of this disulfide exchange dependent on the reaction conditions, offers the possibility to envisage both dissociative and associative DCB-SMPs. Indeed, disulfide bonds can reversibly dissociate in two free thiols by a redox reaction. Disulfides can also exchange following either anionic or radical pathways (figure I.32 – A)[169]. In the anionic pathway (figure I.32 – B), a thiolate anion attacks a disulfide bond resulting in an exchange via heterolytic cleavage of the S-S bond when specific catalyst or base conditions are applied[170]. On the opposite, the radical pathways (figure I.32 – C & D) implies an homolytic cleavage of the disulfide bond in response to light or a radical initiator followed by a radical transfer [171]. Aromatic disulfide metathesis (figure I.32 - E) at room temperature has also been widely reported[172]. Tesoro et al. were among the first to use disulfide exchange to impart recyclability

to a thermoset epoxy resin[173]. Concurrent thiol-disulfide exchange can also occur and is generally much faster than disulfide exchanges, but this reaction is highly pH dependent and mostly only proceeds to its full extent in presence of a strong base[174]. In those cases, the presence of unwanted thiol generated from the interconversion of disulfide or incomplete conversion inevitably add more complexity to the system. This was first evidenced in redox-reversible hydrogels proposed by Saegusa[175].

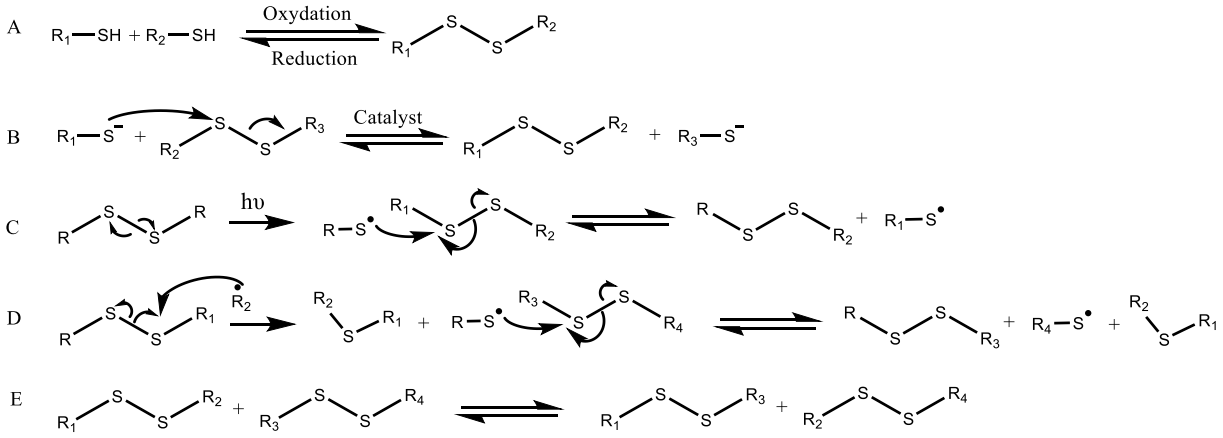

Figure I.32 – (A) Disulfide formation; (B) Anionic thiol-disulfide exchange; (C) light-induced homolytic disulfide cleavage followed by radical reduction of another disulfide bond; (D) radical-induced homolytic disulfide cleavage followed by radical reduction of another disulfide bond; (E) Disulfide metathesis.

Thanks to easily activated exchange reactions at a moderate temperature and without catalysts[170,172,176,177], disulfide exchange has been profusely applied in self-healing and vitrimer systems. Various stimuli such as heat, light and pH can be used as triggers[178]. As representative example related to shape memory materials, Rowan and coworkers developed semi-crystalline polydisulfide networks by thiol–ene photopolymerization of 1,6-hexanedithiol and 1,5-hexadiene, followed by oxidative coupling between thiol end groups with a tetrathiol crosslinker (figure I.33 – A)[179]. This network exhibits thermal shape memory properties by crossing the melting temperature of the crystalline zones and thanks to the disulfide bonds, the reconfiguration of the permanent shape can be induced by light (figure I.33 – B) so as the healing of a scratch.

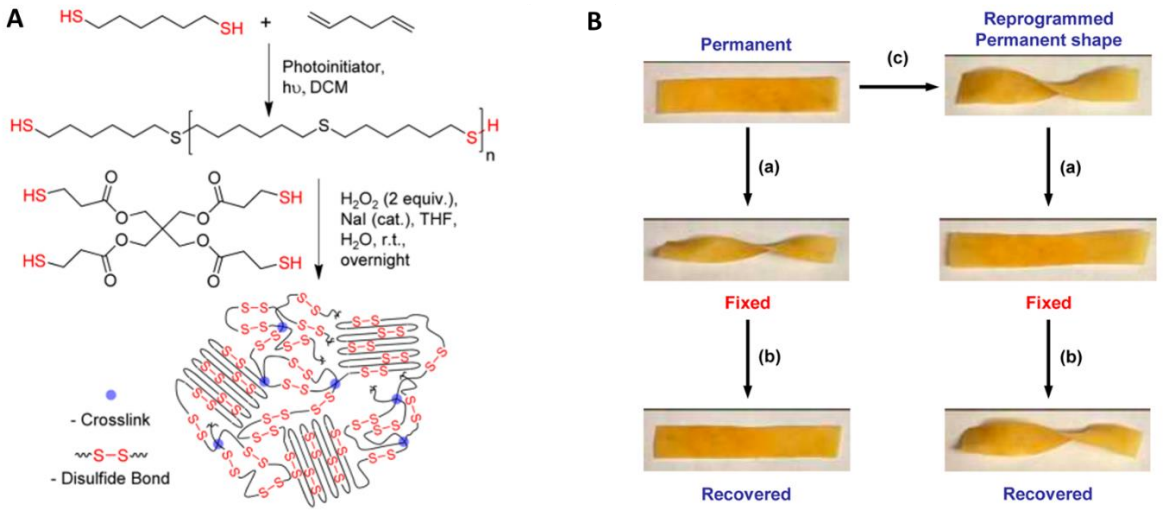

Figure I.33 – (A) Synthesis of the semicrystalline polydisulfide network; (B) Pictures showing the reprogrammable shape memory properties (Reproduced from ref[179]). The sample is pressed as a flat film and then (a) heated to 80 °C while being held in a helical shape. (b) The film is then heated to 80 °C and allowed to recover to the permanent shape. (c) The permanent shape of the film can be photoreprogrammed by holding it in the helical shape while exposing it to UV light.

Other light-sensitive sulfur derivatives were also subject to great attention. Bowman, Scott and co-workers first developed an allyl sulfide bond-based elastomer (figure I.34)[180] with light induced plasticity. When radicals are generated by a photoinitiator, the allyl sulfide functional groups present along the polymer backbone undergo rupture and recombination by an addition–fragmentation process endowing the network with light induced plasticity.

This concept has since been applied by others to produce sulfur-related DCB-SMPs[181–183] as proposed by Dongzhong's group who produced a LCE-SMP from allyl sulfide-based dynamic covalent crosslinks in the LCE matrix[182].

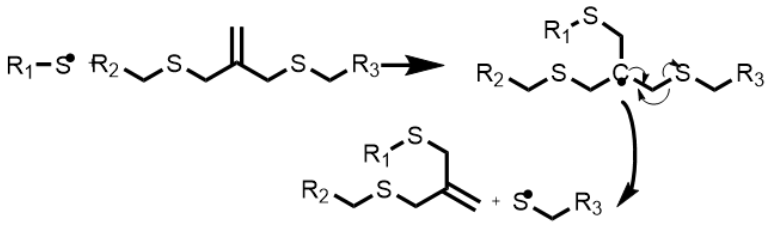

Figure I.34 – Exchange reaction in the polymer backbone of an allyl sulfide based low Tg elastomer (Adapted from ref[180]).

An interesting and quite recent parallel to this sulfur chemistry is the selenide metathesis[184]. It has been shown that selenium has chemical properties similar to sulfur and, consequently, that the Se–Se bond shares a same behavior with the S-S bond when heating or exposed to visible light; at the exception of presenting a lower bond energy (172 kJ/mol as compared to 240 kJ/mol)[185,186]. As DCB-SMPs based on diselenide operates under milder stimuli and no catalyst is generally required[187], they have drawn attention. Self-healing and shape-memory epoxy thermosets based on dynamic diselenide bonds are already described in literature and are expected to expand in short future[188–190].

Finally, boronic esters were recently used to build up vitrimers. Chenxi Bai and coworkers prepared a boronic ester bonds crosslinked vitrimer with shape memory, self-healing and recyclability properties based on an epoxidized natural rubber that formed a boronic ester interface after crosslinking to silica[191] (figure I.35). The boronic ester linkages undergoes catalyst-free exchange reactions via metathesis giving the desired recyclability properties. In addition, silica is implemented to reinforce and increase the material crosslinking, also provides some extra free hydroxy groups triggering the bond exchange.

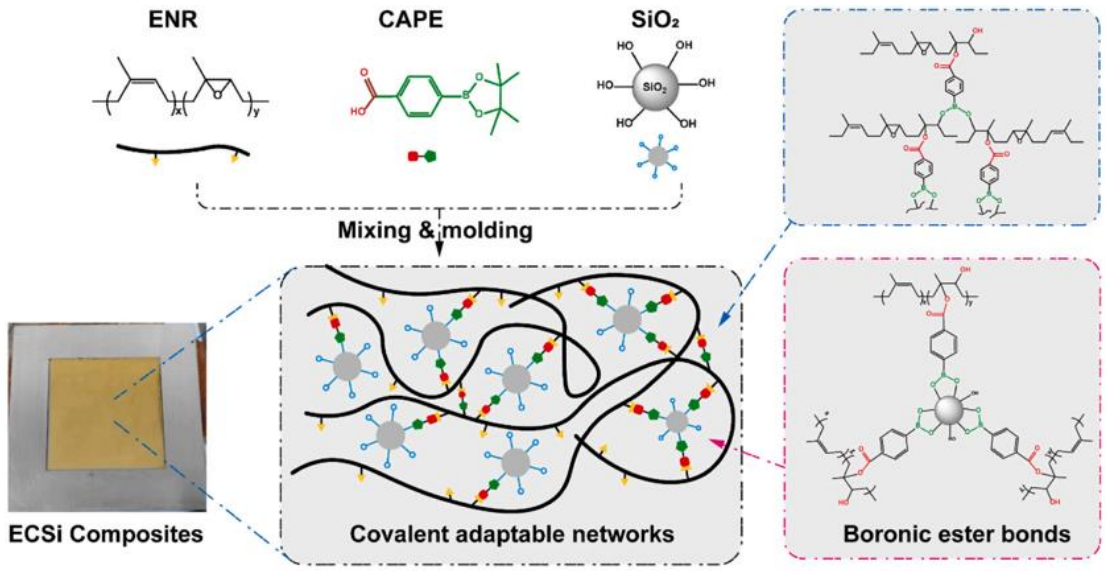

Figure I.35 - Construction of dynamic networks based on boronic esters (Reproduced from[191]).

Besides thermoplastics, hydrogels are another class of materials that might be imparted with shape memory properties. Since they are swollen in water, hydrogels can be sensitive to other triggers such as pH or the concentration of a reactant present in water. Including boronic ester crosslinks in an hydrogel is a valuable way to produce pH or sugar sensitive SM hydrogels based on dissociative mechanism. When the pH of the environment is lower than the pKa of boronic acid[192], the dynamic boronic ester bond is cleaved in boronic acid and a diol (figure I.36). It is noteworthy to mention that this boronic ester cleavage can be also triggered by adding a free 1,2 diol (e.g. a sugar) to the medium. Due to this catalyst-free rapid dynamic exchange at ambient conditions and in aqueous media, crosslinked materials resulting from this reaction show self-healing abilities and can be covalently repaired after failure [193–195].

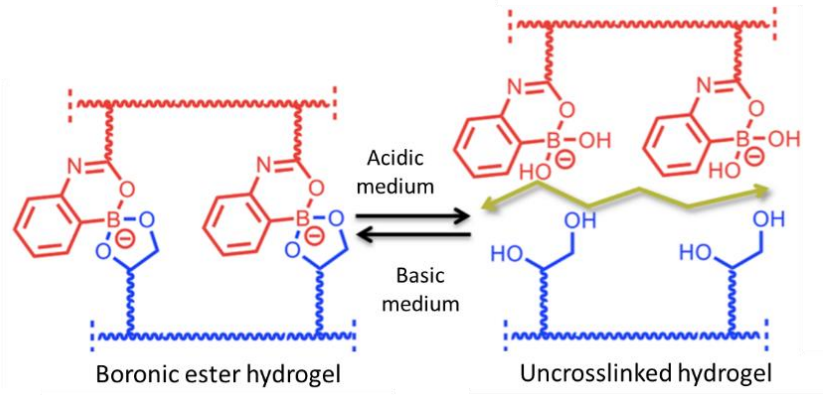

Figure I.36 – Reversible formation of boronic ester from boronic acid and 1,2-diol (Adapted from ref [196]).

Interestingly, boronic ester bonds have also been used as molecular switches that impart hydrogels with shape-memory properties[196]. Sodium alginate partially modified with 3-aminophenylboronic acid was reacted with poly(vinyl alcohol) to form hydrogels[197]. Their permanent shape was insured by crosslinking with calcium cations. Because the boronic esters are unstable at low pH, the hydrogel can be temporarily deformed at pH 6.0 before fixing at pH 10.6. The shape recovery is then achieved either by reducing the pH or by soaking in a sugar solution (figure I.37).

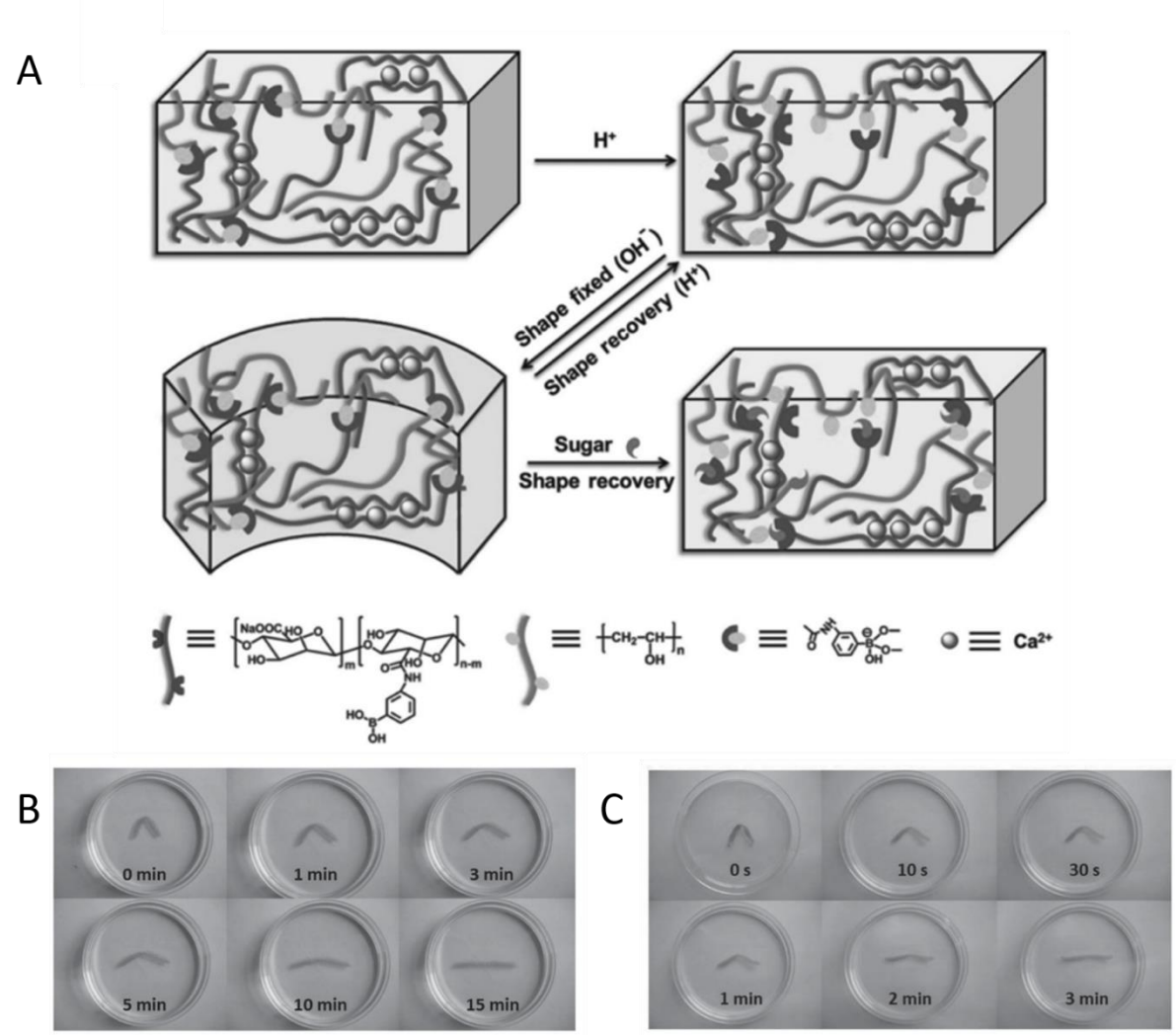

Figure I.37 – a) Sketch of the principle of shape memory hydrogel based on boronic ester switches b) Shape recovery rate upon immersing the hydrogel in a 0.2M Gly (pH 6) solution (B) or in a 0.2M glucose solution (C) (Reproduced from ref[197]).

I.3 Shape memory polymer composites

As highlighted in the previous section, covalent adaptable networks of thermoplastics are remarkable materials combining efficient temperature triggered shape memory properties similar to thermosets, with reconfiguration ability, recyclability, self-healing and multiple shape memory properties. Typically, these shape memory materials are activated by external heating of their environment. However, for some applications notably in the biomedical field, internal heating that would preserve the overheating of the surrounding living tissues so as remote activation of the shape recovery are highly desired. For that purpose, thermoelectric or thermomagnetic shape memory composites have been designed by incorporating active fillers (magnetic or electrically conductive fillers) in the SMP matrix. So, actuation by an electric field via joule effect or by an alternating magnetic field provoking internal local heating provides the desired benefits.

Over the last decades, many different fillers have been investigated for that purpose[198]. Among them, nanofillers such as multiwall carbon nanotubes (MWCNTs) or iron oxide nanoparticles are emerging fillers. Due to their large surface area and resulting strong interactions with polymers, nanofillers are more effective than larger fillers. In this chapter, SMPs properties enhancement from different nanofillers will be highlighted, with a special focus on carbon and ferromagnetic nanofillers.

I.3.1. Carbon-based shape memory nanocomposites

Carbon fillers regroups primarily carbon black (CB)[199–201], carbon nanotubes (CNTs)[202–207] and graphene oxide (GO)[208–211] (figure I.38). Insertion of electrically conductive carbon fillers in polymers can result in the formation of a carbon interconnected conductive network inside the polymer matrix. For that, a required amount of carbon material is needed which is described by the percolation theory. This theory describes the change in a network behavior when nodes or links are added. At a critical conductive filler fraction, called percolation threshold, the addition of a small amount of the nanofiller particles in the matrix results in their merging into a large connected network. Once above the threshold, these linked-clusters reach a size similar to the system its incorporated to. In the case of carbon filler, the resulting

carbon network, who presents high electrical properties, imparts new interesting features to the polymer such as electrical conductivity. When polymer composites are concerned, this limit is commonly used to indicate the transition from insulting to conductive. Carbon fillers can then be used as energy converter to induce joule heating or absorb electromagnetic (IR light) radiations[212]. While primarily used to enhance mechanical properties, the resulting composite exhibits also enhanced thermal conductivity, which is especially advantageous for applications that do not allow direct heating to induce the shape memory effects. Carbon nanofillers are nowadays extensively used in shape memory polymer composites with voltage or remote actuation.

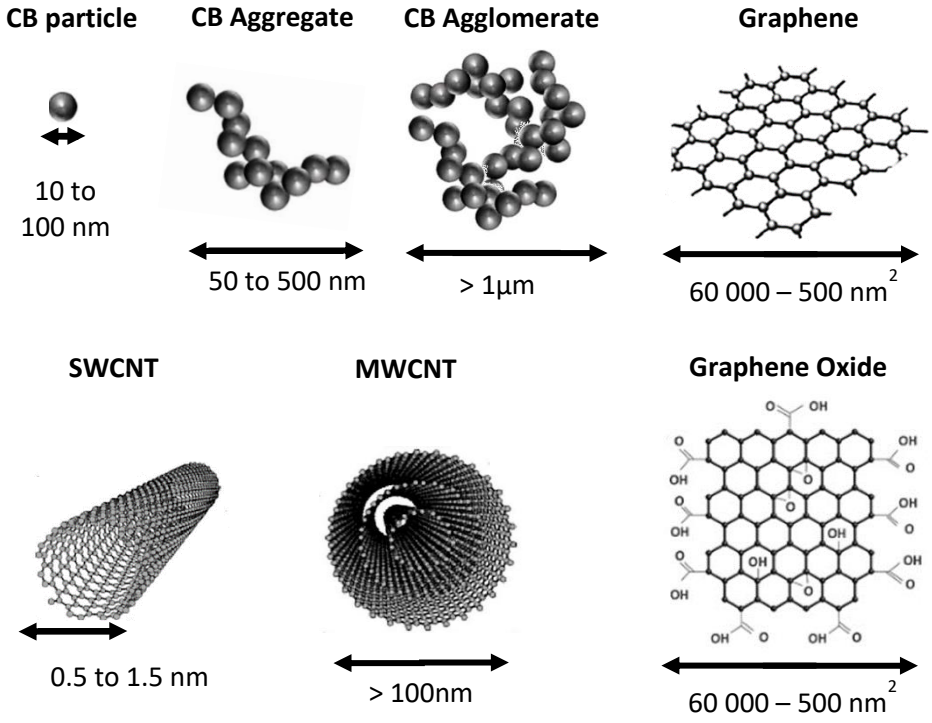

Figure I.38 – Carbon filler and their relative size.

The most traditional carbon filler is carbon black (CB) which is a relatively affordable amorphous form of carbon and thus the first option when conductive fillers are considered. CB particles diameters are between 10 and 100 nm but those can easily form aggregates (primary particles) on the order of microns due to Van der Waals attraction forces [213]. Covalent bonds between these primary particles can be formed and prevent easy CB break-up.

Consequently, they can not be considered as independent from each other which is a major difference between CB and other nano-sized carbonaceous fillers. Due to these considerations, a high concentration is required to reach the percolation the percolation threshold which is about 3 vol% (volume fraction of CB), respectively often about 15wt%[214]. Even if it has been shown that SMCs with CB possess an improved electrical actuation combined with an increase in modulus value[215] (attributed to molecular-level interactions, where the fillers resist the free movement of chain stretching, resulting in a more rigid system[216]), such a high loading of CB has been found to adversely affect their mechanical and shape memory properties, resulting in lower recovery ratios, increased brittleness and premature material failure at lower deformations[216,217]. For example, Le et al.[218] reported the preparation of poly(ethylene-1-octene) composites with 17 wt.% CB. It was found that the conductivity of this material is limited by the CB aggregation caused by the spherical shape of the CB fillers and their uneven distribution, which hinders their contact with each other and thus the formation of a continuous conductive network. Consequently, bunches of microcircuits are formed as aggregations, enabling rapid recovery when a voltage is introduced. On the other hand, mechanical properties are altered by the non-uniform filler dispersion in these composites. In another work, Yu et al.[219] observed a strain-induced softening effect, also known as the Mullins effect[220] induced by micro-damages of the carbon network occurring during the loading cycles. Larger programmed deformations lead to slower shape recovery. Consequently, the damage-induced softening effect in SMPCs increased shape recovery time. Furthermore, significant reduction in shape fixity for CB-SMPCs attributed to a decrease in the number of crystalline regions induced by CB loading is also generally observed[215,221].

Graphene, an exceptional carbon-based filler, has also been employed in SMPCs for its remarkable thermal and electrical conductivities. In order to ensure a consistent dispersion within the SMP, graphene oxide (GO) is frequently used (figure I.38). GO nanosheets contain hydroxyl, carbonyl, carboxyl and epoxide groups on their basal planes and sheet edges. Therefore, GO nanosheets can experience electrostatic, hydrogen or covalent bonding with polymers which contribute to a better filler dispersion. Multiple studies have related the

addition of graphene oxide into SMPs with success[211,222–225]. Martin-Gallego et al. prepared an epoxy material with 1.5 wt% graphene contents enhancing the T_g of the nanocomposites by 40 °C relative to the neat epoxy[226]. More recently, D'Elia et al.[209] have reported a shape memory epoxy/graphene nano composite containing less than 1 wt% of GO. By subjecting the sample to the Joule heating effect, it exhibited fine shape recovery when the electric voltage was less than 10V. Applying a 9V voltage for 1 minute raised the temperature to 58°C, inducing the shape recovery.

Despite the extensive studies on the use of GO in enhancing properties of SMPs, achieving a uniform dispersion of this multilayer-structured carbon filler has proven to be a challenging task. The strong interactions between graphene sheets resulting from the $\pi-\pi$ stacking during its synthesis is typically manifested by the formation of agglomerate as it is the case for CB[227]. Consequently, successful dispersion and exfoliation require specific techniques, such as sonication or chemical modification, to disaggregate the layers and promote interaction with the matrix during the SMC preparation[228]. Although, agglomeration of graphene at high concentrations is hard to avoid and the Mullins effect leads to worsening of the shape memory characteristics of SMPCs. Furthermore, despite the improved electrical properties and mechanical advantages offers by GO, its price being much superior to other carbon fillers (e.g. MWCNTs) limits graphene competitiveness.

For further information on CB or graphene-filled shape memory polymers, the reader can consult recently written reviews on these topics and the references within[229–231].

To avoid significant degradation of the shape memory properties of SMPCs while achieving electrical conductivity, alternative conductive fillers should be explored. Carbon nanotubes are a promising option, possessing beneficial characteristics that allow for the formation of SMPCs with low electrical resistivity even at low filler concentrations. CNTs have tube-like geometries with a large aspect ratio, and are much easier to interact with each other (figure I.38). As a result, the percolation threshold for nanocomposites using CNTs is obtained at lower concentrations than for other conductive fillers. This is advantageous, as a higher concentration of fillers may lead to more brittle structures, higher cost or processing difficulties due to a significant increase in viscosity. Two categories of carbon nanotubes,

respectively single-walled carbon nanotubes (SWCNT) and multi-walled carbon nanotubes (MWCNT) exist. SWCNTs are composed of a single graphene sheet that is rolled up, whereas MWCNTs consist of multiple concentric graphene sheets. The latter being more conductive, they are preferentially used in SMPs[202,232].

Several methods have been developed to create composites of poly(ε-caprolactone) (PCL) and multi-walled carbon nanotubes (MWCNTs), including in-situ polymerization, solution mixing with ultra-sonication, and melt mixing. McNally et al. conducted a comprehensive study on the electrical conduction and rheological behavior of PCL-MWCNT composites[233]. They achieved a highly dispersed and interconnected network of MWCNTs within the PCL matrix by melt mixing, minimizing the presence of MWCNT agglomerates larger than 1 mm and creating an extensive interconnected network of MWCNTs. It is believed that the MWCNTs are mainly dispersed in the amorphous phase of PCL so that the extent of this phase plays a crucial role in achieving percolation. Staufer and Aharony described that the macroscopically measured conductivity (σ) related to the carbon black concentration (ϕ) can be expressed by the formula $\sigma \propto (\Phi - \Phi c)^t$, where *t* is a critical index value predicted by classical lattice percolation theory and Φ_c is the percolation threshold or critical weight fraction of the conductive filler. This formula was here applied by authors to MWCNTs[233]. The DC electrical conductivity of the composites remained negligible below the critical concentration Φ_c but increased significantly at higher Φ, indicating the presence of a percolated MWCNT structure. By fitting the experimental data obtained for MWCNTs/PCL to this equation and plotting it logarithmically, McNally determined Φ_c = 0.299 wt% (0.18 vol%) and *t* = 2.73, with a high relevance (R^2 = 0.9934). The value of *t* describes the dimensionality of the system, when the conductive particles are dispersed uniformly as well as having direct electric (geometric) contacts in a conductive percolation grid, and in the case of a 3D percolating grid, the theoretical value would be *t* = 2. The experimental data, depicted in figure I.39 (with a value of *t* = 2.73), indicates the formation of "rope-type" agglomerated structures of MWCNTs during sample fabrication, as observed in atomic force microscopy (AFM) images of the composites. A three-dimensional grid structure of multi-walled carbon nanotubes where all the nanotubes are interconnected and in contact with each other is thus achieved.

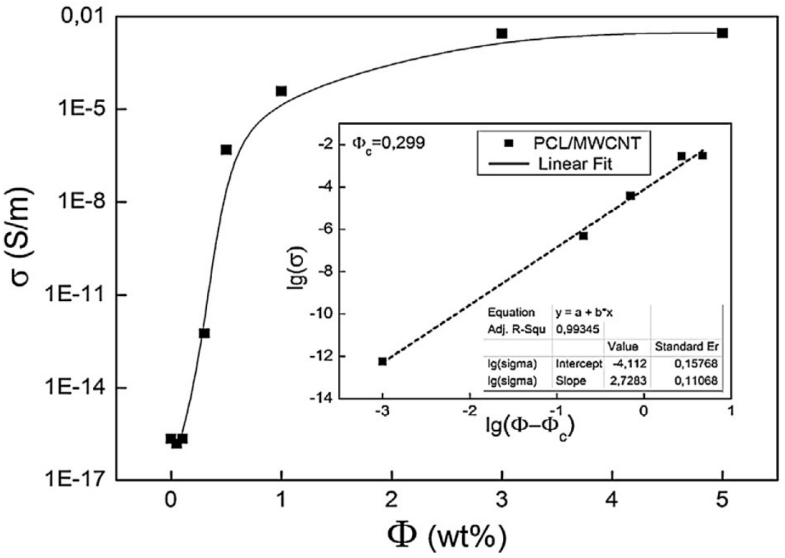

Figure I.39 – (A) DC electrical conductivity (σ) versus MWCNTs concentration(Φ) at a constant room temperature on PCL melt-mixed with MWCNTs (Reproduced from ref[233]).

Low amounts of MWCNTs addition to polymer are necessary to reach the percolation threshold and thus conductivity[237]. By incorporating 5 wt.% of MWCNTs in a shape-memory polyurethane matrix, Cho et al. produced a composite with a conductivity of ~10^{-3} S cm^{-1} and achieved electrically driven shape recovery. The high aspect ratio of MWCNTs, which facilitates the formation of the electrically conductive network within the composite, results in a percolation threshold generally between 1 and 5 wt% of MWCNTs in function of the quality of dispersion[238]. Both electrical and mechanical properties of SMPCs are significantly influenced by the method used for dispersing CNTs, which must ensure bundles disaggregation and a uniform distribution within the composite. Different methods have been explored to improve interfacial cohesiveness and reduce electrical resistivity in SMPCs[239], including mini twin-screw melt mixing[240], crosslinking the polymeric network onto MWCNTs[241], in-situ polymerization[242] and surface modifications[243]. However, caution is needed with surface modification, as it can negatively affect the shape recovery ratio over time and generates defects on the nanotubes' surface.

Besides providing conductivity, CNTs also improve the mechanical properties of polymer composites. In their research, Liu and al.[234] showed that the addition of a small amount of CNTs (0.75 wt.%) significantly increases modulus, strength, and strain at break, as well as

recovery rate and cycle stability of SMPCs[234]. By the only addition of 2 wt.% of MWCNTs with polyamide, Zhang and al.[235] has managed to increase the modulus threefold of their nylon-6 matrix from 0.4 GPa to 1.24 GPa. This addition resulted also in a significant increase in yield strength from 18 to 47 MPa, as well as increases in ultimate tensile strength. Despite these changes, there was only a slight reduction in ductility from 150% to 110%, and no decrease in toughness was observed. These positive outcomes were attributed to the excellent dispersion and adhesion of the nanotubes, which were confirmed through microscopy measurements. More lately, González-Jiménez et al. produced a MWCNTs SMPC with high shape fixity, that they attributed to the alignment of the MWCNTs in the direction of the deformation. Overall, better shape memory characteristics are obtained with MWCNTs compared to other fillers such as CB[236].

To create a conductive network using carbon nanotubes, an alternative approach is to embed them in films or yarns within a polymer matrix. These structures are typically known as MWCNTs nanopapers or buckypapers. In recent times, the potential of buckypaper-based nanocomposites has been widely recognized due to their versatility and suitability for various applications, including gas sensing, supercapacitance, fire retardant coatings, EMI shielding and self-heating composites[244,245]. In their study, Lu et al. synthesized a three-dimensional self-assembled MWCNTs nanopaper on a hydrophilic polycarbonate membrane using a controlled pressure vacuum deposition process[246]. The resulting network was continuous, compact, and highly conductive. The combination of the nanopaper with styrene-based SMP facilitated the actuation of the nanocomposite by electrically resistive heating. Datta et al. produced by soaking buckypapers in shape memory epoxy polymer of an SMPC reaching of 30wt% of MWCNTs and exhibiting shape recovery in very short times (22s at 12V)[247].

Using Joule resistive heating to trigger shape memory polymer filled with multi-walled carbon nanotubes has been found faster, more efficient and cost-effective than traditional external heating. The phenomenon known as the Joule effect, discovered by James Joule in 1841, refers to the generation of heat when an electric current flows through a conductive material. This heating effect occurs as a result of collisions between electrons and the atomic lattice of the conductive material, leading to the conversion of kinetic energy into dissipated

heat. It is also referred to as resistive heating, as described by Paul Drude's model in 1900. In the case of conductive composite materials, such as those containing multi-walled carbon nanotubes, Joule heating occurs through the conductive filler network. As mentioned previously, a three-dimensional structure of interconnected and contacting MWCNTs can be achieved. In addition, this method allows for localized heating, making it possible to sequentially activate shape recovery in specific areas of a SMPC by local voltage application which represents a very practical approach. In their work, Li et al. conducted a study that used large-area buckypaper made of aligned carbon nanotube arrays as a strong and highly anisotropic material for creating a flexible electrode[248]. The electrode was used to produce CNT-loaded double-layer electrothermal actuators (ETAs), consisting of buckypaper and polydimethylsiloxane layers. The study demonstrated that it was possible to control the direction and degree of bending in the ETAs. When the horizontally cut actuator was deformed, it showed a great degree of bending with the CNTs aligned perpendicular to the U-shaped buckypaper band (figure I.40 – A). This concept opened up the possibility of creating bionic actuators that mimic the behavior of human hands, allowing for separate and controlled movements of each finger with separated circuit, as depicted in figure I.40 – B.

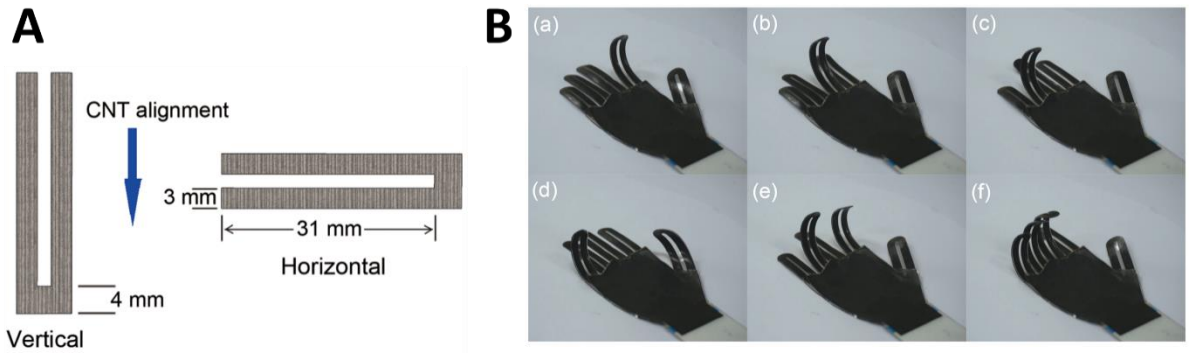

Figure I.40 – (A) Electrothermal actuator preparation; (B) Hand-shaped actuator with separate movements of the five fingers controlled by five independent circuits (Reproduced from ref[248]).

A fascinating approach for improving the electrical and thermal conductivities of materials is to blend two or more electrically sensitive nanofillers. For this purpose, the synergistic effect of both nanofillers upon either Joule heating or the shape recovery can be observed. Decorating or combining MWCNTs with metals like Cu, Fe, Ag, and Pt is a promising

method for rapidly reinforcing and electrically actuating SMCs. These structures have proven highly effective, as only a small amount of the nanofillers is required to achieve the desired outcome. Several studies have been conducted in this field, including the incorporation of Cu-CNT in polylactic acid (PLA)/epoxidized soybean oil[249] and Fe-MWCNTs and Ag-MWCNTs in PUs[250]. Coating the electrically sensitive nanofillers with conductive polymer (polypyrrole-coated MWCNTs) is another effective way of improving the dispersion of the nanofillers and the mechanical and electrical properties of the materials[251].

Up to now, the information given on the different carbonaceous nanofillers in SMCs has been focused on thermally-activated and, in most cases, electrically-triggered nanocomposites. However, it is worth noting that these nanocomposites also offer the potential for alternative triggering mechanisms. Yu et al. showed in 2014 that microwaves could also be an effective means of actuating styrene containing shape memory resin loaded with MWCNTs, which were directly mixed into the resin[252]. When exposed to microwave radiation, the embedded CNTs absorbed electromagnetic energy and converted it into heat, leading to thermally induced shape recovery in the SMPCs. This wireless remote shape control effect became stronger with higher CNT concentrations or increasing irradiation frequencies.

Remote control over SMPCs represents one of the leading and emerging research field especially for DCBs-SMPCs. The dispersion of MWCNTs in shape memory vitrimers also brings them all these new functions including, besides electrical conductivity, photo-thermal responsiveness and dual-triggered shape memory. Photothermal activation of composite vitrimers allows efficient and fast welding by IR-light application (figure I.41 - A). This effect can also advantageously be used to reshape locally the permanent shape of SM vitrimers by irradiation through a photomask (figure I.41 - B).

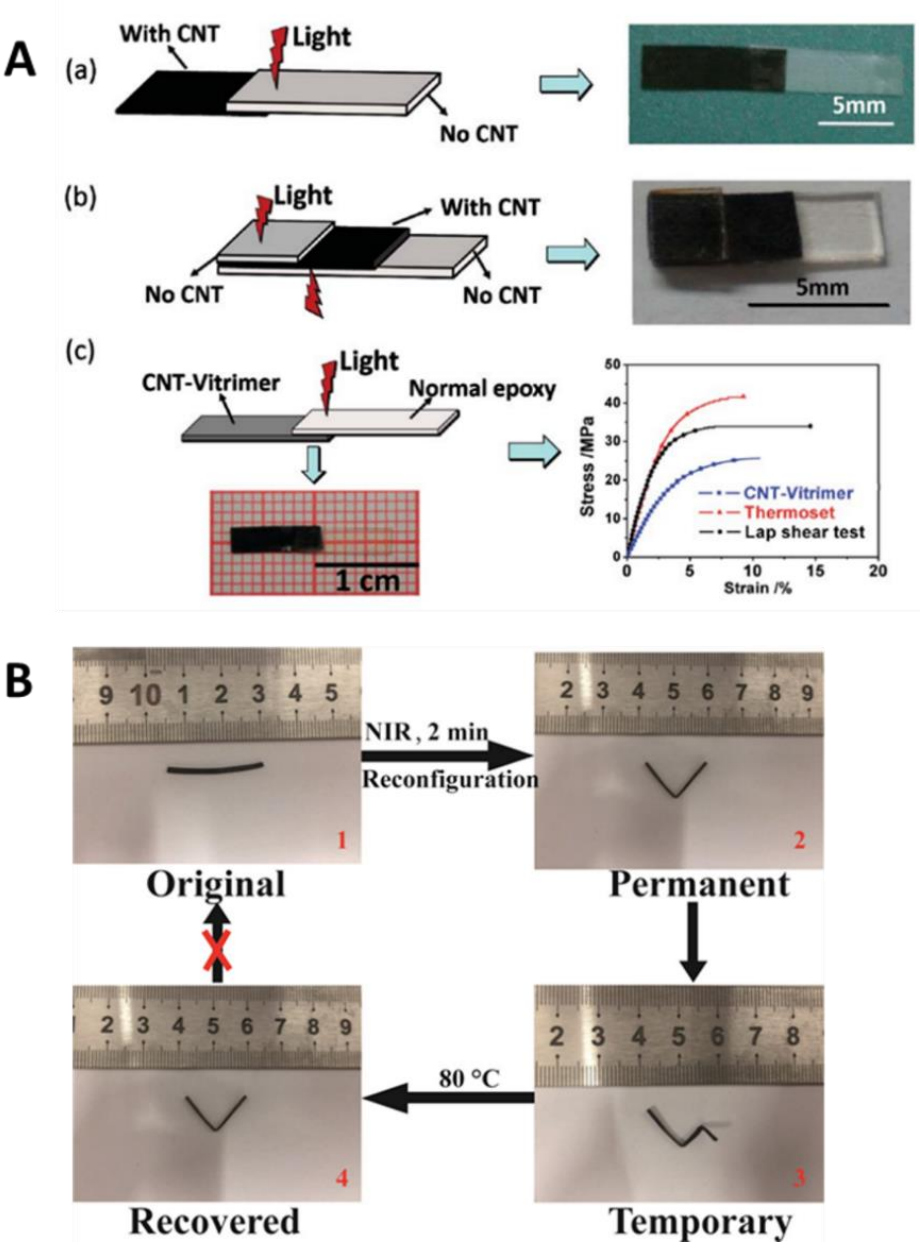

Figure I.41 - Photothermal properties of MWCNT vitrimer composites: (A) Photowelding with IR-light of MWCNT 1wt% /epoxy vitrimer composite (a) joining non-CNT vitrimer with CNT – vitrimer, (b) Joining two pieces of non-CNT vitrimer using CNT–vitrimer as an "adhesive", (c) Joining normal epoxy with CNT–vitrimer (Reproduced from ref[253]); (B) NIR-induced local reconfiguration and partial shape recovery of MWCNT 0.1wt%/ polyurethane vitrimer: (1) Original shape, (2) Reshaped permanent "V" due to NIR-induced transcarbamoylation, (3) The portion on the right was fixed to a temporary shape at lower temperature, (4) Heating to above Tm only recovers the portion on the right (Reproduced from ref[254]).

Self-healing of carbon-based vitrimer composites can be advantageously induced not only by external heating but also by light, voltage or microwaves, as exemplified figure I.42, with restoration of the mechanical performances.

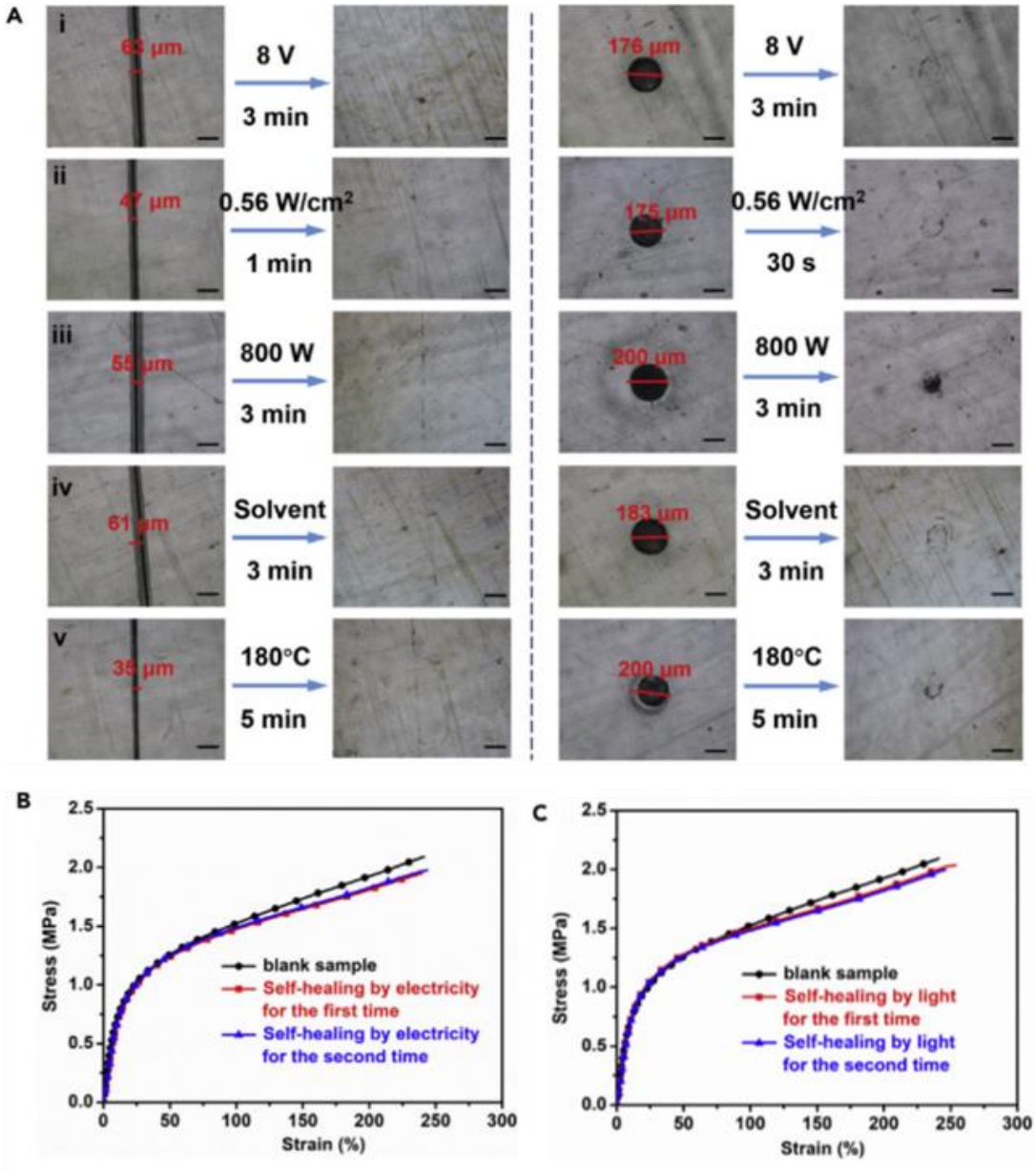

Figure I.42 - Multiple self-healing ability of a carbonized silk fabric (CSF) / epoxy vitrimer composite: (A) Electricity (i), light (ii), wave (iii), solvent (iv), and heat (v) triggered self-healing of vitrimer electromagnetic composite with a narrow cut and aneedle-pierced hole on the vitrimer layer. Scale bars: 100 mm; (B) Stress-strain curves of self-healed CSF-vitrimer composite triggered by electricity and blank CSF-vitrimer composite; (C) Stress-strain curves of self-healed CSF-vitrimer composite triggered by IR light and blank CSF-vitrimer composite (Reproduced from ref[255]).

Finally, besides shape reconfiguration, the shape recovery of MWCNT shape memory vitrimer composites can be triggered by the light, allowing a progressive and remote control of the actuation (figure I.43).

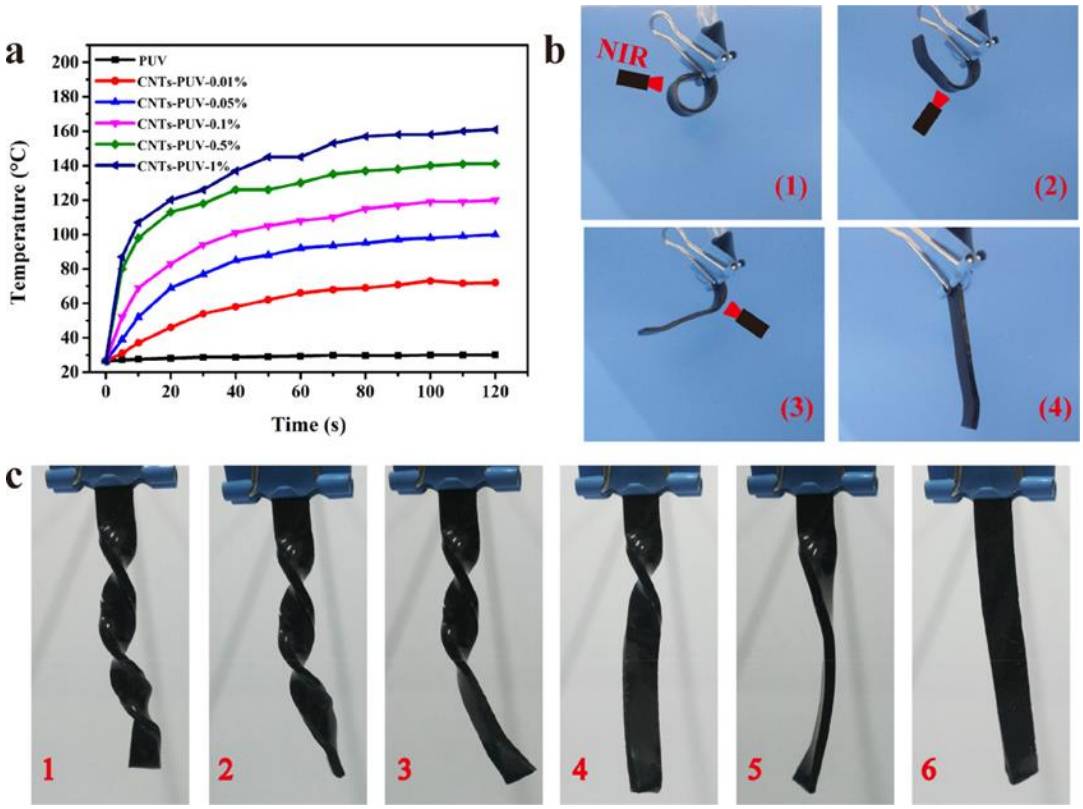

Figure I.43 - Light-triggered shape recovery of MWCNT polyurethane vitrimer: (a) Temperature elevation of different samples as a function of irradiation time, (b) and (c) Images of shape recovery triggered by NIR step by step (Reproduced from ref[254]).

I.3.2. Ferromagnetic shape memory nano-composites

Activation of SMPCs by the application of alternating magnetic fields require preparation of thermomagnetic SMPCs for which ferromagnetic fillers are needed. There are three magnetic heating mechanisms that can arise in magnetosensitive materials: Eddy currents, hysteresis and Néel-Brown relaxation[256]. The size of magnetic fillers greatly impacts the heating efficiency. Microscale fillers can heat through Eddy current and hysteresis losses, but at the nanoscale, these mechanisms become less effective. For instance, Fe_3O_4 (a popular magnetic filler) turns superparamagnetic for particle diameters smaller than 20 nm and no longer exhibit hysteresis. Néel-Brown relaxations are the main magnetic heating mechanisms for nanoparticles, with Néel relaxation dominating for smaller nanoparticles and Brownian motion dominating for larger particles. The Néel relaxation is characterized by the movement of the magnetic moment of the nanoparticles which align with the direction of the magnetic field, while the nanoparticles remain stationary. On the other hand, the Brown relaxation is associated with the actual rotation of the magnetic nanoparticles. These relaxation mechanisms operate simultaneously when the nanoparticles are exposed to an alternating magnetic field. However, when the particles are in viscous media and have a diameter of less than 10 nm, the Néel relaxation tends to dominate, while in low-viscosity media, the Brownian motion tends to dominate for larger particles. Néel-Brown relaxations lead to heat dissipation into the matrix imbedding them, which in this case will be used for triggering the SMC recovery.

Fe_3O_4 is a common magnetic filler with high magnetic capability, small cytotoxicity, and high biocompatibility[257,258]. However, unmodified magnetic particles have a strong agglomeration propensity due to van der Waals and magnetic forces, leading to unsatisfactory composite properties[259]. Techniques such as surface modification, chemical modification, and mechanical ultrasonication have shown promise in improving their dispersion and the composite properties. Shu-Ying Gu and co-authors have for example created a nanocomposite material that exhibits fast response time by using polylactide-based polyurethane (PLAU) reinforced with magnetite (Fe_3O_4/PLAU)[260]. The researchers coated Fe_3O_4 with oleic acid to improve its dispersion within the polymer matrix. Even with 6% and 9% weight loadings, they

observed only small agglomerations. With a 9% weight loading, the material achieved shape recovery in 11 seconds when placed in a hot bath (figure I.44 – A) and 60 seconds when exposed to an alternating magnetic field (figure I.44 – B). Other magnetic fillers have been reported in the literature such as particles of Ni, Ni-Mn-Ga, Ni-ZnFe_3O_4, NdFeB, NiZn, etc[259] and work in the same way.

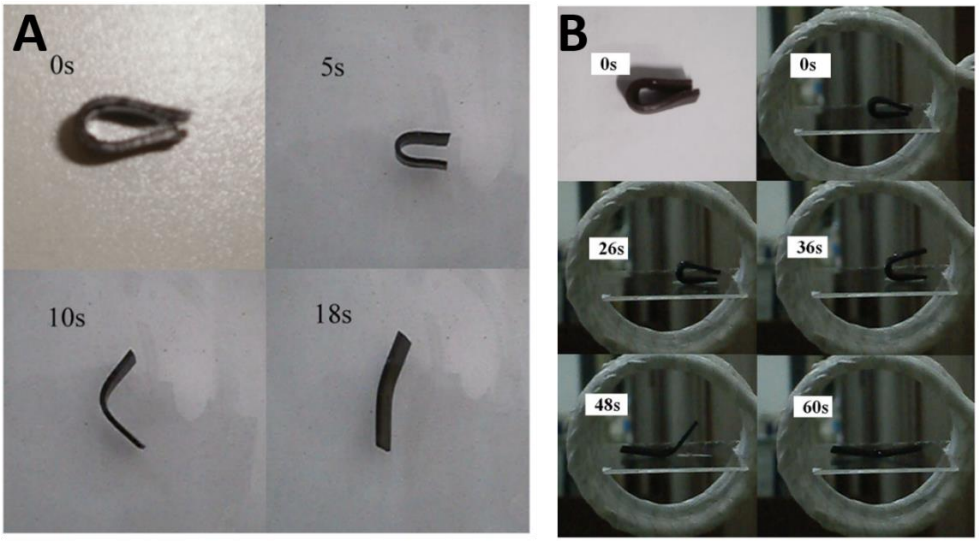

Figure I.44 –Process of shape memory recovery of Fe_3O_4/PLAU (A) in 45°C hotwater; (B) in a magnetic field (f=45 kHz,H=29.7 kA m^{-1}). (Reproduced from ref[260]).

Further researches on how the percentage of magnetic particles (Fe_3O_4) incorporated into a polymer matrix affected induction heating when exposed to an AC magnetic field revealed that this percentage is directly responsible for the induction heating rate while the polymer does not play a significant role[261]. Increasing the nanoparticle concentration and magnetic field strength resulted in higher temperatures. Nevertheless, the environment in which the material was heated also played a role. Lendlein and co-workers described these effects by immerging an Fe_3O_4-based SMCs in different media (water, air and saline solution) with distilled water resulting in a lower temperature compared to air, and a slower heating process when submerged in a saline solution as compared to water[262]. Nanoparticles induce also a Tg decrease due to a plasticization effect[263] which has been observed in many other cases[257,260,264]. Finally, when a large percentage of magnetic particles is added to a polymer matrix, the material experienced irreversible deformation, leading to failure[261].

Similarly to MWCNTs composites, composites made of magnetic nanofillers dispersed in DCB matrices exhibit multiple functions including magnetothermal welding, reprogramming or reshaping abilities, so as remote control of the shape recovery. Figure I.45 illustrates a pioneer work by Zhao et al. on the design of a magnetic dynamic polymer composite that enables both structural and material programming and reprogramming with complex geometries and magnetization distribution for multifunctional and reconfigurable shape morphing. For that purpose, they crosslinked linear poly(ethylene glycol) bearing furan rings precursor with bismaleimide in presence of 15 vol% NdFeB microparticles. The magnetic-assisted welding allows the modular assembly that can be further combined with magnetization reprogramming and permanent reshaping capabilities. This allows to reach complex morphing like 3D kirigami with complex magnetization distribution which can be remotely actuated in a magnetic field.

The production of recyclable shape-memory polymer composites is a high priority for improving human health, as they can be implemented in numerous applications thanks to their unique shape memory features and properties modulation through filler incorporation, but offer the major advantage of recycling. 3D printing of smart materials is an attractive area of future development, with 4D printing offering the ability to create structures that can change their shape over time or external stimuli. Magnetic-responsive SMPs show promise for many applications, but there are still challenges to overcome, such as increasing strength and stiffness for structural applications, improving response times, and achieving more uniform temperature distribution through better dispersion of magnetic nanoparticles.

In view of the highly modulable material properties of SMPCs combined with the excellent shape memory properties with possible multi-stimuli actuation, SMPCs are becoming increasingly present in many areas of research and industry. Significant progress has been made in the development and prototyping of SMPCs for commercially relevant applications. However, there are still several obstacles that must be addressed, such as high-end design principles, synthesis, processing and recycling.

Despite these challenges, the polymer chemistry and physics communities are optimistic about advancing the concept of polymer composites and leveraging them to create sustainable, high-performance materials.

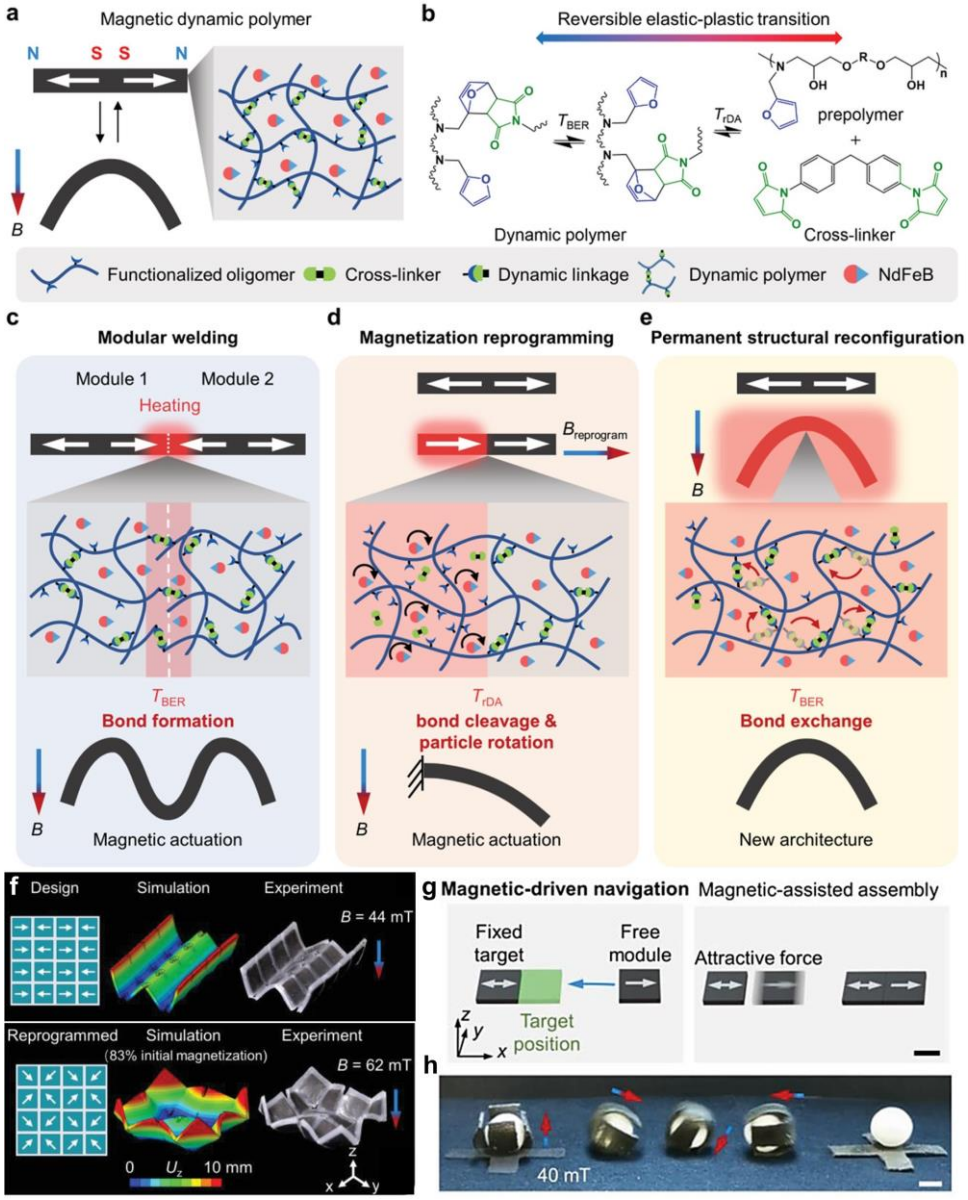

Figure I.45 - Magnetothermal properties of a dynamic polymers that can modularly assemble and reconfigure: Scheme of a) the magnetic dynamic polymer composition, b) reversible elastic-plastic transition of the magnetic dynamic polymer by Diels-Alder reaction, c) modular welding, d) magnetic reprogramming, e) permanent structural reconfiguration by plasticity, f) Design and reprogrammed magnetization of the magnetic dynamic polymer array, g) Scheme of the magnetic-driven remote navigation and assembling of the magnetic dynamic polymer modules, h) A cross structure with a reprogrammed magnetization applied for moving a sphere via an encapsulating and rolling motion under a clockwise rotating magnetic field (Reproduced from ref[265])

Aim of the thesis

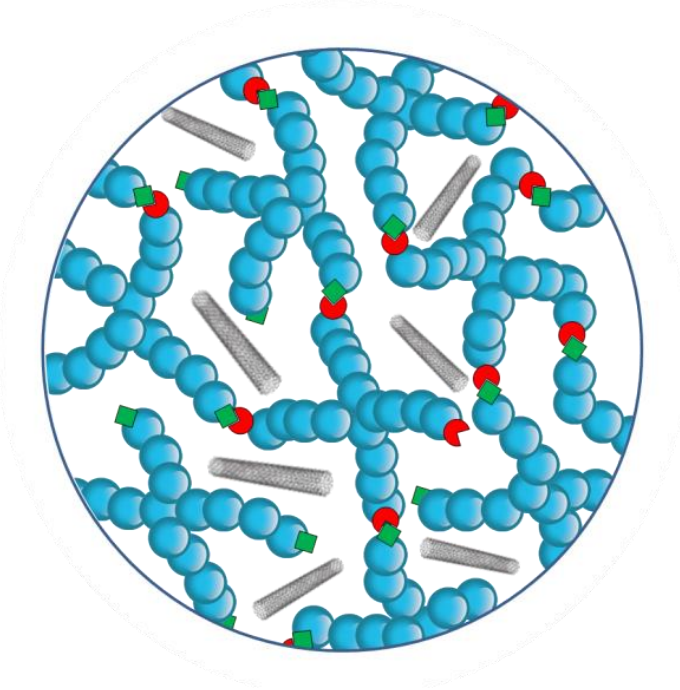

As described in ***Chapter I,*** there has recently been a growing interest in a new class of materials called multi-functional or smart composites. Those composite materials embed the components responsible for the actuation, structural stiffness, thermal behaviour and possibly other properties, while presenting shape-memory properties. Remarkably, smart materials are paving the way to successful applications in many fields, from materials science to biomedical applications.

This work aims at synthesizing well-defined poly-(ε-caprolactone) (PCL) covalent adaptable networks taking advantage of the Diels-Alder reaction for the smart design of composites with performant shape-memory properties. The proposed strategy relies on the quantitative functionalization of star-shaped PCL chain-ends by diene (furan or anthracene) and maleimide moieties to generate well-defined networks upon blending. Different fillers, i.e. multi-walled carbon nanotubes (MWCNTs) or Fe_3O_4 nanoparticles (NP), are added during preparation to get the composites. For the sake of comparison, two types of networks are targeted by the Diels-Alder cycloaddition between maleimide and either furan or anthracene as schematized hereafter (figure I.46).

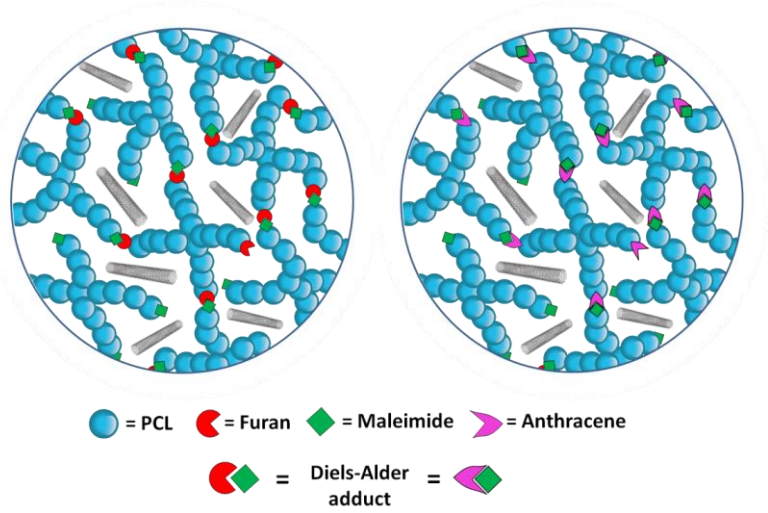

Figure I.46 - Strategy of star-shaped PCL composite networks with MWCNTs.

These shape memory composites (SMCs) were based on semi-crystalline poly(ε-caprolactone) (PCL) as its biocompatibility and remarkable mechanical properties make it particularly appealing for a wide application range in the biomedical field. Furthermore, when

PCL is chemically crosslinked, the resulting covalent networks exhibit excellent shape memory properties particularly enhanced by a melting temperature easily achieved above the body temperature (Tm~ 45 °C) and a low glass transition temperature (Tg~ - 60 °C). By introducing in the semi-crystalline polymer network, various amounts of reversible/irreversible bonds with different dynamics, i.e. maleimide-furan or maleimide-anthracene Diels-Alder adducts, we afford modulation of the bond strength between PCL stars, the creep of the material under stress and the self-healing/recycling properties of the SMC.

In ***Chapter II,*** the benefits and outcomes of the chemistry used for crosslinking is detailed in our comparative study of the two DA systems. Various SMCs have been considered with the aim to compare the advantages and limitations of each filler related to its crosslinking strategy. The fillers having multiple functions; i.e. mechanical reinforcements, thermal/electrical conductivity and magnetic triggering sources for the shape recovery. A clear identification of the interplay between the filler and all those properties is presented, and completed with its correlation with the respective heat mechanisms responsible for the shape recovery actuation (the induced Joule effect or direct magnetic losses).

In the ***Chapter III,*** we extend the use of these PCL covalent adaptable networks (PCL-CAN) to produce recyclable foams. A solvent-free $scCO_2$ batch foaming process is developed which takes advantage of the thermal control of the furane-maleimide Diels-Alder addition, to regulate the degree of branching and crosslinking of the starting PCL reactive mixture allowing to create low-density foams (0.02g/cm^3). These foams possess excellent shape memory properties, including high fixity and recovery ratios, while maintaining good mechanical properties due to their closed-cell morphology. Moreover, these PCL shape memory foams are fully reprocessable. Finally, an example of potential use in a biomedical application illustrated as self-deploying implant for vessel occlusion.

Finally, ***Chapter IV*** is dedicated to a comparative discussion of the PCL-CAN composites prepared during this work in terms of thermal, mechanical, electrical and shape-memory properties together with perspectives of applications and future developments.

Chapter II

Design of high-performance recyclable shape memory PCL composites

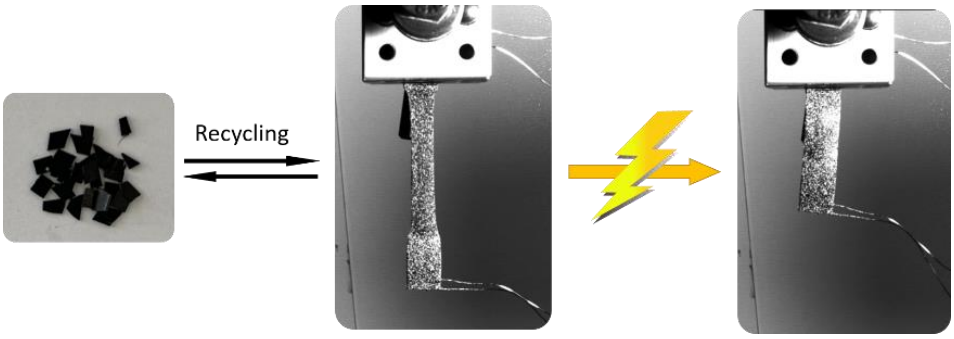

Abstract

Electrically triggered shape memory polymers efficiency and benefits have been described in numerous studies presenting them as novel structural materials for high-end applications. In this field, poly(ε-caprolactone) covalent adaptable networks (PCL-CAN) are particularly appealing since they benefit from excellent shape memory (SM) properties and network reconfiguration making easy the design of complex shape SM devices. Preparation of conducting PCL-CAN networks by melt blending multi-walled carbon nanotubes (MWCNTs) with four-arm star-shaped PCL end-capped with maleimide and furan groups is here investigated. The conventional tensile tester and dynamic mechanical analysis demonstrated the reinforcement of the composite mechanical properties paired with excellent shape memory properties (recovery and fixity ratios about 99%). The simultaneous measurement of the sample resistivity was also integrated to these experiments allowing to follow its evolution during the SM cycles. Rheological measurements highlighted the impact of MWCNTs on the recyclability and self-healing properties of the composite. Electrical triggering of the shape recovery through Joule resistive heating is also deeply studied. The combination of all these properties in the developed material offers unique opportunities to design self-folding multi-materials which is illustrated through the design of smart multi-layered composites. This high-performance composite is especially attractive for reconfiguration of the permanent shape of complex geometry self-deploying devices and their thermal and electrically triggering. Finally, the use of Fe_3O_4 nanoparticles is also considered as an alternative filler. Remote heating through the application of a time varying magnetic field was successfully achieved and potential benefits and prospects of this approach are explored.

Part of this chapter has been submitted for publication in Polymer and is under revision:

Title: MWCNTs filled PCL covalent adaptable networks: towards reprocessable, self-healing and fast electrically-triggered shape-memory composites.
Corresponding author and co-authors: Maxime Houbben; Clara Pereira Sanchez; Philippe Vanderbemden; Ludovic Noels; Christine Jérôme.

CHAPTER II - *Design of high-performance recyclable shape memory PCL composites*

List of abbreviations:

PCL	Poly(ε-caprolactone)
PCL_{82}-4MAL	Poly(ε-caprolactone)$_{82}$-4Maleimide
PCL_{82}-4FUR	Poly(ε-caprolactone)$_{82}$-4Furane
PCL_{82}-4ANTH	Poly(ε-caprolactone)$_{82}$-4Anthracene
PCL-CAN	Poly(ε-caprolactone) Covalent Adaptable Network
PCL-CAN_C	Poly(ε-caprolactone) Covalent Adaptable Network Composite
PCL-CN	Poly(ε-caprolactone) Covalent Network
PCL-CN_C	Poly(ε-caprolactone) Covalent Network Composite
MWCNTs	Multi-walled Carbon Nanotubes
κ	Thermal conductivity
I	Current
V	Voltage
ρ_e	Resistivity
TGA	Thermo gravimetric analysis
DSC	Differential scanning calorimetry
MWCNTs-SMCs	Multi-walled carbon nanotubes shape memory composites
SMP	Shape memory polymers
SMC	Shape memory composite
T_g	Glass transition temperature
T_m	Melting temperature
TEM	Transmission electron microscopy
ρ_e	Electrical resistivity

II. 1. Experimental Section

II. 1. 1. Materials

Toluene (Chem-lab), tetrahydrofuran (THF, Chem-lab), methanol (Chem-lab), dichloromethane (CH_2Cl_2, Chem-lab), diethyl ether (Chem-Lab), chloroform ($CHCl_3$, Chem-lab), *N,N*-dimethylformamide (DMF, Aldrich), ε-Caprolactone (Alfa Aesar), pentaerythritol (Aldrich), succinic anhydride (Aldrich), triethylamine (NEt3, Aldrich), furfuryl alcohol (Aldrich), dicyclohexylcarbodiimide (DCC, Aldrich), 4-*N*,*N*-dimethylaminopyridine (DMAP, Aldrich), anthracenemethanol (Aldrich), multi-walled carbon nanotubes ($MWCNTs_{NC}$, Nanocyl), ferric chloride (Aldrich), ferrous chloride (Aldrich), ammonia (AnalaR NORMAPUR), oleic acid (OA, VWR) were used as received. The synthesis of 4-(2-hydroxy-ethyl)-10-oxa-4-aza-tricyclo[5.2.1.0]dec-8-ene-3,5-dione was reported elsewhere[266]. CAPA™ 4801 (4-arm star-shaped PCL (PCL_{76}-4OH), Mn = 8,800 g/mol, Đ = 1.2) were kindly offered by Perstorp®. Toluene was dried on molecular sieves and kept under inert atmosphere.

II. 1. 2. Synthesis of 4 arm star-shaped PCL (PCL_{82}-4OH)

16,61g (0,488 mmol of hydroxyl function) of pentaerythritol was transferred into a previously dried 5L glass reactor (Büchi). After three azeotropic distillations with anhydrous toluene, 1L of pre-dried and distilled ε-Caprolactone was added to the reactor through a rubber septum with a stainless-steel capillary. Solubilization was achieved by increasing the temperature at 140°C while stirring. Temperature was then reduced to 110° and 1L of dry toluene was added to the reactor. After complete homogenization, 54,74 mL of a previously prepared tin octoate ($SnOct_2$) solution in toluene (1,5526 M, 85 mmol) were added. The solution was then stirred at 110°C for 4 hours. Prior precipitation in heptane, dry and cold toluene (-20°C) was added to the media to stop the reaction. PCL_{82}-4OH was recovered, filtered and dried under vacuum.

^{1}H NMR (400 MHz, CDCl3): δ = 1.37-1.64 (492H, m, CH2-CH2-CH2), 2.30 (164H, t, CH2-C(O)), 4.05 (164H, t, CH2-O-C(O)).

M_n (^{1}H NMR) = 9,484 g/mol, Đ (SEC) = 1.22

II. 1. 3. Synthesis of 4 arm star-shaped carboxylic acid end-capped PCL (PCL_{82}-4COOH)

80 g (40 mmol of hydroxyl function) of PCL_{82}-4OH was transferred into a previously dried 500mL glass reactor. After three azeotropic distillations with anhydrous toluene, 320 ml of anhydrous DMF was added to the reactor through a rubber septum with a stainless-steel capillary. After complete dissolution, 4.4 g (44 mmol) of succinic anhydride and 6.2 ml (44 mmol) of NEt_3 were sequentially added to the DMF solution. The solution was then stirred at 45°C overnight. PCL_{82}-4COOH was recovered by precipitation in diethyl ether, filtered and dried under vacuum.

^{1}H NMR (400 MHz, CDCl3): δ = 1.37-1.64 (492H, m, CH2-CH2-CH2), 2.30 (164H, t, CH2-C(O)), 2.61 (16H, s, C(O)-CH2-CH2-C(O)), 4.05 (164H, t, CH2-O-C(O)).

M_n (^{1}H NMR) = 9,884 g/mol, Đ (SEC) = 1.22

II. 1. 4. Synthesis of 4 arm star-shaped furan end-capped PCL (PCL_{82}-4FUR)

40 g (20 mmol of carboxylic acid functions) of PCL_{82}-4COOH was transferred into a previously dried 500mL glass reactor. 150 ml of anhydrous CH_2Cl_2 was transferred to the reactor through a rubber septum using a stainless-steel capillary. After dissolution of the PCL, 2.4 ml (22 mmol) of furfuryl alcohol, 4.5 g (22 mmol) of DCC and 0.27 g (2.2 mmol) of DMAP were transferred inside the reactor. After one night of reaction at room temperature and filtration of the formed dicyclohexylurea (DCU), PCL_{82}-4FUR was recovered by precipitation in diethyl ether, filtered and dried under vacuum. Functionalization was assessed by ^{1}H NMR characterization.

^{1}H NMR (400 MHz, $CDCl_3$): δ = 1.37-1.64 (492H, m, CH2-CH2-CH2), 2.30 (164H, t, CH2C(O)), 2.61 (14.5H, s, C(O)-CH2-CH2C(O) + 1.5H, s, C(O)-CH2-CH2-C(O)OH), 4.05 (164H, t, CH2-O-C(O)), 5.07 (7H, s, O-CH2-furan), 6.35 (3.6H, t, H furan), 6.38 (3.6H, d, H furan), 7.40 (3.6H, d, H furan).

M_n (^{1}H NMR) = 10,191 g/mol, Đ (SEC) = 1.14

II. 1. 5. Synthesis of 4 arm star-shaped maleimide end-capped PCL (PCL_{82}-4MAL)

40 g (20 mmol of carboxylic acid functions) of PCL_{82}-4COOH was transferred into a previously dried 250 mL glass reactor. 150 ml of anhydrous CH_2Cl_2 was transferred to the reactor through a rubber septum using a stainless-steel capillary. After the dissolution of the PCL, 2.2 g (22 mmol) of 4-(2-hydroxyethyl)-10-oxa-4-aza-tricyclo[5.2.1.0]dec-8-ene-3,5-dione, 2.2 g (21 mmol) of DCC and 0.26 g (2.1 mmol) of DMAP were transferred inside the reactor. After one night of reaction at room temperature and filtration of the formed DCU, the protected PCL_{82}-4MAL was recovered by precipitation in diethyl ether, filtered and dried under vacuum. The polymer was then transferred into a glass reactor before to be heated at 105°C under vacuum for 10 hours to eliminate furan and regenerate the maleimide functions. PCL_{82}-4MAL was kept at room temperature. Functionalization was assessed by ^{1}H NMR characterization.

^{1}H NMR (400 MHz, $CDCl_3$): δ = 1.37-1.64 (492H, m, CH2-CH2-CH2), 2.30 (164H, t, CH2C(O)), 2.61 (16H, s, C(O)-CH2-CH2C(O)), 3.79 (8H, t, N-CH2), 4.05 (164H, t, CH2OC(O)) 4.25 (8H, t, N-CH2-CH2-O), 6.73 (8H, s, CH=CH).
M_n (^{1}H NMR) = 10,336 g/mol, Đ (SEC) = 1.25

II. 1. 6. Synthesis of 4-arm star-shaped anthracene end-capped PCL (PCL_{82}-4ANTHR)

40 g (19 mmol of carboxylic acid functions) of PCL_{82}-4COOH was transferred into a dried 250 mL glass reactor. 150 ml of anhydrous CH_2Cl_2 was transferred to the reactor through a rubber septum using a stainless-steel capillary. After the dissolution of the PCL, 4.6 g (21 mmol) of anthracene methanol, 4.3 g (21 mmol) of DCC and 0.26 g (2.1 mmol) of DMAP were transferred inside the reactor. After one night of reaction at room temperature and filtration of the formed DCU, PCL_{82}-4ANTHR was recovered by precipitation in diethyl ether, filtered and dried under vacuum.

^{1}H NMR (400 MHz, CDCl3): δ = 1.37-1.64 (492H, m, CH2-CH2-CH2), 2.30 (164H, t, CH2C(O)), 2.62 (12H, s, C(O)-CH2-CH2C(O)), 2.68 (4H, s, C(O)-CH2-CH2-C(O)OH), 4.05 (164H, t,

CH2OC(O)) 6.17 (6H, s, anthracene-CH_2-O), 7.50 (12H, m, H aromatic), 8.05 (6H, d, H aromatic), 8.30 (6H, d, H aromatic), 8.51 (6H, s, H aromatic).

M_n (^{1}H NMR) = 10,504 g/mol, Đ (SEC) = 1.28

II. 1. 7. Preparation of MWCNTs PCL composite networks

PCL-Covalent Adaptable Network with $MWCNTs_{NC}$ (PCL_{82}-4FUR/PCL_{82}-4MAL/$MWCNTs_{NC}$)

Stoichiometric amounts in reactive groups (furan and maleimide moieties) of PCL_{82}-4FUR and PCL_{82}-4MAL, were mixed together and finely grounded in order to have 4.5 g of mixture. This mixture was then transferred to a vial and 3wt% of $MWCNTs_{NC}$ were added. This mix was then melt-blended at 105°C in a 6 cm^3 co-rotating twin screw mini-extruder (Xplore, DSM) for 60 min at 150 rpm. After extrusion, the polymer blends were rapidly injected into a mold in order to confer a flat sheet shape to the sample, hot pressed at 105°C and then cured (see next section).

PCL-Covalent Network with $MWCNTs_{NC}$ (PCL_{82}-4ANTH/PCL_{82}-4MAL/$MWCNTs_{NC}$)

Stoichiometric amounts in reactive groups (anthracene and maleimide moieties) of PCL_{82}- 4ANTH and PCL_{82}-4MAL, were mixed together and finely grounded in order to have 4.5 g of mixture. This mixture was then transferred to a vial and 3wt% of $MWCNTs_{NC}$ were added. This mix was then melt-blended at 65°C in a 6 cm^3 co-rotating twin screw mini-extruder (Xplore, DSM) for 10 min at 150 rpm. After extrusion, the polymer blends were rapidly injected into a mold in order to confer a flat sheet shape to the sample and hot pressed to 105°C and then cured (see next section).

II. 1. 8. Curing of MWCNTs PCL networks

The extruded materials were then placed in a 0.5 mm-thick metallic frame and hot pressed at 105°C under a load of 4 metric tons. Each sample was then placed under a load of 10 kg for 72 h in a ventilated oven at 65°C. They were recovered in the form of a flat sheet that was kept min 7 days at room temperature before measurement.

II. 1. 9. Synthesis of Fe_3O_4@OA nanoparticles

21.6 g of ferric chloride was added to 200 ml of deionized water and was stirred for at least 20 min under closed condition with nitrogen bubbling; 8.1 g of ferrous chloride was added to 100 ml of deionized water, stirred also for 20 min under closed conditions with nitrogen bubbling. The two solutions were then mixed together and the mixture was stirred under a closed condition for 25 min.

Aqueous ammonia and OA were slowly added into the mixture at a relative rate of 10 drops of aqueous ammonia for 1 drop of OA until 50 ml of aqueous ammonia and 3 ml of oleic acid were added. The mixture was then stirred for another 25 min. A magnet was placed at the bottom of the beaker to obtain wet precipitate of magnetic particles (MPs) which was washed twice with deionized water and alcohol, respectively. Then the wet precipitate was stirred for 5 min at 75 °C. Finally, the wet precipitate was mixed with toluene at a desired ratio and stirred for 30 min to obtain the dispersion of Fe_3O_4@OA.

II. 1. 10. Preparation of Fe_3O_4@OA nanoparticles PCL network

Stoichiometric amounts in reactive groups (furan or anthracene, and maleimide moieties) of PCL_{82}- 4FUR/PCL_{82}- 4ANTH and PCL_{82}-4MAL were dissolved in the right amount of Fe_3O_4@OA (diluted in toluene) solution (in function of the desired Fe_3O_4 quantity needed). Volume was adjusted to obtain a 2.5 wt % of PCL in total. After 10 min of an ultrasonic treatment, the solution was precipitated in a non-solvent of PCL, i.e., heptane, at - 20 °C. The mix was then recovered by filtration thanks to a Buchner funnel. After drying under vacuum for one night, the material is hot pressed in the desired shape.

II. 1. 11. Curing of Fe_3O_4@OA nanoparticles PCL network

The coprecipitated materials are placed in a 0.5 mm-thick metallic frame and hot pressed at 105°C under a load of 4 metric tons. Each sample are then placed under a load of 10 kg for 72 h in a ventilated oven at 65°C. They were recovered in the form of a flat sheet that was kept min 7 days at room temperature before measurement.

II. 1. 12. Insoluble fraction and swelling ratio

Stripes of cross-linked PCL samples collected after melt-blending and curing were weighed (initial material weight, about 0,25g) and then placed into chloroform, a good solvent for PCL, during 48h at room temperature in order to reach the swelling equilibrium. The gel was then carefully collected without the soluble fraction and weighed (swollen network weight). In order to determine the exact weight of the cross-linked material, without the soluble fraction due to unreacted PCL chains, the gel was then dried under vacuum until reaching constant weight (dried network weight). The swelling ratio and the insoluble fraction (i.e. network fraction) were calculated based on these weight measurements according to equations (II. 1) and (II. 2) respectively.

$$Swelling\ Ratio = \frac{(swollen\ gel\ weight - dried\ material\ weight)}{dried\ material\ weight}\ x\ 100 \quad \text{(II. 1)}$$

$$Insoluble\ fraction = \frac{dried\ material\ weight}{initial\ material\ weight}\ x100 \quad \text{(II. 2)}$$

II. 1. 13. Characterization techniques

Structure characterization

^{1}H NMR spectra were recorded in $CDCl_3$ at 400 MHz in the FT mode with a Bruker Avance 400 apparatus equilibrated at 25°C.

Size exclusion chromatography (SEC) was carried out in THF at 45°C at a flow rate of 0.7 mL/min with Viscotek 305 TDA liquid chromatograph. The PL gel 5µm (104 Å, 103 Å and 100 Å) columns were calibrated with polystyrene standards.

Raman spectra were recorded at room temperature using a Horiba-Jobin-Yvon Labram 300 confocal spectrometer provided with an Olympus BX40 microscope. The 647.1 nm line of a Spectra Physics model 168 Krypton ion laser was focused on a rectangular-shaped solid sample with an Olympus x100 objective. The laser power at the sample level was of the order of 15 mW. Every spectrum was accumulated twice for about 10 seconds or more depending on the sample signal. The detector is an Andor iDus BR-DD 401 CCD. All spectra were scaled up and, if necessary, base line corrected with home-made software.

Transmission electron microscopy (TEM) (Philips M100 microscope working at an accelerating voltage of 100 kV) was used to characterize the MWCNTs dispersion in the composite. Thin slices (90 nm) were prepared by ultracryomicrotomy (ULTRACUT E from Reichert- Jung) at -130 °C. The micrographs were analyzed by using the KS 100 (Kontron Imaging System) software.

The diameter of the micelles was measured by Dynamic Light Scattering (DLS) with a Malvern Instrument Model ZetaSizer Nano ZS.

Thermal properties

Differential scanning calorimetry (DSC) analysis was operated on a TA DSC 250 apparatus. Melting point and endotherm was determined during the second heating run of the sample between -80°C and 70°C at 10K/min with isotherms of 5 minutes at each targeted temeprature. Degree of crystallinity of PCL has been evaluated by comparing the value of the melting enthalpy to the one reported for a PCL presenting 100% of crystallinity.Thermogravimetric analysis (TGA) was carried out with a TA TGA Q500.

The thermal conductivity (κ) is measured on three different samples of SMC at three different power levels, i.e., 61, 122 and 244 mW. Each measurement carried out twice was performed by Dr. Clara Pereira Sánchez at the Electronics, Microsystems, Measurements, and Instrumentation (EMMI) laboratory of the university of Liège.

Thermo-mechanical properties

Rheological measurements were performed using an ARES-G2 Rheometer from TA Instruments. 1 g of a sample disk was placed at 125°C between a plate-plate geometry (diameter 25 mm). The temperature was then decreased and adjusted to the various studied values where both the elastic and viscous moduli were recorded through time at a frequency of 1Hz and a strain of 1%.

Shape-memory properties have been measured by dynamic mechanical analysis (DMA) (Q800, TA Instruments) using the tensile film clamp in controlled force mode. The sample (typically 1,5 x 0,5 x 0,5 cm) was first equilibrated at 65°C for 5 min then experienced a tensile stress ramp (0.06 MPa/min) till 0.6 MPa. Then, the sample is cooled down, under stress at 3°C/min to 0°C and maintained at that temperature for 5 min. The stress is then released and the sample is reheated, stress-free at 3°C/min to 65°C. The process is cycled 4 times. The comparison of the strain at 0°C before and after the release of the stress allows measuring the sample fixity. The fixity ratio (R_f) is given by equation (II.3). The shape recovery is obtained by comparing the strain at 65°C before and after this cycle recovery ratio (R_c) being calculated by equation (II.4).

$$R_f = \frac{\text{strain after stress release at 0°C}}{\text{strain before stress release at 0°C}} * 100 \qquad \text{(II.3)}$$

$$R_c = \frac{\text{strain at 65°C without stress for cycle N at 0°C}}{\text{strain at 65°C without stress for cycle (N-1)}} * 100 \qquad \text{(II.4)}$$

Thermal conductivity, electrical resistivity and self-heating experiments

For electrical resistivity assessment, rectangular samples (15 mm x 5 mm x 0,5 mm) are cut from PCL-CAN_c or PCL-CN_c sheet. The surface of the samples is cleaned with isopropanol

and four electrodes are painted on the surface of the samples with silver paste (Agar scientific Electrodag 1415). Thin copper wires are then placed on them so that the injected current would flow through the length (15 mm) of the sample in a four-point measurement configuration (figure II.1). The used set-up is home-made and was developed by Dr. Clara Pereira Sánchez at the Electronics, Microsystems, Measurements, and Instrumentation (EMMI) laboratory of the University of Liège. The following self-heating experiments were also realized by Dr. Clara Pereira Sánchez.

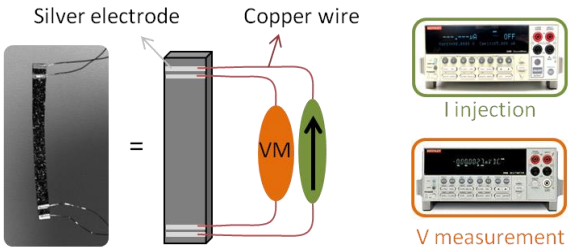

Figure II.1 – Experimental set-up for electrical resistivity assessment

A LabVIEW program controls a Keithley 2400 source (figure II.1, green) that injects the current I and a Keithley 2001 multimeter (figure II.1, orange) that measures the voltage (V) across the sample between the two electrodes (L). The resistivity of the samples (ρ_e) is calculated following equation (II. 3) .

$$\rho_e = \frac{SV}{IL} \qquad \text{(II. 3)}$$

The SMCs samples have a parallelepiped shape and are subjected to an electric current injected in parallel to their longer dimension. The thermal characteristics of the electrical contacts are neglected and the heat losses through the copper wires are assumed to be zero. To measure electrical resistivity, as no resistive heating is needed, the injected current is set to the lowest possible value (0.5 mA), at which no measurable resistive heating occurs. To limit the resistivity variation among samples, their thermal history is erased prior to any test by applying a heating ramp up to 60 °C at various speed (generally the same temperature ramp as implemented in the test), an isotherm at 60 °C for 5 min and a cooling ramp of same speed down to -10 °C.

During self-heating experiments, the sample is suspended vertically in air with its longest side parallel to the horizontal by making use of the mechanical properties of the copper wires according to figure II.1. The temperature on the front surface of the sample is measured using an infrared thermal camera (COX CX320) that was previously calibrated in-house. In order to obtain an accurate temperature measurement (within ±1 ºC), the readings from the IR camera have been corrected for the finite emissivity of the samples (0,91 +- 0,03). The temperature measurement region excludes the electrodes in order to avoid errors due to the different emissivity of the silver and the polymer itself. Five temperature spots are monitored on the sample during analysis and the mean sample temperature is assumed as their mathematical average (P2 to P6, figure II.3). Room temperature is also monitored (P1). Regarding the value of the injected current, it is required to achieve a well-defined resistive heating (to conserve a defined temperature ramp), the value is therefore set by a proportional integral controller described in another work[267]. Since it will be demonstrated later that ρ_e varies with temperature, a controller is required to adjust the value of the injected current so that a well-defined temperature ramp can be achieved.

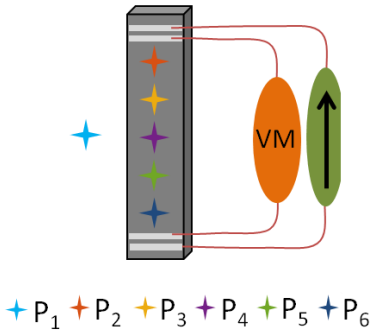

Figure II.3 - Temperature spot set-up for self-heating assessment on an SMC.

Thermal conductivity measurements were performed on disk samples with a bespoke experimental system whose details are reported in a previous work[268]. Disc samples of 13.94 mm diameter are punched out of a 1.86 mm thick SMP or SMP_c plate. The surfaces of the samples are cleaned with isopropanol and coated with silver paste (Agar scientific Electrodag 1415) for better adhesion and thermal contact between the disc and the sample holder. The measurements are carried out at a pressure < $5 \cdot 10^{-8}$ mbar.

Magnetization

Magnetic data were acquired with a Quantum Design PPMS Evercool II system (equipped with a VSM large bore option), on 4.5(1) mg of sample sealed in a propylene bag (20.7 mg) under argon atmosphere. Hysteresis of magnetizations were measured successively at 300, 338 and 398 K, from 0 to 2 T, from 2 to -2 T, and from -2 to 2 T. These measurements were made by Dr. Rodolphe Clérac, M. Rouzières at Centre de Recherche Paul Pascal (Pessac, France) CRPP-CNRS UMR 5031, Research team for "Molecular Materials & Magnetism".

II. 1. 14. Magnetic heating

The induction heating equipment is made by Haituo Intelligent Technology, model LH-15A (also known as HT-15KW) and a COX thermal camera (CX320). The induction heating source supplies a current of 0 to 800 A at high frequency of 30 to 100 kHz. In practice, constant value of the current can not be obtained and frequencies are measured in a range of 35 to 40 kHz. The high frequency current is injected into a hollow coil into which water flows to cool it down. The high frequency current injected in the coil produces a magnetic field that can be used in order to heat up magnetic (nano)materials due to Néels-Brown relaxation and/or hysteresis losses. The set-up was part of the Electronics, Microsystems, Measurements, and Instrumentation (EMMI) laboratory of the University of Liège.

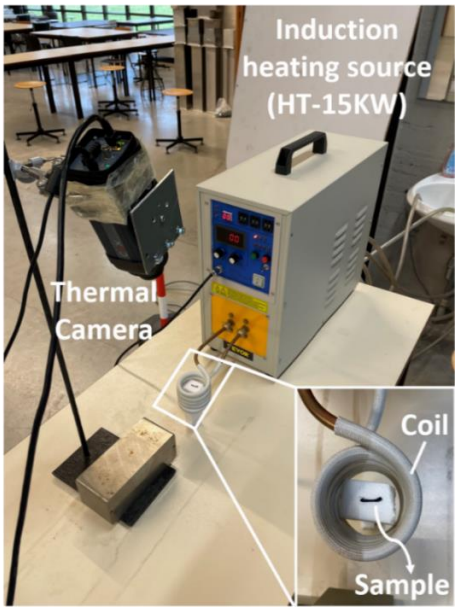

Figure II.4 - Induction heating set up.

II. 2. Results and discussion

II. 2. 1. Functional star-shape PCL synthesis

Based on previous studies on shape memory PCL-CAN prepared from mixture of 4-arm PCL stars end-capped with furan or maleimide[89], the synthesis of a 4-arm star-shaped PCL (PCL_{82}-4OH, figure II.5) with each arm having a molar mass of about 2,300 g/mol, was targeted as starting material for the present study. This star PCL being no more commercially available, we decided to prepare a 1 kg batch of these stars in order to cover the needs of the present PhD work. Therefore, the conventional ring-opening polymerization of εCL initiated by pentaerythritol and catalyzed by $SnOct_2$ at 110 °C was performed in a 5L reactor with 1 L of □-caprolactone (figure II.6). The reaction conditions (time of reaction, concentration of reactants and temperature) have been determined first by a kinetic study of this reaction on a small scale.[269] The same conditions, namely 4h of polymerization, 50 wt% of toluene at 110 °C, were used for the large-scale synthesis. It is interesting to point out that the scaling up followed very similar polymerization rate and so led to the targeted 4-arm PCL star with a total DP of 82 and a narrow dispersity as determined by ^{1}H NMR (Mn 9,500 g/mol PCL_{82}-4OH) and SEC, respectively.

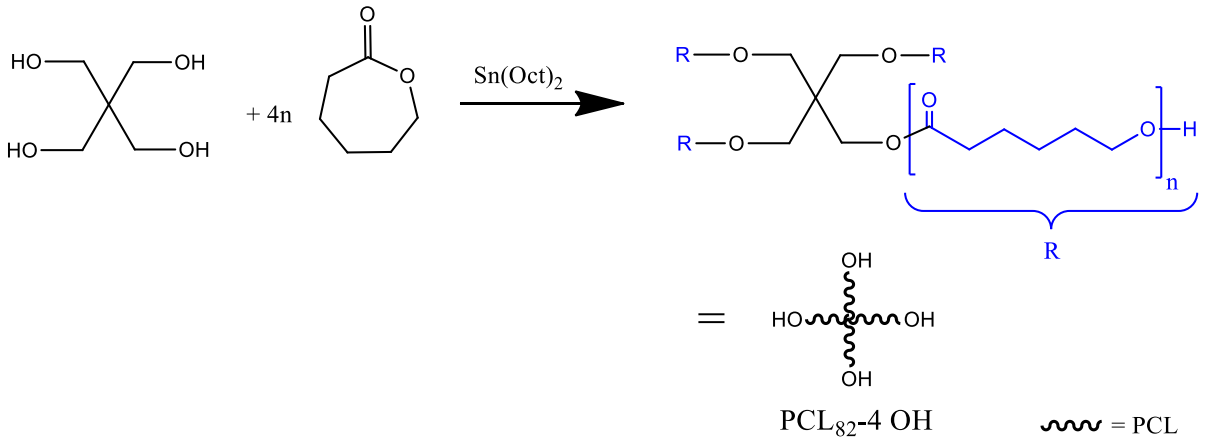

Figure II.5 - Synthesis of PCL_{82}-4OH by ring-opening polymerization of εCL initiated by pentaerythritol and catalyzed by $SnOct_2$

Figure II.6 - Reactor used for 1 kg batch synthesis of PCL_{82}-4OH

The hydroxyl chain-ends of this 4-arm PCL stars were then quantitatively converted into a diene (furan or anthracene) or a dienophile (maleimide) by a two-step process based on the Steglich esterification reaction as depicted in figure II.7.

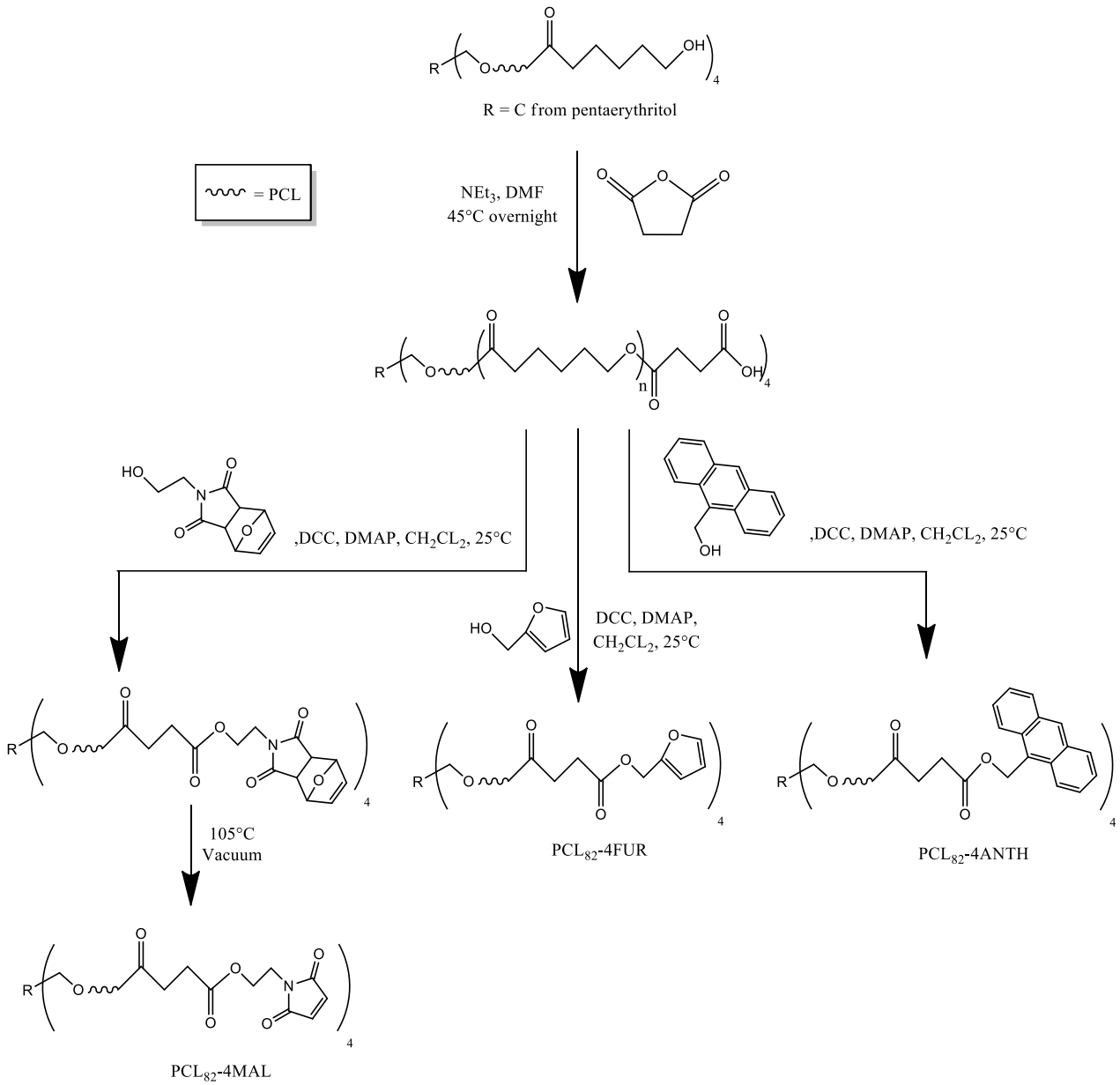

Figure II.7 - Chain-end functionalization of the PCL_{82}-4OH with diene or dienophile moieties

In the first step, the hydroxyl end groups of PCL_{82}-4OH have been reacted with succinic anhydride to yield to a 4-arm star-shaped PCL bearing quantitatively four carboxylic acid end-groups (PCL_{82}-4COOH). The complete conversion is assessed by ^1H NMR analysis by the disappearance of the terminal $–CH_2$-OH signal at 3.6 ppm and the apparition of a new signal at 2.61 ppm corresponding to the C(=O)-CH_2-CH_2-C(=O) protons (figure II.8).

The PCL_{82}-4COOH was then esterified respectively with furfuryl alcohol or a protected maleimide alcohol (4-(2-hydroxyethyl)-10-oxa-4-aza-tricyclo[5.2.1.0]dec-8-ene-3,5-dione, a Diels-Alder adduct of *N*-(2-hydroxyethyl) maleimide with furan) or 9-anthracene methanol in the presence of DCC and DMAP, according to a Steglich esterification mechanism. PCL_{82}-4MAL was quantitatively generated upon thermal cycloreversion of the Diels-Alder adduct at 105°C under vacuum for 6 h as attested by ^{1}HNMR by the disappearance of the characteristic peaks of the DA adduct in favor of a peak at 6.73 ppm, typical of the ethylenic protons of maleimide moiety.

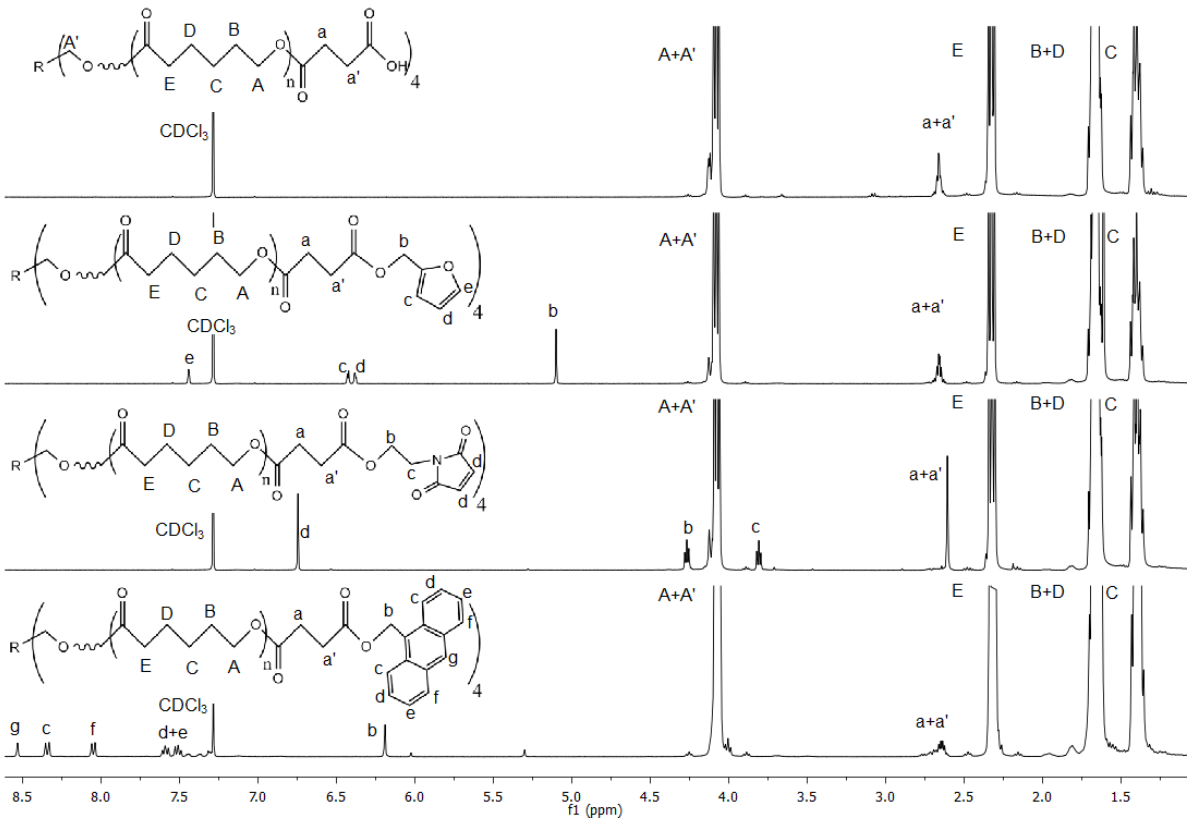

Figure II.8 - ^{1}H NMR spectrum of PCL_{82}-4COOH, PCL_{82}-4FUR, PCL_{82}-4MAL, PCL_{82}-4ANTH

A high degree of conversion was reached for each alcohol (table II.1). Nevertheless, the second esterification is not fully quantitative as evidenced by the weak signal at 2.68 ppm (figure II.9) characteristic of the unreacted chain-ends. A few PCL stars are thus bearing less than 4 Diels-Alder reactive groups.

The superposition of the SEC chromatograms of the various PCL stars shows that no degradation occurred during the functionalization steps (figure II.9). The small variation in the position of the elution volume is attributed to the different end-groups located on relatively short arms (DP=21). Table II.1 gathers the macromolecular characteristics of the various PCL stars prepared in this study.

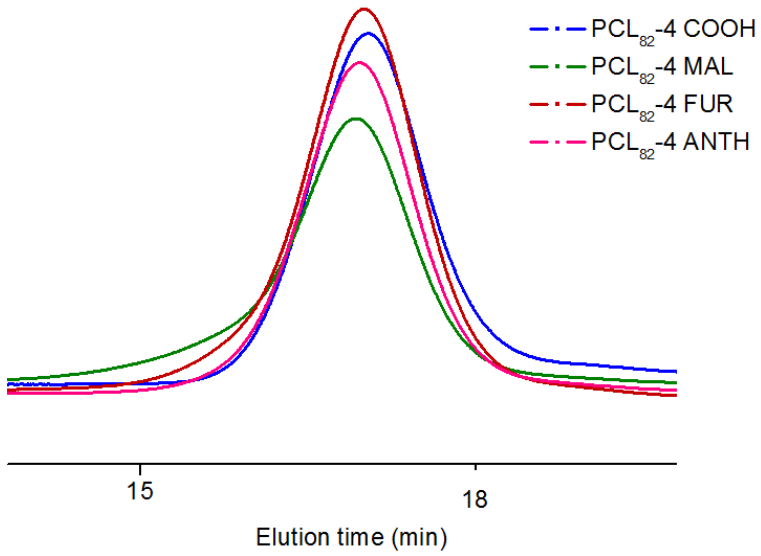

Figure II.9 - SEC traces of PCL_{82}-4COOH (blue curve), PCL_{82}-4MAL (green curve), PCL_{82}-4FUR (red curve), PCL_{82}-4ANTH (purple curve) using refractive index detector

Table II.1 - Macromolecular characteristics of the obtained PCL stars

	Chain-end functionality	Chain-ends conversion[a] (%)	Mn (^{1}H NMR)[b] (g/mol)	Đ (SEC)[c]	Degree of crystallinity[d] (%)	T_m[e] (°C)
PCL_{82}-4OH	Hydroxyl	100	9484	1,22	49,1	49.59
PCL_{82}-4COOH	Carboxylic Acid	> 99	9884	1,22	48,6	48,64
PCL_{82}-4FUR	Furane	95	10191	1,14	43,7	46.91
PCL_{82}-4MAL	Maleimide	92	10336	1,25	38,5	45.30
PCL_{82}-4ANTH	Anthracene	76	10504	1,28	41,3	48,24

a) As determined from ^{1}H NMR including chain-ends
b) Average molar mass (*PCL_{82}-4OH: 82 x 114 g/mol +136 g/mol; PCL_{82}-4COOH: Mn PCL_{82}-4OH +400 g/mol; PCL_{82}-4MAL: Mn PCL_{82}-4COOH +492 g/mol x 0.92; PCL_{82}-4FUR: Mn PCL_{82}-4COOH +324 g/mol x 0.95; PCL_{82}-4ANTH: Mn PCL_{82}-4COOH +832 g/mol x 0.76)*
c) Molar mass distribution measured by SEC in THF at 45°C
d) Crystallization degree as determined from DSC analysis
e) Melting temperature determined from DSC analysis at the peak of the endotherm

As these stars will be used to obtained composite networks exhibiting shape memory effect, the crystallinity of the PCL stars is mandatory to fix the temporary shape. Therefore, the melting point and the degree of crystallinity were determined by DSC during the second heating run of the sample between -80°C and 100°C at 10°C/min. The degree of crystallinity was calculated according to equation (II. 4) in which ΔH_f (T_m) (in J/g) is the enthalpy of melting measured by DSC and $\Delta H_f^0(T_m^0)$ is the enthalpy of melting for a 100 % crystalline PCL, equal to 139.5 Jg^{-1} according to literature[270].

$$X_c = \frac{\Delta H_f(T_m)}{\Delta H_f^0(T_m^0)} \quad \text{(II. 4)}$$

These data summarized in Table II show that all the functionalization of the stars chain-ends slightly affects the crystallization and the crystallite stability by the small decrease of the degree of crystallinity and of T_m.

II. 2. 2. Preparation of MWCNTs PCL composite networks: PCL-CAN / PCL-CAN$_c$ / PCL-CN / PCL-CN$_c$

Covalent adaptable networks of PCL (PCL-CAN) are obtained by melt-blending PCL$_{82}$-4FUR and PCL$_{82}$-4MAL in stoichiometric amounts of reactive groups (figure II.10). The Diels-Alder adduct formed between furan and maleimide is thermosensitive, and retro Diels reactions can occur around or above 105 °C. Below that temperature, despite the still present dynamic equilibrium between DA and retro-DA reactions, the formation of D-A adducts is favored (figure II.10). PCL-CAN present thus a thermosensitive and reversible network. In contrast, the Diels-Alder adduct of maleimide with anthracene is more stable, the retro-reaction occurring above 180 °C (figure II.10). In the polymer stability range (below 150 °C), the blending of the PCL$_{82}$-4MAL with PCL$_{82}$-4FUR will lead to a reversible network (PCL-CAN) while the blending with PCL$_{82}$-4ANTH will lead to a thermostable network (PCL-CN).

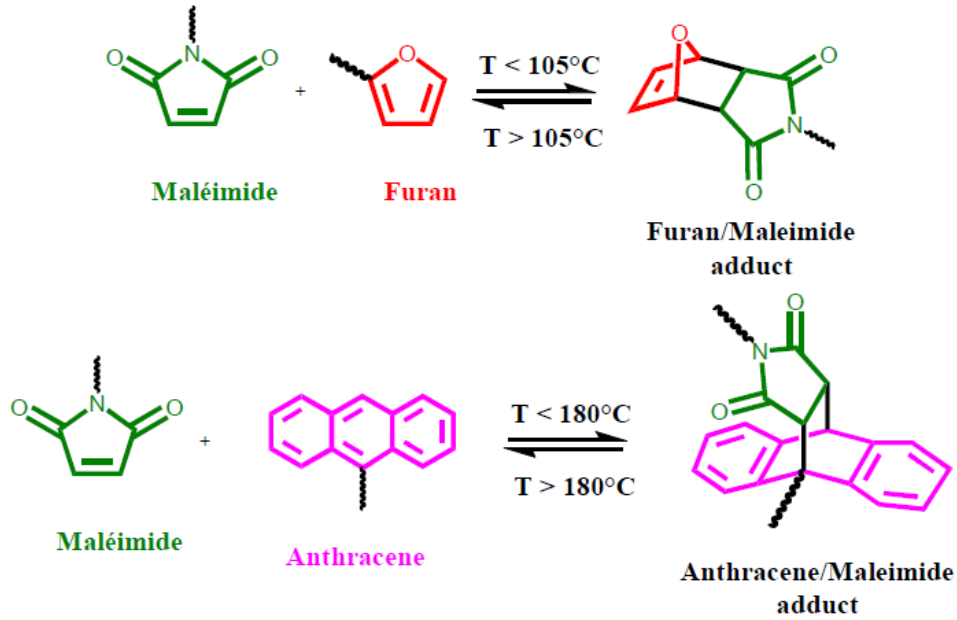

Figure II.10 - DA-based PCL networks

In order to impart electrical conductivity to these PCLs, MWCNTs were dispersed in both types of networks. These composites will be respectively referred as PCL-CAN$_c$ and PCL-CN$_c$ all along this work (figure II.11 and figure II.12). Preliminary experiments showed that using 1 wt% of MWCNTs leads to an average resistivity of the composite below 80 Ωm, i.e., low

enough to enable current driven heating. These experiments are described in my colleague Clara Andrea Pereira Sánchez 's thesis[271]. Nevertheless, in the present work, a concentration of fillers of 3 wt% was selected for two reasons. Firstly, a higher MWCNTs content improves the reproducibility of resistive heating from sample to sample. Secondly, a higher content in MWCNTs will ensure enough electrical conductivity of the composite upon high deformation of the material. Indeed, it was shown that applying a tensile stress to a composite leads to the orientation of carbon nanotubes that can increase the distance voids between them. High deformation can then cause a considerable drop of the conductivity, especially when the material is close to the percolation threshold. The selection of 3 wt% of MWCNTs will prevent any significant decrease in conductivity, even under conditions of high deformation, thereby enabling greater flexibility in the study of shape memory properties.

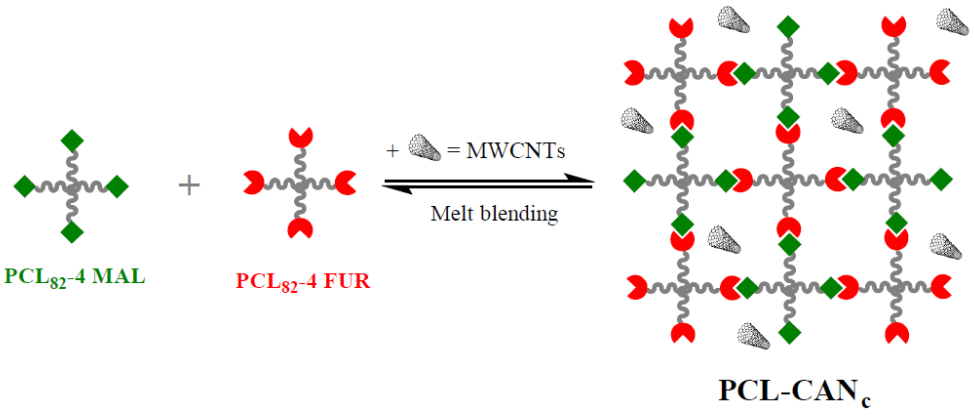

Figure II.11 – DA-based thermo-reversible PCL-CAN$_c$ composite network

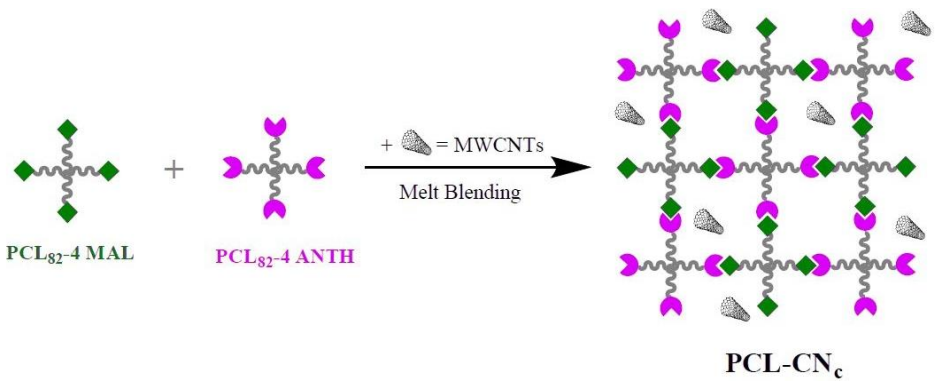

Figure II.12 – DA-based PCL-CN$_c$ composite network

The preparation of PCL-CAN_c is realized by melt-blending stoichiometric amounts in reactive groups (furan and maleimide moieties) of both PCL_{82}-4MAL and PCL_{82}-4FUR with 3 wt% of MWCNTs in a mini-extruder at 105 °C for 60 minutes. This temperature was chosen to favor the retro-DA while mixing and avoid crosslinking into the mixing chamber. Nevertheless, reactions between MWCNTs and either maleimide or furan can occurs which would result in a melt strength increase. These two phenomena result in a small torque increase observed while processing. Considering the low viscosity of the melted PCL stars at this temperature, one hour of mixing time is set up to ensure a proper dispersion of the MWCNTs in the matrix.

The state of MWCNTs dispersion is quite often only characterized using light microscopy, scanning or transmission electron microscopy[272]. Here transmission electron microscopy (TEM) imaging was used for investigation on thin section of prepared films. These thin sections of the composites with 3 wt% MWCNTs had a thickness of about 80 µm. Three sections were prepared from distant parts of the films. For low mixing time (10 min), multiple isolated large MWCNTs agglomerates were observed (figure II.13 – A). These agglomerates are not formed during the blending and molding process, but rather indicate that not enough shearing was present during mixing to disentangle the MWCNTs in its powder form, as they remained in this state of entanglements. The strong intrinsic Van Der Waals attractions among MWCNTs, the poor interfacial interaction between pristine MWCNTs and the PCL matrix and its very low viscosity at the melt state made the dispersion of MWCNTs to be very difficult. That is the primary reasons why mixing is conducted for such a long period of time, in order to allow some chain extension through Diels-Alder reaction, which will inevitably increase the melt-strength of the system and thus the shearing effect during mixing. No remaining agglomerates were observed for 60 minutes of mixing time as presented in figure II.13 - B. It can be observed clearly that the MWCNTs are randomly dispersed in the PCL with some entanglements or bundles. Moreover, they are randomly oriented which leads to formation of some interconnecting structures. It is also possible to quantify the nanotubes dispersion from TEM investigations regarding the part and dimensions of the dispersed nanotubes visible in the two-dimensional thin cuts but it is however much more elaborate and time-consuming. Giving the high MWCNTs concentration, the high mixing time and the absence of MWCNTs

agglomerates, we considered the dispersion to be homogenous enough for the targeted applications.

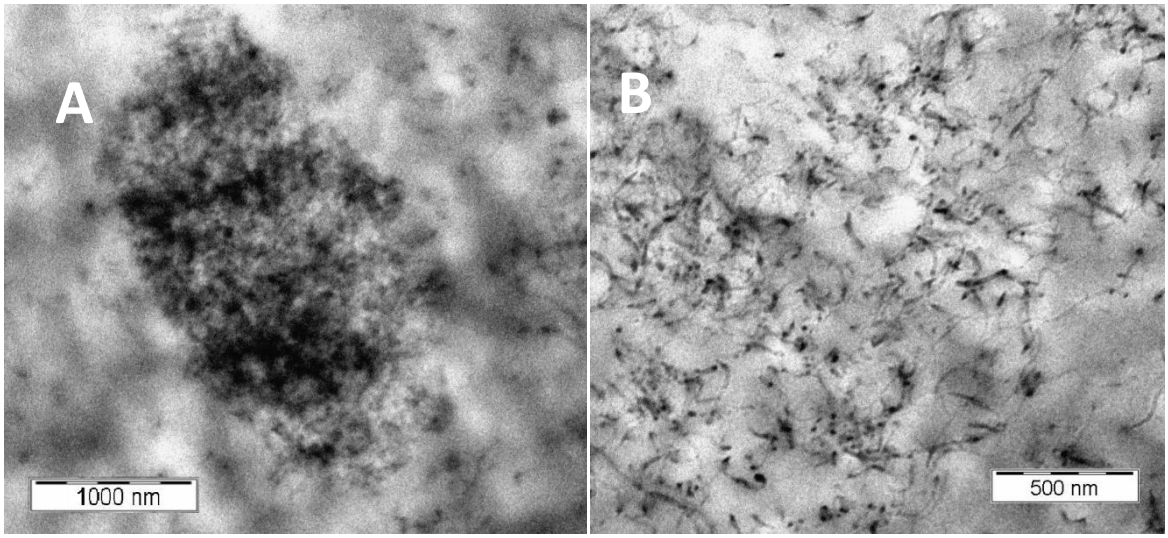

Figure II.13 - TEM imaging of a cross-section of PCL-CAN$_c$: A. for low mixing time (10 min), B. for high mixing time (60 min).

In order to prepare the thermostable composite covalent network counterpart (PCL-CN$_c$), the same process is followed by using PCL$_{82}$-4ANTH in place of PCL$_{82}$-4FUR. In that case, the melt-blending temperature was decreased to 65°C in order to limit as much as possible the crosslinking reaction while still melt-blending the polymers above their melting temperature. The D-A reaction between maleimide and anthracene is fast even at this temperature, which is responsible for a high torque increase while processing. Ten minutes of mixing time was enough to ensure a proper dispersion of the MWCNTs due to the constant increase in melt strength of the polymer mixture as confirmed by transmission electron microscopy (TEM) imaging. Multiple thin sections of the composites were prepared and analysed as for PCL-CAN$_c$. Thanks to the high sheering during mixing (resulting from D-A reaction between maleimide and anthracene), no remaining agglomerates were observed after 10 minutes of mixing as shown in figure II.14. Again, giving the high MWCNTs concentration, the high mixing time and the absence of MWCNTs agglomerates, we considered the dispersion to be homogeneous enough for the targeted applications.

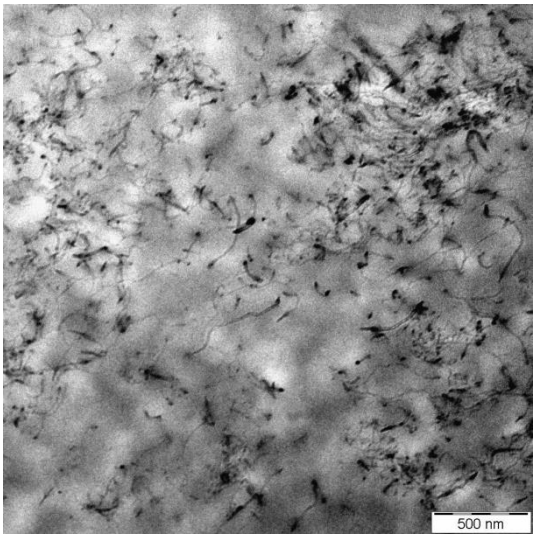

Figure II.14 - TEM imaging of a cross-section of PCL-CN$_c$ for low mixing time (10 min)

Right after extrusion, both polymer blends (PCL-CAN$_c$ and PCL-CN$_c$) were injected into a mold in order to confer a flat sheet shape to the samples and hot pressed at 105°C. Finally, the samples were placed in a thermostated oven at 65°C for curing (72h). This temperature was selected as a good compromise to shift both types of DA equilibrium toward the formation of the DA adduct with enough chain mobility, as this temperature is above the melting temperature of PCL (T_m close to 45°C). Thanks to this curing, PCL networks are obtained by connecting the stars via DA adducts. All samples were then let at room temperature for at least 7 days prior analysis. This procedure is based on previous studies on furan/maleimide DA shape-memory PCLs[273] and optimized for the formation of a highly connected network.

The network formation has been evidenced by swelling tests in $CHCl_3$ a good solvent for the PCL stars. The swelling ratio and the insoluble fraction were measured and compared for the different samples in Table II.1. For all samples, the insoluble fraction is very high showing the large extend of reaction of the stars. As expected, the more reactive anthracene towards maleimide leads to higher crosslinking density for the PCL-CN, which shows lower swelling than PCL-CAN based on furan.

Table II.1 - Swelling ratio and insoluble fraction of the various PCLs network

	PCL-CAN	PCL-CN	PCL-CAN$_C$	PCL-CN$_C$
Swelling ratio (%)	925	840	682,53	638,52
Insoluble fraction (%)	98,50	99,10	98,50	98,85

In addition, the lower swelling ratios observed for both composites as compared to the networks without MWCNTs traduce their higher degree of crosslinking. This originates fromthe possible reaction between furan/maleimide/anthracene moieties with the MWCNTs during processing leading to additional crosslinking nodes. Indeed, functionalization of multi-walled carbon nanotubes with furan or maleimide compounds through Diels–Alder cycloaddition is already demonstrated in the literature[274]. Nevertheless, the formation of a monolithic network indicates that the coupling of the PCL stars chain ends is favored in the followed process. Considering the extensively high number of carbon nanotubes present in the sample (3wt%), which overcomes by far the number of chain end functions, if the MWCNT/end chain function reaction was dominant, the majority of chain ends would be fixed to a MWCNT and no network would be observed, which is not the case. Yet, the addition of the MWCNTs decreases the degree of swelling in both types of networks due to the stiffening of the matrix and the additional crosslinks of the furan, maleimide and anthracene all being reactive with the MWCNTs surface. The influence of these reactions is analyzed in more depth later by rheology.

II. 2. 3. Raman analysis of PCL-CAN

Although the high insoluble fraction during swelling experiment demonstrates that a network is created, it does not reflect a quantitative measurement of the DA yield in the sample. Raman spectroscopy was found as a relevant tool for quantitative analyses, since relative peak intensities of the diffusion bands of three functional groups of interest, i.e. furan, maleimide and DA, are proportional to their relative concentration in the material, allowing the determination of the DA yield[273].

However, this analysis can only be considered for the PCL-CAN as MWCNTs, present in PCL-CAN_c and PCL-CN_c samples, present a high infrared absorbance in the same diffusion bands. The Raman spectra of a PCL-CAN sample and its precursors are presented in figure II.15.

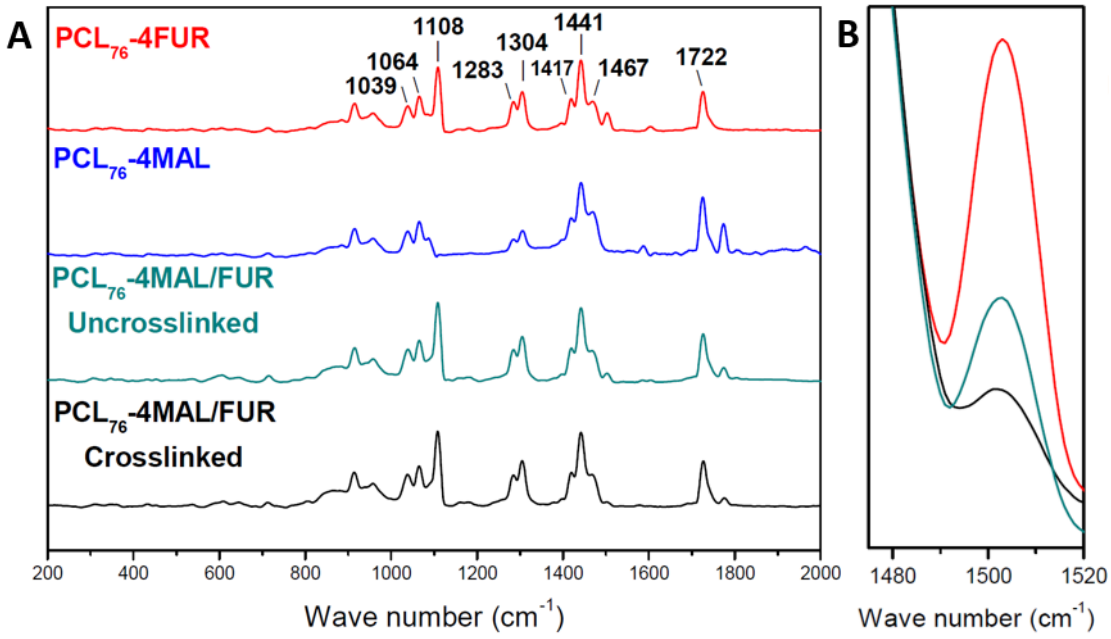

Figure II.15 - A) Raman spectra of PCL_{82}-4FUR (red curve), PCL_{82}-4MAL (blue curve), PCL-CAN before crosslinking (green curve), PCL-CAN after crosslinking (black curve), (black curve). B) Zoom on the diffusion bands of interest of furan (1503 cm^{-1}) of PCL_{82}-4FUR (red curve), PCL-CAN before crosslinking (green curve), PCL-CAN after crosslinking (black curve).

The Raman spectra of each sample (figure II.15 - A) are characterized by several intense diffusion bands at 1722 cm^{-1}, 1467-1417 cm^{-1}, 1304-1283 cm^{-1}, 1108-1039 cm^{-1} respectively attributed to the v-C=O stretching mode, δCH_2 bending mode, tCH_2 twisting mode and skeletal stretching, of the PCL matrix[273]. Characteristic diffusion bands of furan, maleimide and DA adduct are can be identified. Furan end-group presents two stretching bands for the C=C double bond at 1603 and 1503 cm^{-1} (figure II.15 - B, red curve), maleimide end-group exhibits a C=C stretching band at 1587 cm^{-1} and the DA adduct exhibits a diffusion band at 1577 cm^{-1}, corresponding to the stretching band of the remaining C=C double bond. The most intense furan diffusion band at 1503 cm^{-1} is sufficiently separated from others to use for quantitative measurements. The conversion of the furan into DA adduct was calculated by the measurement of the ratio between the intensity of the diffusion band of the furan at 1503 cm^{-1} for the PCL-CAN sample and the PCL_{82}-4FUR after normalization of all the spectra using the more intense band of the PCL at 1441 cm^{-1}(II. 5). The intensity of the diffusion band at 1503 cm^{-1} for PCL_{82}-4FUR was divided by a factor 2, since the PCL-CAN sample contained a stoichiometric amount of PCL_{82}-4FUR and PCL_{82}-4MAL.

$$Fur\ conv.(\%) = 100 - \left(\frac{\text{Normalized intensity at } 1503\ \text{cm}^{-1} \text{ for PCL} - \text{CAN}}{\text{Normalized intensity at } 1503\ \text{cm}^{-1} \text{ for PCL}_{82} - \text{4FUR})/2}\right) \qquad \text{(II. 5)}$$

After curing, the characteristic diffusion bands of furan and maleimide are still present in the spectrum even if their intensity has decreased. This indicates that the DA reaction is not quantitative. A dynamic equilibrium takes place in the material corresponding to 63% conversion of furan into DA adduct. The DA adducts conversion levels up in good agreement with the values reported under the same conditions by previous works[,52].

II. 2. 4. Impact of the MWCNTs on the networks crystallinities

The crystallization of the composite networks is a key parameter for preserving shape memory effects. Nevertheless, the interactions between the matrix and the filler might impact this property. Differential scanning calorimetry (DSC) was used to investigate the crystallinity of the PCLs networks and composites and the impact of the MWCNTs on the crystallite nucleation. DSC measurements for the networks without and with MWCNTs are presented in figure II.16. The melting temperature, the crystallization temperature and the crystallinity degree data extracted from these curves are reported in Table II.2.

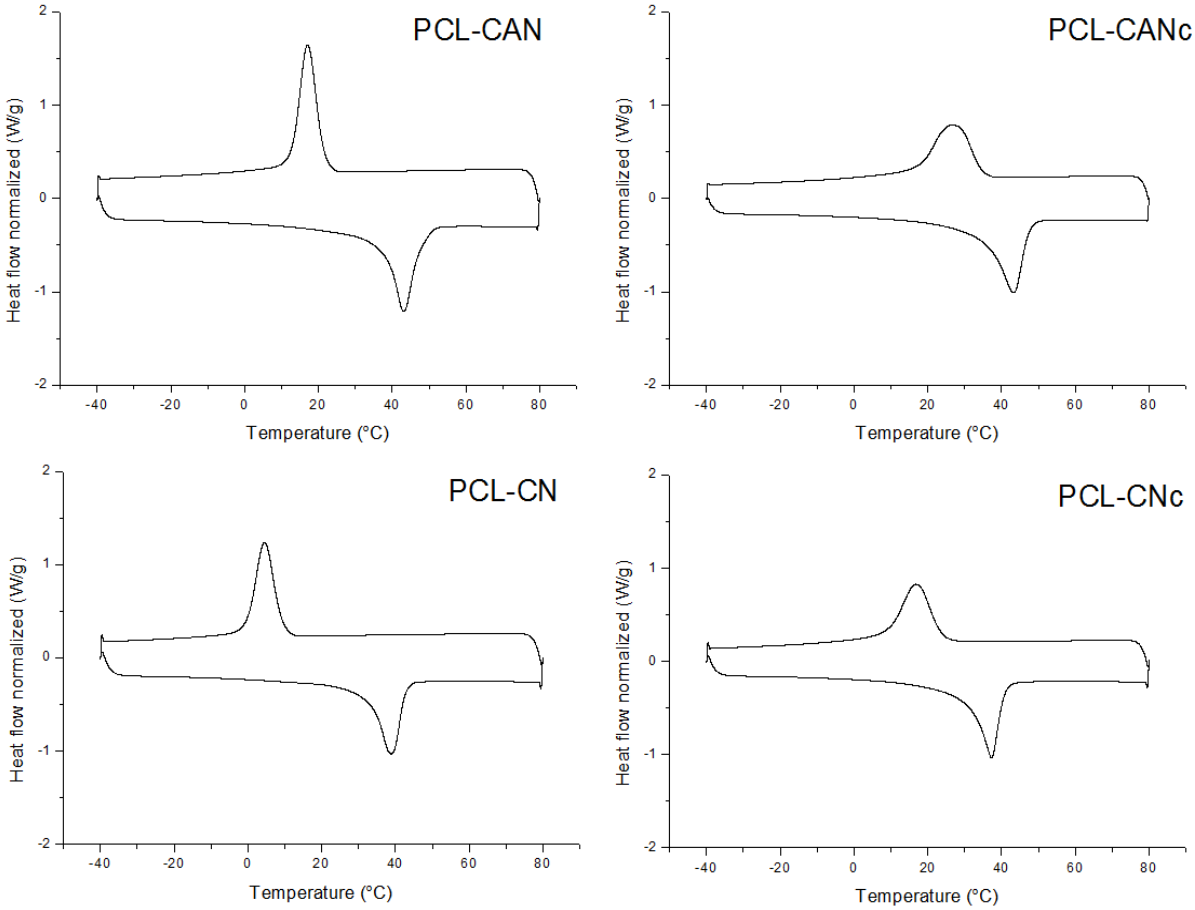

Figure II.16 - Differential scanning calorimetry curves of PCL-CAN, PCL-CAN$_c$, PCL-CN and PCL-CN$_c$

Table II.2 - Thermal and physical characteristics of the various PCL networks

	PCL-CAN	PCL-CN	PCL-CAN$_C$	PCL-CN$_C$
Crystallinity (%)	32,8	26,1	34,6	28,7
T_m (°C)	43,1	38,8	43,3	37,2
T_c (°C)	16,7	4,5	26,6	16,8

The PCL-CAN and PCL-CN networks show a lower crystallinity degree than the starting stars due to the reduced mobility of their chains segments in covalent networks. A lower crystallinity for the irreversible covalent network is observed due to a higher crosslinking degree, in accordance to the smaller swelling ratio previously observed. As already reported, a decrease of the melting and crystallization temperatures is also observed with an increase in crosslinking density and is here observed for PCL-CN[275] as it can be seen on Table II.2.

Comparing the DSC heating curves between of the networks and their corresponding composites, no significant differences are observed. Studying numerous reports in literature, the influence of carbon nanotubes on crystallization is shown to vary respectively to polymer matrices, degree of dispersion, CNT-polymer interactions, thermal treatment, or other parameters, but also from study to study[207,276–281]. Generally, it is shown that MWCNTs can act as efficient nucleation agents, i.e. increasing the rate of polymer crystallization, which naturally influence the crystallization temperature, the degree of crystallinity and crystallite sizes[205,282]. Here, the overall degree of crystallinity of PCL-CAN$_c$ and PCL-CN$_c$ is slightly superior compared to the networks without fillers (Table II.2). If for non-crosslinked polymers, MWCNTs favor the crystallization nucleation leading to higher crystallinity degrees, this effect is reduced in the studied highly crosslinked networks, for which the crystallization is limited by the chain mobility. The positive effect of the MWCNTs on nucleation is thus reduced, resulting in a very low increase of the crystallinity degree. Nevertheless, the incorporation of MWCNTs still favorably impacts the crystallization kinetics since crystallization temperatures about 10°C higher are observed. The melting temperature of the composites remains unchanged. Both composites preserved thus crystallization properties suitable to foresee shape memory applications with a still significant crystallization degree, a melting temperature close or slightly above the body temperature and a crystallization temperature around the room temperature.

II. 2. 5. Shape memory properties of the PCL networks

The PCL-CAN, PCL-CAN$_c$, PCL-CN and PCL-CN$_c$ networks were all proven to be both highly crosslinked and semi-crystalline, thanks to respectively swelling tests and DSC analyses. Therefore, those PCL materials are expected to exhibit shape-memory properties. This behavior was firstly qualitatively demonstrated (figure II.17) by the deformation of a rectangular sample of PCL-CAN$_c$ at 65 °C (above the melting temperature), followed by a cooling down to 0 °C by immersion in cold water while maintaining one specific deformation (uniaxial elongation or curling, figure II.17). After re-heating to room temperature, the stress is released and both deformed samples are keeping the fixed temporary shape as shown by the middle images of figure II.17. These deformed samples in their temporary shape both recover the permanent shape within 2 seconds when immersed in a water bath at 65 °C. The same behavior is observed for all PCL-CAN, PCL-CAN$_c$, PCL-CN and PCL-CN$_c$ samples.

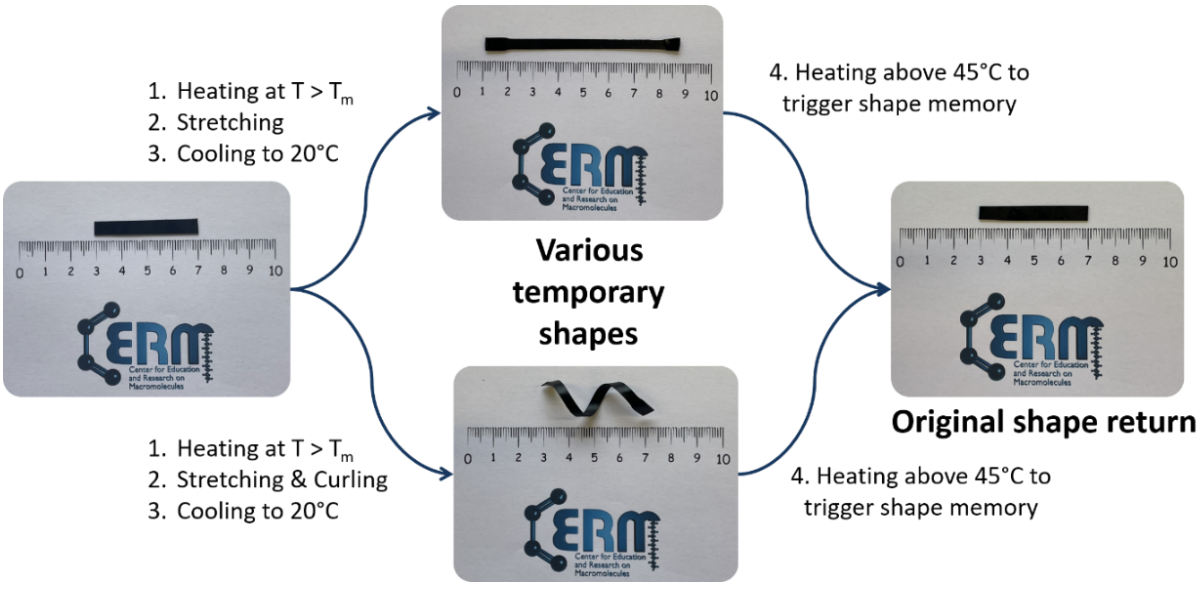

Figure II.17 - Qualitative demonstration of the shape-memory properties of the PCL-CAN$_c$ composite network

The shape-memory properties have then been more quantitatively evaluated using dynamic mechanical analysis (DMA). The figure II.18 shows the DMA curve for 4 successive shape-memory cycles for a PCL-CAN_c sample and sketches of the sample state after each step. These cycles start at 65 °C where the PCL is molten (A, figure II.18), i.e., no crystalline areas are observed in the sample. In a first step, a stress (0,6MPa) is applied to deform the sample at 65°C (A to B, figure II.18). The PCL chains are extended due to the tensile stress and the sample reaches a higher strain. In a second step, the temperature is decreased to 0°C (3°K/min) while keeping constant the applied stress at 0.6 MPa (B to C, figure II.18). Oriented crystallization of the sample occurs upon cooling and is responsible for a further increase of the strain at constant stress[89]. Appearance of crystalline areas is also responsible for the shape fixity of the sample. This fixity is assessed in step 3 where stress is released (C to D, figure II.18). The comparison of the strain before and after the release of the stress allows quantifying the sample fixity by equation (I.1). A high fixity ratio (R_f) above 99%, is generally obtained with PCL. Finally, the sample is heated again to 65°C (3°K/min) in order to allow the sample to recover its permanent shape by melting of the crystalline phase (D to A, figure II.18). Shape recovery is assessed by comparing the strain at 65°C before and after one cycle, the recovery ratio (R_c) being calculated by equation (I.2). High recovery ratios result from a preserved network through the cycle.

This experiment was performed on the 4 types of samples, i.e., PCL-CAN, PCL-CAN_c, PCL-CN and PCL-CN_c. Similar experimental shape memory cycles are recorded for the different networks and composites as shown figure II.19. Excellent fixity and recovery ratios are obtained in each case (Table II. 3), which is common for PCL based SMPs. Classically, the first cycle is characterized by a lower shape recovery ratio, i.e., the strain at the start and the end of a complete shape-memory cycle increases, which is known as a training phenomenon, while the following cycles were all characterized by excellent shape recovery ratios, i.e. higher than 99%.

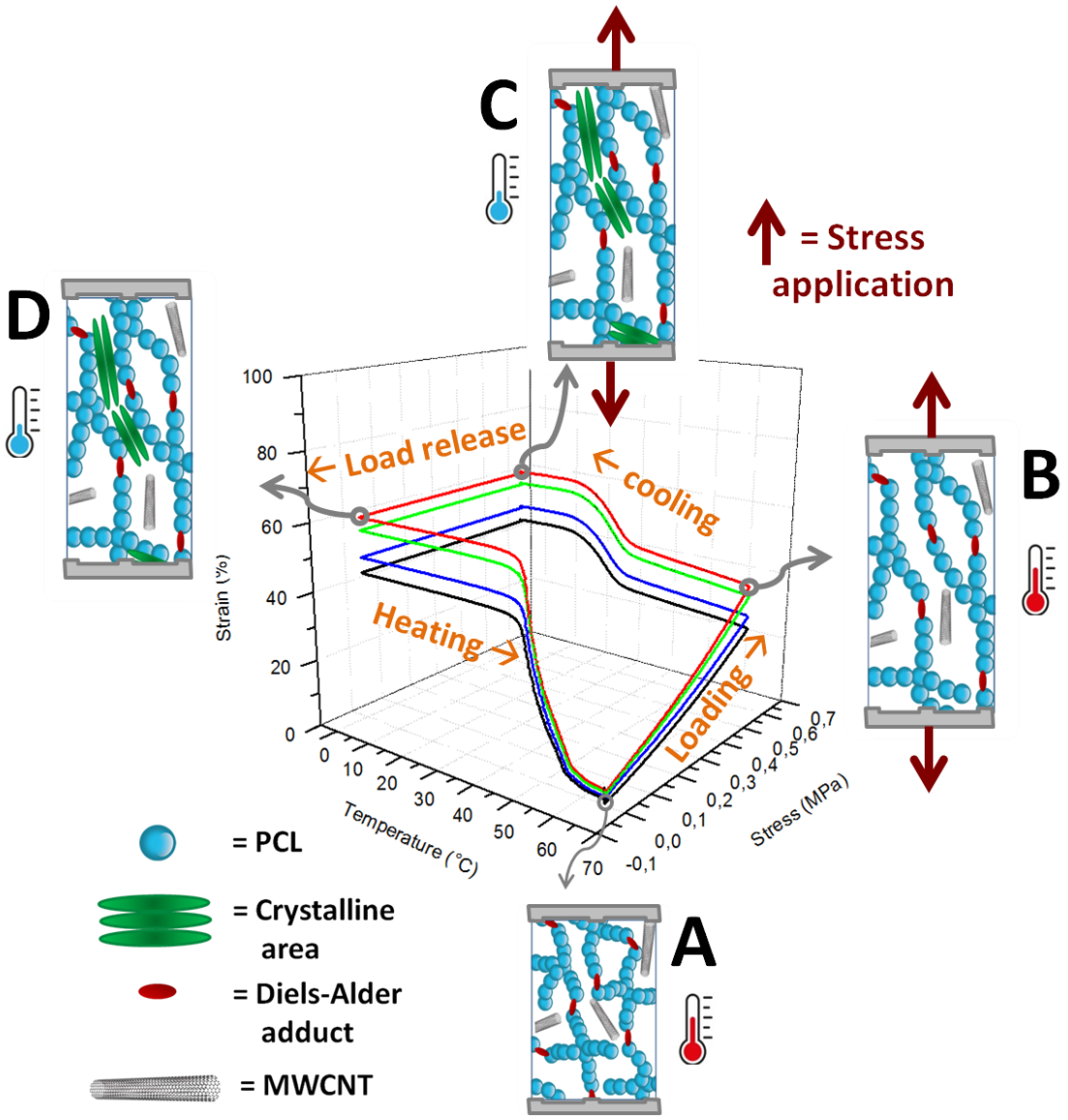

Figure II.18 – DMA curve for 4 successive shape-memory cycles for a PCL-CAN$_c$ sample and sketches of the sample state after each step.

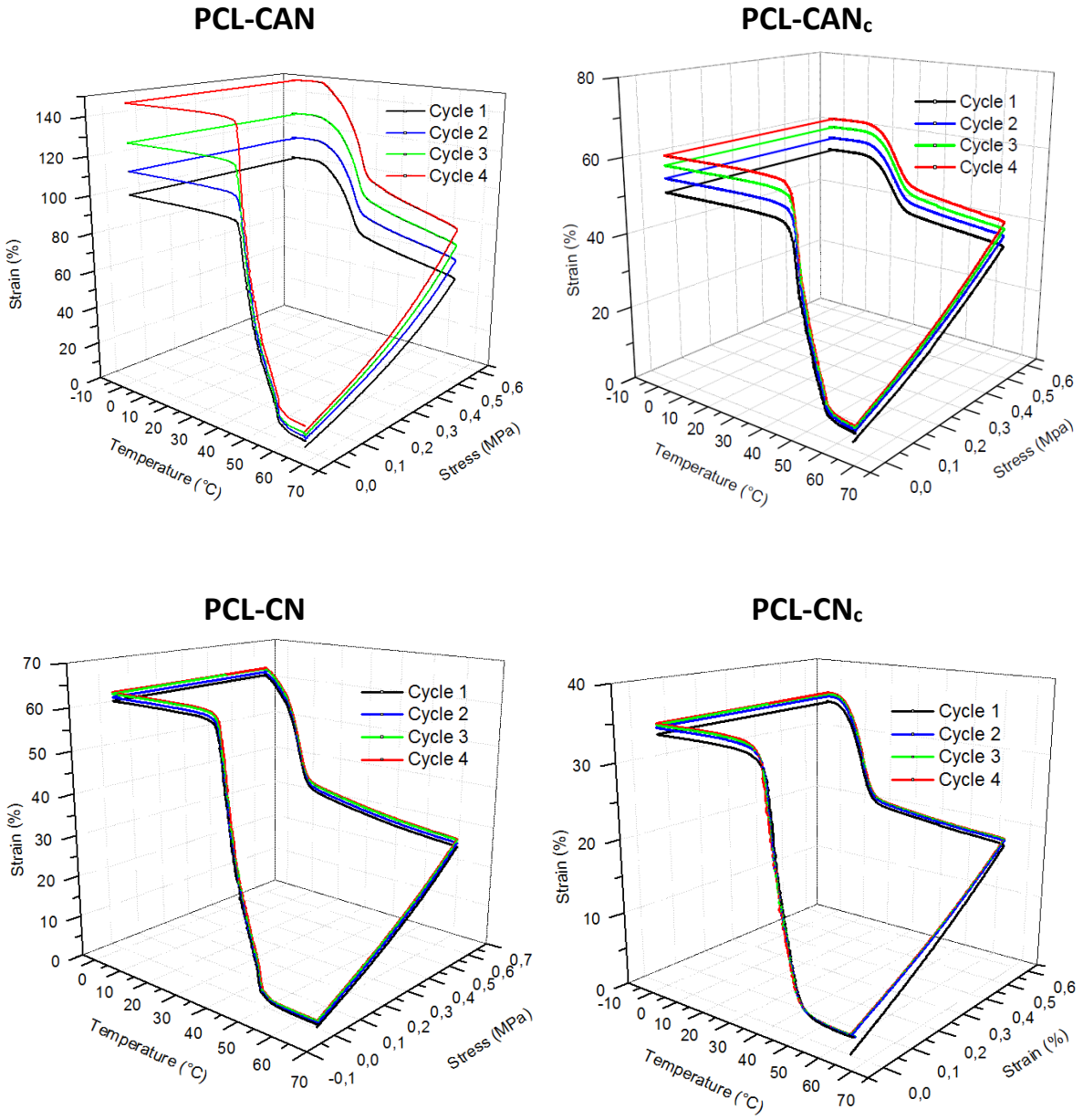

Figure II.19 - Shape-memory cycles evaluated experimentally by DMA upon convection heating/cooling of PCL-CAN, PCL-CAN$_c$, PCL-CN and PCL-CN$_c$ networks after 14 days at room temperature

Table II. 3 Shape memory properties of PCL Networks

PCL-CAN				
	Cycle 1	*Cycle 2*	*Cycle 3*	*Cycle 4*
Fixity Ratio, R_f (%)	99,47	99,99	99,99	99,99
Recovery Ratio, R_c (%)	95,43	98,25	98,53	97,43
Maximal Strain (%)	101,48	113,65	128,06	147,71
PCL-CAN$_c$				
	Cycle 1	*Cycle 2*	*Cycle 3*	*Cycle 4*
Fixity Ratio, R_f (%)	99,44	99,52	99,54	99,56
Recovery Ratio, R_c (%)	96,38	98,52	97,69	96,13
Maximal Strain (%)	44,16	48,75	52,71	56,56
PCL-CN				
	Cycle 1	*Cycle 2*	*Cycle 3*	*Cycle 4*
Fixity Ratio, R_f (%)	98,77	99,05	99,08	99,07
Recovery Ratio, R_c (%)	97,11	98,46	98,71	98,79
Maximal Strain (%)	62,39	62,39	62,91	63,21
PCL-CN$_c$				
	Cycle 1	*Cycle 2*	*Cycle 3*	*Cycle 4*
Fixity Ratio, R_f (%)	99,10	99,15	99,14	99,14
Recovery Ratio, R_c (%)	92,29	98,73	98,87	98,91
Maximal Strain (%)	34,15	34,97	35,31	35,50

During the stress-controlled elongation, an almost linear deformation is observed for every PCL network. It is noteworthy to mention that the composites are stiffer than the neat networks due to the reinforcement effect of the MWCNTs. Therefore, when experiencing the same stress, the strain is about only half for the composite networks. Upon cooling under constant stress, all the samples experience a large increase of the deformation between 35°C and 15°C resulting from the growth of crystallites oriented along the stretching direction whatever the presence or not of MWCNTs. A very high fixity (R_f above 99%, Table II. 3) is obtained for each cycle and all samples thanks to the PCL crystallinity. This ratio defines the ability of the shape-memory material to keep its temporary shape after cooling without any stress applied to it. High fixity is typical for shape-memory materials based on crystallization as the fixing process, especially when the degree of crystallization is high, such as for PCL. The dshape recovery is then triggered by a temperature above 45°C (i.e., close to the melting temperature, Table II.2).

Mechanical properties of the SMPCs have been greatly influenced by the addition of MWCNTs. With focus on the stress strain behavior of the different samples, we observed that even at 65°C, the Young modulus is greatly increased (≈ 70 % increase) while the ultimate stress obtained is reduced (≈ 50 % reduction) for the same stress applied, both variation resulting from the matrix hardening caused by the MWCNTs (figure II.20 & *Table II. 4*).

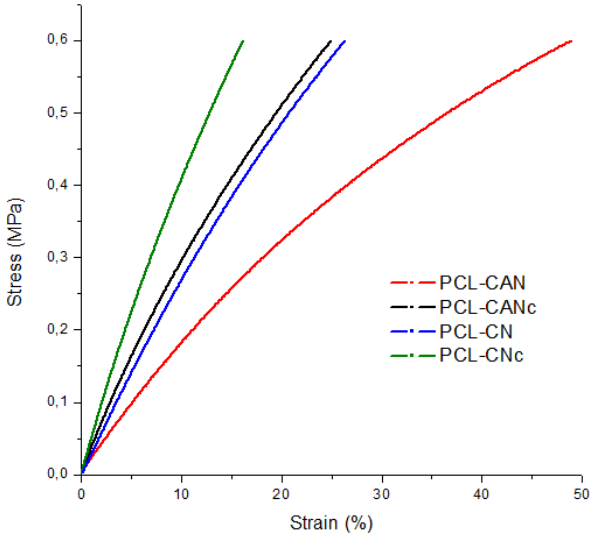

Figure II. 20 - Stress/strain DMA curve at 65°C of PCL-CAN, PCL-CAN$_c$, PCL-CN and PCL-CN$_c$ networks after 14 days at room temperature.

Table II. 5 Young modulus of of PCL-CAN, PCL-CAN$_c$, PCL-CN and PCL-CN$_c$ networks after 14 days at room temperature at 65 °C

	Young Modulus (N/m^2)
PCL-CAN	0,018
PCL-CAN$_c$	0,032
PCL-CN	0,028
PCL-CN$_c$	0,046

As already reported[89], in the case of covalent adaptable networks (PCL-CAN), a steady increase of the strain is observed from cycle to cycle. This phenomenon is attributed to the occurrence of retro-DA reactions upon tensile stress. Some DA adducts undergo cycloreversion leading to the relaxation of the unlinked polymer chains, pulling apart the chain-ends, that will not couple back during the cycle. This phenomenon occurs at each cycle, leading to a repetitively slightly decreased crosslink density and therefore more ductile

material. This phenomenon is less pronounced for PCL-CAN$_c$ due to the reinforcement of the MWCNTs. In contrast, the anthracene-based network is more stable (the retro-DA reaction does not occur easily). Therefore, PCL-CN and PCL-CN$_c$ samples are not subject to such creep effect during successive cycles. In accordance to swelling experiments, the crosslinking degree appears also higher for PCL-CN$_c$ than PCL-CAN$_c$ networks since lower strain are obtained. This is attributed to the incomplete crosslinking of the covalent adaptable material upon curing, due to the dynamic equilibrium of the Diels-Alder reaction. The possible occurrence of further DA addition in the solid-state during ageing is not sufficient to reach the same degree of crosslinking and thus the same stress-strain behavior in the molten state. In case of the PCL-CN and PCL-CN$_c$ networks, retro-DA does not occur at all, the slight drift observed can rather be associated to a small sliding of the sample within the instrument clamp. Superimposition of DMA cycles of PCL-CAN$_c$ and PCL-CN$_c$ makes clear the differences between them as shown on figure II.21.

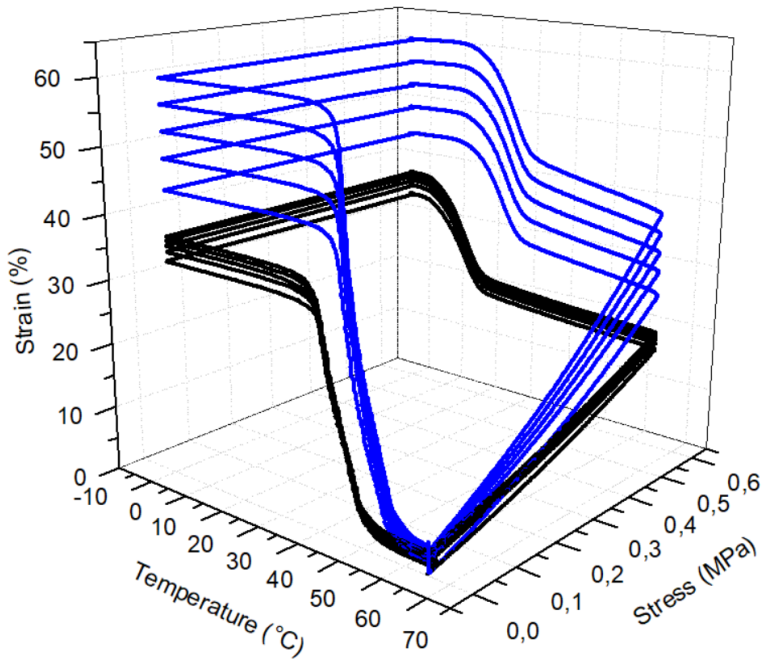

Figure II.21 - Shape-memory cycles evaluated experimentally by DMA upon convection heating/cooling of PCL-CAN$_c$, PCL-CN$_c$.

II. 2. 6. Electrical resistivity assessment

Electrical resistivity measurements were performed on PCL-CAN_c and PCL-CN_c in order to further implement Joule resistive heating. For the Joule effect to take place, a SMPC needs to be electrically conductive. Conductive fillers are thus purposely introduced into the matrix. The amount of fillers required to reach the percolation threshold, i.e. for having an electrically conductive network within the SMC, depends on several factors such as the nature of the fillers themselves, their size, shape, dispersion, etc. MWCNTs were selected as they are electrically conductive fillers with electrical and thermal properties superior than carbon black, carbon fibers or graphene composites while having low density and high aspect ratio. In the present study, a weight ratio of 3wt% of fillers was chosen to preserve enough conductivity to the samples whatever the applied strain and temperature. The electrical resistivity of pure PCL is typically 10^{11} Ω·m. However, due to the loading of MWCNTs well above the percolation threshold (~ 0,5 %), both CAN and CN composites become conductive , with the same measured electrical resistivity (ρ_e) of 0.075±0.025 Ω.m at -10 °C.

Variation of the electrical resistivity was also observed with the temperature of the sample, i.e., when measuring the resistivity of both samples in a ventilated oven (the heating furnace of a DMA) by applying a heating ramp of 1°C.min^{-1} from -10°C to 65°C then a cooling ramp of 1°C.min^{-1} back to -10°C (figure II.22). The variation of the relative resistivity, i.e., the resistivity of the SMC regarding its original one at the beginning of the experiment, measured purposely without applying stress on the sample and by injecting a small current (0,5 mA) at which no measurable resistive heating occurs, is given on figure II.22 - A for PCL-CAN_c and PCL-CN_c. In both cases, a slight increase is first observed upon heating followed by a drop at high temperature, i.e., when the melting of the matrix is complete as clearly evidenced by the overlays with the DSC traces (Figure II.221 II.22 - C and D).

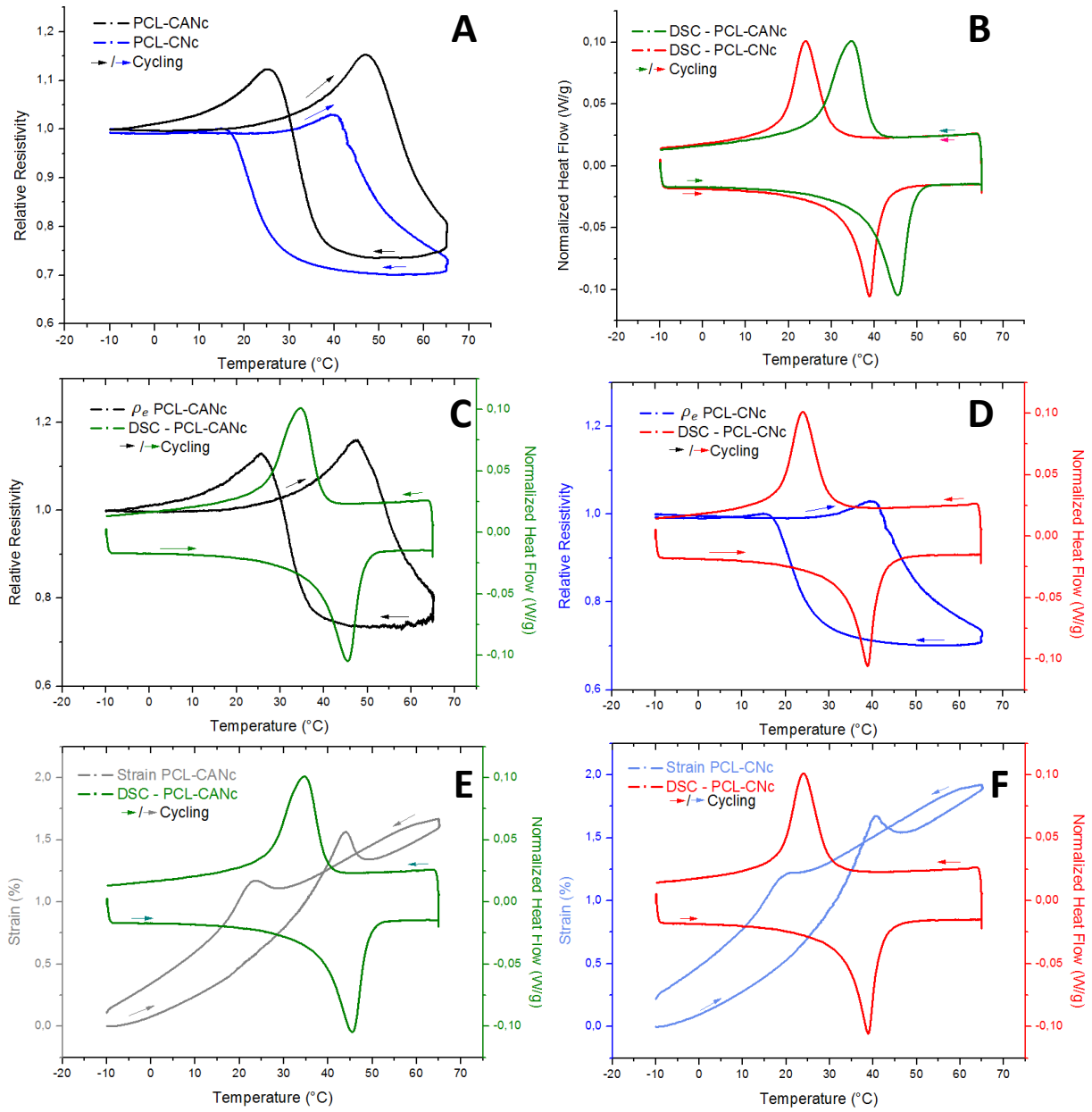

Figure II.221 - A. Relative resistivity of PCL-CAN$_c$ and PCL-CN$_c$ as function of temperature, B. DSC thermograms of PCL-CAN$_c$ and PCL-CN$_c$, C. Relative resistivity and DSC thermogram of PCL-CAN$_c$ in fucnction of temperature, D. Relative resistivity and DSC thermogram of PCL-CN$_c$ in fucnction of temperature, E. DSC thermogram and strain evolution of PCL-CAN$_c$ in function of temperature, F. DSC thermogram and strain evolution of PCL-CN$_c$ in function of temperature.

The melting of the crystalline area gives more mobility to the matrix allowing rearrangements of the conductive filler network which can easily influence the tunneling distances between MWCNTs and thus the electrical resistivity. Upon cooling, the reverse behavior is observed (figure II.22 A). The resistivity increases back during the crystallization

due to the loss of contacts between the conductive filler network pushed apart by the crystallites (figure II.22 C & D). Moreover, as the SMCs expand/shrink with temperature, MWCNTs are brought further apart or closer. This behavior was recorded in terms of length variation and can be seen on figure II.22 E and F. MWCNTs agglomeration can also lead to variation in ρ_e. The combination of all the mechanisms directly impacts, by either aided or disrupted tunneling, the MWCNTs conductive network, thus the overall resistivity of the SMC. It is important to point out that melting and crystallization occurs also at different temperatures for PCL-CN_c and PCL-CAN_c (figure II.22 B), which might causes the small differences in electrical behavior of the two SMCs. Nevertheless, the amplitude of these thermal variations of the electrical resistivity is limited and remains within the range of resistivity variation from sample to sample. In both cases, the initial resistivity is recovered after the thermal cycle at -10°C evidencing the high stability of the crosslinked matrices.

Inspired by these observations, we could demonstrate that appropriate thermal cycles can tune the sample resistivity. Indeed, by cycling PCL-CN_c at 10 °C.min^{-1} between 60 °C and 25 °C with respectively an isotherm of 5 and 10 minutes at those two temperatures (figure II.23 - A), crystallization is uncomplete as revealed by the DSC. Internal stresses induced by the crystalline areas melting or forming during cycling appear to push closer the MWCNTs located in the amorphous part of the PCL, resulting in a higher number of conducting paths and a lower resistivity (figure II.23 - C). This effect increases with cycling. As strain variation is similar through the experiment (figure II.23 - B), only rearrangement of the MWCNTs inside the polymeric matrix can cause the observed decrease in resistivity. In a second time, cycling at 10 °C.min^{-1} between 60 °C and -10°C with 5 minutes isotherm at both temperatures were implemented. DSC analysis provided proof of complete crystallization in those conditions. During cooling, the crystalline areas push further apart from each other the MWCNTs, resulting in an increased resistivity. This effect also increases from cycle to cycle while showing constant strain variation. Here over 3 cycles, i.e., going 3 times from 60°C to 25°C or -10°C, we were able to either increase the resistivity of the SMC by 20%. Even with those effects, the SMCs are still highly conductive and dynamic mechanical analysis can be considered.

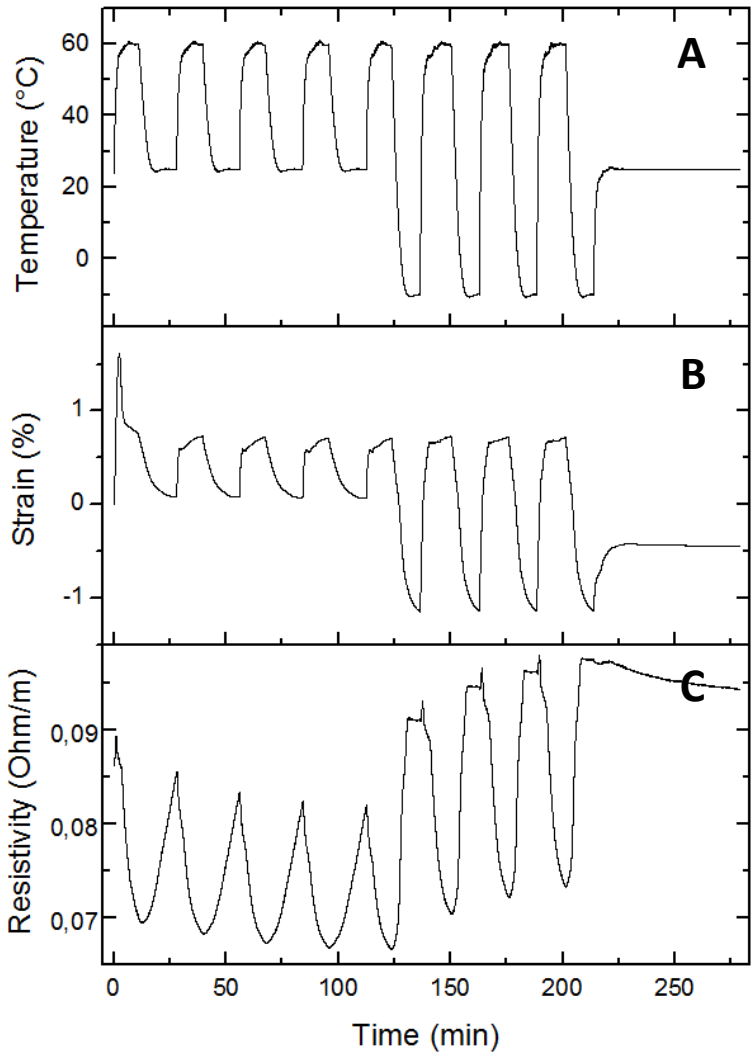

Figure II.232 - Temperature (A), strain (B) and resistivity (C) of PCL-CN$_c$ in function of time while cycling until uncomplete crystallization (60 °C to/from 25 °C) or complete crystallization (60 °C to/from - 10 °C)

Self-heating requires internal generation of heat which depends on the electrical current being injected, the geometry of the SMC and its electrical resistivity. We demonstrated earlier that ρ_e varies with temperature, but it is also subject to variation according to strain and cycling. Those 3 parameters might induce breaking of the conducting MWCNTs network through internal stresses caused by stress application. In a classical dynamic mechanical analysis, both strain and temperature variations will influence ρ_e. Monitoring of ρ_e (reported in Figure II. II.24) was crucial to characterize these effects.

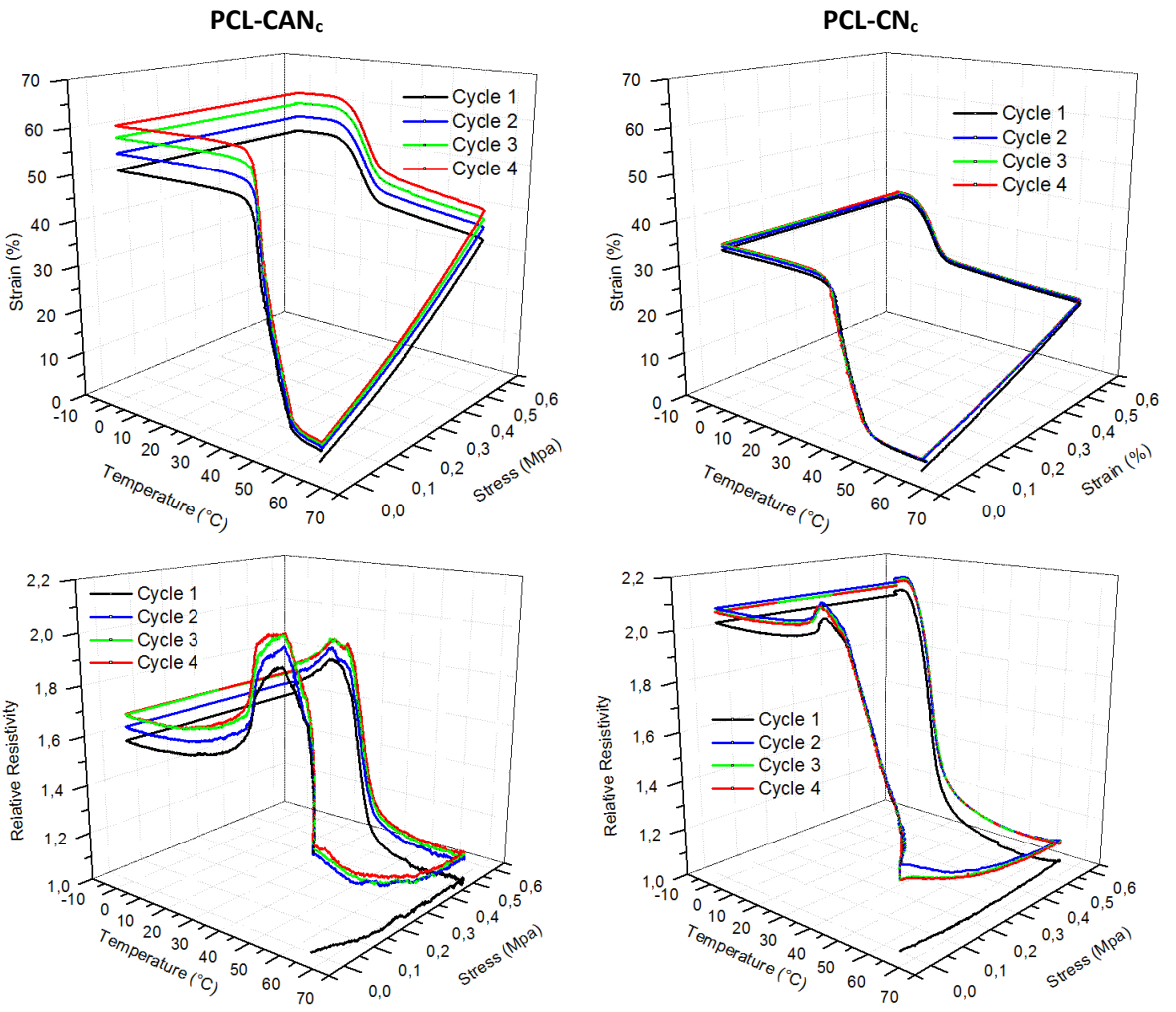

Figure II.24 - Shape-memory cycles (up curves) evaluated by DMA upon convection heating/cooling of PCL-CAN$_c$ and PCL-CN$_c$ networks after 14 days at room temperature with concomitant monitoring of the electrical resistivity (down curves).

An increase in electrical resistivity by two times of the original value is observed while performing a DMA cycle, ρ_e reaching 0.15±0.025 Ω.m in the worse situation. This can be related to the partial destruction of the conductive nanotubes network due to strain and temperature. During the stress-controlled elongation at 65°C (molten state), almost no variation of the resistivity is observed for the first cycle later followed by a small decrease at cycle 2, 3 and 4 for both SMCs. Although loading involves stretching the sample, which increases the distance between electrodes and decreases the cross-section, the measured resistance of the SMC decreases with deformation, which may seem counterintuitive. Normally, the increasing length of the sample should contribute to an increase in resistance

more than the reduction in cross-section. This unexpected behavior is likely due to the alignment of MWCNTs along the direction of elongation under stress, which enhances conductivity. While cooling under constant stress, all SMCs experience a large increase in resistivity upon crystallization. This behavior has already been evidenced in our previous thermal stress-free analysis but appears enhanced when a tensile force is applied (increase up to 2 times the original resistivity as compared 1,15 times for stress-free samples). The measured resistivity is likely to be subject to the phenomenon we have just described. The high elongation experienced results from the oriented crystallization induced by the stress, elongation obviously leading to disruption of the MWCNTs tunneling effect. The relative resistivity then gradually decreases, possibly due to re-organization of the MWCNTs within the matrix. However, this reduction stops quickly once the overall length stops varying. Even though, the SMCs remain conductive enough to allow a Joule effect and efficient heating of stretched samples and to insure reproducibility between experiments. Figure II.25 is another representation of the variation of relative resistivity as a function of the applied strain during DMA cycling. PCL-CAN$_c$ shows a higher increase in resistance, which can be attributed to the higher disruption of the MWCNTs network within the sample (due to higher deformation experienced by the sample) as compared to PCL-CN$_c$.

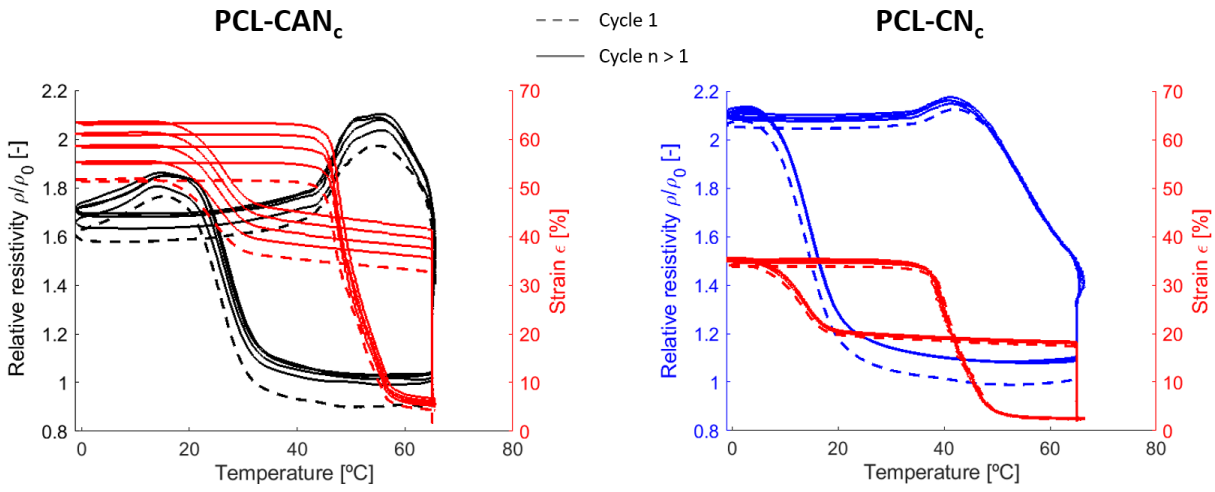

Figure II.25 – Strain and concomitant electrical resistivity variation during shape-memory cycles recorded by DMA upon convection heating/cooling for PCL-CAN$_c$ and PCL-CN$_c$ networks after 14 days at room temperature.

II. 2. 7. Electrically triggered heating by Joule effect

The objective of incorporating MWCNTs in the PCL matrix is to create a shape memory composite with electrical conductivity that can be activated by an electric current. The shape memory properties of PCL-CAN are not altered by the addition of 3 wt% MWCNTs, indicating that shape recovery through the Joule effect can be achieved. The heating of an undeformed PCL-CAN$_c$ by Joule effect is triggered as soon as the electric current is passed through the material (figure II.26 – I & III), the temperature rises due to resistive heating as anticipated. By controlling the injected current, the samples are heated from room temperature to 60 °C with a rate of 10 °C/min. A cooling ramp from 60 °C to the room temperature can be achieved with a similar rate by progressively decreasing the current (figure II.26 – II & IV). As evidenced by the temperature recorded at different locations (figure II.26 – P2 to P6) of the PCL-CAN$_c$ stripe, the sample is heating uniformly and follows linear increasing or decreasing temperature ramps.

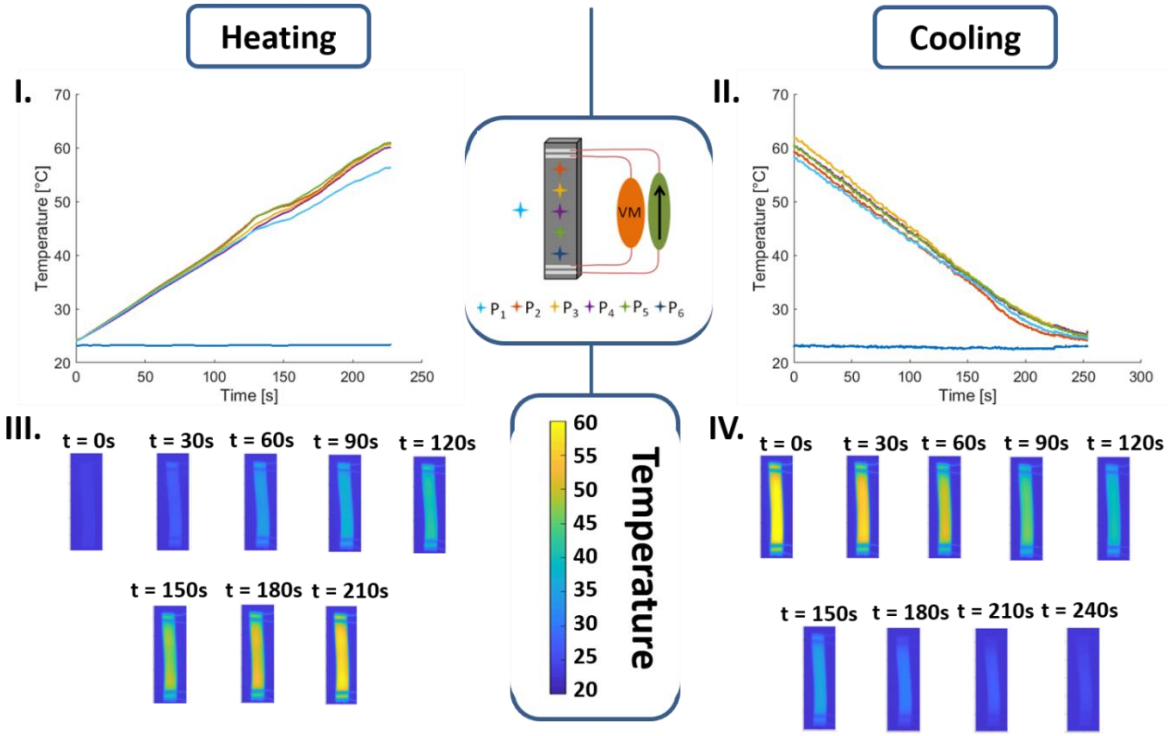

Figure II.26 - Controlled heating (I) and cooling (II) ramps of PCL-CAN$_c$ by Joule effect with a rate of 10 °C·min^{-} and infrared images of both heating (III) and cooling (IV) on an undeformed PCL-CAN$_c$ samples.

The observed homogeneous overall temperature of the whole sample, recorded by the IR camera during the resistive heating at a constant temperature rate also confirms the homogeneity of the dispersion of MWCNTs inside the matrix as previously determined by TEM analysis (figure II.26 – III). The blending process appears thus robust to produce homogeneously conductive samples so that homogeneous actuation of the shape recovery is expected.

Electrically triggered shape recovery was thus conducted and monitored using a normal and an IR camera. Figure II.27 displays the current injection actuated shape-recovery behavior for a PCL-CAN_c sample. The sample was initially a rectangular strip (41.2 mm x 8.1 mm x 0.5 mm) that was programmed in a stretched temporary shape (length stretched sample 62.87 mm). The original shape of the sample was completely recovered once melting temperature was reached. The tests being conducted with a 10 °C/min temperature ramp, about 2 minutes were needed to trigger the shape recovery starting from a room temperature of 25°C. Interestingly, it was observed that the sample heats up faster in stretched areas. Pictures of the thermal camera show that the undeformed area close to the grip remains underheated while the deformed one heat significally more. Unhomogeneous heating is here observed due to the deformation imposed to the sample. Stretching induced perturbations in the MWCNTs network and thus resistivity increases in those areas, causing the inhomogeneous temperature increase. Despite the observed fluctuations in electrical resistivity, the temperature controller effectively maintained a temperature of 60 °C throughout the process by adjusting the injected current.

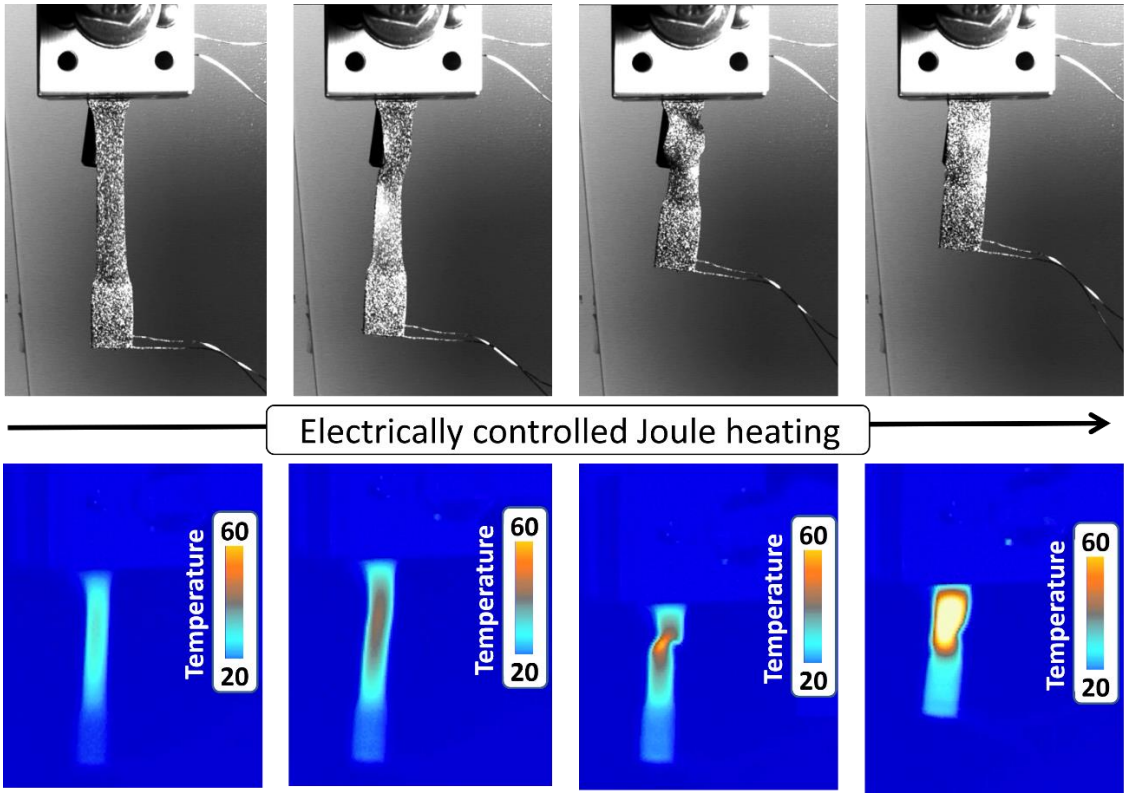

Figure II.27 - Classical and infrared images of electrical actuation of the shape recovery by Joule effect as described in section II.2.13.

Comparing convective and resistive heating is straightforward since both methods allows shape recovery easily. The behavior of shape recovery differs however slightly between the two systems. Conductive heating ensures that the whole sample is at a constant temperature, and thus, the recovery process begins simultaneously for the entire sample. On the other hand, resistive heating causes some parts of the sample to heat before others, leading to a recovery process that occurs primarily in some areas. As a result, the sample undergoes twisting or bending, depending on which parts recover first. Although both systems have the same initial and final stages (same length and recovery), the path taken by resistive heating causes a twisting motion, which is not observed with conductive heating. Nevertheless, PCL-CAN$_c$ is suitable for both conductive and convective heating reaching both high recovery ratio.

II. 2. 8. Recycling of PCL-CAN$_c$

The furan-maleimide adduct used in PCL-CAN and PCL-CAN$_c$ samples is known to undergo significant cycloreversion at temperature above 100 °C[80]. This property has been used to test recycling of the materials. Rheological measurements were performed to study the formation and the breaking up of the PCL network by small amplitude flow experiments. Our study focuses on the behavior of the PCL-CAN and PCL-CAN$_c$ vs. the temperature, i.e., during the formation and the rupture of the DA adducts. Three heating/cooling cycles were performed at the two optimal temperatures, i.e., 65 °C for DA adduct formation and 125 °C for retro DA reaction. Staying above the melting temperature of the PCL (> 45 °C) during the experiment confers enough mobility to the polymer chains enabling crosslinking by the creation of the DA adduct but it also prevents perturbations due to PCL crystallites during the rheological measurement. Measurements for PCL-CAN and PCL-CAN$_c$ previously prepared and fully crosslinked can be seen respectively on figure II.28 and figure II.29.

Considering PCL-CAN, a first conditioning step of 1 hour at 125 °C is performed to shift the equilibrium towards the retro-DA reaction. The gel point being defined as the point at which the G' becomes larger than G'' indicates the transition from fluid flow like behaviour to solid elastic behaviour. The network break-up is achieved at the start of the analysis as the loss modulus (G'') is higher than the storage modulus (G'), which indicates that the system is back to the typical viscous behavior of uncross-linked PCL. The temperature is then decreased until 65 °C. The decrease of the temperature leads to an increase of both moduli. Moreover, both moduli continuously increase during the isotherms at 65°C, which can be attributed to the network formation since G' and G'' remain constant for PCL$_{82}$-4OH at 65 °C. After 120 minutes, the moduli were still increasing meaning that the DA equilibrium is not achieved yet under these conditions, nevertheless the isotherm is stopped and the temperature is increased back to 125 °C to shift again the equilibrium towards retro-DA and to test the reversibility. A one-hour isotherm turned out to be more than sufficient to reach the thermodynamic equilibrium and an uncrosslinked state since the G' and G" reach a plateau for all isotherms. It was however quickly reached. The faster kinetics of the retro-DA reaction,

compared to the DA reaction is explained by the fast disruption of the DA adduct which is a monomolecular reaction compared to the DA addition that is bimolecular and where an efficient coupling of furan and maleimide chain-ends in the PCL bulk is mandatory. Furthermore, in case of the DA reaction, the diffusion rate is continuously decreased due to the network formation, which slows down the bimolecular coupling of both reactive moieties for DA addition. Through cycling, similar profiles were obtained during the other curing isotherms confirming the remarkable network reversibility for PCL-CAN with G'' always dominating and being constant at 125°C for all the cycles, so as the gel point at 65°C.

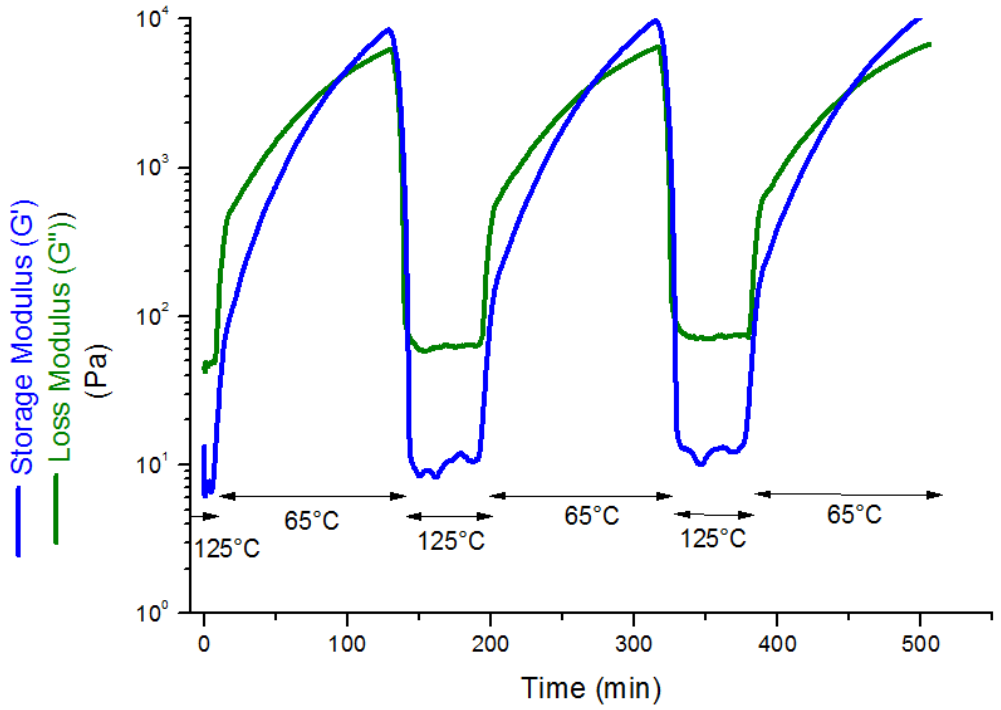

Figure II.28 - Rheological study of thermo-reversibility of crosslinking of PCL-CAN

As far as PCL-CAN$_c$ is concerned (figure II.29), similar moduli variation is observed during the conditioning step at 125°C leading to the network break-up (G'' dominating at start) as the equilibrium is now shifted towards the furan and maleimide regeneration. Cooling to 65°C, leads to very rapid increase of the moduli especially G'. This rapid increase of the storage modulus at 65°C also observed for non-reactive PCL$_{82}$-4OH composite (figure II.30) is typically due to the network formed by the MWCNT above the percolation threshold in the polymer

matrix[283–287]. This phenomenon thus dominates the response masking the gel point of the PCL-CAN_c. This result confirms both the existence of a percolated network in PCL-CAN_c, in accordance to conductivity data, and the moduli increase induced by the MWCNTs.

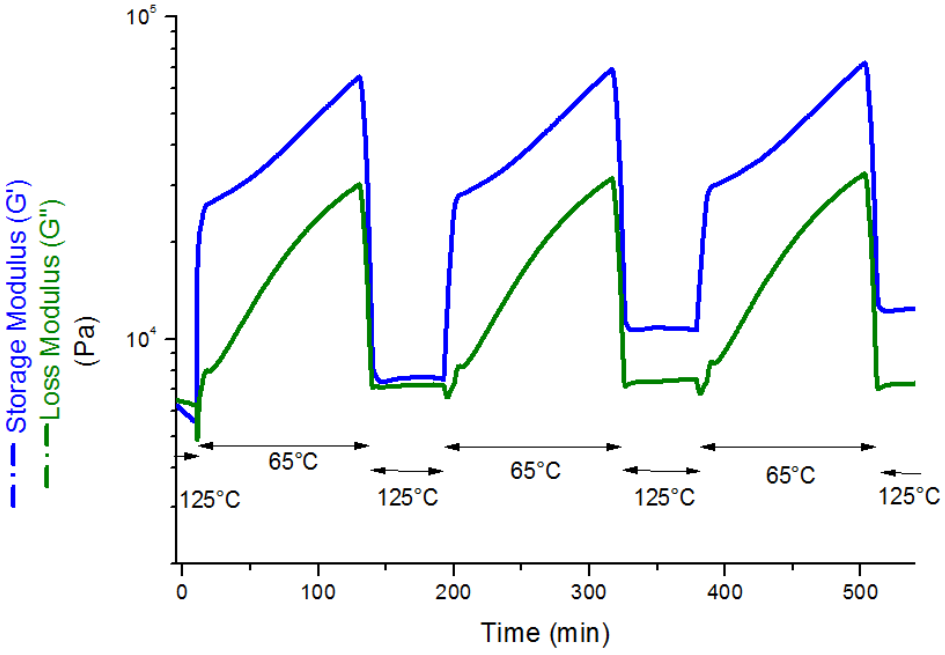

Figure II.29 - Rheological study of thermo-reversibility of crosslinking of PCL-CAN_c

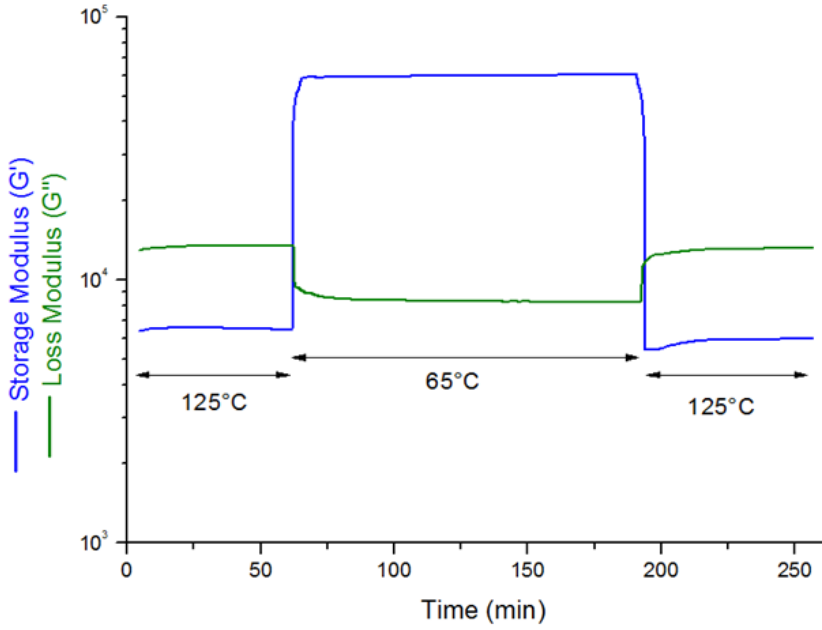

Figure II. 30 – Rheological study of PCL_{82}-4OH with a 3wt% MWCNTs content at 125°C and 65°C

Nevertheless, both moduli continuously increase during the isotherms at 65 °C for PCL-CAN_c, traducing the occurrence of the DA addition. . The G' or G'' at the end of each temperature cycle is reported in table II.7 for PCL-CAN and PCL-CAN_c.

Table II.7 - Maximum storage and loss modulus for PCL-CAN and PCL-CAN_c during cycling between 65°C and 125°C

PCL-CAN						
	Cycle 1		Cycle 2		Cycle 3	
Temperature	65°C	125°C	65°C	125°C	65°C	125°C
End storage modulus - G' (Pa)	9 341	72,18	10 837	71,5	11 571	72,5
End loss modulus - G'' (Pa)	6 480	3,97	6 881	20,6	6 771	30,2
PCL-CAN_c						
	Cycle 1		Cycle 2		Cycle 3	
Temperature	65°C	125°C	65°C	125°C	65°C	125°C
End storage modulus - G' (Pa)	67 200	7 500	71 075	10 731	74 434	12 419
End loss modulus - G'' (Pa)	30 861	7 200	32 205	7 370	33 353	7 506

By considering only the end value of the 65°C isotherm, from one cycle to the other, PCL-CAN_c presents a similar and quite low increase in both loss and storage modulus. This confirms the remarkable reversibility of the maleimide-furan Diels-Alder addition, who is responsible for the similar profiles obtained through cycling in both cases. The main difference is observed for the G' at 125 °C. For PCL-CAN, as the DA equilibrium is totally shifted toward the retro Diels-Alder, no differences are observed between cycles and G'' dominates. This is not the case for PCL-CAN_c where G' remains above G'' and progressively increases over cycling. This can be explained by the irreversible reaction of the PCL chain-ends with the MWCNT during temperature cycling leading to a more stable network at 125°C.

Usually, thermosetting polymers contain only permanent covalent bonds and can thus not be reprocessed. Since the CAN SMCs contain reversible crosslinks, they present reprocessability. To better highlight the recyclability behavior observed during rheological analysis and measure its impact on mechanical properties, recycling of PCL-CAN_c was conducted using the temperature protocol of the rheological analysis. Stripes of the SMP_c (figure II.31 - A) are chunked in small parts (figure II.31- B) which are piled in a flat sheet mold and hot pressed at 125°C for 60 minutes. The new film (figure II.31 - C) is cooled down to 65°C for 2 hours before being chunked again and piled for another cycle. This process is repeated 3 times and delivers a flat PCL-CAN_c film. This film is cured for 72 h at 65°C to form again an SMP_c that has been tested to evaluate its properties after resting a week at room temperature.

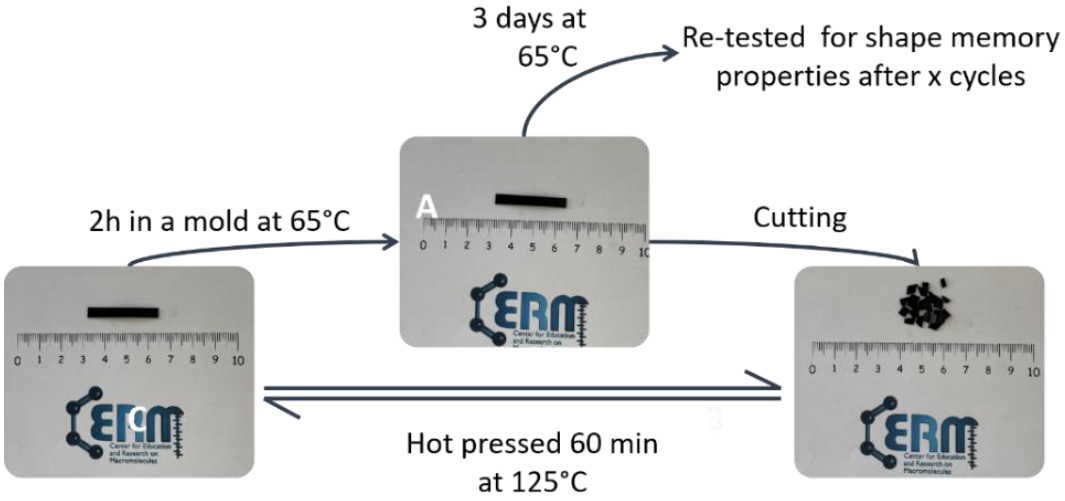

Figure II.31 - Demonstration of PCL-CAN_c recyclability. Stripes of the SMP_c (A) are chunked in small parts (B) which are piled in a flat sheet mold and hot pressed at 125°C for 60 minutes. The new film is cooled down to 65°C for 2 hours before being chunked again and piled for another cycle. This process is repeated 3 times and delivers a flat PCL-CAN_c film (C). This film is cured for 72 h at 65°C to form again an SMP_c that has been tested to evaluate its properties.

Immersion of the recycled samples in $CHCl_3$ leads to the formation of a gel with gel fractions of respectively 92,45 and 91,69 wt% and swelling ratios of 1012 and 1047wt% for PCL-CAN_c recycled once and three times as show in table II.8 . This indicates that the recycled material presents a lower global level of crosslinking than the initially prepared material. This is in good agreement with the rheological observations that confirms side reactions between the chain-ends and MWCNTs. Less reactive moieties are thus present to create the furan-

maleimide network, resulting in a lower overall crosslinking degree. However, similar swelling ratio and insoluble fraction of the recycled PCL-CAN_c between the one time and three times recycled samples suggests that these SMP_c are crosslinked in an almost identical way. Quantitative cyclic thermo-mechanical analysis has thus been carried out to investigate the impact of recycling on mechanical behavior (results are displayed in figure II.32). Cycle 4 of the dynamic mechanical analysis is here not represented on the figure for better visibility but its shape memory properties are still described in table II.9 as for the other cycles.

Table II.8 - Swelling ratio and insoluble fraction of the PCL-CAN_c recycled network

Recycling cycles	*Swelling ratio*	*% insoluble*
0 x (Original)	682,53	98,5
1 x	1012,24	92,45
3 x	1047,06	91,69

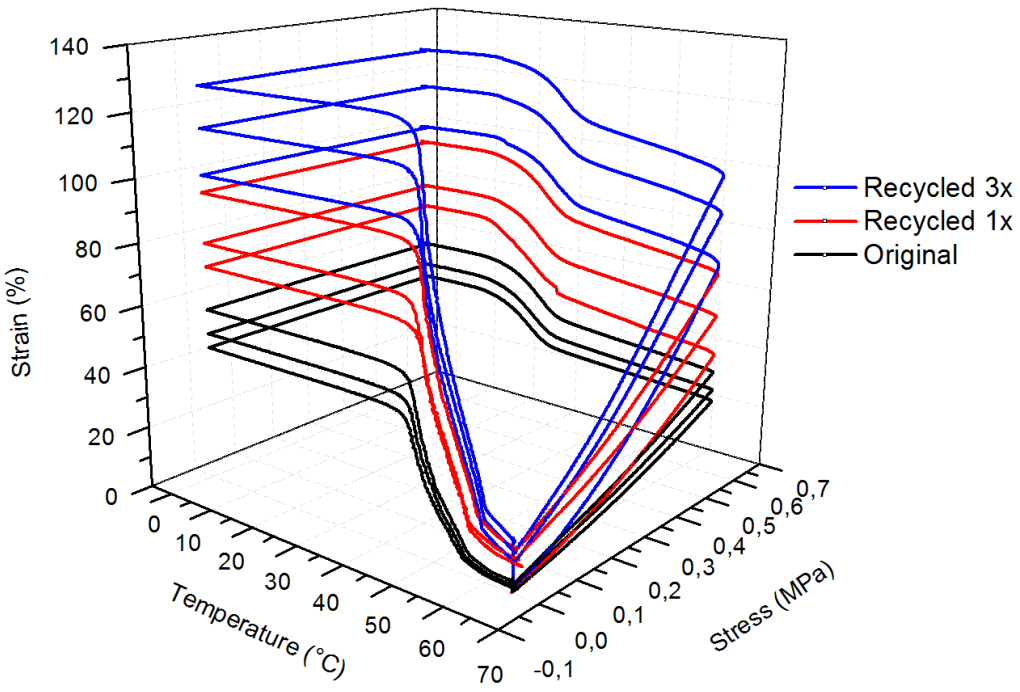

Figure II.32 - Shape-memory properties evaluated by thermo-mechanical cycling of the recycled PCL-CAN_c networks (0x, 1x and 3x; stress ramp: 0.06 MPa/min; temperature ramp: 3 °C/min on heating and cooling) measured 7 days after end of curing.

Table II.9 - Shape memory properties of PCL-CAN$_c$ and PCL-CAN$_c$ recycle networks

PCL-CAN$_c$ - Original sample				
	Cycle 1	*Cycle 2*	*Cycle 3*	*Cycle 4*
Fixity Ratio, R_f (%)	99,44	99,52	99,54	99,56
Recovery Ratio, R_c (%)	96,38	98,52	97,69	96,13
Maximal Strain (%)	44,16	48,75	52,71	56,56
PCL-CAN$_c$ - Recycled 1 times				
	Cycle 1	*Cycle 2*	*Cycle 3*	*Cycle 4*
Fixity Ratio, R_f (%)	99,47	99,99	99,99	99,99
Recovery Ratio, R_c (%)	87,07	97,89	96,15	98,35
Maximal Strain (%)	70,75	78,24	86,59	94,25
PCL-CAN$_c$ - Recycled 3 times				
	Cycle 1	*Cycle 2*	*Cycle 3*	*Cycle 4*
Fixity Ratio, R_f (%)	99,7	99,73	99,73	99,74
Recovery Ratio, R_c (%)	90,5	96,82	97,04	99,16
Maximal Strain (%)	99,77	114,27	127,3	153,83

The recycled PCL-CAN$_c$ networks are characterized by a first cycle with relatively high recovery (87,07 % for a sample recycled 1x and 90,5 % for a sample recycled 3x) but reached their maximal values directly during the second cycle (>96 %). These differences in R_c behavior as compared to the original sample may derive from several origins such as the thermal history of the sample that could delay differently the setting up of a steady state behavior during cyclic testing, but also the difference in crosslinking ratio that leads to materials with dissimilar ductility and therefore different crystallization ability upon stress application. Both samples exhibit excellent fixity (> 99 %) and recovery (> 96 %) for cycle 2, 3 and 4. When comparing the three curves, the main arising difference is the higher strain experienced by the recycled networks (1times and 3times) for the same applied stress. The measured elongations are respectively 70,75 % and 99,77 % of deformation at the 1st cycle for PCL-CAN$_c$ recycled once and three times, where the initial material only deformed by 44,16 % upon the same stress. This is caused by a lower crosslinking rate of the recycled networks. It is here also confirmed that the addition of the MWCNTs decreases the degree of crosslinking due to additional crosslinks furan and maleimide being reactive with the MWCNTs surface. Nevertheless, the

behavior of recycled material does not vary from the original one, i.e., the steady increase in strain from cycle to cycle is also present and can be related too to the same occurrence of retro-DA reactions upon tensile stress.

Interestingly, if recycling is conducted over a smaller time scale, i.e., hot molding for 15 minutes and isotherm at 65 °C for 15 minutes, the mechanical performances of the recycled SMCs are identical. It seems that the impacting step in terms of mechanical losses is the PCL mixing. We postulate that mixing the PCL stars favors the meeting between MWCNTs and the chains-ends. The DA addition of furane/maleimide being possible with both a MWCNT or another chain-end, it is likely that two configurations occur: when a chain-end is in contact with a MWCNT, the addition to the MWCNT is favored; while when no MWCNT is present close enough to the chain-end, it is the addition to another chain-end that is favored. This could be explained by the higher mobility of the chain-ends in the melt matrix than MWCNTs. The PCL network is still reformed during curing; demonstrating that even though the number of MWCNTs is high, chain-ends addition is mostly favored.

II. 2. 9. Self-healing of PCL-CAN$_c$

Considering the reversibility of the maleimide-furan network, self-healing performances of PCL-CAN$_c$ were studied by using two different thermal repairing processes: convection heating and electrical heating. In both cases, the shape memory effect plays an important assistance to the self-healing process. When external force damages the material up to fracture, the break in the continuity of the matrix is subjected to mechanical deformation which prevents high contact between the crack borders. Thanks to the shape memory effect, the initial morphology before the fracture recovers rapidly bringing back in closer contact the crack borders and consequently fasten the healing process and its efficiency [288].

SEM was used to characterize the morphology of the cracked surfaces and healed samples for PCL-CAN$_c$ with convection heating (figure II.34) and PCL-CAN$_c$ with resistive heating (figure II.35). Figure II.33 illustrates schematically the self-healing process of such

SMC. The material was prepared so that its surface was flat and smooth (picture A on figure II.33, figure II.34 and figure II.35). A scratch was made on the sample surface by knife-cutting (picture B on figure II.33, figure II.34 and figure II.35). The damaged sample was then thermally treated at 90°C for 20 min (picture C on figure II.33, figure II.34 and figure II.35). Then, a thermal healing at 65°C for 3 days was conducted in a ventilated oven at constant temperature. The first thermal treatment (90 °C, 20 min) was realized in an oven (figure II.34-C) and by joule heating (figure II.35-C). The fracture was immediately narrowed by shape recovery when Tm is reached and the two cut sections are then in full contact. Partial debonding of the DA adduct is carried during this thermal treatment which makes the two new exposed PCLs border adhesive. The cross-linked networks are then reformed during the second thermal treatment (65 °C, 3 days) in a ventilated oven, leading to self-repair (picture D on figure II.33, figure II.34 and figure II.35). The crack-healing ability of the developed materials are thus demonstrated.

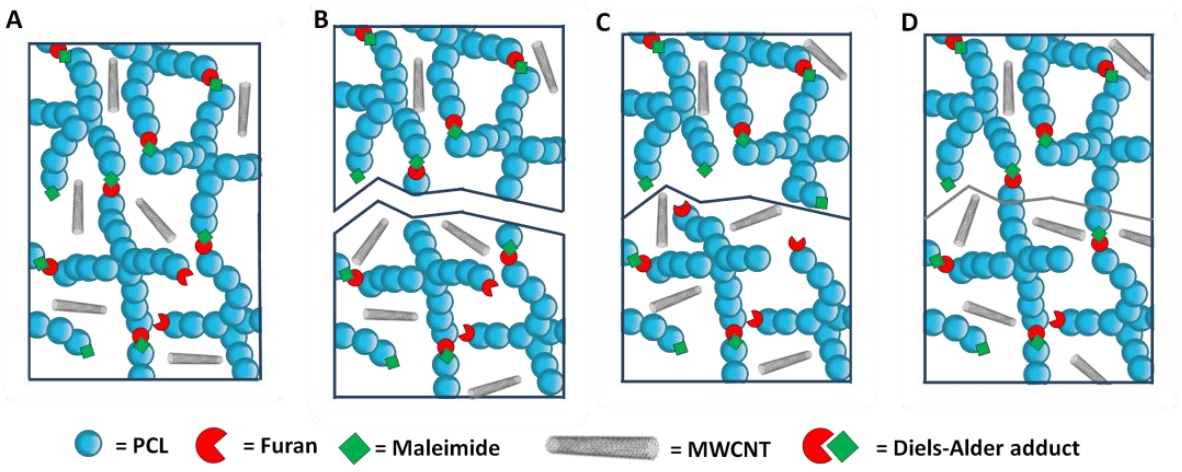

Figure II.33 - Schematic illustration of the self-healing process of a PCL-CAN$_c$: initial material (A), cracked material (B), reduction of the crack gap by thermal triggered shape memory effect (C), healed material by formation of new covalent bonds (D).

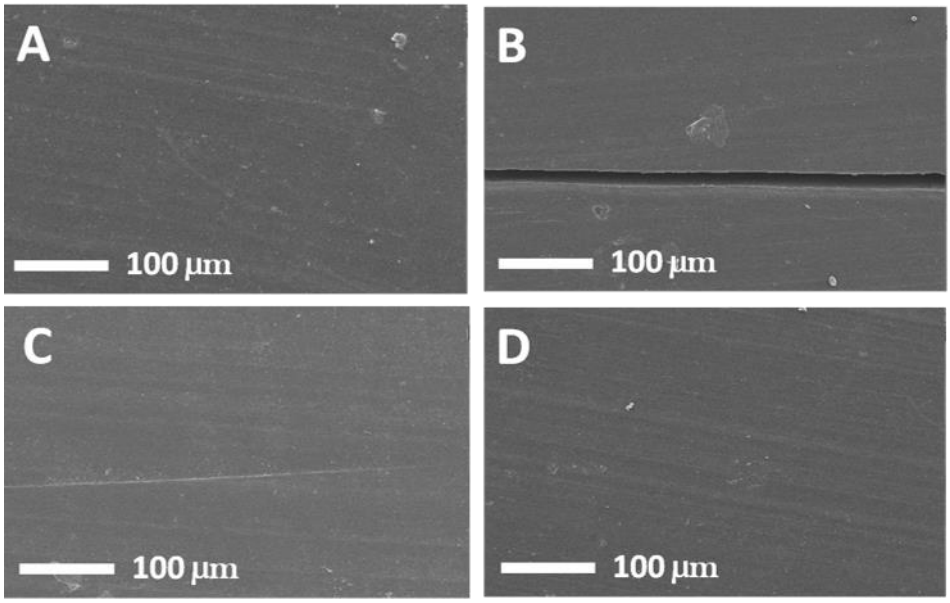

Figure II.34 - SEM images of surfaces of PCL-CAN after production (A), PCL-CAN cracked surface after knife cutting (B), PCL-CAN cracked surface healed by convection heating at 90°C for 20 minutes (C) and PCL-CAN surface healed by convection heating at 65°C for 3 days (D).

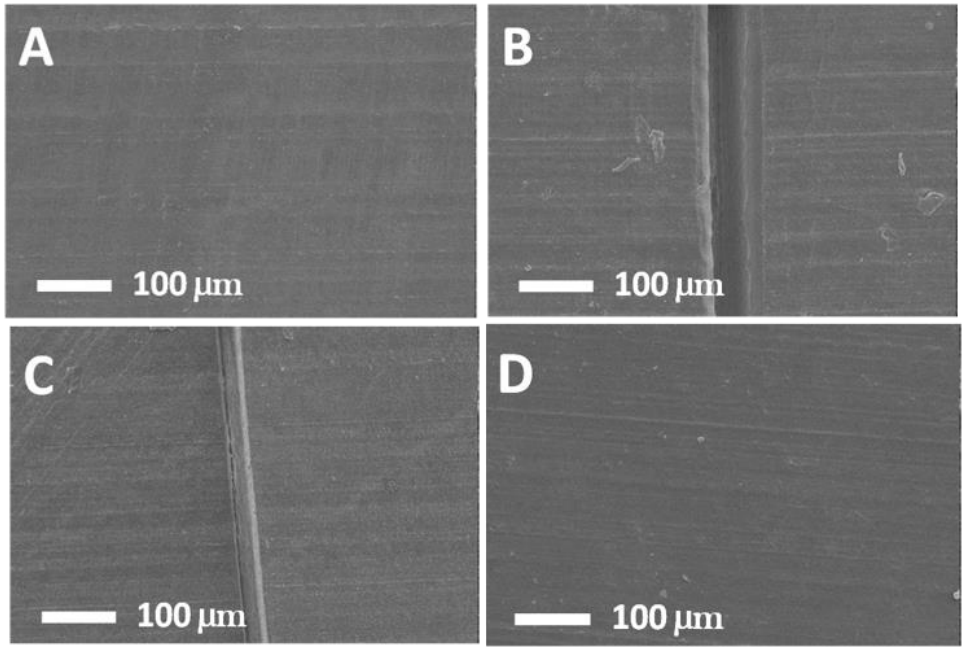

Figure II.353 - SEM images of the surface of PCL-CAN$_c$ after production (A), PCL-CAN$_c$ cracked surface after knife cutting (B), PCL-CAN$_c$ cracked surface healed by resistive heating at 90°C for 20 min, (C) and PCL-CAN$_c$ surface healed by convection heating at 65°C for 3 days (D).

When repaired either by convection or electric heating, the narrowing crack shape memory effect of the PCL-CAN_c is quickly triggered within 1 minute of heating, this is called shape memory assisted self-healing (SMASH) and has already been described in chapter I (Section I.2.1). The heating of the material induces a shape memory response leading to a shrinking of the wounded area promoting contact between the damaged surfaces. The main particularity of internal self-heating by Joule effect over classical oven heating is the local increase of the temperature in the damaged area due to the local increase of resistivity at the tip of the cracks[289]. Unfortunately, this effect is known to happen but we were not able to observe it with our thermal camera, due to the limited resolution of our camera. Results demonstrated high-efficiency and repeatability of the PCL-CAN_c self-healing performance via both electrical and thermal healings indicating the high potential for various uses in industrial applications. Simple implementation of cracks detection through temperature monitoring or crack growth arrest through self-healing leads to the preparation of smart and low energy cost self-healing materials.

II. 2. 10. Multi-layered electro-active SMPC

The developed PCL-CAN$_c$ exhibiting auto-repair abilities offers straightforward processing perspectives by welding to design multilayer devices of complex shapes such as self-deploying devices with sequential triggering of the shape recovery. Covalent crosslinking between several layers of PCL-CAN/PCL-CAN$_c$ can easily be implemented to assemble a multi-SMP/SMPC layers composite. This is here illustrated by welding a composite stripe to a stripe without MWCNTs. CAN systems can simply be juxtaposed next to each other in a specific configuration and welded together by heating /curing into a single piece (figure II.36). Once the smart SMPC is designed, it can be easily programmed in a temporary shape and then by triggering shape recovery selectively in the conductive layer, a transition to a second temporary shape occurs by self-folding of the device leading to a two-way SM (figure II.37). In the present example, the bilayer sample self-folds into a L-bended shape. After what, by maintaining the current ramp in the active layer for an extended period of time, conduction heat from the conductive layer heats up the insulating layer (PCL-CAN) and triggers the return of the device to the permanent shape (figure II.37). The fine control of the current through the device allows thus the progressive transformation in various programmed shapes thanks to dedicated design of the smart multi-layered of PCL-CAN and its MWCNTs composites.

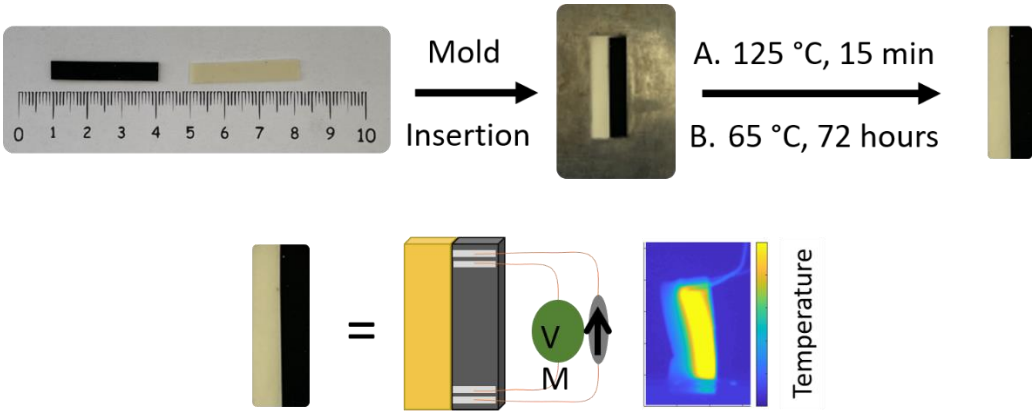

Figure II.36 - Welding of a smart multi-layered SMC by hot molding.

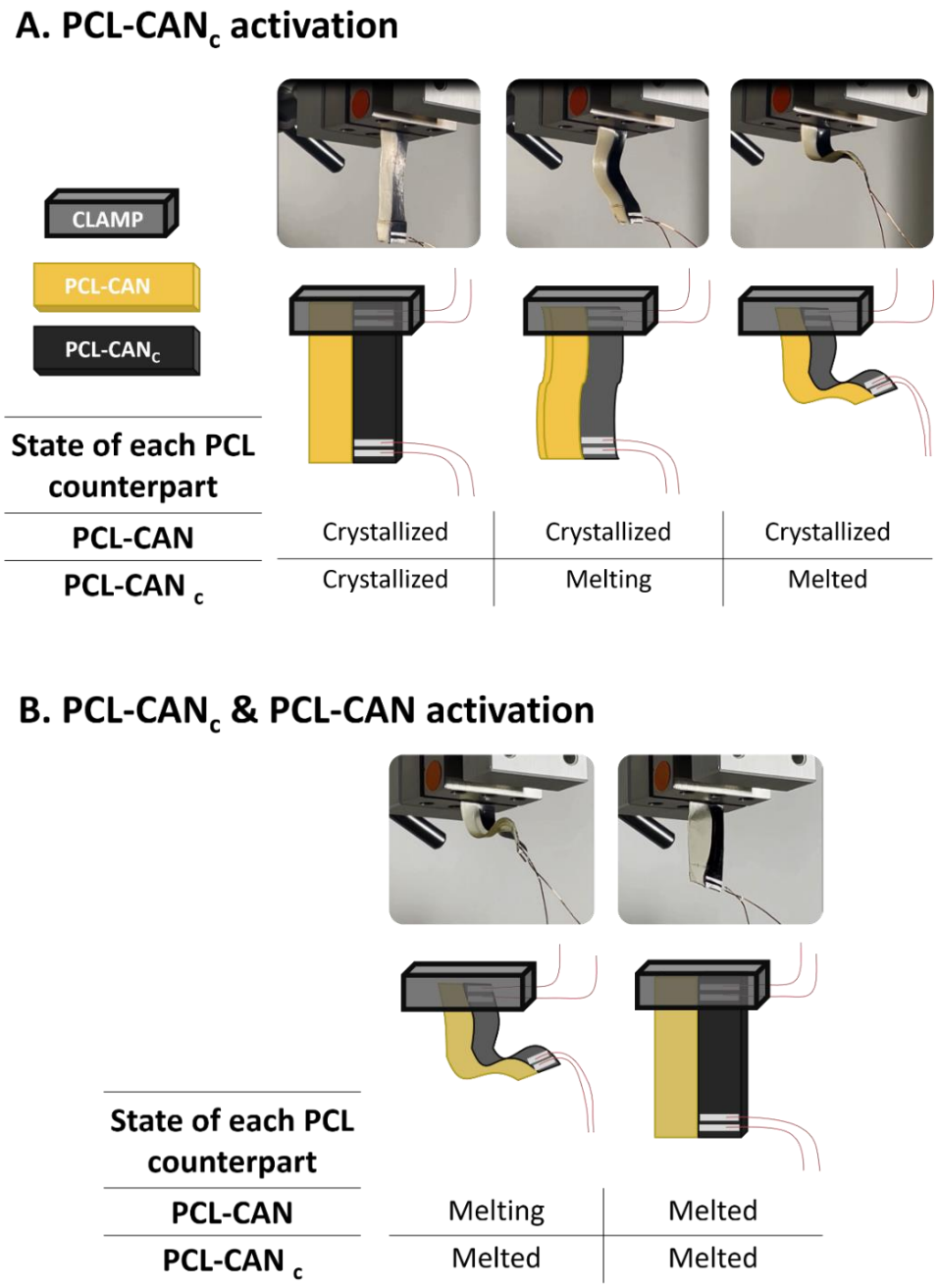

Figure II.37 – (A) Activation of smart multi-layered SMC by Joule heating: heating of PCL-CAN$_c$; (B) Activation of smart multi-layered SMPC by joule heating : heating of PCL-CAN$_c$ and then convection heating of the PCL-CAN layer.

II. 2. 11. Preparation and activation of magnetically sensitive PCL-CAN@Fe_3O_4

In parallel to the classical oven and the electrical activation of the shape-memory effect, another alternative has been envisioned which consists in the activation of the SMPCs by application of an alternating magnetic fields. This requires the preparation of magnetosensitive SMPCs for which ferromagnetic fillers are needed. Fe_3O_4 nanoparticles coated with oleic acid (Fe_3O_4 NP@OA) were selected as they are one of the most popular magnetic fillers. Synthesis of those nanoparticles is detailed in section II.2.9. Coating the NP with an organic layer is mandatory for a good dispersion in PCL, which is hydrophobic. The positively charged iron oxide nanoparticle can be coated by the negatively charged oleic acid, through electrostatic interactions (figure II.38). Transmission electron microscopy (TEM) was used to characterized the formed Fe_3O_4NP@OA (figure II.38 & II.39). As Fe_3O_4 nanoparticles turn superparamagnetic for particle diameters smaller than 20 nm and no longer exhibit hysteresis, great efforts were putted to produce NPs with such diameter. In this sense, we can expect Néel-Brown relaxations as the main magnetic heating mechanism and implement a thermal activation of the SMPCs by application of an alternating magnetic field.

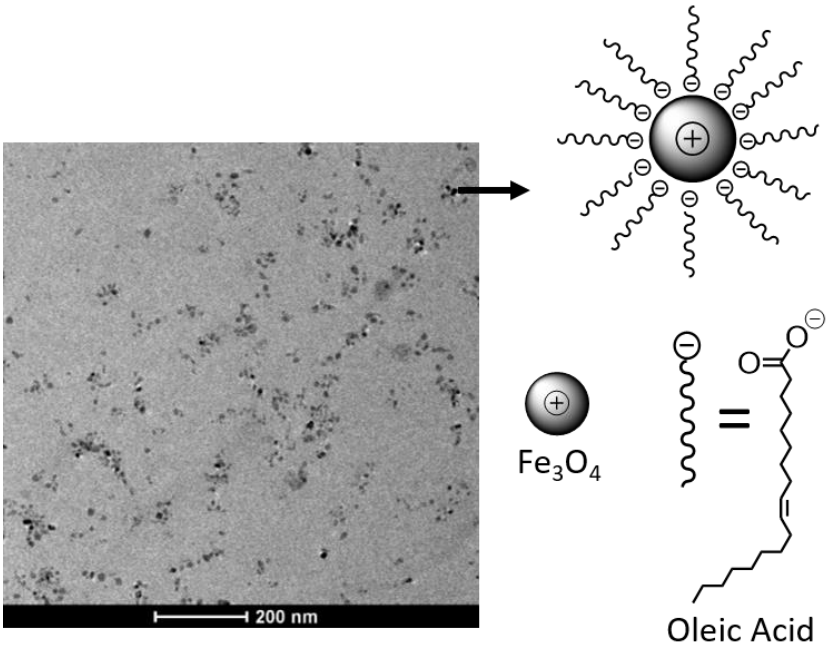

Figure II.38 – TEM analysis of Fe_3O_4 NP and schematic representation of the particle.

Figure II.38 shows a TEM image of the dispersed nanoparticles in toluene and a schematic representation of the particles, stabilized by an oleic acid (OA) coating during synthesis. Coating the NP allows also an easy dispersion in non-polar organic solvents, which is mandatory for the co-precipitation process with the PCL stars. The internal program of our TEM equipment was used to measure the particles size and confirmed the reaching of the targeted size limit below 20nm in diameter (figure II.39).

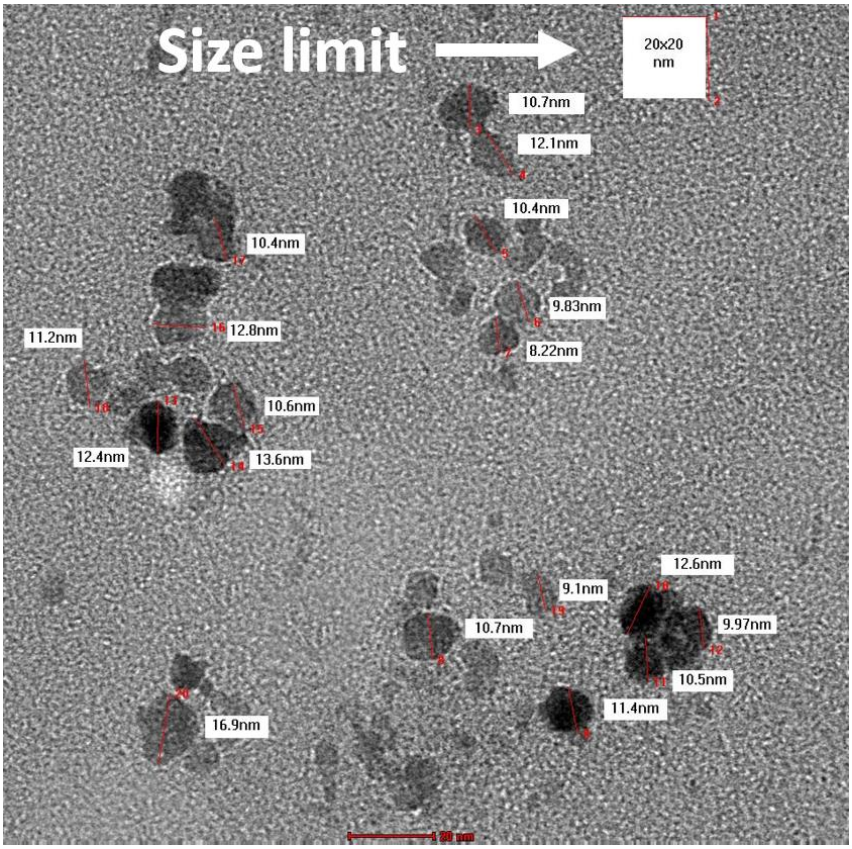

Figure II.39 – TEM analysis of Fe_3O_4 N@OA and size measurements.

The particle size and polydispersity were also assessed by Dynamic Light Scattering (DLS). Magnetostatic (magnetic dipole–dipole) interactions of the particles can cause their agglomeration in solution even in the absence of an external magnetic field. This phenomenon was observed experimentally[290] and confirmed by Monte Carlo simulations, which showed the formation of closed rings and long open loops of particles with no preferred spatial orientation. These aggregates tend to have a lower diffusion coefficient than single particles, and their equivalent sphere radius measured by light scattering is larger than the elementary

particle size obtained from TEM. Additionally, the hydrodynamic radius measured by DLS can increase due to the presence of oleic acid coating on the NP surface, resulting in an average diameter of 30.6nm. Despite this, the polydispersity index remains low at 0.039, and multiple analyses yielded consistent result.

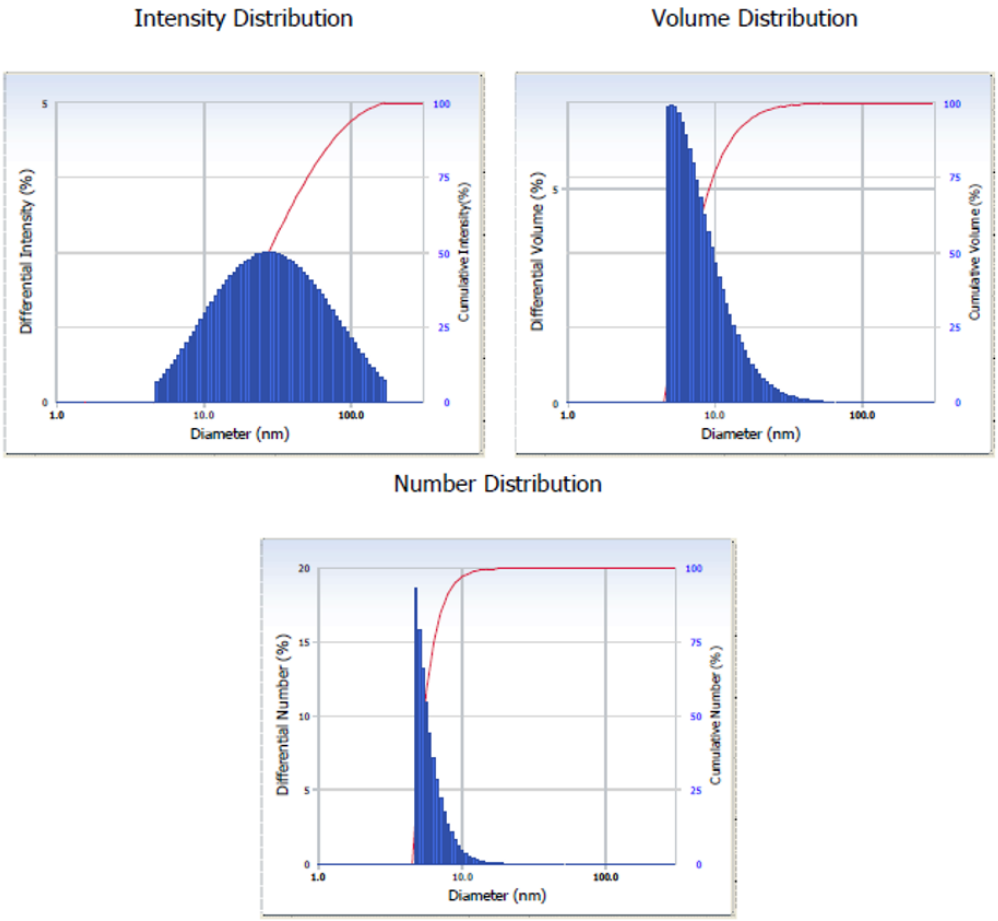

Figure II.40 – Dynamic light scattering analysis of Fe_3O_4 NP@OA.

The magnetization of the nanoparticles was measured as a function of the applied magnetic field (H) at 3 different temperatures (300K,338K and 398K) as depicted in figure II.41. The magnetization disappeared instantaneously when the external field was suppressed, which indicates that their magnetic remanence and coercivity are close to zero at room temperature. This behavior is typical of superparamagnetic materials, which is desirable for the thermal activation of the SMPCs by application of an alternating magnetic field.

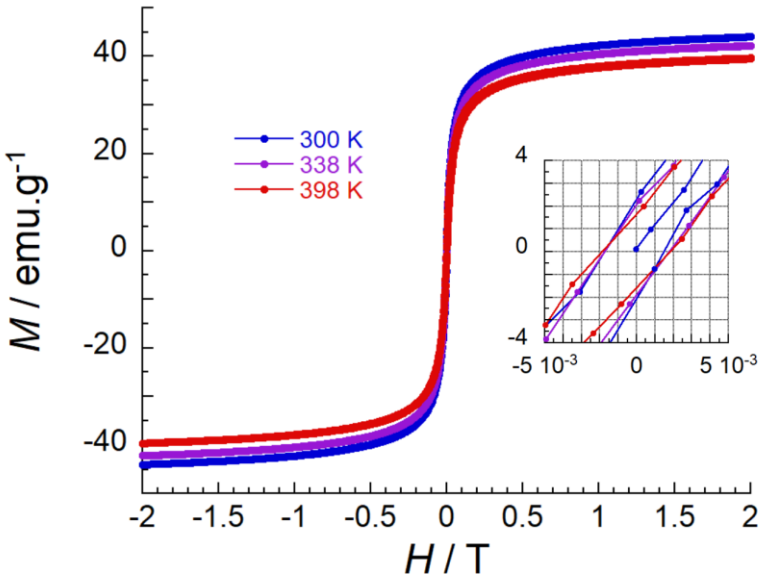

Figure II.41 – Magnetization curve of* Fe_3O_4@OA *nanoparticles at 300, 338 and 398 K.

Preliminary experiments showed that incorporating the synthetized Fe_3O_4@OA nanoparticles enable magnetically driven heating with measurable effect from 25 wt% of NP. Nevertheless, in the present work, a concentration of 70 wt% was selected in order to reach a temperature of about 60 °C with the available soil set-up described in section II.2.14. Indeed, for a lower amount of 40 wt% the maximal temperature obtained reached 40°C which is not enough to melt the PCL composite. Blends of PCL-CAN/Fe_3O_4NP@OA with a weight ratio of 70 wt% of NP@OA respectively to the PCL were analyzed by TEM (figure II.41) to confirm the homogeneous dispersion in the PCL matrix. Thanks to the coating with oleic acid allowing dispersion in non-polar media, the NP were well dispersed in the PCL matrix (figure II.42 – A). For the sake of comparison, non-coated NP form aggregate after coprecipitation with the PCL (figure II.42 – B).

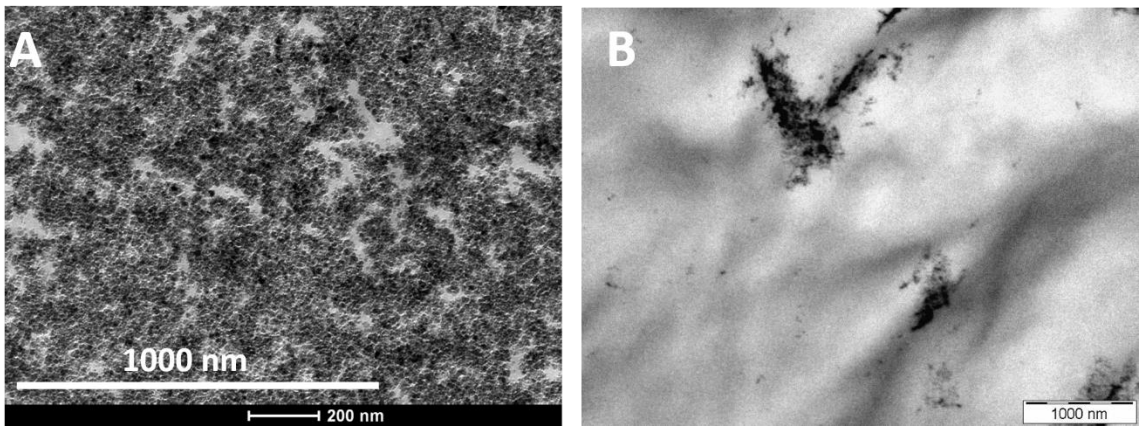

Figure II.42 –TEM analysis of (A) PCL-CAN-Fe_3O_4@OA; (B) PCL-CAN-Fe_3O_4.

Infrared imaging was used to evaluate the remote heating of a PCL-CAN Fe_3O_4@OA pellet (8 mm in diameter, 2 mm in width) by an alternating magnetic field. Figure II.43 shows a thermal image of the running experiment, along with the corresponding temperature increase over time as measured by an IR camera. The time evolution of two spots is depicted: spot 1 on the sample surface and spot 2 located beside of the sample. The sample was placed on an expanded polystyrene stand in the center of the coil.

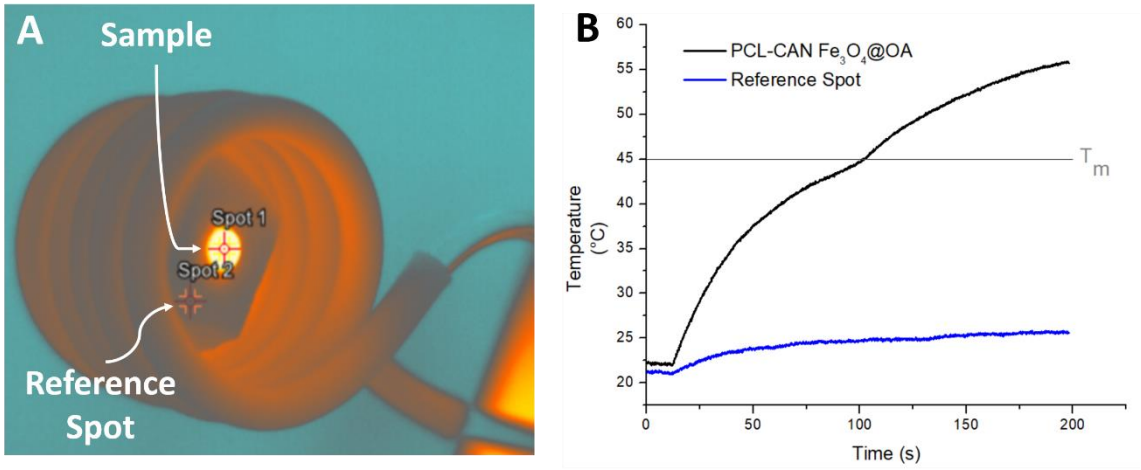

Figure II.43 – (A) Thermal images of the surface of the SMC during magnetic heating detailed in section II.2.14; (B) Evolution of temperature with time resulting from magnetic heating of a PCL-CAN Fe_3O_4@OA (Spot 1) and a reference spot (Spot 2).

The IR camera picture of the sample indicates an homogeneous temperature of the whole sample which traduces the homogeneity of the heat dissipation and thus of the NP

dispersion within the matrix. The melting temperature of the sample (45 °C) was reached within 100 s, and a final temperature of about 60 °C is reached after 200 s. Upon reaching the melting temperature, there is a slight decrease in the rate of temperature increase, likely caused by the melting of crystalline regions, which uses part of the heat induced by the NPs. Heating continues to increase after melting. By monitoring the temperature of a reference spot adjacent to the sample, it is evident that there is no external temperature increase beside the sample's thermal radiation. This proves that the sample is being heated through the magnetic field and not merely by heat transfer from the coil (which is water-cooled to prevent such occurrences). These results demonstrate that enough heat is produced by magnetic activation to melt the PCL and thus to potentially actuate the shape recovery of programmed SMPCs.

After establishing that magnetic heating can achieve a uniform temperature distribution on the SMPC, the subsequent crucial factor to examine is the mechanical properties of the SMC for enabling well-regulated shape memory cycles. Regrettably, such a substantial loading of NPs significantly deteriorated the mechanical characteristics of the PCL matrix. The sample becomes brittle at room temperature and requires some heating to display sufficient flexibility for shape memory cycling. There are two potential causes for this observation. The first is the impact of NP loading, which could have a negative effect on mechanical properties due to lack of interfacial interactions and thus at high loading, interface increases leading weakening the composite properties. The second possibility would be a reaction occurring with the reactive moieties at the PCL chain ends and the NP coating. NP are coated with oleic acid, which contains an unsaturation. If the reactive chain ends were to attach to the oleic acid coating, they may be unable to participate in network formation. As we have seen in a similar example involving MWCNTs, this could significantly affect mechanical properties.

However, the composite becoming much less brittle above the melting temperature, it can be programmed in an elongated shape and as demonstrated in Figure II.44, the shaperecovery can be efficiently actuated by the magnetic field. As compared to figure II.43 where the sample is a dense pellet, the elongated thin PCL-CAN Fe_3O_4@OA stripe takes longer

to reach its T_m. This delay can be attributed to thermal losses caused by convection cooling in the ambient air, whereby the sample loses a significant amount of energy. Multiple attempts to heat samples of same composition but varying thickness, have confirmed this effect. Samples with lower thicknesses achieve lower final temperatures. This effect is further exacerbated during shape memory cycling, where the temporary shape adopted by the sample typically involves elongation, leading to a reduction in cross-section and greater losses. Therefore, determining the optimal thickness of the sample for the intended application is crucial and should be considered as an important parameter.

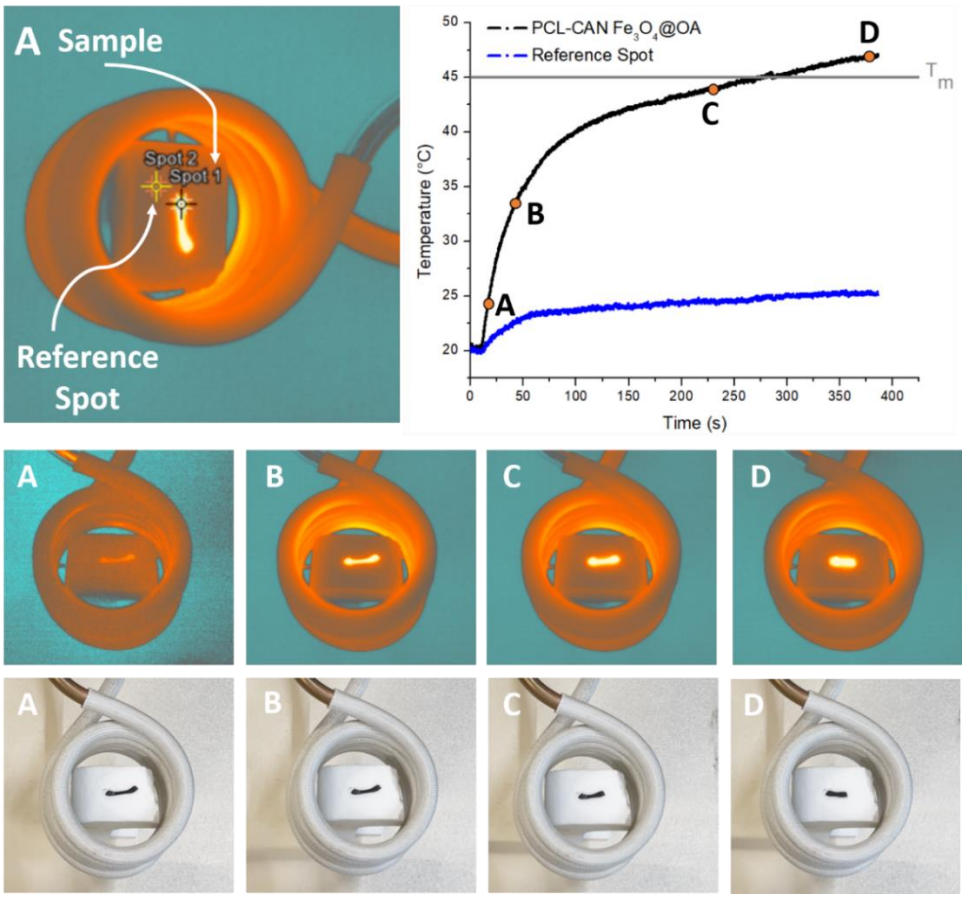

Figure 44 – Thermal images of the surface of the SMC during magnetic heating of a PCL-CAN Fe_3O_4@OA (Spot 1) and a reference spot (Spot 2); (A-D) Evolution of temperature with time resulting from magnetic heating.

Additional investigations would be necessary to optimize the loading of magnetic particles in the composite in order to avoid brittleness while preserving enough magnetic heating capability. However, due to the timeframe of the magnetic heating implementation in the project, this is still an ongoing work and can not be presented in this manuscript.

II. 3. Conclusions

In this work, smart shape memory self-healable and recyclable composites were developed from PCL covalent adaptable networks. In-depth investigation of the Joule effect triggered shape memory properties was made possible by integrating to the conventional characterization methods, namely tensile tester and dynamic mechanical analysis, with the simultaneous measurement of the sample resistivity. The electrical activation of the shape recovery through Joule effect is particularly attractive to finely control the triggering of the shape recovery while avoiding overheating of the surrounding. This is especially of interest when a sequential recovery of a multi-material device is foreseen. Indeed, it allows to trigger shape transitions in dedicated parts of multilayered materials allowing the precise control of multiple and progressive shape transitions. In addition, this easy to reprocess and reconfigurable PCL-CAN material makes straightforward the elaboration of multilayered smart devices of various conductivities by loading or not the network with MWCNTs. Fabrication of a self-deploying devices of complex shapes integrating parts with selectively triggered shape recovery has been presented. Finally, the inclusion of Fe_3O_4 nanoparticles was evaluated. The application of a magnetic field successfully induced heating, thereby enabling remote activation of the shape memory effect in a PCL composite loaded with Fe_3O_4. However, further research is needed to improve the mechanical properties and ultimately produce a composite with shape memory characteristics that can be activated remotely.

Chapter III

Design of low density reprocessable chemically crosslinked polymer foams thanks to Diels–Alder Cycloaddition

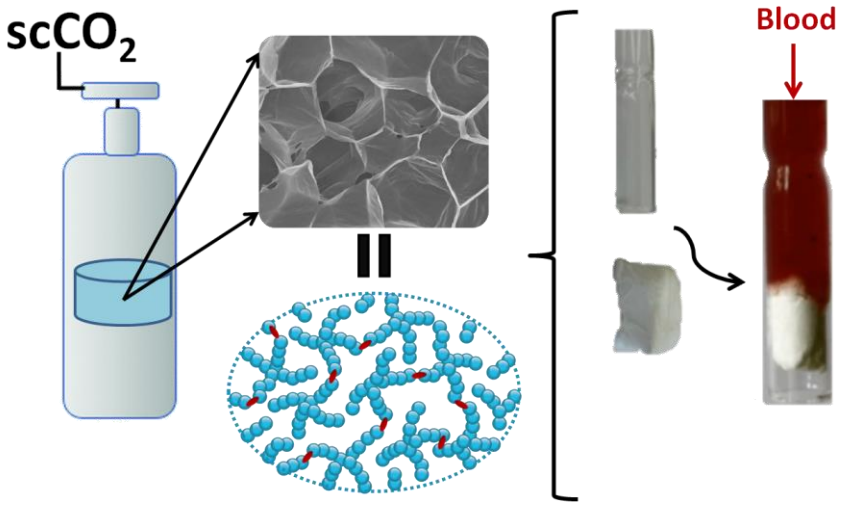

Abstract

Recent studies have highlighted the efficacy and benefit of shape-memory polymer foams over bulk materials, especially for self-deploying medical devices. In that field, poly(ε-caprolactone) covalent adaptable networks (PCL-CAN) are materials of choice since they combine biocompatibility, excellent shape memory properties with reconfiguration ability of the network allowing the design of biomedical devices of complex shapes. The preparation of PCL-CAN foams was here investigated by using a solvent-free supercritical CO_2 foaming process. Starting from a mixture of low molar mass PCL stars bearing furan or maleimide as end-groups, a two-step foaming process was developed that leads to highly porous foams of unprecedented low density (0.02 g/cm^3). We took advantage of the thermo-reversible Diels-Alder addition to control the molar mass and the network crosslinking density of the PCL throughout the foaming process. Adjusting the amount of Diels-Alder adducts at each foaming step is key to allow foaming of the mixture and reach closed-cell foams of low density that exhibit excellent shape memory properties. Thanks to the thermoreversibility of the Diels-Alder reaction, these foams are also recyclable at high temperature. These innovative shape memory PCL-CAN foams are attractive candidates as self-deploying implants for vessels occlusion, as shown by dynamic mechanical analysis and illustrated by mechanical occlusion of a large simulated vessel. Finally, this process was applied to MWCNT composites. The impact of the addition of the filler on the foam density, conductivity and shape-memory behavior is investigated.

Part of this chapter has been published:

Houbben, M., Thomassin, J.-M., & Jérôme, C. (2022). Supercritical CO2 blown poly(ε-caprolactone) covalent adaptable networks towards unprecedented low density shape memory foams. *Materials Advances*, *3*(6), 2918–2926. https://doi.org/10.1039/D2MA00040G

CHAPTER III - Design of low density reprocessable chemically crosslinked polymer foams thanks to Diels-Alder cycloaddition

List of abbreviations:

PCL	Poly(ε-caprolactone)
PCL_{82}-4MAL	Poly(ε-caprolactone)$_{82}$-4Maleimide
PCL_{82}-4FUR	Poly(ε-caprolactone)$_{82}$-4Furane
PCL-CAN	Poly(ε-caprolactone) Covalent Adaptable Network
TGA	Thermo gravimetric analysis
DSC	Differential scanning calorimetry
MWCNT	Multi-walled carbon nanotubes
SMP	Shape memory polymers
$scCO_2$	Supercritical CO_2

Design of low density reprocessable chemically crosslinked polymer foams thanks to Diels–Alder Cycloaddition

III.1 Introduction

Polymer foams are versatile materials that allow combining the advantageous properties offered by polymers with the remarkable properties of their intrinsic architecture giving attractive light-weight materials with high mechanical strength[291]. In the past years, the design of porous materials by environmentally friendly foaming processes provided foams of many thermoplastics covering a wide range of applications in various fields, from materials science to medecine[291–296]. In the latter, biodegradable foams are particularly interesting to design implants for therapeutic purposes[297–299] as well as scaffolds for tissue engineering[300–302]. Among the biodegradable materials used for biomedical purposes, semi-crystalline poly(ε-caprolactone) (PCL) has been widely studied because of its biocompatibility and remarkable mechanical properties afforded by a low glass transition temperature (T_g~-60 °C) and a melting temperature easily achieved above the body temperature (T_m~60°C). Furthermore, when PCL is chemically crosslinked, the resulting covalent networks exhibit excellent shape memory properties, making them particularly appealing for the development of the mini-invasive surgery making available self-deploying devices[303]. For example, easy-to-implement endovascular occlusion systems rely on the delivery of a temporary low-volume SMP foam to the confined space of a vessel where, when in place, an externally triggered expansion shifts the foam to its original expanded shape, so filling the vessel[304].

Therefore, many processes have been studied and developed to get porous structures of PCL. Among the diverse foaming processes, the solvent-free supercritical CO_2 ($scCO_2$) foaming received great emphasis[305–313]; CO_2 being non-toxic, non-flammable, and inexpensive[312–315]. As illustrated in table III.1 that gathers some reported foaming conditions and the corresponding PCL foams characteristics, this $scCO_2$ process leads to PCL foams of low density (lower limit about 0.2 g/cm^3 which corresponds to 80 % porosity) in mild conditions, namely by processing the PCL at a temperature between 30 to 65 °C in a pressure range from 10 to 20 MPa with variable depressurization rates. Table III.1 also evidences that PCL with a molar mass above 40 kg/mol is required in order to get enough chain entanglement to insure an appropriate viscosity to sustain the expansion during the depressurization. On the other hand, if the viscosity would be too high, it would limit the material expansion preventing to

achieve low density foams. Therefore, the preparation of crosslinked PCL foams by this process is scarcely described[314] and relies mostly on post-foaming crosslinking treatment. Until now, foaming processes rather include microwave assisted solvent foaming, high internal phase emulsion, particle leaching or glass microsphere incorporation when the preparation of porous PCL covalent networks is foreseen [316–321].

Table III.1 Summary of reported PCL foams of low density obtained via a supercritical CO_2 process

Material and additives	Mw (kDa)	Density (g/cm^3)	Porosity (%)	$ScCO_2$ pressure (MPa)	Foaming T° (°C)	Depressurization rate (MPa/s)	
PCL	50	0,29-0,35	68-72.5	14	39	5	ref[309]
PCL	45	0,07-0,72	36.7-93.8	10-15	31,5-65	5	ref[322]
PCL	45	0,2-0.5	55-85	20	50	0.02	ref[323]
PCL	80	0,22	80	5-20	40-50	7-12	ref[324]
PCL/DXMT/ glycofurol	48 - 90	0,29-0,93	18,5-74,5	20	45	0,016-0,05	ref[325]
PCL/PEO	50 - 70	0,103	80-94,6	10-17	45-95	Fast	ref[326]
PCL/HA nanocomposites	65	0,2-0,5	55-85	10-20	37-40	0,02-10	ref[327]
PCL/ethanol	80	0,22-0,42	62-80	12,3-20,5	35-45	0,24-4,1	ref[316]
PCL/MWNT	50	0,18-0,31	72-84	20	60	10	ref[328]

Introducing adaptable crosslinks in polymer materials allows today to resolve the intersection between thermoplastics and thermosets[329,330]. Advantageously, shape-memory polymers based on covalent adaptable networks (CAN) have emerged since they remarkably combine efficient shape memory properties with reconfiguration and/or recycling capabilities[331]. Indeed, these CANs make possible the reprocessing of the permanent shape so as the full recycling of cross-linked scrapes (e.g. resulting of processing). They are thus eco-friendlier than the non-reversible covalent networks. In addition, they are preferred when shape memory devices of complex design are foreseen for their reconfiguration ability which facilitates their manufacturing[332].

Design of low density reprocessable chemically crosslinked polymer foams thanks to Diels–Alder Cycloaddition

In this chapter, we are taking advantage of the temperature-controlled equilibrium of the Diels-Alder cycloaddition to tune the content of Diels-Alder adducts in the furane/maleimide PCL stars mixture. Consequently, the mixture viscosity and the material crosslinking degree can be adjusted in function of the $scCO_2$ foaming step requirements. In a first step, the partial formation of Diels-Alder adducts allows the coupling of the PCL stars increasing their molar mass and so the viscosity of the material. This allows $scCO_2$ blowing and the formation of PCL foams stabilized by the PCL crystallization occurring upon venting[333–335]. Then, the stabilization of the expanded foams is improved by increasing further the Diels-Alder adducts content until maximum crosslinking of the foamed PCL is reached. This crosslinking ensures the foams stability above T_m providing them shape memory properties and leading to potential biomedical application as self-deploying implant for vessels occlusion.

III.2 Experimental section

III.2.1. Materials

All the PCL stars used in this work were obtained by end-groups functionalization of commercially available star-shaped PCL samples (CAPA™ 4801, kindly offered by Perstorp® UK limited) according to a previously reported procedure[273]. All the characteristics of the used PCL stars are reported in the Table III.2. PCL 80 000g/mol (PCL_{700}-2OH - Aldrich), CO_2 (Air Liquide), 4,4'-Methylenebis(cyclohexyl isocyanate) (Acros Organics) and chloroform (VWR) were used as received.

Table III.2 : Macromolecular parameters of the starting PCL stars

Code	End-group function	M_n[a] g mol^{-1}	Funct. %[b]	Cryst. %[c]	Melting point °C
PCL_{76}-4OH	Hydroxyl	8 800	100	55	49.59
PCL_{76}-4FUR	Furan	9 500	95	43	46.91
PCL_{76}-4MAL	Maleimide	9 600	81	39	45.30

a) As determined from ^{1}H NMR including chain-ends; *b) Degree of functionalization of the PCL chain-ends measured by ^{1}H NMR; c) Crystallization degree as determined from DSC analysis*

III.2.2. Preparation of PCL disks

PCL-CAN disks: stoichiometric amounts in reactive groups (furan and maleimide moieties) of PCL_{76}-4FUR and PCL_{76}-4MAL (Table III**.2**) powders were grinded together in a mortar in order to get 4 g of mixture. This mixture was melt-blended at 125 °C in a 6 cm^3 co-rotating twin screw mini-extruder (Xplore, DSM) for 10 min at 150 rpm. After extrusion, the polymer blend was let to cool down to room temperature. Then, the blends were displayed into a disk mold (8 mm in diameter and 0.5 mm in thickness), heated at 105°C and compressed under a load of 75 N for 90 seconds. They were then quickly cooled down to room temperature, extracted from the mold and stored at -20°C under a dry atmosphere. Just before foaming, a 60 min. thermal treatment at 105°C was applied to these disks placed back

in the mold in order to adjust the cross-linking degree of these PCL-CANs. The optimal time of 60 min. was experimentally determined.

PCL-PU disks: PCL_{76}-4OH was melted in a beaker at 60°C under stirring and then 4,4'-methylenebis(cyclohexyl isocyanate) (0,6 equivalent) was added. After 30 seconds of stirring, the mixture was poured into a flat sheet mold (50x50 mm with a thickness of 0,5mm) and compressed under a load of 75 N for 90 seconds. Disks (8mm in diameter and 0.5 mm in thickness) were then cut from this sheet.

PCL_{700}-2OH (Mn~80.000g/mol) disks: they were prepared by direct hot molding of the material into a disk mold (8 mm in diameter and 0.5 mm in thickness).

III.2.3. Supercritical CO_2 foaming process

The PCL disks were introduced in a 316 stainless-steel high-pressure reactor (100 mL) from Parr Instruments, for $scCO_2$ foaming. First, the reactor was thermostatically controlled at 65°C in an oil bath for 30 min. Then, a CO_2 pressure of 25 MPa was applied with an ISCO 260D high pressure syringe pump for 15 min. This step was followed by a rapid decompression in a few seconds to ambient pressure. Finally, the reactor was let in an oil bath at 40°C for 5 minutes. The final foams were then collected from the reactor. These foaming pressure and temperature were optimized in this study.

III.2.4. Foams characterization

Foams density (ρ_F) was determined as the ratio between the mass and volume of the sample. The mass was measured by using a high accuracy balance and the volume is measured by pycnometry using water as liquid of known density at 25°C. Each foam was weighted prior and after analysis to confirm that the closed cell porosity and water being non-wetting for PCL were enough to ensure no penetration of the liquid inside the foam. The porosity of the foams, expressed in %, was then calculated by the following equation III.1:

$$\text{Porosity} = \left(1 - \frac{\rho_F}{\rho_P}\right) * 100 \qquad \text{(III.1)}$$

where ρ_F is the density of the foam, ρ_P is the density of the bulk PCL (i.e. 1,14). The expansion ratio of the foams was calculated according to equation III.1.

$$\text{Expansion ratio} = \frac{\text{Initial disk density}}{\text{Foamed disk density}} \qquad \text{(III.1)}$$

Scanning electron microscopy (SEM) was used to determine the cells size and morphology of the produced foams using an acceleration voltage of 20 keV. The samples were mounted on metal holder and fixed using a double-sided adhesive tape. Samples cross-section were vacuum-coated with a layer of gold prior to analysis with a FEI-Phillips Quanta 600 microscope using an acceleration voltage of 20 kV.

III.2.5. PCL network characterization

Swelling experiments were performed to evaluate the crosslinking density of the PCL networks. The samples were weighted (initial material weight) and then placed in $CHCl_3$ for 24h at room temperature. The swollen samples (gels) were weighted (swollen network weight). These gels were then dried under vacuum for 24h and weighted (dried network weight). From these data, the swelling ratio and the insoluble fraction of the networks were calculated based on the equations (III.2) and (III.3).

$$\text{Swelling ratio (\%)} = \frac{\text{(swollen network weight-dried network weight)}}{\text{dried network weight}} \text{x } 100 \qquad \text{(III.2)}$$

$$\text{Insoluble fraction (\%)} = \frac{\text{dried network weight}}{\text{nitial material weight}} \text{x } 100 \qquad \text{(III.3)}$$

The conversion of the furan end-groups into Diels-Alder adducts within the cross-linked materials was evaluated by Raman spectroscopy as already described elsewhere[273]. Raman spectra were recorded at room temperature using a Horiba-Jobin-Yvon Labram 300 confocal spectrometer equipped with an Olympus BX40 microscope. A Spectra Physics model 168 Krypton ion laser with a 647.1 nm line was focused on the different samples with an Olympus_50 objective. The laser power at the sample level was of the order of 15 mW. The spectrum was accumulated twice for 20s. The detector is an Andor iDus BRDD 401 CCD. All

spectra baselines were corrected using a home-made software. After normalization of the spectra on the PCL band at 1750cm^{-1}, the furan conversion is estimated by measuring the intensity of the band at 1503cm^{-1} (I) typical for the furan ring and for the starting PCL_{76}-4FUR by applying equation III.4.

$$\text{Conversion (\%)} = \frac{\text{I on PCL stars mixture spectrum}}{\frac{\text{I}}{2}\text{on } PCL_{76}\text{-4FUR spectrum}} \text{ x } 100 \qquad \text{(III.4)}$$

Measurements of the number average molar mass (Mn) and polydispersity were carried out by size exclusion chromatography (SEC) in THF (flow rate: 1 ml / min^{-1}) at 318 ° K using a viscotek 305 TDA liquid chromatograph equipped with two PSS SDV linear M columns calibrated with poly(styrene) standards.

Transmission electron microscopy (TEM) (Philips M100 microscope working at an accelerating voltage of 100 kV) was used to characterize the MWCNTs dispersion in the composite. Thin slices (90 nm) were prepared by ultracryomicrotomy (ULTRACUT E from Reichert- Jung) at -130 °C. The micrographs were analyzed by using the KS 100 (Kontron Imaging System) software.

Differential scanning calorimetry (DSC) analysis was operated on a TA DSC 250 apparatus. Melting point and endotherm was determined during the second heating run of the sample between -80°C and 70°C at 10K/min with isotherms of 5 minutes at each targeted temeprature. Degree of crystallinity of PCL has been evaluated by comparing the value of the melting enthalpy to the one reported for a PCL presenting 100% of crystallinity.

III.2.6. Shape memory characterization

The shape memory properties, namely, the fixity of the temporary shape (i.e. the capacity of the foam to retain the temporary shape when the stress is released below T_m) and the recovery of the permanent shape (i.e. the fidelity of the recovered permanent shape after 1 SM cycle) of the PCL-CAN foams were determined by thermo-mechanical traction and compression analysis using a TA Q800 DMA equipment. The foam sample was cut (1,5 x 0,5

x0,5 cm cut foam for traction and 1 x 1 x 1 cm cut foam for compression), clamped and equilibrated at 65 °C in the DMA. Then, it was respectively elongated up to 0.03 MPa or compressed with a force of 0.06 N, following a controlled stress or force ramp, then cooled down to 0°C at 3°C/min before releasing the stress. The comparison of the strain at 0°C before and after the release of the stress allows measuring the sample fixity. The fixity ratio (R_f) is given by equation (III.5). Finally, the sample is heated again to 65°C at 3°C/min in order to allow the sample to recover its permanent shape. The shape recovery is obtained by comparing the strain at 65°C before and after this cycle, the recovery ratio (R_c) being calculated by equation (III.6). This shape memory cycle was repeated 4 times for both tensile and compressive testing.

$$R_f = \frac{\text{strain after stress release at 0°C}}{\text{strain before stress release at 0°C}} * 100 \qquad \text{(III.5)}$$

$$R_c = \frac{\text{strain at 65°C without stress for cycle N at 0°C}}{\text{strain at 65°C without stress for cycle (N-1)}} * 100 \qquad \text{(III.6)}$$

III.3 Results and discussion

III.3.1. Preparation of PCL-CAN foams

As previously reported[89], PCL-CAN can be prepared by melt blending a mixture of 4-arm PCL stars bearing maleimide or furan moieties at the chain-ends in a stoichiometric amount. By controlling the temperature, a thermo-reversible PCL-CAN is obtained by the formation of Diels-Alder adducts below 125°C between both types of stars (figure III.1, insert). This network can be cleaved back to a fluid mixture of the stars by heating above 125°C. With the goal to get foams of this material, a stoichiometric mixture of 4-arm PCL stars (~9kDa) bearing maleimide or furan moieties at their chain-ends was hot-melt blended, then hot molded as a disk and kept 1h at 105°C before $scCO_2$ foaming (figure III.1). Based on literature data (table III.1), these disks are placed under 250 bar of CO_2 at 65 °C (i.e. above the melting temperature) in order to dissolve $scCO_2$ into the molten material. Then, CO_2 gas expansion is induced by the rapid depressurization of the vessel, leading to the disk foaming. When these disks are

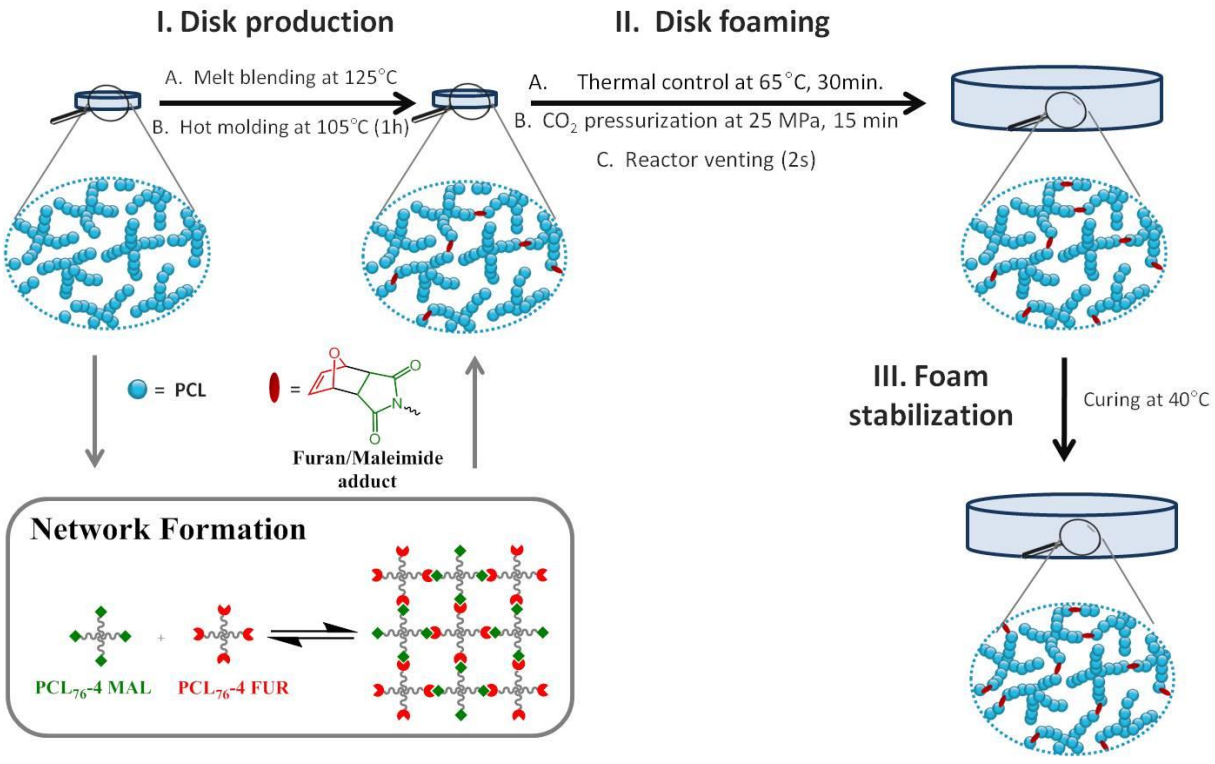

Figure III.1 - Sketch of the progressive network formation in function of the different steps of the PCL-CAN foaming and crosslinking starting from the PCL-CAN precursors.

thermostatized 30min. at 65°C in the high-pressure reactor before pressurization, a foam exhibiting an unprecedented low density is remarkably obtained (figure III.2 - b).

Figure III.2 - (a) PCL-CAN disk before foaming, and foams of (b) PCL-CAN disk cured at 105 °C for 1 hour, (c) PCL-CAN disk cured at 65 °C for 72hours, (d) PCL-PU network, (e) linear high molar mass PCL.

If the same process is performed with PCL stars exhibiting OH groups at the chain-ends and therefore unable to react together, no foaming is observed at the end of the process. This is expected for low molar mass materials due to the limited chain entanglement leading to too low melt strength to get stable foam. When this process is applied to a disk of linear PCL of high molar mass (80 kDa), a foam is obtained (figure III.2 - e) but exhibiting a much lower expansion as compared to the PCL-CAN. Indeed, a density of 0.16 g/cm^3 is measured for the linear PCL foam which is in line with reported literature data, while remarkably, the volume expansion is very high for the PCL-CAN, leading to foams with a very low density of 0.02 g/cm^3 (table III.3). This behavior originates from the peculiar feature of the thermo-reversible Diels-Alder (DA) reaction which allows tuning of the molar mass and network crosslinking density of the stars mixture by adjusting the thermal treatment of the disk. As sketched in figure III.1, the starting stars mixture is initially not foamable due to the low melt strength of the short-arm stars. By taking advantage of the DA reaction, the matrix strength can be increased by formation of Diels-Alder adducts between stars, increasing the molar mass. Therefore, the disks are first hot molded at 105 °C for 60 minutes before placing them, at 65 °C for 30 min. in the high-pressure reactor before pressurizing with $scCO_2$. To follow this thermal process is

crucial since it forms an optimal number of DA adducts so that the resulting molar mass is on one side increased enough to ensure a melt strength allowing foaming but on the other side is kept low enough to reach high foam expansion. Indeed, as evidenced on figure III.2 - c, when a disk is cured for a much longer time, e.g. 72 h, at 65 °C instead of 30 min., the material expansion remains limited during foaming. This is explained by the crosslinking of the material reached before foaming thanks to the long curing time at 65 °C. This is supported by the similar expansion observed for a PCL-PU network crosslinked by diisocyanate before foaming (figure III.2 - d). Table III.3 summarizes the foams densities and expansion ratios of these samples and evidences the critical role of cross-linking on the foam expansion. When the material is highly crosslinked before foaming, whatever the used chemistry (reversible vs irreversible bonds), the foam expansion is limited.

Table III.3: Foams density and expansion ratio of various PCL disks

Disk used for foaming	Density (g/cm^3)	Porosity (%)	Expansion ratio
1. PCL-CAN disk before foaming	1,14	-	-
2. PCL-CAN cured at 105°C for 1h.	0,02	98,2	58
3. PCL CAN cured at 65°C for 72 hours	0,23	80	5
4. PCL-PU network	0,23	80	5
5. Linear PCL 80.000 g/mol	0,16	86	7

Figure III.3 shows the expansion ratio of PCL-CAN foams obtained for disks hot molded for various time at 105°C. It clearly evidences the impact of the thermal treatment of the disks on their foaming capacity, the maximum expansion being observed for a curing time of 60 minutes. The increase of the molar mass without reaching crosslinking of the sample has been evidenced by swelling tests, SEC and Raman spectroscopy.

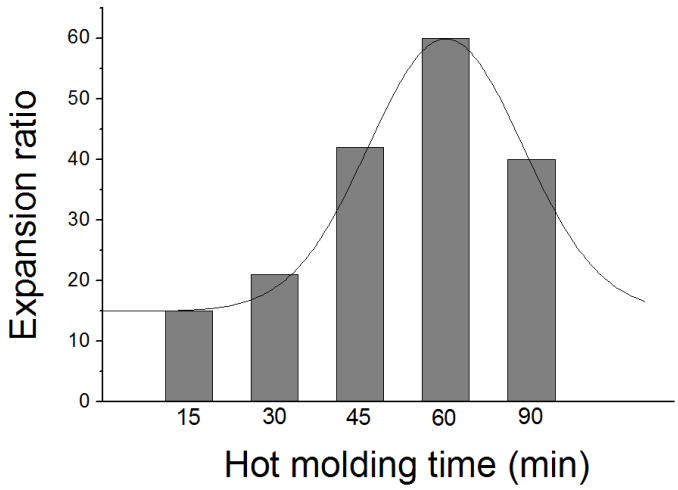

Figure III.3 - Expansion ratio of PCL foamed at 65°C in function of hot molding time at 105°C

After hot molding for 1h at 105°C, the disk remains fully soluble in chloroform. At that temperature a few Diels-Alder adducts are formed leading to chain extension but a network is not achieved. After thermostatization for 30min in the high-pressure cell at 65°C and impregnation for 15 min in $scCO_2$, the material does not dissolve anymore but highly swells in $CHCl_3$ forming a very fragile jelly fish structure difficult to handle, characteristic of a network of very low crosslinking density. This sample was also analyzed by size exclusion chromatography (SEC) after dispersion/swelling in THF. The SEC analysis of the soluble fraction remaining after filtration on a 2-micron filter confirms the increase of the molar mass of the sample by the broad trace at low elution volume (figure III.4). It also reveals that some unreacted stars are still present in the sample.

Just as previously described in section II.3.3, raman spectroscopy demonstrated to be a powerful tool to follow the formation of the DA adduct in this PCL matrix. Typically, the three functional groups of interests (furan, maleimide and DA adduct) can be distinguished in the Raman spectrum and the conversions of the furan and maleimide end-groups into corresponding DA adducts can be quantitatively measured. Raman analyses were performed at each step of the process and the results can be seen on table III.4. After hot molding, the conversion of both maleimide and furan moieties into DA adducts is 16% (figure III.1 - Disk production). It points out that after processing, a few DA adducts are formed, which is in line

with the full solubility of the processed disk. After thermostatization in the $scCO_2$ reactor at 65 °C, and impregnation in supercritical CO_2 for 15 min, the DA adduct conversion increases to 24 % (figure III.1 - Disk foaming) but remains below the gel point of this PCL_{76}-4MAL and PCL_{76}-4FUR mix that is about 33 % of DA conversion[89]. This confirms that foaming occurs when the molar mass of the sample is higher than the one of the starting stars, but before the formation of the network which accounts for the exceptionally high-volume expansion. Let us mention that both the synthesized PCL-PU as well as the PCL-CAN let 72h at 65°C exhibit the same swelling ratio of 1500 % in $CHCl_3$ and an insoluble fraction of 97 %. This demonstrates that a network was formed through the whole disks before foaming, which explains the limited foam expansion observed in these cases.

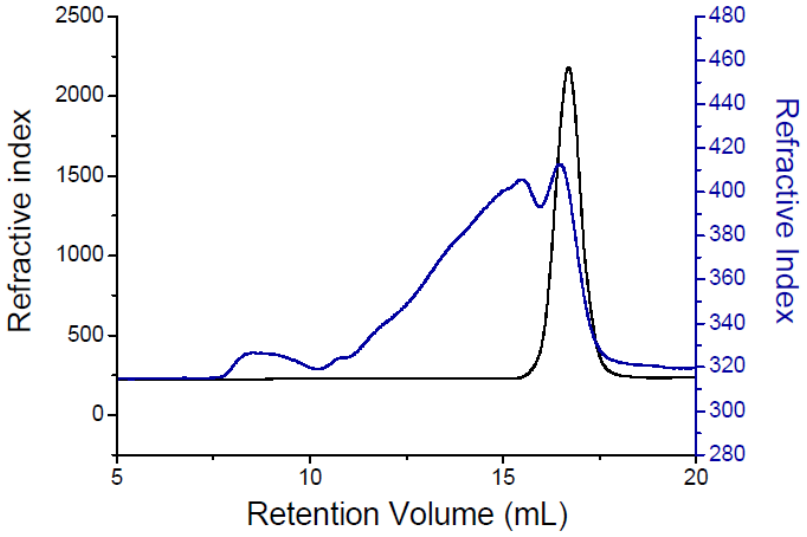

Figure III.4 - SEC chromatograms of a PCL stars mixture before hot molding (before step I of figure III.1) (black) and after hot molding, reactor thermostatization, pressurization and venting (after step II of figure III.1) (blue).

Table III.4: Raman study of the PCL-CAN foaming process

	Foaming step	Treatment	Furan Conv.
1.	Disk Production	1h, 105°C	16%
2.	Disk Foaming	30 min, 65°C	
		15 min, 65°C, 250bar of $scCO_2$, Venting	24%
3.	Foam stabilization	40°C, 7 days	62%
	Disk not foamed	40°C, 7 days	63%

Finally, after $scCO_2$ foaming, an additional curing step is performed at 40°C with the purpose to increase the DA adducts conversion and reach the network formation to stabilize the foamed structure (figure III.1 - Foam stabilization). After 7 days of curing at 40°C, the DA adducts conversion levels up at 62% which is in good agreement with the values reported under the same conditions by previous works[336]. Interestingly, a similar conversion is achieved for a non-foamed PCL-CAN disk experiencing the same thermal curing which confirms that foaming does not alter the Diels-Alder reaction.

At the term of the foaming process, the morphology of the scaffolds was observed by scanning electron microscopy (SEM). Figure III.5 shows the SEM micrographs of the cross-section of the foam revealing a porous closed cell morphology with pores of a hundred of microns. This is in line with reported $scCO_2$ foaming with low soaking time and high depressurization rate[337] and follows the predictions of the nucleation theory [338,339]. If a few pores allow some interconnexions between adjacent cells, most of them are closed as usually observed for the $scCO_2$ foaming process. Thanks to this closed-cell structure, good mechanical properties are preserved for these extremely expanded foams. We observe a young modulus of 0,04 MPa in compression at r.t. allowing the maintain structural integrity to withstand blood pressure.

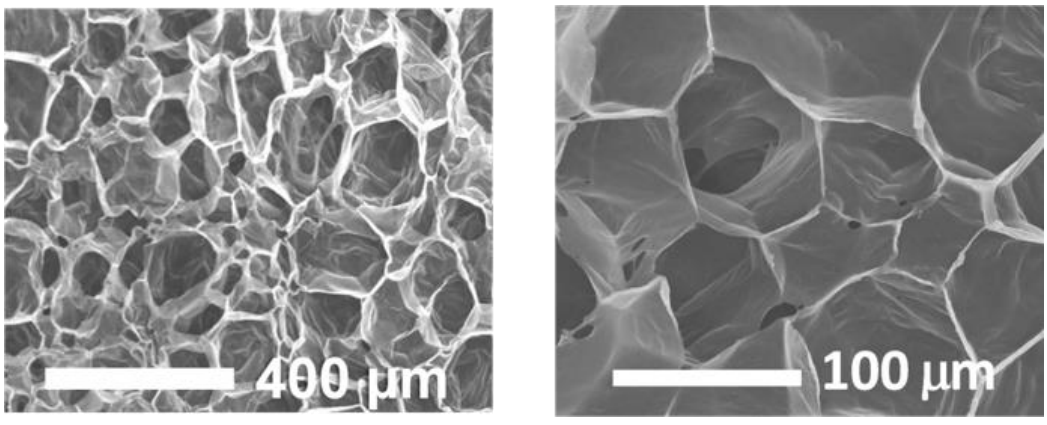

Figure III.5 - SEM analysis of foamed PCL-CAN after a hot molding of 1 hour at 105°C and foaming at 65°C

The advantage of getting a covalent PCL network after the material foaming is that crosslinking preserves the foam structure above the melting temperature. This thermal stability was demonstrated by placing foamed samples at 80°C for 15 minutes and determining the volume expansion retention (VER) after thermal treatment according to equation III.7.

$$\text{VER} = \frac{\text{Expansion ratio after thermal treatment}}{\text{Initial expansion ratio}} \text{x } 100 \qquad \text{(III.7)}$$

Figure III.6 - a shows the effect of the foam curing time at 40°C on the VER. Without a curing period at 40°C after foaming, the foam structure is lost as soon as the PCL is molten traducing the absence of crosslinking as evidenced in the previous section. A curing time above 4 days allows to reach a maximum crosslinking of the material which is then able to retain more than 70% of its expansion. SEM micrographs of the cross-section of the foam before and after thermal testing (figure III.6 - b) on a sample cured for 14 days show that the foam structure is well preserved for the crosslinked PCL-CAN.

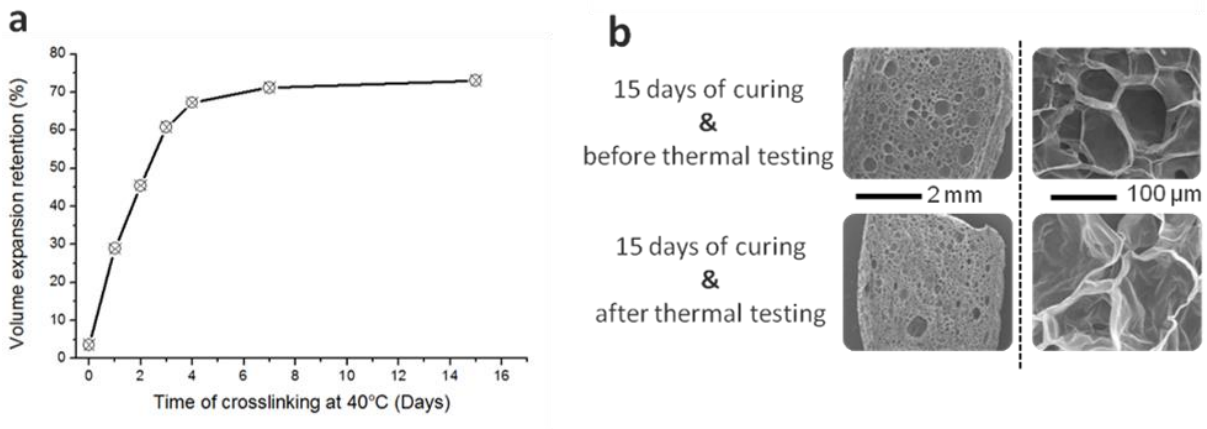

Figure III.6 - PCL-CAN foam thermal stability assessment: a) VER in function of the curing time at 40 °C after foaming and b) SEM micrographs of the cross-section of a foam cured for 14 days, before (top) and after (bottom) heating at 80 °C for 15 min.

The decrease of the foam expansion at 80 °C is caused by the disappearance of the PCL crystalline regions leading to the softening and relaxation of the cell walls. The network relaxation has previously been described by the loss of oriented crystallization occurring when the material crystallizes under load. This is the case when the crystallization occurs during the expansion of the material under foaming[340,341]. Thus, when such foam is placed over T_m, the load that was induced by foaming being no longer present, chain relaxation can occur. Once the sample goes back under T_m, crystallization is no more oriented leading to a partial decrease of the foam porosity. Nevertheless, thanks to the induced crosslinking at the foamed state, the foam architecture is maintained. The stabilizing effect of the network formation is well represented on figure III.6 where low curing time lead to low volume expansion retention. The volume reduction is less and less significant upon curing resulting in about 70% of the initially expanded volume after 7 days. Even with this expansion reduction, the density is still low reaching 0,03 g/cm^3.

Besides, an additional advantage of these PCL-CAN is the reversible thermal cleavage of the DA adducts at high temperature allowing full reprocessing of the material[273]. The reprocessability/recyclability of the foamed PCL-CAN was confirmed by heating the sample at 125°C for 1 hour. A fluid mixture is then obtained that can be reprocessed as a foam by following the developed protocol. The expansion ratio of the recycled material reached 54 that is very close to the one to the pristine material (i.e., 58). A VER of 73 is obtained for foams of the recycled material and cured at 40°C for 14 days that is also comparable to the value of 76 obtained from a pristine stars mixture. This is another evidence that the foaming process based on $scCO_2$ is not altering the Diels Alder reaction so that the PCL-CAN fully preserves its network adaptability and reprocessability.

III.3.2. Shape memory properties of PCL-CAN foams

Figure III.7 shows 4 consecutive shape memory cycles of the PCL-CAN foam (crosslinked during 7 days) in tensile mode. This protocols for this experiment is the exact similar to the ones realized in chapter II section II.2.5, on PCL-CAN_c and PCL-CN_c non-foamed samples, to the exception that the forces involved are reduced for two reasons. Firstly, the material we are dealing with is more malleable, since the sample has been foamed and therefore has lower mechanical properties than a non-foamed sample. Secondly, the foam has expanded to a significant extent, which means that only a small amount of actual material can be analyzed using DMA due to the size limitation. Otherwise, upon cooling under constant stress, the sample experiences also a large increase of its deformation between 35°C and 15°C resulting from the growth of crystallites oriented along the stretching direction. This observation is similar to the behavior of non-foamed PCL-CAN samples[340,341]. A very high fixity (above 99 %, table III.5) is obtained for each cycle thanks to the foam crystallinity, which is also in line with non-foamed PCL films.

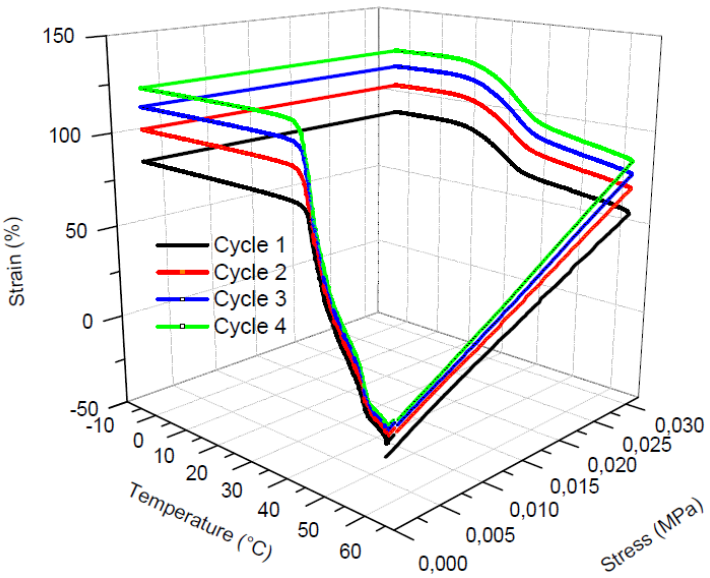

Figure III.7 - Shape-memory properties evaluated by tensile thermo-mechanical cycling of PCL-CAN foam after 7 days of curing.

Table III.5: Shape memory properties of PCL-CAN foam in tensile testing

Cycle	**1**	**2**	**3**	**4**
Fixity ratio, R_f (%)	99,4	99,5	99,5	99,5
Recovery Ratio, R_c (%)	91,18	96,78	97,5	98,18

The foams shape recovery is trigger by a temperature above 45°C. As shown in table III.5, the first cycle is characterized by a lower shape recovery (91%), known as training phenomenon[342], while the following cycles are characterized by excellent recovery ratios close to 97%, which is very close to the already demonstrated properties of PCL-CAN films[273]. It can be observed on figure III.7 that, the deformation obtained at 65°C increases with the number of cycles. This particular phenomenon also observed for PCL-CAN film[273] can attributed to the occurrence of some retro-DA reactions triggered at 65°C under stress. In addition, some gas leaching can occur from the foam because of the network relaxation caused by the rupture of some DA adducts. The material becomes more ductile and stretches then more. Nevertheless, this phenomenon is attenuated with the number of cycles and do not affect the shape recovery.

Shape memory cycling in compressive mode has also been conducted. The experimental setup for shape memory cycling in compressive mode is illustrated in figure III.8. It is worth noting that the dynamic mechanical analyzer needs to apply a pre-load to ensure proper functioning and contact with the foam. This force (0.01N) is ten times greater than the force applied in tensile mode (to pull and the sample and ensure contact) and is necessary due to the equipment sensitivity. However, this pre-load causes an initial contraction of the foam even before the start of the analysis. As a result, the deformation experienced by the foam in compression mode depends on two factors: the actual losses of the foamed system and the pre-load applied. This mode of analysis produces larger deformations, as explained later.

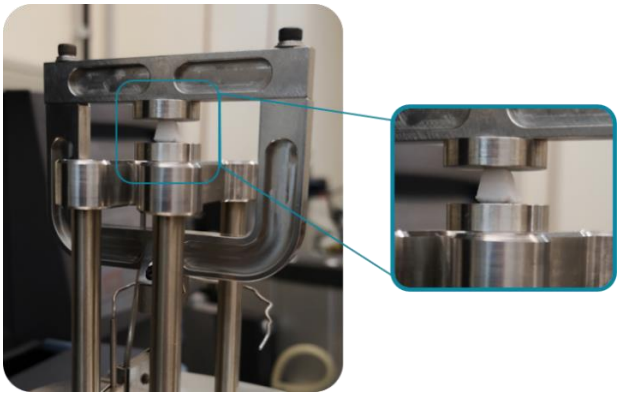

Figure III.8 – Foam sample of PCL-CAN placed in the dynamic mechanical analyzer in compression mode.

Figure III.9 shows 4 consecutive shape memory cycles of the PCL-CAN foam (crosslinked during 7 days) in compressive mode. Note that for a clearer visualization, the axis of this graph have been placed in a different manner than the classical 3D graph previously presented in this manuscript. The cycling starts at high temperature and without load implemented, excepted the pre-load needed by the DMA (figure III.9 – A). During the second step, load is applied (figure III.9 – B). Upon cooling under constant stress, the foam experiences a strain variation in the direction of the applied force just as like for tensile testing which stops after crystallization, between 35°C and 15°C. A very high fixity (above 99%, table III.6) is obtained for each cycle thanks to the foam crystallinity, which is also in line with non-foamed PCL films.

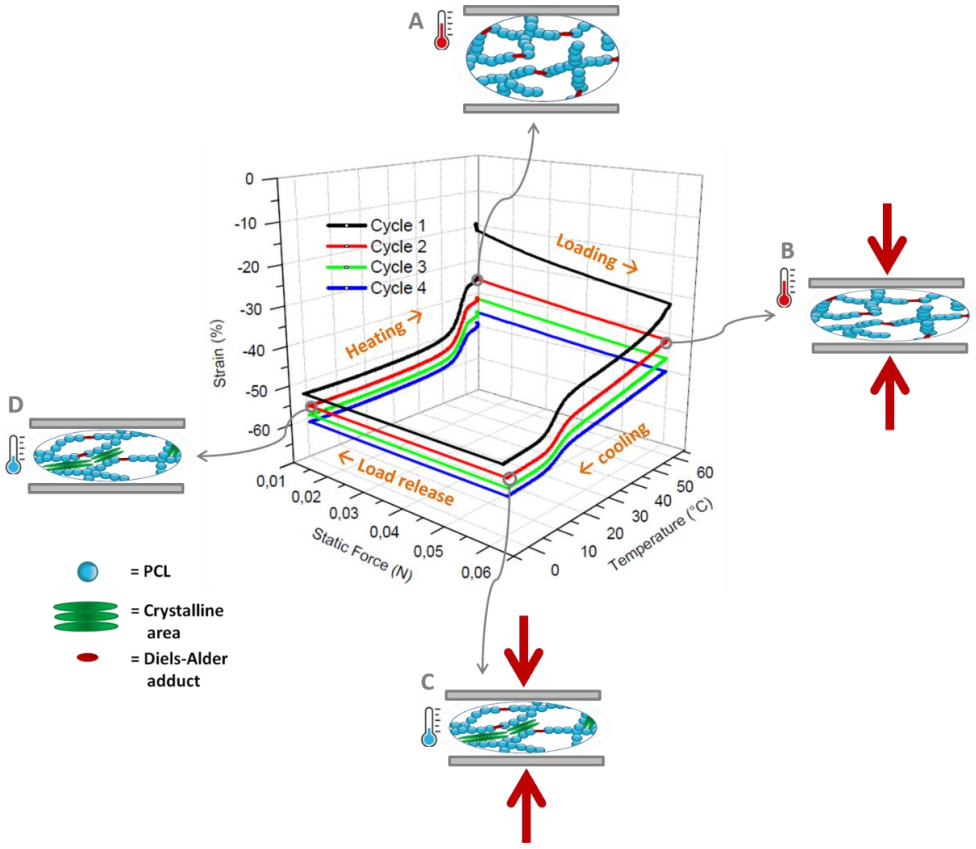

Figure III.9 - Shape-memory properties evaluated by compression thermo-mechanical cycling of PCL-CAN foam after 7 days of curing.

Table III.6: Shape memory properties of PCL-CAN foam in compressive testing

Cycle	**1**	**2**	**3**	**4**
Fixity ratio, Rf (%) (a)	99,6	99,7	99,8	99,8
Recovery Ratio, Rc (%) (b)	62,40	72,30	75,80	77,40

Figure III.9 demonstrates that the foam undergoes a 35 % reduction in strain after the first cycle, which correspond to a 35 % reduction of the foam's height. Since the foam was initially cut as an expanded square shape, we can infer that the volume reduction will be proportional to its height. The first cycle in this context corresponds to the previously described volume loss resulting from the foam's first heating, which was measured to be approximately 30 % (i.e., the volume expansion retention was 70 %, implying a loss of 30 % in volume). The additional 5 % decrease can be attributed to the pre-load force exerted on the sample.

Thanks to their demonstrated shape memory properties, the PCL-CAN foams developed in this study can be very attractive for various biomedical applications. As an example, the potential of these foams for vessel occlusion applications[343] was qualitatively demonstrated (figure III.10). For that purpose, a cylindrical monolith of PCL-CAN foam was cut with a length 15 mm, and a diameter of 8 mm. Then, it is heated above 45 °C, stretched and cooled down to the room temperature to fix a temporary shape with a length about 25 mm and a diameter of about 5mm. This stretching is similar to the first cycle of the thermo-mechanical cycling described earlier with an increase of 75 % of the foam’s original length. The foam in this temporary shape is now able to easily penetrate a glass tube of 6mm in diameter. When heated above 45 °C, by recovering its permanent shape, the foam efficiently seals the glass tube and prevents an aqueous solution to flow through the tube. This PCL-CAN foam presents the advantage of an externally triggered expansion at temperatures closed to body temperature. Furthermore, thanks to the high-volume expansion, the energy required to trigger that shape memory behavior is significantly lower as compared to less expanded devices.

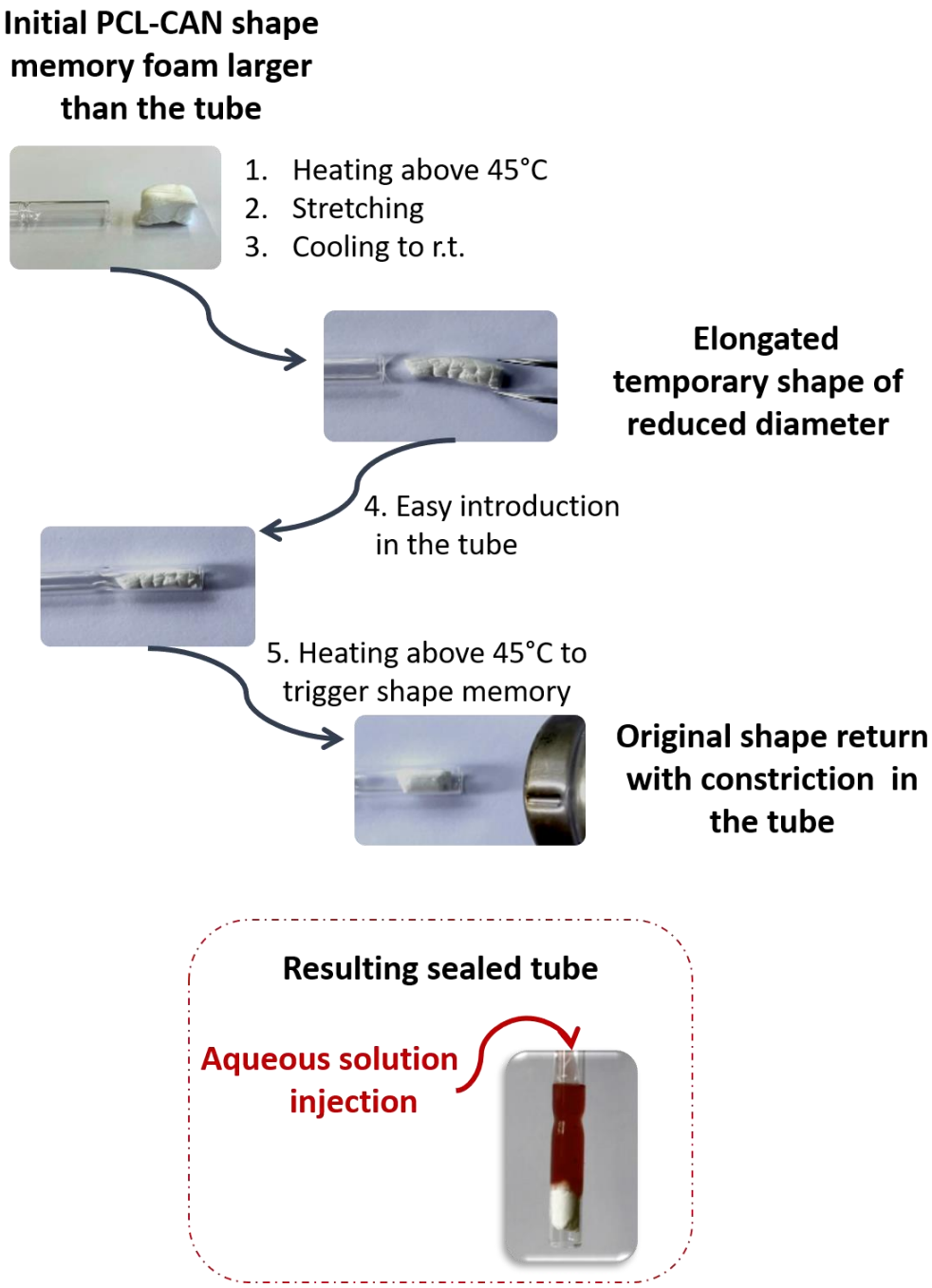

Figure III.10 - Qualitative demonstration of a simulated vessel occlusion thanks to the shape-memory PCL-CAN foam.

III.3.3. Preparation of PCL-CAN$_c$ composite foams

A composite foam version was also explored to capitalize on the knowledge gained from analyzing its non-foamed equivalent. I It was found that adding a MWCNT to PCL-CAN and foaming the composite in the same conditions as a sample without filler lead to a less expended material. It appears that when 3wt% of MWCNTs are added, it increases the strength of the matrix to the point that foaming is almost no longer feasible. Consequently, it was necessary to reduce the MWCNTs content to 1 wt% to achieve significant expansion.

Figure III.11 - PCL-CAN$_c$ with 1wt% MWCNTs composite foam.

Figure III.11 depict the 1 wt% MWCNTs composite before and after the foaming process, for which expansion ratios reaching 45 to 50 times the original volume were obtained. Figure III.12 shows a SEM image of the cross-section of the foam revealing a porous closed cell morphology with pores of a hundred of microns. This is in line with reported $scCO_2$ foaming with low soaking time and high depressurization rate[337] and follows the predictions of the nucleation theory [338,339]. If a few pores allow some interconnexions between adjacent cells, most of them are closed as usually observed for the $scCO_2$ foaming process. Thanks to this closed-cell structure, good mechanical properties are preserved.

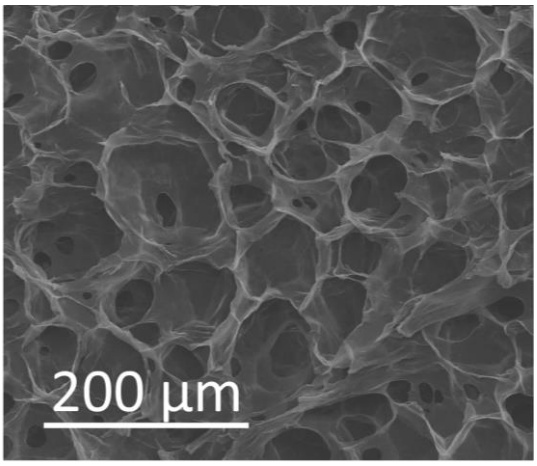

Figure III.12 - SEM analysis of foamed PCL-CAN after a hot molding of 1 hour at 105 °C and foaming at 65 °C.

Furthermore, MWCNTs act as nucleation sites which increases the homogeneity of the pore formation. As compared to a PCL-CAN sample (figure III.13), the composite foam presents pores that are much more homogeneous and smaller.

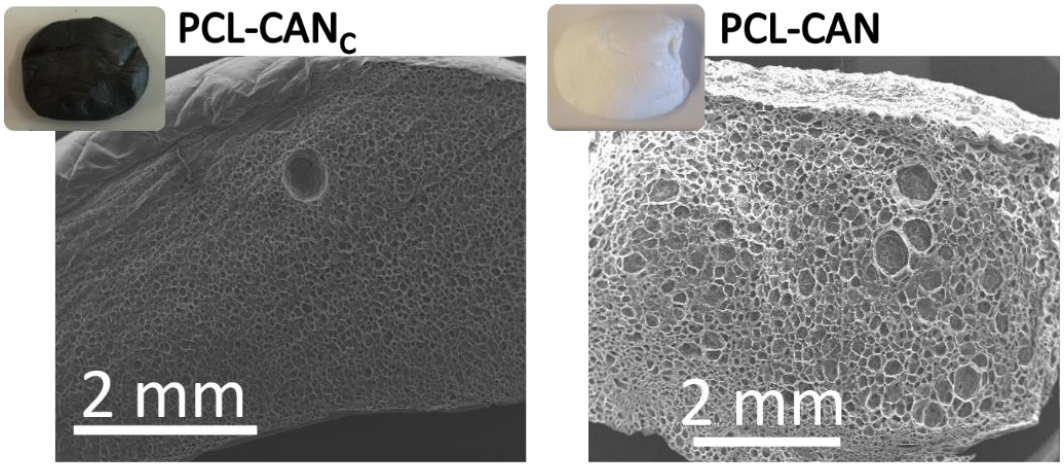

Figure III.13 - SEM analysis of foamed PCL-CAN and PCL-CAN$_c$ after a hot molding of 1 hour at 105 °C and foaming at 65 °C.

III.3.4. Shape memory properties of PCL-CAN$_c$ foams

The shape-memory properties have then been quantitatively evaluated using DMA. Figure III.14 shows consecutive shape memory cycles of the PCL-CAN$_c$ foam (crosslinked during 7 days) in both tensile and compressive mode. Comparable observations can be observed as those for the PCL-CAN foam, with the exception that reduced deformations are noticed due to the stiffer PCL-CAN$_c$ composite. Fixity and recovery ratios are depicted in table III.7.

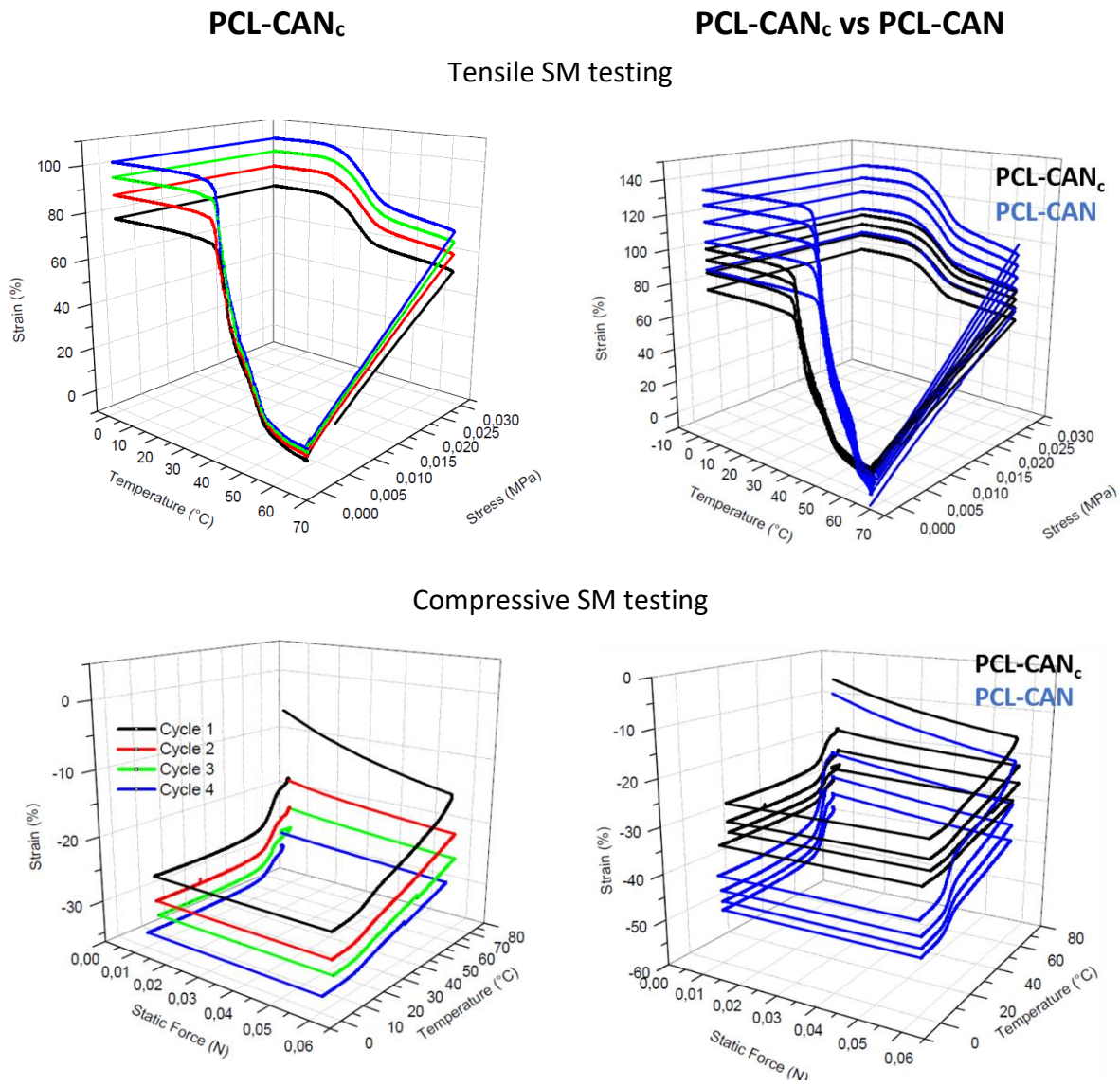

Figure III.14 - Shape-memory cycles evaluated in both compression and tension experimentally by DMA upon convection heating/cooling of PCL-CAN$_c$ and PCL-CAN networks after 14 days at room temperature.

Table III.7 : Shape memory properties of PCL Networks

PCL-CAN$_c$ - Tensile test				
	Cycle 1	*Cycle 2*	*Cycle 3*	*Cycle 4*
Fixity Ratio, R_f (%)	99,4	99,5	99,5	99,5
Recovery Ratio, R_c (%)	91,2	96,8	97,5	98,2
PCL-CAN$_c$ - Compressive test				
	Cycle 1	*Cycle 2*	*Cycle 3*	*Cycle 4*
Fixity Ratio, R_f (%)	99,7	99,8	99,8	99,9
Recovery Ratio, R_c (%)	39,7	57,8	59,5	68,9

During cooling under constant stress, the foam experiences a variation in strain along the direction of the applied force, which ceases upon crystallization between 35°C and 15°C. The foam high fixity (above 99%, as shown in table III.7) is due to its crystallinity, which is comparable to the other PCL films or foams previously studied. The composite foam undergoes a 20% reduction in strain, and thus volume as it was initially cut in a cubic form, after the first cycle. This reduction corresponds to the previously observed volume loss resulting from the foam first heating, which was measured in DMA to be approximately 35% for the non-composite foam. As expected, MWCNTs lead to the production of stiffer materials.

III.3.5. Electrical resistivity assessment of PCL-CAN$_c$ foams

In chapter II, section II.2.2, we mentioned preliminary studies on our PCL-CAN$_c$ system (bulk form)[271]. A PCL-CAN$_c$ sample containing 1 wt% MWCNTs was prepared and exhibited a resistivity on the order of 0.5 ohm*m. However, the foam equivalent of this PCL-CAN$_c$ presents a resistivity on the order of 150 Gohm*m. We previously discussed how the conductivity of heterogeneous mixtures is influenced by the conductive filler content, as supported by literature. However, this relationship is more complex in cellular materials. Experimental data and statistical percolation models have demonstrated that reducing foam density leads to a higher percolation threshold for cellular materials containing conductive filler[344]. This suggests that the critical volume of CNTs needed to form a conductive network is not solely dependent on the CNT content, as CO_2 bubbles also play a crucial role in network formation. The

distribution of CNTs is affected by foam cells, which influence the characteristics of the resulting conductive network. This outcome is intuitive, as a denser foam has fewer cells and, thus, a less restricted conductive network. In contrast, a lighter foam requires a larger amount of CNTs to achieve a dispersed network effectively. Additionally, the microstructure present in the foam consists of very thin conductive pathways, which creates a significant resistive path for the current being injected, resulting in high resistance. In their study, Athanasopoulos N & al. provided a material design for conductive lightweight PU/MWCNT[344]. They used density ratio (relative density compared to the bulk material) as key parameter for this description. By a straight comparison with our system, it appears that we would require a significantly higher weight percentage of MWCNTs (MWCNTs wt% > 5) to achieve conductivity. As previously discussed, our goal was to produced highly expanded foams and was thus more leading toward a reduction in MWCNTs content.

III.4 Conclusion

In this work, a solvent-free $scCO_2$ batch foaming process was developed allowing preparation of PCL-CAN foams. These foams exhibit a remarkable low density (0,02 g/cm^3) keeping good mechanical properties thanks to the closed-cells morphology. Their covalent crosslinking achieved by post-curing the foam at 40 °C for a few days imparts these foams with excellent shape memory properties (high fixity and recovery ratios). The high temperature reversibility of the crosslinking of these PCL-CANs that include furane-maleimide Diels-Alder adducts in their structure makes them fully reprocessable. Advantage was taken from the thermal control of the furane-maleimide Diels-Alder addition to regulate the degree of branching and crosslinking of the starting end-functional PCL reactive mixture. The success of this foaming process relies on this precise control of crosslinking degree of the material at each step. These PCL shape memory foams are quite attractive for biomedical applications such as self-deploying implants for vessels occlusion, which was illustrated through dynamic mechanical analysis and mechanical occlusion of a large simulated vessel.

Chapter IV

Conclusions

Chapter IV

Conclusions

The terms shape memory polymers refer to polymeric materials that have the capability to recover their original shape after undergoing temporary deformation under specific conditions and external stimuli. Conventional methods of initiating shape recovery require direct application of heat, however, for some applications, alternative actuation mechanisms may be preferred due to safety or applications' specific considerations. These alternative mechanisms may include the use of electric or magnetic fields. The aim of this thesis was to develop and characterize high-performance smart shape-memory composites exhibiting recycling abilities by using covalent adaptable bonds for building the networks embedding the fillers. The strategy to involve star-shaped PCL chain end-capped with Diels-Alder reversibly reactive moieties combined with MWCNTs or Fe_3O_4 fillers resulted in advanced materials. Comparison with more stable networks allowed better understanding of the observed shape memory properties.

The suggested approach is based on the quantitative end-functionalization of star-shaped PCL chains with reactive moieties in order to create a well-organized network. Two kinds of networks are formed using Diels-Alder cycloaddition between maleimide and either furan or anthracene. The functionalization strategy that has been chosen is highly efficient and versatile. Synthesis of end-capped star-shaped PCL with functional properties, all starting

from the same PCL precursor, offered relevant comparisons. Reversible (maleimide-furan) and irreversible (maleimide-anthracene) networks were compared to their composite counterpart, imparted with 3 wt% MWCNTs during preparation. High conductivity was obtained even outclassing some other PCL-based reported systems with the same 3 wt% of nanocyl7000 MWCNTs[345,346]. The use differential scanning calorimetry showed that the crystallization properties of both Diels-Alder systems were similar, regardless of the presence or absence of fillers, which preserves crystallization properties suitable to foresee shape memory applications. Furthermore, a Young modulus increase of around 70 % and ultimate stress reduction of around 50 % was obtained which is commonly observed even for other systems[347]. Still, all systems present excellent shape-memory properties with high fixity (> 99 %) and recovery (> 95 %) ratios which is in good agreement with literature over shape-memory materials based on crystallization as the fixing process, especially when the degree of crystallization is high, such as for PCL.

In-depth investigation of the electrical resistivity and Joule triggering effect was made possible by integrating to dynamic mechanical analysis the simultaneous measurement of the sample resistivity. Emphasis was placed on the maleimide-furan composite network (PCL-CAN_c), which has the benefit of being reversible and straightforward to reprocess and restructure. The interplay between the samples resistivities relative to their thermal expansion/contraction, to the experience of shape memory cycling or to resistive heating through Joule effect is deeply depicted. Our findings indicate that the electrical resistivity of the SMPC shows a non-linear temperature dependence, with a peak observed at the melting temperature. Still, the resistivity remained low enough to accommodate resistive heating throughout the intended temperature range. Electrical activation of the shape recovery through Joule effect remains particularly attractive to finely control the triggering of the shape recovery while avoiding overheating of the surrounding. Common issues associated with similar materials such as the increase in electrical resistance during deformation is overcome thanks to the homogeneous distribution of the MWCNTs. Precisely controlled heating and cooling rates lead to repeatability across samples, which is not always observed in other works. In this sense, our PCL-CAN_c electro-active shape-recovery system is proven suitable for

sequential recovery of multi-layered devices with fine control of multiple and progressive shape transitions. Consequently, a wide range of applications such as flexible actuation, multi-form deformations or displays, and even in bionic robotics can be considered. In addition, integration of Fe_3O_4 nanoparticles was considered and remote magnetic triggering of the shape memory behavior made possible. This work lays the foundation for remotely activated PCL-CAN with Fe_3O_4 nanoparticles, even if additional testing is required for optimization.

Reprocessing is easily obtained by heating at 125 °C followed by curing in a mold for further crosslinking. The material easily returns below the gel point upon heating, allowing for effortless reprocessing. This ability to be reprocessed in any shape is the primary advantage of this network. Furthermore, self-healing is also part of the benefit taken by the dynamic nature of the PCL-CAN. In this regard, having a SMC that can be heated via current is advantageous, as it allows for straightforward repair procedures to be carried out

Beside bulk materials, the formulation of foams using a solvent-free batch foaming process utilizing supercritical carbon dioxide ($scCO_2$) was investigated. The thermal control of the viscosity and network density provided by the furane-maleimide Diels-Alder addition is used as a tool to regulate the foaming process. Low-density foams exhibiting respectable shape memory properties while retaining good mechanical properties were hereby produced. Furthermore, these PCL shape memory foams are entirely reprocessable. PCL being known for its biocompatibility, these foams are foreseen for use in biomedical applications, such as self-deploying implants for vessel occlusion.

The findings presented in this thesis provide insight into behaviour and performance of the different prepared high-performance smart shape memory systems, with a peculiar emphasis on the maleimide-furan based composite which has the benefit of being reversible and straightforward to reprocess and restructure. In view of these highly valuable properties (i.e. self-healing, recyclability, conductive heating or remote magnetic heating) combined with the excellent shape memory properties and possible multi-stimuli activation, we are optimistic about its potential as a valuable platform for polymer composite applications.

Conclusions

To sum up, this thesis offers a thorough exploration aimed at gaining a deeper understanding of the properties and behavior of electro-active thermally-triggered recyclable SMPCs. Our objective is for this document to aid in decrypting performance and facilitating the conception and design of future applications requiring SMPCs.

Chapter V

Perspectives

Chapter V

Perspectives

In today's world, society tends to underestimate the significance of natural resources and raw materials, despite their crucial role in enabling the creation of various modern commoditiess. The manufacturing process for everyday products relies heavily on a stable and sustainable supply of essential raw materials. Additionally, the development of new products requires the use of hybrid materials to achieve specific objectives, such as construction of lightweight structures. Unfortunately, current manufacturing industry does not always prioritize the mandatory recyclability of these novel products or materials.

In the introduction, we discussed various interesting chemical strategies for incorporating reversible bonds into polymer materials, highlighting their potential benefits for shape memory systems. We then presented our approach to designing smart shape memory materials with a specific objective of integrating recycling capabilities. By adopting this approach, the focus is no longer on the ultimate recycling at the end of a product's life but instead prioritizes it right from the early stages of material development. The aim is to integrate recyclability as a fundamental attribute during the initial phases of material design, aligning with the principles of both material development and the upcoming market needs. Other benefits are derived from this strategy such as self-healing, which could be highly

desirable for many applications such as self-healing coatings, self-healing electrical devices, and implants in the medical field.

Within this context, an important area for potential further research related to our project lies in the exploration of the material's self-healing capabilities. Our investigations have shown that conventional heating can effectively restore damages in the shape memory composite thanks to the retro-Diels-Alder reaction. To further investigate this behaviour, the subsequent step would be to evaluate the effectiveness of self-healing achieved through resistive heating. It is crucial to consider that the electrical resistivity of the SMPC may be influenced by the dimensions and morphology of the cut. As a result, the path of the electric current may differ between the damaged region and the pristine portion. Consequently, the presence of a crack and its potential influence on the local cross-section could result in elevated temperatures in the adjacent areas during resistive heating. This localized heating has the potential to facilitate the self-healing process. Moreover, it would be valuable to conduct a more comprehensive analysis of the variations in resistivity as a function of deformation or temperature during resistive heating. The data extracted from these analyses can then be compared to previously documented studies found in the literature. Such development could also be implemented for the magnetic heating of the SMPC. In a similar way, the effectiveness of self-healing achieved through this process is still to be investigated. Such research could form the basis of future projects that may stem from the findings of this current study.

Another significant area of potential research involves investigating controlled and selective multi-shape recovery through alternative methods. One of them is to use localized near-infrared (NIR) lasers on specific regions of the sample to induce complex intermediate shapes and achieve multi-shape recovery. In comparison to heat-induced methods, the NIR-induced method offers distinct advantages, such as remote, localized, and non-contact control, without being affected by environmental interference. This system holds great potential for various applications, particularly in biomedicine, where precise and personalized shape memory behaviour is crucial. Furthermore, exploring alternative electrode placements could be considered to enable more intricate and selective multi-step shape recoveries. The

potential applications for these SMPCs are extensive and diverse. They encompass a wide range of fields, including aerospace for control surfaces, robotics for walking or swimming robots, as well as medical implants, among others.

Additionally, it is crucial to explore the processing techniques employed for the implementation of the material. The use of three-dimensional (3D) printing offers the advantage of creating precisely defined structures and sizes for materials tailored to meet specific requirements. Already, the integration of 3D printing technology with smart materials has given rise to an innovative concept called four-dimensional (4D) printing. This innovative approach goes beyond traditional 3D printing by incorporating the fourth dimension of 'time', opening up a multitude of potential applications across diverse fields. In 4D printing, objects can reshape or self-assemble over time through the strategic combination of rigid and expandable materials within a single 3D printed piece. This requires the use of two materials that behaves differently to a stimulus or in various environmental conditions. For example, water expandable segments can be 3D printed with another rigid material. In contact with water, the activation of the expandable material prompts a transformation of the entire structure, leading to a different overall shape, hence unlocking the 'time' dimension of 4D printing.

Building upon this concept, the combination of multi-step 3D printing with multi-step shape memory actuation holds great potential for the development of novel processing techniques. For instance, performing additional 3D printing steps on a previously printed component that is temporarily shaped in a specific configuration could expand the possibilities for intricate designs in high-end applications. This advancement in processing techniques could enable the creation of highly complex and customizable structures. Our previously described material holds great potential for such applications since its crosslinking can be triggered at any times, resulting in a 'first stage' temporarily fixed piece, later combined with further 3D printed segments, the whole piece resulting at the end in a single 3D network after crosslinking. This technique could hold great potential in soft robotics, flexible electronics, and other fields.

Perspectives

Amongst many, one of our aims for this manuscript is to help in predicting the performance, conceiving, and design future applications that use SMPCs. In this broader context, the experimental techniques and setups devised and advanced in this thesis have the potential to contribute to the development of more advanced devices. The examination, experimental tools, and findings presented in this thesis enhance our comprehension of the behaviour of electro-active thermally-triggered shape memory composites.

Bibliography

Bibliography

1. Zhang X, Chen L, Lim KH, et al. The Pathway to Intelligence: Using Stimuli-Responsive Materials as Building Blocks for Constructing Smart and Functional Systems. *Advanced Materials*. 2019;31(11). doi:10.1002/adma.201804540

2. Vernon LB. Process of Manufacturing Articles of Thermoplastc Syntheticresns. *United States Patent Office*. 1941;234:993.

3. Lorenzelli V. *Advances in Polymer Science. Vol. 54. Spectroscopy*. Vol 11.; 1984. doi:10.1016/0254-0584(84)90091-9

4. Zeng H, Leng J, Gu J, Sun H. A thermoviscoelastic model incorporated with uncoupled structural and stress relaxation mechanisms for amorphous shape memory polymers. *Mechanics of Materials*. 2018;124(February):18-25. doi:10.1016/j.mechmat.2018.05.010

5. Polymers M. Memory Polymers. Published online 2021:1-15.

6. Scalet G, Pandini S, Messori M, Toselli M, Auricchio F. A one-dimensional phenomenological model for the two-way shape-memory effect in semi-crystalline networks. *Polymer (Guildf)*. 2018;158(October):130-148. doi:10.1016/j.polymer.2018.10.027

7. Gao Y, Liu W, Zhu S. Reversible Shape Memory Polymer from Semicrystalline Poly(ethylene-co-vinyl acetate) with Dynamic Covalent Polymer Networks. *Macromolecules*. 2018;51(21):8956-8963. doi:10.1021/acs.macromol.8b01724

8. Yu L, Shahsavan H, Rivers G, Zhang C, Si P, Zhao B. Programmable 3D Shape Changes in Liquid Crystal Polymer Networks of Uniaxial Orientation. *Adv Funct Mater*. 2018;28(37). doi:10.1002/adfm.201802809

9. Biswas MC, Chakraborty S, Bhattacharjee A, Mohammed Z. 4D Printing of Shape Memory Materials for Textiles: Mechanism, Mathematical Modeling, and Challenges. *Adv Funct Mater*. 2021;31(19). doi:10.1002/adfm.202100257

10. Hu J, Meng H, Li G, Ibekwe SI. A review of stimuli-responsive polymers for smart textile applications. *Smart Mater Struct*. 2012;21(5). doi:10.1088/0964-1726/21/5/053001

11. Holman H, Kavarana MN, Rajab TK. Smart materials in cardiovascular implants: Shape memory alloys and shape memory polymers. *Artif Organs*. 2021;45(5):454-463. doi:https://doi.org/10.1111/aor.13851

12. Basak S. Redesigning the modern applied medical sciences and engineering with shape memory polymers. *Adv Compos Hybrid Mater*. 2021;4(2):223-234. doi:10.1007/s42114-021-00216-1

13. Pringpromsuk S, Xia H, Ni QQ. Thermal triggering on plasticized shape memory polyurethane actuators and its tubes target to biomedical applications. *Sens Actuators A Phys*. 2021;332:113164. doi:10.1016/j.sna.2021.113164

14. Sachyani Keneth E, Scalet G, Layani M, et al. Pre-Programmed Tri-Layer Electro-Thermal Actuators Composed of Shape Memory Polymer and Carbon Nanotubes. *Soft Robot*. 2019;7(2):123-129. doi:10.1089/soro.2018.0159

15. Patadiya J, Gawande A, Joshi G, Kandasubramanian B. Additive Manufacturing of Shape Memory Polymer Composites for Futuristic Technology. *Ind Eng Chem Res*. 2021;60(44):15885-15912. doi:10.1021/acs.iecr.1c03083

16. Jang JH, Hong SB, Kim JG, Goo NS, Yu WR. Accelerated Testing Method for Predicting Long-Term Properties of Carbon Fiber-Reinforced Shape Memory Polymer Composites in a Low Earth Orbit Environment. *Polymers* . 2021;13(10). doi:10.3390/polym13101628

17. Schönfeld D, Chalissery D, Wenz F, Specht M, Eberl C, Pretsch T. Actuating Shape Memory Polymer for Thermoresponsive Soft Robotic Gripper and Programmable Materials. *Molecules* . 2021;26(3). doi:10.3390/molecules26030522

18. Choi JG, Spinks GM, Kim SJ. Mode Shifting Shape Memory Polymer and Hydrogel Composite Fiber Actuators for Soft Robots. *Sens Actuators A Phys*. Published online 2022:113619. doi:https://doi.org/10.1016/j.sna.2022.113619

19. Herath M, Islam M, Epaarachchi J, Zhang F, Leng J. 4D Printed Shape Memory Polymer Composite Structures for Deployable Small Spacecrafts. Published online September 9, 2019. doi:10.1115/SMASIS2019-5583

20. Subash A, Kandasubramanian B. 4D printing of shape memory polymers. *Eur Polym J*. 2020;134:109771. doi:https://doi.org/10.1016/j.eurpolymj.2020.109771

21. Lendlein A, Jiang H, Jünger O, Langer R. Light-induced shape-memory polymers. *Nature*. 2005;434(7035):879-882. doi:10.1038/nature03496

22. Yakacki CM, Shandas R, Safranski D, Ortega AM, Sassaman K, Gall K. Strong, Tailored, Biocompatible Shape-Memory Polymer Networks. *Adv Funct Mater*. 2008;18(16):2428-2435. doi:https://doi.org/10.1002/adfm.200701049

23. Tian M, Gao W, Hu J, et al. Multidirectional Triple-Shape-Memory Polymer by Tunable Cross-linking and Crystallization. *ACS Appl Mater Interfaces*. 2020;12(5):6426-6435. doi:10.1021/acsami.9b19448

24. Li T, Li Y, Wang X, Li X, Sun J. Thermally and Near-Infrared Light-Induced Shape Memory Polymers Capable of Healing Mechanical Damage and Fatigued Shape Memory Function. *ACS Appl Mater Interfaces*. 2019;11(9):9470-9477. doi:10.1021/acsami.8b21970

25. Patel KK, Purohit R. Improved shape memory and mechanical properties of microwave-induced shape memory polymer/MWCNTs composites. *Mater Today Commun*. 2019;20:100579. doi:https://doi.org/10.1016/j.mtcomm.2019.100579

26. Basak S, Bandyopadhyay A. Solvent Responsive Shape Memory Polymers- Evolution, Current Status, and Future Outlook. *Macromol Chem Phys*. 2021;222(19):2100195. doi:https://doi.org/10.1002/macp.202100195

27. Li Y, Chen H, Liu D, Wang W, Liu Y, Zhou S. pH-Responsive Shape Memory Poly(ethylene glycol)–Poly(ε-caprolactone)-based Polyurethane/Cellulose Nanocrystals Nanocomposite. *ACS Appl Mater Interfaces*. 2015;7(23):12988-12999. doi:10.1021/acsami.5b02940

28. Fang Y, Ni Y, Leo SY, Taylor C, Basile V, Jiang P. Reconfigurable photonic crystals enabled by pressure-responsive shape-memory polymers. *Nat Commun*. 2015;6(1):7416. doi:10.1038/ncomms8416

29. Kong D, Li J, Guo A, Xiao X. High temperature electromagnetic shielding shape memory polymer composite. *Chemical Engineering Journal*. 2021;408:127365. doi:https://doi.org/10.1016/j.cej.2020.127365

30. Wen Z, Yang K, Raquez JM. A Review on Liquid Crystal Polymers in Free-Standing Reversible Shape Memory Materials. *Molecules* . 2020;25(5). doi:10.3390/molecules25051241

31. Lee KM, Wang DH, Koerner H, Vaia RA, Tan LS, White TJ. Enhancement of photogenerated mechanical force in azobenzene-functionalized polyimides. *Angewandte Chemie - International Edition*. 2012;51(17):4117-4121. doi:10.1002/anie.201200726

32. Lendlein A, Gould OEC. Reprogrammable recovery and actuation behaviour of shape-memory polymers. *Nat Rev Mater*. 2019;4(2):116-133. doi:10.1038/s41578-018-0078-8

33. Huang WM, Zhao Y, Wang CC, Ding Z. Thermo / chemo-responsive shape memory effect in polymers : a sketch of working mechanisms , fundamentals and optimization. Published online 2012. doi:10.1007/s10965-012-9952-z

34. Zhao Q, Behl M, Lendlein A. Shape-memory polymers with multiple transitions: Complex actively moving polymers. *Soft Matter*. 2013;9(6):1744-1755. doi:10.1039/c2sm27077c

35. Zhao Q, Qi HJ, Xie T. Recent progress in shape memory polymer: New behavior, enabling materials, and mechanistic understanding. *Prog Polym Sci*. 2015;49-50:79-120. doi:https://doi.org/10.1016/j.progpolymsci.2015.04.001

36. Ota S. Current status of irradiated heat-shrinkable tubing in Japan. *Radiation Physics and Chemistry (1977)*. 1981;18(1):81-87. doi:https://doi.org/10.1016/0146-5724(81)90066-2

37. Palmaz JC. Intravascular Stents in the Last and the Next 10 Years. *Journal of Endovascular Therapy*. 2004;11(6_suppl):II-200-II-206. doi:10.1177/15266028040110S621

38. Xie T. Recent advances in polymer shape memory. *Polymer (Guildf)*. 2011;52(22):4985-5000. doi:https://doi.org/10.1016/j.polymer.2011.08.003

39. Zhang X, Zhu C, Xu B, Qin L, Wei J, Yu Y. Rapid, Localized, and Athermal Shape Memory Performance Triggered by Photoswitchable Glass Transition Temperature. *ACS Appl Mater Interfaces*. 2019;11(49):46212-46218. doi:10.1021/acsami.9b17271

40. Chatani S, Kloxin CJ, Bowman CN. The power of light in polymer science: photochemical processes to manipulate polymer formation, structure, and properties. *Polym Chem*. 2014;5(7):2187-2201. doi:10.1039/C3PY01334K

41. Scott TF, Draughon RB, Bowman CN. Actuation in Crosslinked Polymers via Photoinduced Stress Relaxation. *Advanced Materials*. 2006;18(16):2128-2132. doi:https://doi.org/10.1002/adma.200600379

42. Jiang HY, Kelch S, Lendlein A. Polymers Move in Response to Light. *Advanced Materials*. 2006;18(11):1471-1475. doi:https://doi.org/10.1002/adma.200502266

43. Zare M, Prabhakaran MP, Parvin N, Ramakrishna S. Thermally-induced two-way shape memory polymers: Mechanisms, structures, and applications. *Chemical Engineering Journal*. 2019;374:706-720. doi:https://doi.org/10.1016/j.cej.2019.05.167

44. Chung T, Romo-uribe A, Mather PT. Two-Way Reversible Shape Memory in a Semicrystalline Network. Published online 2008:184-192.

45. Defize T, Riva R, Raquez JM, Dubois P, Jérôme C, Alexandre M. Thermoreversibly crosslinked poly(ε-caprolactone) as recyclable shape-memory polymer network. *Macromol Rapid Commun*. 2011;32(16):1264-1269. doi:10.1002/marc.201100250

46. Behl M, Kratz K, Zotzmann J, Nöchel U, Lendlein A. Reversible Bidirectional Shape-Memory Polymers. *Advanced Materials*. 2013;25(32):4466-4469. doi:https://doi.org/10.1002/adma.201300880

47. Finkelmann H, Kock HJ, Rehage G. Investigations on liquid crystalline polysiloxanes 3. Liquid crystalline elastomers — a new type of liquid crystalline material. *Die Makromolekulare*

Chemie, Rapid Communications. 1981;2(4):317-322. doi:https://doi.org/10.1002/marc.1981.030020413

48. C. H. Legge FJD and GRM. Memory Effects in liquid crystal elastomers. *J Phys II France 1*. Published online 1991:1253-1261. doi:https://doi.org/10.1051/jp2:1991131

49. Ouchi Y, Feller MB, Moses T, Shen YR. Surface memory effect at the liquid-crystal--polymer interface. *Phys Rev Lett*. 1992;68(20):3040-3043. doi:10.1103/PhysRevLett.68.3040

50. White TJ, Broer DJ. Programmable and adaptive mechanics with liquid crystal polymer networks and elastomers. *Nat Mater*. 2015;14(11):1087-1098. doi:10.1038/nmat4433

51. Marotta A, Lama GC, Ambrogi V, Cerruti P, Giamberini M, Gentile G. Shape memory behavior of liquid-crystalline elastomer/graphene oxide nanocomposites. *Compos Sci Technol*. 2018;159:251-258. doi:https://doi.org/10.1016/j.compscitech.2018.03.002

52. Li Y, Rios O, Keum JK, Chen J, Kessler MR. Photoresponsive Liquid Crystalline Epoxy Networks with Shape Memory Behavior and Dynamic Ester Bonds. *ACS Appl Mater Interfaces*. 2016;8(24):15750-15757. doi:10.1021/acsami.6b04374

53. Wu Y, Hu J, Han J, et al. Two-way shape memory polymer with "switch–spring" composition by interpenetrating polymer network. *J Mater Chem A Mater*. 2014;2(44):18816-18822. doi:10.1039/C4TA03640A

54. Chung T, Romo-Uribe A, Mather PT. Two-Way Reversible Shape Memory in a Semicrystalline Network. *Macromolecules*. 2008;41(1):184-192. doi:10.1021/ma071517z

55. Ahir SV, Tajbakhsh AR, Terentjev EM. Self-Assembled Shape-Memory Fibers of Triblock Liquid-Crystal Polymers. *Adv Funct Mater*. 2006;16(4):556-560. doi:https://doi.org/10.1002/adfm.200500692

56. Fan LF, Rong MZ, Zhang MQ, Chen XD. A Facile Approach Toward Scalable Fabrication of Reversible Shape-Memory Polymers with Bonded Elastomer Microphases as Internal Stress Provider. *Macromol Rapid Commun*. 2017;38(16):1700124. doi:https://doi.org/10.1002/marc.201700124

57. Silverstein MS. Interpenetrating polymer networks: So happy together? *Polymer (Guildf)*. 2020;207:122929. doi:https://doi.org/10.1016/j.polymer.2020.122929

58. Behl M, Zhao Q, Lendlein A. Glucose-responsive shape-memory cryogels. *J Mater Res*. 2020;35(18):2396-2404. doi:10.1557/jmr.2020.204

59. Chen S, Hu J, Zhuo H, Zhu Y. Two-way shape memory effect in polymer laminates. *Mater Lett*. 2008;62(25):4088-4090. doi:https://doi.org/10.1016/j.matlet.2008.05.073

60. Chen S, Hu J, Zhuo H. Properties and mechanism of two-way shape memory polyurethane composites. *Compos Sci Technol*. 2010;70(10):1437-1443. doi:https://doi.org/10.1016/j.compscitech.2010.01.017

61. Kang TH, Lee JM, Yu WR, Youk JH, Ryu HW. Two-way actuation behavior of shape memory polymer/elastomer core/shell composites. *Smart Mater Struct*. 2012;21(3):35028. doi:10.1088/0964-1726/21/3/035028

62. Zhang H, Wang H, Zhong W, Du Q. A novel type of shape memory polymer blend and the shape memory mechanism. *Polymer (Guildf)*. 2009;50(6):1596-1601. doi:https://doi.org/10.1016/j.polymer.2009.01.011

63. Peng B, Yang Y, Ju T, Cavicchi KA. Fused Filament Fabrication 4D Printing of a Highly Extensible, Self-Healing, Shape Memory Elastomer Based on Thermoplastic Polymer Blends. *ACS Appl Mater Interfaces*. 2021;13(11):12777-12788. doi:10.1021/acsami.0c18618

64. Wang J, Zhang H, Lei J, Wu M, Liu W, Qu JP. Stress-Free Two-Way Shape-Memory Mechanism of a Semicrystalline Network with a Broad Melting Transition. *Macromolecules*. 2022;55(22):10113-10123. doi:10.1021/acs.macromol.2c01971

65. Dolog R, Weiss RA. Shape Memory Behavior of a Polyethylene-Based Carboxylate Ionomer. *Macromolecules*. 2013;46(19):7845-7852. doi:10.1021/ma401631j

66. Xia Y, He Y, Zhang F, Liu Y, Leng J. A Review of Shape Memory Polymers and Composites: Mechanisms, Materials, and Applications. *Advanced Materials*. 2021;33(6). doi:10.1002/adma.202000713

67. Podgórski M, Wang C, Bowman CN. Multiple shape memory polymers based on laminates formed from thiol-click chemistry based polymerizations. *Soft Matter*. 2015;11(34):6852-6858. doi:10.1039/C5SM01260K

68. Kloxin CJ, Scott TF, Adzima BJ, Bowman CN. Covalent Adaptable Networks (CANs): A Unique Paradigm in Cross-Linked Polymers. *Macromolecules*. 2010;43(6):2643-2653. doi:10.1021/ma902596s

69. Peng S, Sun Y, Ma C, Duan G, Liu Z, Ma C. Recent advances in dynamic covalent bond-based shape memory polymers. *E-Polymers*. 2022;22(1):285-300. doi:10.1515/epoly-2022-0032

70. Peng S, Sun Y, Ma C, Duan G, Liu Z, Ma C. Recent advances in dynamic covalent bond-based shape memory polymers. 2022;22(1):285-300. doi:doi:10.1515/epoly-2022-0032

71. Zou W, Dong J, Luo Y, Zhao Q, Xie T. Dynamic Covalent Polymer Networks: from Old Chemistry to Modern Day Innovations. *Advanced Materials*. 2017;29(14). doi:10.1002/adma.201606100

72. Zhang B, Digby ZA, Flum JA, Foster EM, Sparks JL, Konkolewicz D. Self-healing, malleable and creep limiting materials using both supramolecular and reversible covalent linkages. *Polym Chem*. 2015;6(42):7368-7372. doi:10.1039/C5PY01214G

73. Yang L, Tan X, Wang Z, Zhang X. Supramolecular Polymers: Historical Development, Preparation, Characterization, and Functions. *Chem Rev*. 2015;115(15):7196-7239. doi:10.1021/cr500633b

74. Aida T, Meijer EW, Stupp SI. Functional Supramolecular Polymers. *Science (1979)*. 2012;335(6070):813-817. doi:10.1126/science.1205962

75. Liu T, Zhao B, Zhang J. Recent development of repairable, malleable and recyclable thermosetting polymers through dynamic transesterification. *Polymer (Guildf)*. 2020;194:122392. doi:https://doi.org/10.1016/j.polymer.2020.122392

76. Denissen W, Winne JM, du Prez FE. Vitrimers: permanent organic networks with glass-like fluidity. *Chem Sci*. 2016;7(1):30-38. doi:10.1039/C5SC02223A

77. Capelot M, Unterlass MM, Tournilhac F, Leibler L. Catalytic Control of the Vitrimer Glass Transition. *ACS Macro Lett*. 2012;1(7):789-792. doi:10.1021/mz300239f

78. Fortman DJ, Brutman JP, Cramer CJ, Hillmyer MA, Dichtel WR. Mechanically Activated, Catalyst-Free Polyhydroxyurethane Vitrimers. *J Am Chem Soc*. 2015;137(44):14019-14022. doi:10.1021/jacs.5b08084

79. Wong KF, Eckert CA. Solution thermodynamics and kinetic solvent effects on a Diels-Alder reaction. *Transactions of the Faraday Society*. 1970;66(0):2313-2319. doi:10.1039/TF9706602313

80. Gandini A. The furan/maleimide Diels–Alder reaction: A versatile click–unclick tool in macromolecular synthesis. *Prog Polym Sci*. 2013;38(1):1-29. doi:https://doi.org/10.1016/j.progpolymsci.2012.04.002

81. Fang Y, Du X, Jiang Y, et al. Thermal-Driven Self-Healing and Recyclable Waterborne Polyurethane Films Based on Reversible Covalent Interaction. *ACS Sustain Chem Eng*. 2018;6(11):14490-14500. doi:10.1021/acssuschemeng.8b03151

82. Zhang G, Zhao Q, Yang L, Zou W, Xi X, Xie T. Exploring Dynamic Equilibrium of Diels–Alder Reaction for Solid State Plasticity in Remoldable Shape Memory Polymer Network. *ACS Macro Lett*. 2016;5(7):805-808. doi:10.1021/acsmacrolett.6b00357

83. Han G, Nie J, Zhang H. Facile preparation of recyclable photodeformable azobenzene polymer fibers with chemically crosslinked networks. *Polym Chem*. 2016;7(32):5088-5092. doi:10.1039/C6PY01100D

84. Mondal P, Behera PK, Voit B, Böhme F, Singha NK. Tailor-Made Functional Polymethacrylates with Dual Characteristics of Self-Healing and Shape-Memory Based on Dynamic Covalent Chemistry. *Macromol Mater Eng*. 2020;305(6):2000142. doi:https://doi.org/10.1002/mame.202000142

85. Cai C, Zhang Y, Li M, et al. Multiple-responsive shape memory polyacrylonitrile/graphene nanocomposites with rapid self-healing and recycling properties. *RSC Adv*. 2018;8(3):1225-1231. doi:10.1039/C7RA11484B

86. Cao Y, Zhang J, Zhang D, et al. A novel shape memory-assisted and thermo-induced self-healing boron nitride/epoxy composites based on Diels–Alder reaction. *J Mater Sci*. 2020;55(25):11325-11338. doi:10.1007/s10853-020-04842-w

87. Nguyen LT, Pham HQ, Thi Phung DT, et al. Macromolecular design of a reversibly crosslinked shape-memory material with thermo-healability. *Polymer (Guildf)*. 2020;188:122144. doi:https://doi.org/10.1016/j.polymer.2019.122144

88. Raquez JM, Vanderstappen S, Meyer F, et al. Design of cross-linked semicrystalline poly(ε-caprolactone)-based networks with one-way and two-way shape-memory properties through Diels-Alder reactions. *Chemistry - A European Journal*. 2011;17(36):10135-10143. doi:10.1002/chem.201100496

89. Defize T, Riva R, Raquez JM, Dubois P, Jérôme C, Alexandre M. Thermoreversibly crosslinked poly(ε-caprolactone) as recyclable shape-memory polymer network. *Macromol Rapid Commun*. 2011;32(16):1264-1269. doi:10.1002/marc.201100250

90. Houk KN, Liu F, Yang Z, Seeman JI. Evolution of the Diels–Alder Reaction Mechanism since the 1930s: Woodward, Houk with Woodward, and the Influence of Computational Chemistry on Understanding Cycloadditions. *Angewandte Chemie International Edition*. 2021;60(23):12660-12681. doi:https://doi.org/10.1002/anie.202001654

91. Zhang J, Niu Y, Huang C, et al. Self-healable and recyclable triple-shape PPDO–PTMEG co-network constructed through thermoreversible Diels–Alder reaction. *Polym Chem*. 2012;3(6):1390-1393. doi:10.1039/C2PY20028G

92. Stevens MP, Jenkins AD. Crosslinking of polystyrene via pendant maleimide groups. *Journal of Polymer Science: Polymer Chemistry Edition*. 1979;17(11):3675-3685. doi:https://doi.org/10.1002/pol.1979.170171123

93. Yamashiro M, Inoue K, Iji M. Recyclable Shape-memory and Mechanical Strength of Poly(lactic acid) Compounds Cross-linked by Thermo-reversible Diels-Alder Reaction. *Polym J*. 2008;40(7):657-662. doi:10.1295/polymj.PJ2008042

94. Rivero G, Nguyen LTT, Hillewaere XKD, du Prez FE. One-Pot Thermo-Remendable Shape Memory Polyurethanes. *Macromolecules*. 2014;47(6):2010-2018. doi:10.1021/ma402471c

95. Liu YL, Chen YW. Thermally Reversible Cross-Linked Polyamides with High Toughness and Self-Repairing Ability from Maleimide- and Furan-Functionalized Aromatic Polyamides. *Macromol Chem Phys*. 2007;208(2):224-232. doi:https://doi.org/10.1002/macp.200600445

96. Toncelli C, de Reus DC, Picchioni F, Broekhuis AA. Properties of Reversible Diels–Alder Furan/Maleimide Polymer Networks as Function of Crosslink Density. *Macromol Chem Phys*. 2012;213(2):157-165. doi:https://doi.org/10.1002/macp.201100405

97. Polgar LM, van Duin M, Broekhuis AA, Picchioni F. Use of Diels–Alder Chemistry for Thermoreversible Cross-Linking of Rubbers: The Next Step toward Recycling of Rubber Products? *Macromolecules*. 2015;48(19):7096-7105. doi:10.1021/acs.macromol.5b01422

98. Yang H, Zheng X, Sun Y, Yu K, He M, Guo Y. A molecular dynamics study on the surface welding and shape memory behaviors of Diels-Alder network. *Comput Mater Sci*. 2017;139:48-55. doi:https://doi.org/10.1016/j.commatsci.2017.07.029

99. Zheng K, Tian Y, Fan M, Zhang J, Cheng J. Recyclable, shape-memory, and self-healing soy oil-based polyurethane crosslinked by a thermoreversible Diels–Alder reaction. *J Appl Polym Sci*. 2018;135(13):46049. doi:https://doi.org/10.1002/app.46049

100. Heo Y, Sodano HA. Self-Healing Polyurethanes with Shape Recovery. *Adv Funct Mater*. 2014;24(33):5261-5268. doi:https://doi.org/10.1002/adfm.201400299

101. Orozco F, Kaveh M, Santosa DS, et al. Electroactive Self-Healing Shape Memory Polymer Composites Based on Diels–Alder Chemistry. *ACS Appl Polym Mater*. 2021;3(12):6147-6156. doi:10.1021/acsapm.1c00999

102. Braunecker WA, Matyjaszewski K. Controlled/living radical polymerization: Features, developments, and perspectives. *Prog Polym Sci*. 2007;32(1):93-146. doi:https://doi.org/10.1016/j.progpolymsci.2006.11.002

103. Yuan C, Rong MZ, Zhang MQ, Zhang ZP, Yuan YC. Self-healing of polymers via synchronous covalent bond fission/radical recombination. *Chemistry of Materials*. 2011;23(22):5076-5081. doi:10.1021/cm202635w

104. Higaki Y, Otsuka H, Takahara A. A Thermodynamic Polymer Cross-Linking System Based on Radically Exchangeable Covalent Bonds. *Macromolecules*. 2006;39(6):2121-2125. doi:10.1021/ma052093g

105. Zhang ZP, Rong MZ, Zhang MQ, Yuan C. Alkoxyamine with reduced homolysis temperature and its application in repeated autonomous self-healing of stiff polymers. *Polym Chem*. 2013;4(17):4648-4654. doi:10.1039/C3PY00679D

106. Amamoto Y, Kikuchi M, Masunaga H, Sasaki S, Otsuka H, Takahara A. Reorganizable Chemical Polymer Gels Based on Dynamic Covalent Exchange and Controlled Monomer Insertion. *Macromolecules*. 2009;42(22):8733-8738. doi:10.1021/ma901746n

107. Fan LF, Rong MZ, Zhang MQ, Chen XD. Dynamic reversible bonds enable external stress-free two-way shape memory effect of a polymer network and the interrelated intrinsic self-healability of wider crack and recyclability. *J Mater Chem A Mater*. 2018;6(33):16053-16063. doi:10.1039/C8TA05751F

108. Fan LF, Rong MZ, Zhang MQ, Chen XD. Repeated Intrinsic Self-Healing of Wider Cracks in Polymer via Dynamic Reversible Covalent Bonding Molecularly Combined with a Two-Way Shape Memory Effect. *ACS Appl Mater Interfaces*. 2018;10(44):38538-38546. doi:10.1021/acsami.8b15636

109. Lei Y, Fu X, Jiang L, Liu Z, Lei J. Oxime–Urethane Structure-Based Dynamically Crosslinked Polyurethane with Robust Reprocessing Properties. *Macromol Rapid Commun*. 2022;43(13):2100781. doi:https://doi.org/10.1002/marc.202100781

110. Wang J, Lin X, Wang R, Lu Y, Zhang L. Self-Healing, Photothermal-Responsive, and Shape Memory Polyurethanes for Enhanced Mechanical Properties of 3D/4D Printed Objects. *Adv Funct Mater*. 2022;n/a(n/a):2211579. doi:https://doi.org/10.1002/adfm.202211579

111. Liu WX, Zhang C, Zhang H, Zhao N, Yu ZX, Xu J. Oxime-Based and Catalyst-Free Dynamic Covalent Polyurethanes. *J Am Chem Soc*. 2017;139(25):8678-8684. doi:10.1021/jacs.7b03967

112. Zhong K, Guan Q, Sun W, et al. Hot-Melt Adhesive Based on Dynamic Oxime–Carbamate Bonds. *Ind Eng Chem Res*. 2021;60(19):6925-6931. doi:10.1021/acs.iecr.1c00768

113. Cai Y, Li C, Yang Y, Li H, Wang Y, Zhang Q. Self-Healable and Reprocessable Cross-Linked Poly(urea-urethane) Elastomers with High Mechanical Performance Based on Dynamic Oxime–Carbamate Bonds. *Ind Eng Chem Res*. 2021;60(37):13585-13593. doi:10.1021/acs.iecr.1c02245

114. Otera Junzo. Transesterification. *Chem Rev*. 1993;93(4):1449-1470. doi:10.1021/cr00020a004

115. Capelot M, Montarnal D, Tournilhac F, Leibler L. Metal-Catalyzed Transesterification for Healing and Assembling of Thermosets. *J Am Chem Soc*. 2012;134(18):7664-7667. doi:10.1021/ja302894k

116. Montarnal D, Capelot M, Tournilhac F, Leibler L. Silica-Like Malleable Materials from Permanent Organic Networks. *Science (1979)*. 2011;334(6058):965-968. doi:10.1126/science.1212648

117. Niu X, Wang F, Li X, Zhang R, Wu Q, Sun P. Using Zn2+ Ionomer To Catalyze Transesterification Reaction in Epoxy Vitrimer. *Ind Eng Chem Res*. 2019;58(14):5698-5706. doi:10.1021/acs.iecr.9b00090

118. Chen M, Zhou L, Wu Y, Zhao X, Zhang Y. Rapid Stress Relaxation and Moderate Temperature of Malleability Enabled by the Synergy of Disulfide Metathesis and Carboxylate Transesterification in Epoxy Vitrimers. *ACS Macro Lett*. 2019;8(3):255-260. doi:10.1021/acsmacrolett.9b00015

119. Gablier A, Saed MO, Terentjev EM. Rates of transesterification in epoxy–thiol vitrimers. *Soft Matter*. 2020;16(22):5195-5202. doi:10.1039/D0SM00742K

120. Isogai T, Hayashi M. Critical Effects of Branch Numbers at the Cross-Link Point on the Relaxation Behaviors of Transesterification Vitrimers. *Macromolecules*. 2022;55(15):6661-6670. doi:10.1021/acs.macromol.2c00560

121. Altuna FI, Hoppe CE, Williams RJJ. Epoxy vitrimers: The effect of transesterification reactions on the network structure. *Polymers (Basel)*. 2018;10(1). doi:10.3390/polym10010043

122. Liu T, Zhao B, Zhang J. Recent development of repairable, malleable and recyclable thermosetting polymers through dynamic transesterification. *Polymer (Guildf)*. 2020;194:122392. doi:https://doi.org/10.1016/j.polymer.2020.122392

123. Niu X, Wang F, Kui X, et al. Dual Cross-linked Vinyl Vitrimer with Efficient Self-Catalysis Achieving Triple-Shape-Memory Properties. *Macromol Rapid Commun*. 2019;40(19):1900313. doi:https://doi.org/10.1002/marc.201900313

124. Miao W, Zou W, Luo Y, Zheng N, Zhao Q, Xie T. Structural tuning of polycaprolactone based thermadapt shape memory polymer. *Polym Chem*. 2020;11(7):1369-1374. doi:10.1039/C9PY01891C

125. Feng Z, Hu J, Zuo H, et al. Photothermal-Induced Self-Healable and Reconfigurable Shape Memory Bio-Based Elastomer with Recyclable Ability. *ACS Appl Mater Interfaces*. 2019;11(1):1469-1479. doi:10.1021/acsami.8b18002

126. Yang X, Guo L, Xu X, Shang S, Liu H. A fully bio-based epoxy vitrimer: Self-healing, triple-shape memory and reprocessing triggered by dynamic covalent bond exchange. *Mater Des*. 2020;186:108248. doi:https://doi.org/10.1016/j.matdes.2019.108248

127. Yang Z, Wang Q, Wang T. Dual-Triggered and Thermally Reconfigurable Shape Memory Graphene-Vitrimer Composites. *ACS Appl Mater Interfaces*. 2016;8(33):21691-21699. doi:10.1021/acsami.6b07403

128. Ning L, Yuan L, Liang G, Gu A. Thermally resistant and strong remoldable triple-shape memory thermosets based on bismaleimide with transesterification. *J Mater Sci*. 2021;56(4):3623-3637. doi:10.1007/s10853-020-05469-7

129. Erice A, Ruiz de Luzuriaga A, Matxain JM, et al. Reprocessable and recyclable crosslinked poly(urea-urethane)s based on dynamic amine/urea exchange. *Polymer (Guildf)*. 2018;145:127-136. doi:https://doi.org/10.1016/j.polymer.2018.04.076

130. Denissen W, de Baere I, van Paepegem W, Leibler L, Winne J, du Prez FE. Vinylogous Urea Vitrimers and Their Application in Fiber Reinforced Composites. *Macromolecules*. 2018;51(5):2054-2064. doi:10.1021/acs.macromol.7b02407

131. Denissen W, Rivero G, Nicolaÿ R, Leibler L, Winne JM, du Prez FE. Vinylogous Urethane Vitrimers. *Adv Funct Mater*. 2015;25(16):2451-2457. doi:https://doi.org/10.1002/adfm.201404553

132. Engelen S, Wróblewska AA, de Bruycker K, et al. Sustainable design of vanillin-based vitrimers using vinylogous urethane chemistry. *Polym Chem*. 2022;13(18):2665-2673. doi:10.1039/D2PY00351A

133. Hamzehlou S, Ruipérez F. Computational study of the transamination reaction in vinylogous acyls: Paving the way to design vitrimers with controlled exchange kinetics. *Journal of Polymer Science*. 2022;60(13):1988-1999. doi:https://doi.org/10.1002/pol.20220099

134. Holloway JO, Taplan C, du Prez FE. Combining vinylogous urethane and β-amino ester chemistry for dynamic material design. *Polym Chem*. 2022;13(14):2008-2018. doi:10.1039/D2PY00026A

135. van Lijsebetten F, de Bruycker K, Winne JM, du Prez FE. Masked Primary Amines for a Controlled Plastic Flow of Vitrimers. *ACS Macro Lett*. 2022;11(7):919-924. doi:10.1021/acsmacrolett.2c00255

136. van Lijsebetten F, Debsharma T, Winne JM, du Prez FE. A Highly Dynamic Covalent Polymer Network without Creep: Mission Impossible? *Angewandte Chemie International Edition*. 2022;n/a(n/a):e202210405. doi:https://doi.org/10.1002/anie.202210405

137. Weerathaworn S, Abetz V. Tailor-Made Vinylogous Urethane Vitrimers Based on Binary and Ternary Block and Random Copolymers: An Approach toward Reprocessable Materials. *Macromol Chem Phys*. 2022;n/a(n/a):2200248. doi:https://doi.org/10.1002/macp.202200248

138. Bai L, Zheng J. Robust, reprocessable and shape-memory vinylogous urethane vitrimer composites enhanced by sacrificial and self-catalysis Zn(II)–ligand bonds. *Compos Sci Technol*. 2020;190:108062. doi:https://doi.org/10.1016/j.compscitech.2020.108062

139. Liu Z, Zhang C, Shi Z, Yin J, Tian M. Tailoring vinylogous urethane chemistry for the cross-linked polybutadiene: Wide freedom design, multiple recycling methods, good shape memory behavior. *Polymer (Guildf)*. 2018;148:202-210. doi:https://doi.org/10.1016/j.polymer.2018.06.042

140. Zhu Y, Gao F, Zhong J, Shen L, Lin Y. Renewable castor oil and DL-limonene derived fully bio-based vinylogous urethane vitrimers. *Eur Polym J*. 2020;135:109865. doi:https://doi.org/10.1016/j.eurpolymj.2020.109865

141. Chen F, Cheng Q, Gao F, et al. The effect of latent plasticity on the shape recovery of a shape memory vitrimer. *Eur Polym J*. 2021;147:110304. doi:https://doi.org/10.1016/j.eurpolymj.2021.110304

142. Boucher D, Madsen J, Yu L, et al. Polystyrene Hybrid-Vitrimer Based on the Hemiacetal Ester Exchange Reaction. *Macromolecules*. 2021;54(14):6772-6779. doi:10.1021/acs.macromol.1c00948

143. Hendriks B, Waelkens J, Winne JM, du Prez FE. Poly(thioether) Vitrimers via Transalkylation of Trialkylsulfonium Salts. *ACS Macro Lett*. 2017;6(9):930-934. doi:10.1021/acsmacrolett.7b00494

144. Dhers S, Vantomme G, Avérous L. A fully bio-based polyimine vitrimer derived from fructose. *Green Chemistry*. 2019;21(7):1596-1601. doi:10.1039/C9GC00540D

145. Kar GP, Saed MO, Terentjev EM. Scalable upcycling of thermoplastic polyolefins into vitrimers through transesterification. *J Mater Chem A Mater*. 2020;8(45):24137-24147. doi:10.1039/D0TA07339C

146. Yang Y, Song Q, Li C, et al. Reprocessable Epoxy Resins Based on Hydroxy-Thioester and Thiol-Thioester Dual Exchanges. *Ind Eng Chem Res*. 2020;59(11):4936-4944. doi:10.1021/acs.iecr.9b06520

147. Worrell BT, Mavila S, Wang C, et al. A user's guide to the thiol-thioester exchange in organic media: scope, limitations, and applications in material science. *Polym Chem*. 2018;9(36):4523-4534. doi:10.1039/C8PY01031E

148. Wang C, Mavila S, Worrell BT, Xi W, Goldman TM, Bowman CN. Productive Exchange of Thiols and Thioesters to Form Dynamic Polythioester-Based Polymers. *ACS Macro Lett*. 2018;7(11):1312-1316. doi:10.1021/acsmacrolett.8b00611

149. Yang Y, Song Q, Li C, et al. Reprocessable Epoxy Resins Based on Hydroxy-Thioester and Thiol-Thioester Dual Exchanges. *Ind Eng Chem Res*. 2020;59(11):4936-4944. doi:10.1021/acs.iecr.9b06520

150. Vidil T, Llevot A. Fully Biobased Vitrimers: Future Direction toward Sustainable Cross-Linked Polymers. *Macromol Chem Phys*. 2022;223(13):2100494. doi:https://doi.org/10.1002/macp.202100494

151. Fortman DJ, Brutman JP, Cramer CJ, Hillmyer MA, Dichtel WR. Mechanically Activated, Catalyst-Free Polyhydroxyurethane Vitrimers. *J Am Chem Soc*. 2015;137(44):14019-14022. doi:10.1021/jacs.5b08084

152. Zheng N, Fang Z, Zou W, Zhao Q, Xie T. Thermoset Shape-Memory Polyurethane with Intrinsic Plasticity Enabled by Transcarbamoylation. *Angewandte Chemie - International Edition*. 2016;55(38):11421-11425. doi:10.1002/anie.201602847

153. Brutman JP, Fortman DJ, de Hoe GX, Dichtel WR, Hillmyer MA. Mechanistic Study of Stress Relaxation in Urethane-Containing Polymer Networks. *J Phys Chem B*. 2019;123(6):1432-1441. doi:10.1021/acs.jpcb.8b11489

154. Elizalde F, Aguirresarobe RH, Gonzalez A, Sardon H. Dynamic polyurethane thermosets: tuning associative/dissociative behavior by catalyst selection. *Polym Chem*. 2020;11(33):5386-5396. doi:10.1039/D0PY00842G

155. Zhang J, Zhang C, Song F, et al. Castor-oil-based, robust, self-healing, shape memory, and reprocessable polymers enabled by dynamic hindered urea bonds and hydrogen bonds. *Chemical Engineering Journal*. 2022;429:131848. doi:https://doi.org/10.1016/j.cej.2021.131848

156. Gebert PH, Batich CD, Tanner DB, Herr SL. Polyaniline via schiff base chemistry. *Synth Met*. 1989;29(1):371-376. doi:https://doi.org/10.1016/0379-6779(89)90320-2

157. Belowich ME, Stoddart JF. Dynamic imine chemistry. *Chem Soc Rev*. 2012;41(6):2003-2024. doi:10.1039/C2CS15305J

158. Zheng H, Wang S, Lu C, et al. Thermal, Near-Infrared Light, and Amine Solvent Triple-Responsive Recyclable Imine-Type Vitrimer: Shape Memory, Accelerated Photohealing/Welding, and Destructing Behaviors. *Ind Eng Chem Res*. 2020;59(50):21768-21778. doi:10.1021/acs.iecr.0c04257

159. Zhang Y, Tao L, Li S, Wei Y. Synthesis of Multiresponsive and Dynamic Chitosan-Based Hydrogels for Controlled Release of Bioactive Molecules. *Biomacromolecules*. 2011;12(8):2894-2901. doi:10.1021/bm200423f

160. Chao A, Negulescu I, Zhang D. Dynamic Covalent Polymer Networks Based on Degenerative Imine Bond Exchange: Tuning the Malleability and Self-Healing Properties by Solvent. *Macromolecules*. 2016;49(17):6277-6284. doi:10.1021/acs.macromol.6b01443

161. Fukuda K, Shimoda M, Sukegawa M, Nobori T, Lehn JM. Doubly degradable dynamers: dynamic covalent polymers based on reversible imine connections and biodegradable polyester units. *Green Chemistry*. 2012;14(10):2907-2911. doi:10.1039/C2GC35875A

162. Zheng H, Wang S, Lu C, et al. Thermal, Near-Infrared Light, and Amine Solvent Triple-Responsive Recyclable Imine-Type Vitrimer: Shape Memory, Accelerated Photohealing/Welding, and Destructing Behaviors. *Ind Eng Chem Res*. 2020;59(50):21768-21778. doi:10.1021/acs.iecr.0c04257

163. Liang K, Zhang G, Zhao J, Shi L, Cheng J, Zhang J. Malleable, Recyclable, and Robust Poly(amide–imine) Vitrimers Prepared through a Green Polymerization Process. *ACS Sustain Chem Eng*. 2021;9(16):5673-5683. doi:10.1021/acssuschemeng.1c00626

164. Zheng H, Wang S, Lu C, et al. Thermal, Near-Infrared Light, and Amine Solvent Triple-Responsive Recyclable Imine-Type Vitrimer: Shape Memory, Accelerated Photohealing/Welding, and Destructing Behaviors. *Ind Eng Chem Res*. 2020;59(50):21768-21778. doi:10.1021/acs.iecr.0c04257

165. Osthoff RC, Bueche AM, Grubb WT. Chemical Stress-Relaxation of Polydimethylsiloxane Elastomers1. *J Am Chem Soc*. 1954;76(18):4659-4663. doi:10.1021/ja01647a052

166. Zheng P, McCarthy TJ. A Surprise from 1954: Siloxane Equilibration Is a Simple, Robust, and Obvious Polymer Self-Healing Mechanism. *J Am Chem Soc*. 2012;134(4):2024-2027. doi:10.1021/ja2113257

167. Debsharma T, Amfilochiou V, Wróblewska AA, De Baere I, Van Paepegem W, Du Prez FE. Fast Dynamic Siloxane Exchange Mechanism for Reshapable Vitrimer Composites. *J Am Chem Soc*. 2022;144(27):12280-12289. doi:10.1021/jacs.2c03518

168. Tobolsky A v, Prettyman IB, Dillon JH. Stress Relaxation of Natural and Synthetic Rubber Stocks. *Rubber Chemistry and Technology*. 1944;17(3):551-575. doi:10.5254/1.3546676

169. Canadell J, Goossens H, Klumperman B. Self-Healing Materials Based on Disulfide Links. *Macromolecules*. 2011;44(8):2536-2541. doi:10.1021/ma2001492

170. Black SP, Sanders JKM, Stefankiewicz AR. Disulfide exchange: exposing supramolecular reactivity through dynamic covalent chemistry. *Chem Soc Rev*. 2014;43(6):1861-1872. doi:10.1039/C3CS60326A

171. Fairbanks BD, Singh SP, Bowman CN, Anseth KS. Photodegradable, Photoadaptable Hydrogels via Radical-Mediated Disulfide Fragmentation Reaction. *Macromolecules*. 2011;44(8):2444-2450. doi:10.1021/ma200202w

172. Ji F, Liu X, Sheng D, Yang Y. Epoxy-vitrimer composites based on exchangeable aromatic disulfide bonds: Reprocessibility, adhesive, multi-shape memory effect. *Polymer (Guildf)*. 2020;197:122514. doi:https://doi.org/10.1016/j.polymer.2020.122514

173. Tesoro GC, Sastri V. Reversible crosslinking in epoxy resins. I. Feasibility studies. *J Appl Polym Sci*. 1990;39(7):1425-1437. doi:https://doi.org/10.1002/app.1990.070390702

174. Pepels M, Filot I, Klumperman B, Goossens H. Self-healing systems based on disulfide–thiol exchange reactions. *Polym Chem*. 2013;4(18):4955-4965. doi:10.1039/C3PY00087G

175. Chujo Y, Sada K, Naka A, Nomura R, Saegusa T. Synthesis and redox gelation of disulfide-modified polyoxazoline. *Macromolecules*. 1993;26(5):883-887. doi:10.1021/ma00057a001

176. Otsuka H, Nagano S, Kobashi Y, Maeda T, Takahara A. A dynamic covalent polymer driven by disulfide metathesis under photoirradiation. *Chemical Communications*. 2010;46(7):1150-1152. doi:10.1039/B916128G

177. Fortman DJ, Snyder RL, Sheppard DT, Dichtel WR. Rapidly Reprocessable Cross-Linked Polyhydroxyurethanes Based on Disulfide Exchange. *ACS Macro Lett*. 2018;7(10):1226-1231. doi:10.1021/acsmacrolett.8b00667

178. Imbernon L, Oikonomou EK, Norvez S, Leibler L. Chemically crosslinked yet reprocessable epoxidized natural rubber via thermo-activated disulfide rearrangements. *Polym Chem*. 2015;6(23):4271-4278. doi:10.1039/C5PY00459D

179. Michal BT, Jaye CA, Spencer EJ, Rowan SJ. Inherently Photohealable and Thermal Shape-Memory Polydisulfide Networks. *ACS Macro Lett*. 2013;2(8):694-699. doi:10.1021/mz400318m

180. Scott TF, Schneider AD, Cook WD, Bowman CN. Photoinduced Plasticity in Cross-Linked Polymers. *Science (1979)*. 2005;308(5728):1615-1617. doi:10.1126/science.1110505

181. McBride MK, Podgorski M, Chatani S, Worrell BT, Bowman CN. Thermoreversible Folding as a Route to the Unique Shape-Memory Character in Ductile Polymer Networks. *ACS Appl Mater Interfaces*. 2018;10(26):22739-22745. doi:10.1021/acsami.8b06004

182. Wu Z, Cheng P, Zhao W, Fang J, Xu T, Chen D. Allyl sulfide-based visible light-induced dynamically reshaped liquid crystalline elastomer/SWCNT nanocomposites capable of multimode NIR photomechanical actuations. *New Journal of Chemistry*. 2020;44(26):10902-10910. doi:10.1039/D0NJ01314E

183. McBride MK, Hendrikx M, Liu D, Worrell BT, Broer DJ, Bowman CN. Photoinduced Plasticity in Cross-Linked Liquid Crystalline Networks. *Advanced Materials*. 2017;29(17):1606509. doi:https://doi.org/10.1002/adma.201606509

184. Liu R, Li S, Yao N, et al. Castor oil-based polyurethane networks containing diselenide bonds: Self-healing, shape memory, and high flexibility. *Prog Org Coat*. 2022;163:106615. doi:https://doi.org/10.1016/j.porgcoat.2021.106615

185. Xu H, Cao W, Zhang X. Selenium-Containing Polymers: Promising Biomaterials for Controlled Release and Enzyme Mimics. *Acc Chem Res*. 2013;46(7):1647-1658. doi:10.1021/ar4000339

186. Xia J, Li T, Lu C, Xu H. Selenium-Containing Polymers: Perspectives toward Diverse Applications in Both Adaptive and Biomedical Materials. *Macromolecules*. 2018;51(19):7435-7455. doi:10.1021/acs.macromol.8b01597

187. Ji S, Cao W, Yu Y, Xu H. Dynamic Diselenide Bonds: Exchange Reaction Induced by Visible Light without Catalysis. *Angewandte Chemie International Edition*. 2014;53(26):6781-6785. doi:https://doi.org/10.1002/anie.201403442

188. Ji S, Fan F, Sun C, Yu Y, Xu H. Visible Light-Induced Plasticity of Shape Memory Polymers. *ACS Appl Mater Interfaces*. 2017;9(38):33169-33175. doi:10.1021/acsami.7b11188

189. Du W, Jin Y, Pan J, Fan W, Lai S, Sun X. Thermal induced shape-memory and self-healing of segmented polyurethane containing diselenide bonds. *J Appl Polym Sci*. 2018;135(22):46326. doi:https://doi.org/10.1002/app.46326

190. Xia J, Li T, Lu C, Xu H. Selenium-Containing Polymers: Perspectives toward Diverse Applications in Both Adaptive and Biomedical Materials. *Macromolecules*. 2018;51(19):7435-7455. doi:10.1021/acs.macromol.8b01597

191. Huang L, Yang Y, Niu Z, et al. Boronic ester bonds crosslinked vitrimer elastomers with mechanical robustness, shape memory, self-healing and recyclability properties. *Compos Sci Technol*. 2022;228:109621. doi:https://doi.org/10.1016/j.compscitech.2022.109621

192. Perera MM, Ayres N. Dynamic covalent bonds in self-healing, shape memory, and controllable stiffness hydrogels. *Polym Chem*. 2020;11(8):1410-1423. doi:10.1039/C9PY01694E

193. Hong SH, Kim S, Park JP, et al. Dynamic Bonds between Boronic Acid and Alginate: Hydrogels with Stretchable, Self-Healing, Stimuli-Responsive, Remoldable, and Adhesive Properties. *Biomacromolecules*. 2018;19(6):2053-2061. doi:10.1021/acs.biomac.8b00144

194. Brooks WLA, Sumerlin BS. Synthesis and Applications of Boronic Acid-Containing Polymers: From Materials to Medicine. *Chem Rev*. 2016;116(3):1375-1397. doi:10.1021/acs.chemrev.5b00300

195. Guan Y, Zhang Y. Boronic acid-containing hydrogels: synthesis and their applications. *Chem Soc Rev*. 2013;42(20):8106-8121. doi:10.1039/C3CS60152H

196. Deng CC, Brooks WLA, Abboud KA, Sumerlin BS. Boronic Acid-Based Hydrogels Undergo Self-Healing at Neutral and Acidic pH. *ACS Macro Lett*. 2015;4(2):220-224. doi:10.1021/acsmacrolett.5b00018

197. Meng H, Zheng J, Wen X, Cai Z, Zhang J, Chen T. pH- and Sugar-Induced Shape Memory Hydrogel Based on Reversible Phenylboronic Acid–Diol Ester Bonds. *Macromol Rapid Commun*. 2015;36(6):533-537. doi:https://doi.org/10.1002/marc.201400648

198. Hussain F, HM, OM and GRE. Hussain, F., Hojjati, M., Okamoto, M. and Gorga, R.E., 2006. Polymer-matrix nanocomposites, processing, manufacturing, and application: an overview. Journal of composite materials, 40(17), pp.1511-1575.

199. Lotfi Mayan Sofla R, Rezaei M, Babaie A, Nasiri M. Preparation of electroactive shape memory polyurethane/graphene nanocomposites and investigation of relationship between rheology, morphology and electrical properties. *Compos B Eng*. 2019;175:107090. doi:https://doi.org/10.1016/j.compositesb.2019.107090

200. Sun X, Sun H, Li H, Peng H. Developing Polymer Composite Materials : Carbon Nanotubes or Graphene ? Published online 2013:5153-5176. doi:10.1002/adma.201301926

201. Luo X, Wu Y, Guo M, et al. Multi-functional polyurethane composites with self-healing and shape memory properties enhanced by graphene oxide. *J Appl Polym Sci*. 2021;138(33):50827. doi:https://doi.org/10.1002/app.50827

202. Liu Y, Lv H, Lan X, Leng J, Du S. Review of electro-active shape-memory polymer composite. *Compos Sci Technol*. 2009;69(13):2064-2068. doi:https://doi.org/10.1016/j.compscitech.2008.08.016

203. Lei M, Chen Z, Lu H, Yu K. Recent progress in shape memory polymer composites: methods, properties, applications and prospects. 2019;8(1):327-351. doi:doi:10.1515/ntrev-2019-0031

204. DEFENG WU, LIANG WU, YURONG SUN MZS. Rheological Properties and Crystallization Behavior of Multi-Walled Carbon Nanotube/Poly(e-caprolactone) Composites. Published online 2004:3137-3147. doi:10.1002/polb

205. Grady BP. Effects of carbon nanotubes on polymer physics. *J Polym Sci B Polym Phys*. 2012;50(9):591-623. doi:10.1002/polb.23052

206. Xia L, Qiu G. Shape memory behavior of carbon nanotube - reinforced trans - 1 , 4 - polyisoprene and low - density polyethylene composites. 2020;(October 2018):107-113. doi:10.1002/pat.4751

207. Mosnáčková K, Mrlík M, Mičušík M, et al. Light-Responsive Hybrids Based on Carbon Nanotubes with Covalently Attached PHEMA- g-PCL Brushes. *Macromolecules*. 2021;54(5):2412-2426. doi:10.1021/acs.macromol.0c02701

208. Tilve-Martinez D, Neri W, Horaud D, et al. Graphene Oxide Based Transparent Resins For Accurate 3D Printing of Conductive Materials. *Adv Funct Mater*. 2023;n/a(n/a):2214954. doi:https://doi.org/10.1002/adfm.202214954

209. D'Elia E, Ahmed HS, Feilden E, Saiz E. Electrically-responsive graphene-based shape-memory composites. *Appl Mater Today*. 2019;15:185-191. doi:https://doi.org/10.1016/j.apmt.2018.12.018

210. Sasikala SP, Neri W, Poulin P, Aymonier C. An effective in situ reduction strategy assisted by supercritical fluids for the preparation of graphene - polymer composites. *Carbon N Y*. 2018;139:572-580. doi:https://doi.org/10.1016/j.carbon.2018.06.076

211. Xiang Z, Zhang L, Yuan T, Li Y, Sun J. Healability Demonstrates Enhanced Shape-Recovery of Graphene-Oxide-Reinforced Shape-Memory Polymeric Films. *ACS Appl Mater Interfaces*. 2018;10(3):2897-2906. doi:10.1021/acsami.7b14588

212. Lei M, Chen Z, Lu H, Yu K. Recent progress in shape memory polymer composites: methods, properties, applications and prospects. 2019;8(1):327-351. doi:doi:10.1515/ntrev-2019-0031

213. Kausar A. Contemporary applications of carbon black-filled polymer composites: An overview of essential aspects. *Journal of Plastic Film & Sheeting*. 2018;34(3):256-299.

214. Rafique, M.M.A., Qiu, D. and Brandt, M., 2019. Retracted: Development of Bulk Metallic Glasses and their Composites by Additive Manufacturing–Evolution, Challenges and a Proposed Novel Solution. In Advanced Materials Research (Vol. 1155, pp. 1-28). Trans Tech Publications Ltd.

215. Gunes IS, Jimenez GA, Jana SC. Carbonaceous fillers for shape memory actuation of polyurethane composites by resistive heating. *Carbon N Y*. 2009;47(4):981-997. doi:https://doi.org/10.1016/j.carbon.2008.11.053

216. Arun DI, Santhosh Kumar KS, Satheesh Kumar B, Chakravarthy P, Dona M, Santhosh B. High glass-transition polyurethane-carbon black electro-active shape memory nanocomposite for aerospace systems. *Materials Science and Technology*. 2019;35(5):596-605. doi:10.1080/02670836.2019.1575054

217. Arun DI, Chakravarthy P, Girish BS, Santhosh Kumar KS, Santhosh B. Experimental and Monte Carlo simulation studies on percolation behaviour of a shape memory polyurethane carbon black nanocomposite. *Smart Mater Struct*. 2019;28(5):055010. doi:10.1088/1361-665X/ab083b

218. Le HH, Kolesov I, Ali Z, et al. Effect of filler dispersion degree on the Joule heating stimulated recovery behaviour of nanocomposites. *J Mater Sci*. 2010;45(21):5851-5859. doi:10.1007/s10853-010-4661-7

219. Ponnamma D, Sadasivuni KK, Grohens Y, Guo Q, Thomas S. Carbon nanotube based elastomer composites – an approach towards multifunctional materials. *J Mater Chem C Mater*. 2014;2(40):8446-8485. doi:10.1039/C4TC01037J

220. Mullins L. Softening of rubber by deformation. *Rubber chemistry and technology*. 1969;42(1):339-362.

221. Zhao J, Dai K, Liu C, et al. A comparison between strain sensing behaviors of carbon black/polypropylene and carbon nanotubes/polypropylene electrically conductive composites. *Compos Part A Appl Sci Manuf*. 2013;48:129-136. doi:https://doi.org/10.1016/j.compositesa.2013.01.004

222. Romero-Zúñiga GY, Navarro-Rodríguez D, Treviño-Martínez ME. Enhanced mechanical performance of a DGEBA epoxy resin-based shape memory polymer by introducing graphene oxide via covalent linking. *J Appl Polym Sci*. 2022;139(2):51467. doi:https://doi.org/10.1002/app.51467

223. Wang W, Liu D, Liu Y, Leng J, Bhattacharyya D. Electrical actuation properties of reduced graphene oxide paper/epoxy-based shape memory composites. *Compos Sci Technol*. 2015;106:20-24. doi:https://doi.org/10.1016/j.compscitech.2014.10.016

224. Zhang L, Jiao H, Jiu H, Chang J, Zhang S, Zhao Y. Thermal, mechanical and electrical properties of polyurethane/(3-aminopropyl) triethoxysilane functionalized graphene/epoxy resin interpenetrating shape memory polymer composites. *Compos Part A Appl Sci Manuf*. 2016;90:286-295. doi:https://doi.org/10.1016/j.compositesa.2016.07.017

225. Lotfi Mayan Sofla R, Rezaei M, Babaie A. Investigation of the effect of graphene oxide functionalization on the physical, mechanical and shape memory properties of polyurethane/reduced graphene oxide nanocomposites. *Diam Relat Mater*. 2019;95:195-205. doi:https://doi.org/10.1016/j.diamond.2019.04.012

226. Martin-Gallego M, Verdejo R, Lopez-Manchado MA, Sangermano M. Epoxy-Graphene UV-cured nanocomposites. *Polymer (Guildf)*. 2011;52(21):4664-4669. doi:https://doi.org/10.1016/j.polymer.2011.08.039

227. Stankovich S, Dikin DA, Piner RD, et al. Synthesis of graphene-based nanosheets via chemical reduction of exfoliated graphite oxide. *Carbon N Y*. 2007;45(7):1558-1565. doi:https://doi.org/10.1016/j.carbon.2007.02.034

228. Tang LC, Wan YJ, Yan D, et al. The effect of graphene dispersion on the mechanical properties of graphene/epoxy composites. *Carbon N Y*. 2013;60:16-27. doi:https://doi.org/10.1016/j.carbon.2013.03.050

229. Bhanushali H, Amrutkar S, Mestry S, Mhaske ST. Shape memory polymer nanocomposite: a review on structure–property relationship. *Polymer Bulletin*. 2022;79(6):3437-3493. doi:10.1007/s00289-021-03686-x

230. Pradhan S, Kumar Sahu S, Pramanik J, Dhar Badgayan N. An insight into mechanical & thermal properties of shape memory polymer reinforced with nanofillers; a critical review. *Mater Today Proc*. 2022;50:1107-1112. doi:https://doi.org/10.1016/j.matpr.2021.07.504

231. Kausar A. Shape memory polymer/graphene nanocomposites: State-of-the-art. 2022;22(1):165-181. doi:doi:10.1515/epoly-2022-0024

232. Liu T, Zhou T, Yao Y, et al. Stimulus methods of multi-functional shape memory polymer nanocomposites: A review. *Compos Part A Appl Sci Manuf*. 2017;100:20-30. doi:https://doi.org/10.1016/j.compositesa.2017.04.022

233. Chin SJ, Vempati S, Dawson P, et al. Electrical conduction and rheological behaviour of composites of poly(ε-caprolactone) and MWCNTs. *Polymer (Guildf)*. 2015;58:209-221. doi:https://doi.org/10.1016/j.polymer.2014.12.034

234. Liu Y, Zhao J, Zhao L, et al. High Performance Shape Memory Epoxy/Carbon Nanotube Nanocomposites. *ACS Appl Mater Interfaces*. 2016;8(1):311-320. doi:10.1021/acsami.5b08766

235. Liu, Phang IY, Shen L, Chow SY, Zhang WD. Morphology and Mechanical Properties of Multiwalled Carbon Nanotubes Reinforced Nylon-6 Composites. *Macromolecules*. 2004;37(19):7214-7222. doi:10.1021/ma049132t

236. González-Jiménez A, Bernal-Ortega P, Salamanca FM, Valentin JL. Shape-memory composites based on ionic elastomers. *Polymers (Basel)*. 2022;14(6):1230.

237. Pilate F, Toncheva A, Dubois P, Raquez JM. Shape-memory polymers for multiple applications in the materials world. *Eur Polym J*. 2016;80:268-294. doi:10.1016/j.eurpolymj.2016.05.004

238. Orozco F, Salvatore A, Sakulmankongsuk A, et al. Electroactive performance and cost evaluation of carbon nanotubes and carbon black as conductive fillers in self-healing shape memory polymers and other composites. *Polymer (Guildf)*. 2022;260:125365. doi:https://doi.org/10.1016/j.polymer.2022.125365

239. Lu H, Yao Y, Lin L. Carbon-based reinforcement in shape-memory polymer composite for electrical actuation. *Pigment & Resin Technology*. 2014;43(1):26-34.

240. Xu X, Fan P, Ren J, et al. Self-healing thermoplastic polyurethane (TPU)/polycaprolactone (PCL) /multi-wall carbon nanotubes (MWCNTs) blend as shape-memory composites. *Compos Sci Technol*. 2018;168:255-262. doi:https://doi.org/10.1016/j.compscitech.2018.10.003

241. Amirian M, Nabipour Chakoli A, Sui J, Cai W. Enhanced shape memory effect of poly(L-lactide-co-ε-caprolactone) biodegradable copolymer reinforced with functionalized MWCNTs. *Journal of Polymer Research*. 2012;19(2):9777. doi:10.1007/s10965-011-9777-1

242. Kalita H, Karak N. Hyperbranched polyurethane/triethanolamine functionalized multi-walled carbon nanotube nanocomposites as remote induced smart materials. *Polym Int*. 2014;63(7):1295-1302. doi:https://doi.org/10.1002/pi.4674

243. Raja M, Ryu SH, Shanmugharaj AM. Influence of surface modified multiwalled carbon nanotubes on the mechanical and electroactive shape memory properties of polyurethane (PU)/poly(vinylidene diflouride) (PVDF) composites. *Colloids Surf A Physicochem Eng Asp*. 2014;450:59-66. doi:https://doi.org/10.1016/j.colsurfa.2014.03.008

244. Ribeiro B, Botelho EC, Costa ML, Bandeira CF. Carbon nanotube buckypaper reinforced polymer composites: a review. *Polímeros*. 2017;27:247-255.

245. Zhou G, Zhang H, Xu S, et al. Fast triggering of shape memory polymers using an embedded carbon nanotube sponge network. *Sci Rep*. 2016;6(1):1-8.

246. Lu H, Liu Y, Gou J (Jan), Leng J, Du S. Surface coating of multi-walled carbon nanotube nanopaper on shape-memory polymer for multifunctionalization. *Compos Sci Technol*. 2011;71(11):1427-1434. doi:https://doi.org/10.1016/j.compscitech.2011.05.016

247. Datta S, Henry TC, Sliozberg YR, Lawrence BD, Chattopadhyay A, Hall AJ. Carbon nanotube enhanced shape memory epoxy for improved mechanical properties and electroactive shape recovery. *Polymer (Guildf)*. 2021;212:123158. doi:https://doi.org/10.1016/j.polymer.2020.123158

248. Li Q, Liu C, Lin YH, Liu L, Jiang K, Fan S. Large-Strain, Multiform Movements from Designable Electrothermal Actuators Based on Large Highly Anisotropic Carbon Nanotube Sheets. *ACS Nano*. 2015;9(1):409-418. doi:10.1021/nn505535k

249. Alam J, Khan A, Alam M, Mohan R. Electroactive Shape Memory Property of a Cu-decorated CNT Dispersed PLA/ESO Nanocomposite. *Materials*. 2015;8(9):6391-6400. doi:10.3390/ma8095313

250. Raja M, Shanmugharaj AM, Ryu SH, Subha J. Influence of metal nanoparticle decorated CNTs on polyurethane based electro active shape memory nanocomposite actuators. *Mater Chem Phys*. 2011;129(3):925-931. doi:https://doi.org/10.1016/j.matchemphys.2011.05.028

251. Sahoo NG, Jung YC, Yoo HJ, Cho JW. Influence of carbon nanotubes and polypyrrole on the thermal, mechanical and electroactive shape-memory properties of polyurethane nanocomposites. *Compos Sci Technol*. 2007;67(9):1920-1929. doi:https://doi.org/10.1016/j.compscitech.2006.10.013

252. Yu K, Liu Y, Leng J. Shape memory polymer/CNT composites and their microwave induced shape memory behaviors. *RSC Adv*. 2014;4(6):2961-2968. doi:10.1039/C3RA43258K

253. Yang Y, Pei Z, Zhang X, Tao L, Wei Y, Ji Y. Carbon nanotube–vitrimer composite for facile and efficient photo-welding of epoxy. *Chem Sci*. 2014;5(9):3486-3492. doi:10.1039/C4SC00543K

254. Yan P, Zhao W, Jiang L, et al. Reconfiguration and shape memory triggered by heat and light of carbon nanotube–polyurethane vitrimer composites. *J Appl Polym Sci*. 2018;135(5):45784. doi:https://doi.org/10.1002/app.45784

255. Yang Y, Wang H, Zhang S, et al. Vitrimer-based soft actuators with multiple responsiveness and self-healing ability triggered by multiple stimuli. *Matter*. 2021;4(10):3354-3365. doi:https://doi.org/10.1016/j.matt.2021.08.009

256. Cotin G, Perton F, Blanco-Andujar C, Pichon B, Mertz D, Bégin-Colin S. Chapter 2 - Design of Anisotropic Iron-Oxide-Based Nanoparticles for Magnetic Hyperthermia. In: Fratila RM, De La Fuente JM, eds. *Nanomaterials for Magnetic and Optical Hyperthermia Applications*. Elsevier; 2019:41-60. doi:https://doi.org/10.1016/B978-0-12-813928-8.00002-8

257. Zhang L, Gu FX, Chan JM, Wang AZ, Langer RS, Farokhzad OC. Nanoparticles in Medicine: Therapeutic Applications and Developments. *Clin Pharmacol Ther*. 2008;83(5):761-769. doi:https://doi.org/10.1038/sj.clpt.6100400

258. Gong T, Li W, Chen H, Wang L, Shao S, Zhou S. Remotely actuated shape memory effect of electrospun composite nanofibers. *Acta Biomater*. 2012;8(3):1248-1259. doi:https://doi.org/10.1016/j.actbio.2011.12.006

259. Namathoti S, V.M. R kumar, P.S. RS. A review on progress in magnetic, microwave, ultrasonic responsive Shape-memory polymer composites. *Mater Today Proc*. 2022;56:1182-1191. doi:https://doi.org/10.1016/j.matpr.2021.11.151

260. Cai Y, Jiang JS, Zheng B, Xie MR. Synthesis and properties of magnetic sensitive shape memory Fe3O4/poly(ε-caprolactone)-polyurethane nanocomposites. *J Appl Polym Sci*. 2013;127(1):49-56. doi:https://doi.org/10.1002/app.36849

261. Yakacki CM, Satarkar NS, Gall K, Likos R, Hilt JZ. Shape-memory polymer networks with Fe3O4 nanoparticles for remote activation. *J Appl Polym Sci*. 2009;112(5):3166-3176. doi:https://doi.org/10.1002/app.29845

262. Weigel T, Mohr R, Lendlein A. Investigation of parameters to achieve temperatures required to initiate the shape-memory effect of magnetic nanocomposites by inductive heating. *Smart Mater Struct*. 2009;18(2):025011. doi:10.1088/0964-1726/18/2/025011

263. Zheng X, Zhou S, Xiao Y, Yu X, Li X, Wu P. Shape memory effect of poly(d,l-lactide)/Fe3O4 nanocomposites by inductive heating of magnetite particles. *Colloids Surf B Biointerfaces*. 2009;71(1):67-72. doi:https://doi.org/10.1016/j.colsurfb.2009.01.009

264. Zou H, Weder C, Simon YC. Shape-Memory Polyurethane Nanocomposites with Single Layer or Bilayer Oleic Acid-Coated Fe3O4 Nanoparticles. *Macromol Mater Eng*. 2015;300(9):885-892. doi:https://doi.org/10.1002/mame.201500079

265. Kuang X, Wu S, Ze Q, et al. Magnetic Dynamic Polymers for Modular Assembling and Reconfigurable Morphing Architectures. *Advanced Materials*. 2021;33(30):2102113. doi:https://doi.org/10.1002/adma.202102113

266. Heath WH, Palmieri F, Adams JR, et al. Degradable cross-linkers and strippable imaging materials for step-and-flash imprint lithography. *Macromolecules*. 2008;41(3):719-726. doi:10.1021/ma702291k

267. Sánchez CP, Jérôme C, Noels L, Vanderbemden P. Review of Thermoresponsive Electroactive and Magnetoactive Shape Memory Polymer Nanocomposites. *ACS Omega*. 2022;7(45):40701-40723. doi:10.1021/acsomega.2c05930

268. Fagnard JF, Stoukatch S, Laurent P, et al. Preparation and Characterization of a Thermal Insulating Carbon Xerogel-Epoxy Composite Adhesive for Electronics Applications. *IEEE Trans Compon Packaging Manuf Technol*. 2021;11(4):606-615. doi:10.1109/TCPMT.2021.3059478

269. Defize T, Riva R, Thomassin JM, et al. Reversible TAD Chemistry as a Convenient Tool for the Design of (Re)processable PCL-Based Shape-Memory Materials. *Macromol Rapid Commun*. 2017;38(1):1-7. doi:10.1002/marc.201600517

270. Yang Z, Peng H, Wang W, Liu T. Crystallization behavior of poly(ε-caprolactone)/layered double hydroxide nanocomposites. *J Appl Polym Sci*. 2010;116(5):2658-2667. doi:10.1002/app

271. Pereira Sánchez CA. *Investigation of Thermal, Electrical and Mechanical Properties of Shape Memory Polymer Composites during Electric Activation*.; 2022.

272. Göldel A, Marmur A, Kasaliwal GR, Pötschke P, Heinrich G. Shape-dependent localization of carbon nanotubes and carbon black in an immiscible polymer blend during melt mixing. *Macromolecules*. 2011;44(15):6094-6102. doi:10.1021/ma200793a

273. Defize T, Thomassin JM, Alexandre M, Gilbert B, Riva R, Jérôme C. Comprehensive study of the thermo-reversibility of Diels-Alder based PCL polymer networks. *Polymer (United Kingdom)*. 2016;84:234-242. doi:10.1016/j.polymer.2015.11.055

274. Chang CM, Liu YL. Functionalization of multi-walled carbon nanotubes with furan and maleimide compounds through Diels-Alder cycloaddition. *Carbon N Y*. 2009;47(13):3041-3049. doi:10.1016/j.carbon.2009.06.058

275. Khonakdar HA, Morshedian J, Wagenknecht U, Jafari SH. An investigation of chemical crosslinking effect on properties of high-density polyethylene. *Polymer (Guildf)*. 2003;44(15):4301-4309. doi:10.1016/S0032-3861(03)00363-X

276. Toda A, Androsch R, Schick C. Insights into polymer crystallization and melting from fast scanning chip calorimetry. *Polymer (Guildf)*. 2016;91:239-263. doi:10.1016/j.polymer.2016.03.038

277. Chen YF, Tan YJ, Li J, Hao YB, Shi YD, Wang M. Graphene oxide-assisted dispersion of multi-walled carbon nanotubes in biodegradable Poly(ε-caprolactone) for mechanical and electrically conductive enhancement. *Polym Test*. 2018;65(December 2017):387-397. doi:10.1016/j.polymertesting.2017.12.019

278. Huang B, Vyas C, Roberts I, et al. Fabrication and characterisation of 3D printed MWCNT composite porous scaffolds for bone regeneration. *Materials Science and Engineering C*. 2019;98(December 2018):266-278. doi:10.1016/j.msec.2018.12.100

279. El Sayed AM. Synthesis, optical, thermal, electric properties and impedance spectroscopy studies on P(VC-MMA) of optimized thickness and reinforced with MWCNTs. *Results Phys*. 2020;17(March):103025. doi:10.1016/j.rinp.2020.103025

280. Lorenzelli V. *Advances in Polymer Science. Vol. 54. Spectroscopy*. Vol 11.; 1984. doi:10.1016/0254-0584(84)90091-9

281. PEKDEMİR ME, KÖK M, QADER IN, AYDOĞDU Y. Preparation and physicochemical properties of mwcnt doped polyvinyl chloride / poly (ε-caprolactone) blend. *Journal of Polymer Research*. 2022;29(4):1-9. doi:10.1007/s10965-022-02947-1

282. Wurm A, Lellinger D, Minakov AA, et al. Crystallization of poly(ε-caprolactone)/MWCNT composites: A combined SAXS/WAXS, electrical and thermal conductivity study. *Polymer (Guildf)*. 2014;55(9):2220-2232. doi:10.1016/j.polymer.2014.02.069

283. Xu D, Wang Z. Role of multi-wall carbon nanotube network in composites to crystallization of isotactic polypropylene matrix. *Polymer (Guildf)*. 2008;49(1):330-338. doi:10.1016/j.polymer.2007.11.041

284. Prashantha K, Soulestin J, Lacrampe MF, Krawczak P, Dupin G, Claes M. Masterbatch-based multi-walled carbon nanotube filled polypropylene nanocomposites: Assessment of rheological and mechanical properties. *Compos Sci Technol*. 2009;69(11-12):1756-1763. doi:10.1016/j.compscitech.2008.10.005

285. Kota AK, Cipriano BH, Duesterberg MK, et al. Electrical and rheological percolation in polystyrene/MWCNT nanocomposites. *Macromolecules*. 2007;40(20):7400-7406. doi:10.1021/ma0711792

286. Landa M, Canales J, Fernández M, Muñoz ME, Santamaría A. Effect of MWCNTs and graphene on the crystallization of polyurethane based nanocomposites, analyzed via calorimetry, rheology and AFM microscopy. *Polym Test*. 2014;35:101-108. doi:10.1016/j.polymertesting.2014.03.008

287. Menzer K, Krause B, Boldt R, Kretzschmar B, Weidisch R, Pötschke P. Percolation behaviour of multiwalled carbon nanotubes of altered length and primary agglomerate morphology in melt mixed isotactic polypropylene-based composites. *Compos Sci Technol*. 2011;71(16):1936-1943. doi:10.1016/j.compscitech.2011.09.009

288. Ren D, Chen Y, Li H, Rehman HU, Cai Y, Liu H. High-efficiency dual-responsive shape memory assisted self-healing of carbon nanotubes enhanced polycaprolactone/thermoplastic polyurethane composites. *Colloids Surf A Physicochem Eng Asp*. 2019;580(July):123731. doi:10.1016/j.colsurfa.2019.123731

289. Orellana J, Moreno-villoslada I, Bose RK, Picchioni F, Flores ME, Araya-hermosilla R. Self-healing polymer nanocomposite materials by joule effect. *Polymers (Basel)*. 2021;13(4):1-24. doi:10.3390/polym13040649

290. Maity D, Agrawal DC. Synthesis of iron oxide nanoparticles under oxidizing environment and their stabilization in aqueous and non-aqueous media. *J Magn Magn Mater*. 2007;308(1):46-55. doi:https://doi.org/10.1016/j.jmmm.2006.05.001

291. Mohebbi A, Mighri F, Ajji A, Rodrigue D. Current issues and challenges in polypropylene foaming: A review. *Cellular Polymers*. 2015;34(6):299-337. doi:10.1177/026248931503400602

292. Yin D, Mi J, Zhou H, Wang X, Tian H. Fabrication of branching poly (butylene succinate)/cellulose nanocrystal foams with exceptional thermal insulation. *Carbohydr Polym*. 2020;247(March):116708. doi:10.1016/j.carbpol.2020.116708

293. Qiao Y, Li Q, Jalali A, et al. In-situ microfibrillated Poly(ε-caprolactone)/ Poly(lactic acid) composites with enhanced rheological properties, crystallization kinetics and foaming ability. *Compos B Eng*. 2021;208(December 2020):108594. doi:10.1016/j.compositesb.2020.108594

294. Wang G, Zhao J, Wang G, et al. Strong and super thermally insulating in-situ nanofibrillar PLA/PET composite foam fabricated by high-pressure microcellular injection molding. *Chemical Engineering Journal*. 2020;390(November 2019):124520. doi:10.1016/j.cej.2020.124520

295. Wang J, Chai J, Wang G, et al. Strong and thermally insulating polylactic acid/glass fiber composite foam fabricated by supercritical carbon dioxide foaming. *Int J Biol Macromol*. 2019;138:144-155. doi:10.1016/j.ijbiomac.2019.07.071

296. Kuska R, Milovanovic S, Frerich S, Ivanovic J. Thermal analysis of polylactic acid under high CO2 pressure applied in supercritical impregnation and foaming process design. *Journal of Supercritical Fluids*. 2019;144(October 2018):71-80. doi:10.1016/j.supflu.2018.10.008

297. Valor D, Montes A, Monteiro M, García-Casas I, Pereyra C, de la Ossa EM. Determining the optimal conditions for the production by supercritical co2 of biodegradable plga foams for the controlled release of rutin as a medical treatment. *Polymers (Basel)*. 2021;13(10). doi:10.3390/polym13101645

298. Pyun DG, Yoon HS, Chung HY, et al. Evaluation of AgHAP-containing polyurethane foam dressing for wound healing: synthesis, characterization, in vitro and in vivo studies. *J Mater Chem B*. 2015;3(39):7752-7763. doi:10.1039/c5tb00995b

299. Gan Q, Zhu J, Yuan Y, Liu H, Zhu Y, Liu C. A proton-responsive ensemble using mesocellular foam supports capped with N,O-carboxymethyl chitosan for controlled release of bioactive proteins. *J Mater Chem B*. 2015;3(11):2281-2285. doi:10.1039/c5tb00219b

300. Ferreira F V., Otoni CG, De France KJ, et al. Porous nanocellulose gels and foams: Breakthrough status in the development of scaffolds for tissue engineering. *Materials Today*. 2020;37(August):126-141. doi:10.1016/j.mattod.2020.03.003

301. Marques LM, Alves MM, Eugénio S, et al. Potential anti-cancer and anti-: Candida activity of Zn-derived foams. *J Mater Chem B*. 2018;6(18):2821-2830. doi:10.1039/c7tb02726e

302. Han SK, Song M, Choi K, Choi SW. Fabrication of Biodegradable Polyurethane Foam Scaffolds with Customized Shapes and Controlled Mechanical Properties by Gas Foaming Technique. *Macromol Mater Eng*. 2021;306(7):1-10. doi:10.1002/mame.202100114

303. Hu J, Albadawi H, Chong BW, et al. Advances in Biomaterials and Technologies for Vascular Embolization. *Advanced Materials*. 2019;31(33). doi:10.1002/adma.201901071

304. Singhal P, Small W, Cosgriff-Hernandez E, Maitland DJ, Wilson TS. Low density biodegradable shape memory polyurethane foams for embolic biomedical applications. *Acta Biomater*. 2014;10(1):67-76. doi:10.1016/j.actbio.2013.09.027

305. Khodaverdi E, Reza Abbaspour M, Oroojalian F, et al. Dexamethasone delivery of porous PEG-PCL-PEG scaffolds with supercritical carbon dioxide gas foaming. *J Drug Deliv Sci Technol*. 2021;66(April):102547. doi:10.1016/j.jddst.2021.102547

306. Li J, Wang H, Zhou H, Jiang J, Wang X, Li Q. Fabrication of Highly Interconnected Poly(ε-caprolactone)/cellulose Nanofiber Composite Foams by Microcellular Foaming and Leaching Processes. *ACS Omega*. Published online 2021. doi:10.1021/acsomega.1c02768

307. Sarver JA, Kiran E. Foaming of polymers with carbon dioxide – The year-in-review – 2019. *Journal of Supercritical Fluids*. 2021;173(September 2020):105166. doi:10.1016/j.supflu.2021.105166

308. Qiao Y, Li Q, Jalali A, et al. In-situ microfibrillated Poly(ε-caprolactone)/ Poly(lactic acid) composites with enhanced rheological properties, crystallization kinetics and foaming ability. *Compos B Eng*. 2021;208(December 2020):108594. doi:10.1016/j.compositesb.2020.108594

309. Hatami T, Johner JCF, de Castro KC, Mei LHI, Vieira MGA, Angela M. New insight into a step-by-step modeling of supercritical CO2 foaming to fabricate poly(ε-caprolactone) scaffold. *Ind Eng Chem Res*. 2020;59(45):20033-20044. doi:10.1021/acs.iecr.0c04372

310. Santos-Rosales V, Gallo M, Jaeger P, Alvarez-Lorenzo C, Gómez-Amoza JL, García-González CA. New insights in the morphological characterization and modelling of poly(ε-caprolactone) bone scaffolds obtained by supercritical CO2 foaming. *Journal of Supercritical Fluids*. 2020;166. doi:10.1016/j.supflu.2020.105012

311. Baldino L, Cardea S. Generation of biocompatible PCL foams by supercritical foaming. *Chem Eng Trans*. 2020;79(February):241-246. doi:10.3303/CET2079041

312. Nofar M, Batı B, Küçük EB, Jalali A. Effect of soft segment molecular weight on the microcellular foaming behavior of TPU using supercritical CO2. *Journal of Supercritical Fluids*. 2020;160. doi:10.1016/j.supflu.2020.104816

313. López-Periago AM, Domingo C. Features of supercritical CO2 in the delicate world of the nanopores. *Journal of Supercritical Fluids*. 2018;134(September 2017):204-213. doi:10.1016/j.supflu.2017.11.011

314. Di Maio E, Kiran E. Foaming of polymers with supercritical fluids and perspectives on the current knowledge gaps and challenges. *Journal of Supercritical Fluids*. 2018;134(November 2017):157-166. doi:10.1016/j.supflu.2017.11.013

315. Chauvet M, Sauceau M, Fages J. Extrusion assisted by supercritical CO2: A review on its application to biopolymers. *Journal of Supercritical Fluids*. 2017;120:408-420. doi:10.1016/j.supflu.2016.05.043

316. Tsivintzelis I, Pavlidou E, Panayiotou C. Biodegradable polymer foams prepared with supercritical CO2-ethanol mixtures as blowing agents. *Journal of Supercritical Fluids*. 2007;42(2):265-272. doi:10.1016/j.supflu.2007.02.009

317. Pahovnik D. Shape Memory Behavior of Emulsion-Templated Poly(ε - Caprolactone) Synthesized by Organocatalyzed Ring-Opening Polymerization˘ ,. Published online 2019. doi:10.1021/acs.macromol.9b01780

318. Zhang F, Zhou T, Liu Y, Leng J. Microwave synthesis and actuation of shape memory polycaprolactone foams with high speed. *Nature Publishing Group*. Published online 2015:1-12. doi:10.1038/srep11152

319. Quadrini F, Bellisario D, Santo L, et al. Shape Memory Foams of Microbial Polyester for Biomedical Applications Shape Memory Foams of Microbial Polyester for Biomedical Applications. 2013;2559. doi:10.1080/03602559.2012.762526

320. Salerno A, Maio E Di, Iannace S, Netti PA. Tailoring the pore structure of PCL scaffolds for tissue engineering prepared via gas foaming of multi-phase blends. Published online 2012:181-188. doi:10.1007/s10934-011-9458-9

321. Lu L, Cao J, Li G. A polycaprolactone-based syntactic foam with bidirectional reversible actuation. 2017;45225:29-34. doi:10.1002/app.45225

322. Salerno A, Leonardi AB, Pedram P, Di Maio E, Fanovich MA, Netti PA. Tuning the three-dimensional architecture of supercritical CO2 foamed PCL scaffolds by a novel mould patterning approach. *Materials Science and Engineering C*. 2020;109(December 2019):110518. doi:10.1016/j.msec.2019.110518

323. Salerno A, Domingo C. Polycaprolactone foams prepared by supercritical CO2 batch foaming of polymer/organic solvent solutions. *J Supercrit Fluids*. 2019;143:146-156. doi:https://doi.org/10.1016/j.supflu.2018.08.006

324. Chen CX, Peng HH, Guan YX, Yao SJ. Morphological study on the pore growth profile of poly(ε-caprolactone) bi-modal porous foams using a modified supercritical CO2 foaming process. *J Supercrit Fluids*. 2019;143:72-81. doi:https://doi.org/10.1016/j.supflu.2018.07.029

325. Boia R, Dias PAN, Martins JM, et al. Porous poly (ε -caprolactone) implants : A novel strategy for e ffi cient intraocular drug delivery. 2019;316(June):331-348. doi:10.1016/j.jconrel.2019.09.023

326. Zhang K, Wang Y, Jiang J, et al. Fabrication of highly interconnected porous poly(ε-caprolactone) scaffolds with supercritical CO2 foaming and polymer leaching. *J Mater Sci*. 2019;54(6):5112-5126. doi:10.1007/s10853-018-3166-7

327. Salerno A, Di Maio E, Iannace S, Netti PA. Solid-state supercritical CO2 foaming of PCL and PCL-HA nano-composite: Effect of composition, thermal history and foaming process on foam pore structure. *Journal of Supercritical Fluids*. 2011;58(1):158-167. doi:10.1016/j.supflu.2011.05.009

328. Thomassin J michel, Pagnoulle C, Bednarz L, Huynen I, Jerome R, Detrembleur C. Foams of polycaprolactone / MWNT nanocomposites for efficient EMI reduction. Published online 2008:792-796. doi:10.1039/b709864b

329. Scheutz GM, Lessard JJ, Sims MB, Sumerlin BS. Adaptable Crosslinks in Polymeric Materials: Resolving the Intersection of Thermoplastics and Thermosets. *J Am Chem Soc*. 2019;141(41):16181-16196. doi:10.1021/jacs.9b07922

330. Kloxin CJ, Bowman CN. Covalent adaptable networks: Smart, reconfigurable and responsive network systems. *Chem Soc Rev*. 2013;42(17):7161-7173. doi:10.1039/c3cs60046g

331. McBride MK, Worrell BT, Brown T, et al. Enabling applications of covalent adaptable networks. *Annu Rev Chem Biomol Eng*. 2019;10:175-198. doi:10.1146/annurev-chembioeng-060718-030217

332. Zhang G, Zhao Q, Yang L, Zou W, Xi X, Xie T. Exploring Dynamic Equilibrium of Diels-Alder Reaction for Solid State Plasticity in Remoldable Shape Memory Polymer Network. *ACS Macro Lett*. 2016;5(7):805-808. doi:10.1021/acsmacrolett.6b00357

333. Dow T, Company C, Solutions DB. REVIEW CO 2 -Blown Nanocellular Foams. 2014;41293. doi:10.1002/app.41293

334. Marrazzo C, Maio E Di, Iannace S. Conventional and Nanometric Nucleating Agents in Poly (e -caprolactone) Foaming : Crystals vs . Bubbles Nucleation. doi:10.1002/pen.20937

335. Taki K, Kitano D, Ohshima M. Effect of Growing Crystalline Phase on Bubble Nucleation in Poly (L -Lactide)/ CO 2 Batch Foaming. Published online 2011:3247-3252.

336. Defize T, Thomassin JM, Alexandre M, Gilbert B, Riva R, Jérôme C. Comprehensive study of the thermo-reversibility of Diels-Alder based PCL polymer networks. *Polymer (Guildf)*. 2016;84:234-242. doi:10.1016/j.polymer.2015.11.055

337. Tsivintzelis I, Angelopoulou AG, Panayiotou C. Foaming of polymers with supercritical CO2: An experimental and theoretical study. *Polymer (Guildf)*. 2007;48(20):5928-5939. doi:10.1016/j.polymer.2007.08.004

338. White LJ, Hutter V, Tai H, Howdle SM, Shakesheff KM. The effect of processing variables on morphological and mechanical properties of supercritical CO 2 foamed scaffolds for tissue engineering. *Acta Biomater*. 2012;8(1):61-71. doi:10.1016/j.actbio.2011.07.032

339. Chen CX, Liu QQ, Xin X, Guan YX, Yao SJ. Pore formation of poly(ε-caprolactone) scaffolds with melting point reduction in supercritical CO2 foaming. *Journal of Supercritical Fluids*. 2016;117:279-288. doi:10.1016/j.supflu.2016.07.006

340. Chung T, Romo-uribe A, Mather PT. Two-Way Reversible Shape Memory in a Semicrystalline Network. Published online 2008:184-192.

341. Floudas G, Hilliou L, Lellinger D, Alig I. Shear-Induced Crystallization of Poly (-caprolactone). 2 . Evolution of Birefringence and Dichroism. Published online 2000:6466-6472.

342. Diani J, Gall K. Challenges of Shape Memory Polymers: A Review of the Progress Toward Overcoming SMP's Limitations Ingrid. *Society*. Published online 2006:1-10. doi:10.1002/pen

343. Hasan SM, Fletcher GK, Monroe MBB, Wierzbicki MA, Nash LD, Maitland DJ. Shape memory polymer foams synthesized using glycerol and hexanetriol for enhanced degradation resistance. *Polymers (Basel)*. 2020;12(10):1-16. doi:10.3390/polym12102290

344. Athanasopoulos N, Baltopoulos A, Matzakou M, Vavouliotis A, Kostopoulos V. Electrical conductivity of polyurethane/MWCNT nanocomposite foams. *Polym Compos*. 2012;33(8):1302-1312. doi:https://doi.org/10.1002/pc.22256

345. Pötschke P, Krause B, Buschhorn ST, et al. Improvement of carbon nanotube dispersion in thermoplastic composites using a three roll mill at elevated temperatures. *Compos Sci Technol*. 2013;74:78-84. doi:https://doi.org/10.1016/j.compscitech.2012.10.010

346. Chin SJ, Vempati S, Dawson P, et al. Electrical conduction and rheological behaviour of composites of poly(ε-caprolactone) and MWCNTs. *Polymer (Guildf)*. 2015;58:209-221. doi:https://doi.org/10.1016/j.polymer.2014.12.034

347. Motloung MP, Mofokeng TG, Ojijo V, Ray SS. A review on the processing–morphology–property relationship in biodegradable polymer composites containing carbon nanotubes and nanofibers. *Polym Eng Sci*. 2021;61(11):2719-2756. doi:https://doi.org/10.1002/pen.25798

Publications

&

Scientific contributions

Publications in international journals

As first author:

Houbben, M., Sànchez, C. P., Vanderbemden, P., Noels, L., & Jérôme, C. (13 June 2023). **MWCNTs filled PCL covalent adaptable networks: towards reprocessable, self-healing and fast electrically-triggered shape-memory composites**. Polymer, 278, 125992. doi:10.1016/j.polymer.2023.125992.

Houbben, M., Thomassin, J.-M., & Jérôme, C. (21 March 2022). **Supercritical CO2 blown poly(ε-caprolactone) covalent adaptable networks towards unprecedented low density shape memory foams**. Materials Advances, 3 (6), 2918-2926. doi:10.1039/d2ma00040g.

Houbben, M., & Jérôme, C. (2023) '**A review on thermo-responsive electro-active and magneto-active shape memory polymer nanocomposites**', to be submitted.

As coauthor:

Pereira Sánchez, C.A., Houbben M., Fagnard, J.-F, Laurent, P., Jérôme, C., Noels, L. and Vanderbemden, P. (2021) '**Resistive heating of a shape memory composite: analytical, numerical and experimental study**', Smart Materials and Structures, 31(2) 025003. Available at: https://doi.org/10.1088/1361-665X/ac3ebd.

Pereira Sánchez, C.A., Houbben M., Fagnard, J.-F, Harmeling, P., Jérôme, C., Noels, L. and Vanderbemden, P. (2022) '**Experimental characterization of the thermo-electromechanical properties of a shape memory composite during electric activation**', Smart Materials and Structures, 31(9) 095029. Available at: https://doi.org/10.1088/1361- 665X/ac8297.

Gülaşık, H.; Houbben, M.; Pereira Sánchez, C.A.; Calleja Vázquez, J.M; Vanderbemden, P.; Jérôme, C.; Noels, L. '**A Thermo-Mechanical, Viscoelasto-Plastic Model for Semi-Crystalline Polymers Exhibiting One-Way and Two-Way Shape Memory Effects Under Phase Change**', submitted to Journal of the Mechanics and Physics of Solids on 31 May 2023.

Poster and oral presentations

Houbben, M., Thomassin, J.-M., & Jérôme, C. (2019) '**Supercritical CO2 Foaming of PCL Covalent Networks: taking benefit from the thermoreversible Diels– Alder Cycloaddition**'. Poster presented by M. Houbben at Belgian Polymer Group (BPG2019), Houffalize, Belgique.

Houbben, M., & Jérôme, C. (2021) '**Supercritical CO Foaming of PCL Covalent Networks: taking benefit from the thermoreversible Diels– Alder Cycloaddition**'. Poster presented by M. Houbben at Material Research Society (Virtual MRS spring meeting 2021), Virtual.

Houbben, M., Thomassin, J.-M., & Jérôme, C. (2021) '**Thermoreversible Diels-Alder Cycloaddition as a convienent tool for the design of Shape Memory Foams**'. Oral presentation presented by M. Houbben at virtual Belgian Polymer Group (BPG2021), Virtual.

Houbben, M., Thomassin, J.-M., & Jérôme, C. (2021) '**Supercritical CO2 Foaming of PCL Reversible Covalent Networks towards highly expanded biodegradable shapememory foam**'. Poster presented by M. Houbben at Advanced Functional Polymers for Medicine (AFPM 2021), Virtual.

Houbben, M., Thomassin, J.-M., & Jérôme, C. (2021) '**Supercritical CO2 blown poly(e-caprolactone) covalent adaptable networks as smart materials for biomedical applications**'. Oral presentation presented by M. Houbben at European Polymer Congress 2022 (EPF 2022), Prague, Czech Republic.

Houbben, M., Pereira Sánchez, C.A., Vanderbemden, P., Noels, L. and Jérôme, C. (2022) '**Comprehensive study of adding MWCNT to covalent adaptable networks of PCL towards fast and electrically triggered shape memory remoldable composites**'. Poster presented by M. Houbben at Polymer Network Group (PNG2022), Rome, Italy.

Awards

Best poster award nominee at virtual Material Research Society (MRS 2021).
Best poster award at Polymer Network Group (PNG 2022).